

**HYBRID NANOCOMPOSITES FOR HIGH-PERFORMANCE LI-  
ION BATTERY ELECTRODES: CARBOXYLATED  
POLYTHIOPHENE-BASED ELECTRODES**

A Dissertation  
Presented to  
The Academic Faculty

by

Yo Han Kwon

In Partial Fulfillment  
of the Requirements for the Degree  
Doctor of Philosophy in the  
School of Chemical & Biomolecular Engineering

Georgia Institute of Technology  
May 2018

**COPYRIGHT © 2018 BY YO HAN KWON**

**HYBRID NANOCOMPOSITES FOR HIGH-PERFORMANCE LI-  
ION BATTERY ELECTRODES: CARBOXYLATED  
POLYTHIOPHENE-BASED ELECTRODES**

Approved by:

Dr. Elsa Reichmanis, Advisor  
School of Chemical & Biomolecular  
Engineering  
*Georgia Institute of Technology*

Dr. J. Carson Meredith  
School of Chemical & Biomolecular  
Engineering  
*Georgia Institute of Technology*

Dr. Thomas F. Fuller  
School of Chemical & Biomolecular  
Engineering  
*Georgia Institute of Technology*

Dr. Seung Woo Lee  
School of Mechanical Engineering  
*Georgia Institute of Technology*

Dr. Paul A. Kohl  
School of Chemical & Biomolecular  
Engineering  
*Georgia Institute of Technology*

Date Approved: [March 08, 2018]

*A dedication to*

*God,*

*My wife, Hyeyoung & my children, Jueun and Juan*

*who are my precious and make my life more special and significant...*

## ACKNOWLEDGEMENTS

First and foremost, I would like to thank my PhD advisor, Elsa, for her constant trust, encouragement, support, and guidance during my entire course of study. Specially, her nice personality and humbleness has been one of the great lessons beyond compare. Besides, her dedication and enthusiasm towards research has been a great inspiration to me. She is a great mentor who considers students' growth, safety, health and their family as the topmost priority and I am very happy and fortunate to have her as an advisor. I would also like to thank all my other committee members: Profs. Thomas F. Fuller, Paul A. Kohl, J. Carson Meredith, and Seung Woo Lee, for evaluating my thesis and giving me some valuable suggestions.

I would like to thank the Reichmanis group members for their wonderful company, assistance and encouragement throughout my doctoral studies. Among them, I would like to mention Krysten Minnici, Guoyan Zhang, Ji-Hwan Kang, Dalsu Choi, Sujin Lee, Michael McBride, Bailey Risteen, Zhibo Yuan and Brian Khau. Especially, I would like to appreciate my collaborators, Jung Jin Park who was a visiting scholar from KAIST in 2016 and helped with synthesis of  $\text{Fe}_3\text{O}_4$  spheres, and Byeongyong Lee who is working in Prof. Seung Woo Lee group, suggesting FWNT materials. Thanks also to all the friends/members in the Korean Student Association of ChBE, with whom I shared both my successes and my failures as a grad student and further helped me with soft-landing to unfamiliar environment when I started studying here. Their encouragement and assistance have been a great support to me. In particular, my gratitude to Won Min Park, Hyuk Taek



Kwon, Yongmin Cho, Won Tae Choi, Donglee Shin, Jungseob So, Chunjae Yoo, Byunghyun Min, Jongwoo Park.

For my battery works, Prof. Thomas Fuller, Prof. Nian Liu, and their group members all are much appreciated to give me a great chance to use their electrochemical equipment. Among them, I want to mention Dr. Rajiv Jaini, Gregory Chipman, Jung Fang, Yamin Zhang, Yutong Wu for their kind assistance.

Most importantly, I thank my family. I am utmost indebted to my wife, Hyeyoung Seok for her unconditional love and support. She has given constant encouragement in every step I have taken and thereby helped realize my dreams. I would also like to thank both my children, Jueun and Juan, for their absolute love and encouragement in every phase of my life. They all are my utmost precious in my whole life.

Finally, I would like to attribute the whole glory to God.

## TABLE OF CONTENTS

<b>ACKNOWLEDGEMENTS</b>	<b>iv</b>
<b>LIST OF TABLES</b>	<b>viii</b>
<b>LIST OF FIGURES</b>	<b>ix</b>
<b>SUMMARY</b>	<b>xx</b>
<b>CHAPTER 1. Introduction</b>	<b>1</b>
1.1 General understanding of lithium-ion (Li-ion) batteries <sup>1-7</sup>	1
1.1.1 Li-ion Batteries	2
1.1.2 Battery Configuration	4
1.2 Research Motivation	6
1.3 Thesis Overview	9
<b>CHAPTER 2. Oleic Acid Capped Fe<sub>3</sub>O<sub>4</sub> and P3HT-Based Electrodes</b>	<b>11</b>
2.1 Introduction	11
2.2 Experimental Section	15
2.3 Results and Discussion	18
2.3.1 Materials Morphology	19
2.3.2 Physical Affinity Relationship	25
2.3.3 Electrical Properties	30
2.3.4 Electrochemical Evaluation	34
2.4 Conclusion	39
<b>CHAPTER 3. Electron and Ion Transport Enhancer: PEG-Coated Fe<sub>3</sub>O<sub>4</sub> and PPBT Water-Soluble Carboxylate Polythiophene-Based Electrodes</b>	<b>41</b>
3.1 Introduction	41
3.2 Experimental Section	44
3.3 Results and Discussion	46
3.3.1 Electrochemical properties of PPBT	46
3.3.2 Effect of PEG coating on the Fe <sub>3</sub> O <sub>4</sub> surface	49
3.3.3 Electrochemical Performance	52
3.3.4 Surface Analysis	56
3.3.5 Proposed Mechanism	58
3.4 Conclusion	61
<b>CHAPTER 4. Carbon Nanotube Web with Carboxylated Polythiophene “Assist” for High-Performance Battery Electrodes</b>	<b>63</b>
4.1 Introduction	63
4.2 Experimental Section	67
4.3 Results and Discussion	70
4.3.1 Materials Preparation	71

4.3.2	Fabrication of FWNT Web Electrode	76
4.3.3	Surface Analysis	81
4.3.4	Electrochemical Evaluation	83
4.3.5	Comparison with SDBS Surfactant-Assisted Electrode System	93
<b>4.4</b>	<b>Conclusion</b>	<b>97</b>
<b>CHAPTER 5. SWNT Anchoring on High-Capacity Anode Materials with Carboxylated Polythiophene ‘Links’</b>		<b>99</b>
<b>5.1</b>	<b>Introduction</b>	<b>99</b>
<b>5.2</b>	<b>Experimental Section</b>	<b>102</b>
<b>5.3</b>	<b>Results and Discussion</b>	<b>106</b>
5.3.1	Approach	106
5.3.2	SWNT-Anchored $\text{sFe}_3\text{O}_4$ with Carboxylated Polythiophene (PPBT) Links.	107
5.3.3	SWNT-Anchored Si NPs with Carboxylated Polythiophene (PPBT) Links.	116
5.3.4	SWNT-Anchored $\text{c-SiO}_x$ with Carboxylated Polythiophene (PPBT) Links.	122
5.3.5	SWNT-Anchored $\text{c-SiO}_x$ and Graphite Blended Electrode System.	128
5.3.6	Pouch-Type Full-Cell Evaluation	132
5.3.7	Proposed Mechanism	135
<b>5.4</b>	<b>Conclusion</b>	<b>137</b>
<b>CHAPTER 6. Conclusions</b>		<b>139</b>
<b>6.1</b>	<b>Summary</b>	<b>139</b>
<b>6.2</b>	<b>Future Works</b>	<b>143</b>
6.2.1	Elastomeric components	143
<b>References</b>		<b>147</b>
<b>VITA</b>		<b>163</b>

## LIST OF TABLES

<b>Table 3.1.</b> Comparison of electroactive anode materials for Li-ion batteries.....	42
<b>Table 5.1.</b> Electrochemical kinetic parameters obtained from CV analysis with various scan rates: transfer coefficient ( $\alpha$ ) and apparent lithium-ion diffusion coefficient ( $D_{Li}$ ).....	114

## LIST OF FIGURES

<b>Figure 1.1.</b> Schematic diagram of a Li-ion cell. During charging, lithium ions flow to the negative electrode through the electrolyte and electrons flow from the external circuit. During discharge the directions are reversed, generating useful power to be consumed by the device.....	2
<b>Figure 1.2.</b> Galvanostatic charge-discharge voltage profiles of (a) a graphite anode, (b) LiCoO <sub>2</sub> cathode, and (c) full cell comprising the graphite anode and LiCoO <sub>2</sub> cathode.....	3
<b>Figure 1.3.</b> Schematic illustration of various Li-ion battery configurations: (a) Cylindrical cell, (b) prismatic cell, (c) coin cell, (d) thin and flat cell (or pouch cell).....	4
<b>Figure 1.4.</b> Schematic illustration of battery electrodes.....	5
<b>Figure 1.5.</b> Coin cell assembly of the electrode half-cells.....	6
<b>Figure 2.1.</b> (a) Dispersion state in different solvents. Capped Fe <sub>3</sub> O <sub>4</sub> is well-dispersed in chloroform and chlorobenzene. (b) OM images of uncapped Fe <sub>3</sub> O <sub>4</sub> /P3HT composites and OA-capped Fe <sub>3</sub> O <sub>4</sub> /P3HT composites. Samples were prepared by spin coating on glass substrates using chloroform solvent.....	19
<b>Figure 2.2.</b> (a) OM images of OA-Fe <sub>3</sub> O <sub>4</sub> /carbon/polymer composites according to different carbon content. The absolute amount of OA-Fe <sub>3</sub> O <sub>4</sub> and polymer was kept constant. The volume percent of carbon content was converted by material density. (b) OM images of carbon/polymer composites with different carbon content. P3HT system shows much more favorable uniform dispersion than PVDF system. (c) Tapping mode AFM height and phase images of 49 vol. % of carbon/P3HT composite film, demonstrating the conductive percolation networks.....	22
<b>Figure 2.3.</b> AFM images of OA-Fe <sub>3</sub> O <sub>4</sub> /carbon/P3HT composites according to different carbon content. AFM images exhibit the network formation of carbon additives connected with OA-Fe <sub>3</sub> O <sub>4</sub> nanoparticles by the change of carbon content.....	23
<b>Figure 2.4.</b> SEM images of OA-Fe <sub>3</sub> O <sub>4</sub> /carbon/polymer composite electrodes (Top view). (a) P3HT-based electrode (blade coating). (b) PVDF-based electrode (blade coating). (c) P3HT-based electrode (spin coating, inset: carbon/P3HT). (d) PVDF-based electrode (spin coating, inset: carbon/PVDF). The spin coated material shows the distinct morphology associated with the material dispersion state.....	24
<b>Figure 2.5.</b> Hansen solubility parameter (HSP) spheres of interaction for (a) OA-Fe <sub>3</sub> O <sub>4</sub> /carbon/P3HT and (b) OA-Fe <sub>3</sub> O <sub>4</sub> /carbon/PVDF. Tables show HSPs of the composite	

battery electrode components and superimposed volume portions ( $\%V_{int}$ ) for each polymer volume ( $V_{polymer}$ ).....27

**Figure 2.6.** Surface physical affinities between oleic acid (OA) and polymer (P3HT & PVDF): (a) contact angle measurement (OA droplet on polymer film) and (b) HSP spheres of interaction. Table represents the values of HSP,  $R_a$  and RED. The RED of unsaturated hydrocarbon part of OA (OA-Hydrophobic) with P3HT is less than 1, predicting they are miscible.....28

**Figure 2.7.** (a) Schematic structure and photo-image of bottom contact electrode device. (b) Schematic diagram of mold casting process showing fabrication of the electrode devices for measuring the electronic conductivity. The respective composite slurries were mold-casted onto the device substrates (channel width = 10  $\mu\text{m}$  and length = 50  $\mu\text{m}$ ). The thickness of composite films was approx. 4~10 $\mu\text{m}$ .....31

**Figure 2.8.** Electronic conductivities of (a) carbon/polymer composites (spin-coating method): inset figures showing the OM images of 45 vol. % of carbon/P3HT and 57% vol. % of carbon/PVDF which are considered the percolation threshold concentration in spin-coated electrodes, (b) carbon/polymer composites (mold-casting method) and (c) OA- $\text{Fe}_3\text{O}_4$ /carbon/polymer composites (mold-casting method) with constant amount of OA- $\text{Fe}_3\text{O}_4$  and polymer. The graph has the sphere symbols expressing the average conductivity, together with the upper bar for the largest value and the lower bar for the smallest value.....32

**Figure 2.9.** Voltage profiles for  $\text{Fe}_3\text{O}_4$  half-cells.....35

**Figure 2.10.** Electrochemical Impedance Spectroscopy (EIS) results for coin cells before cycling. (a) Nyquist plot of EIS results, (b) Nyquist plot of EIS results with smaller axes values, (c) Bode plot of EIS results, (d) equivalent circuit used to fit EIS data, and (e) results from fitting EIS with equivalent circuit.....37

**Figure 3.1.** Electrochemical characterization of PPBT binder. (a) CV profiles of PPBT binder in the potential window of 0.01 to 3 V vs  $\text{Li}/\text{Li}^+$  collected at the rate of 0.5  $\text{mV s}^{-1}$  (inset: PPBT vs PVDF at 1<sup>st</sup> cycle). (b) Trend of charge transfer resistance with the change of applied voltage measured by EIS in the frequency range from 1 MHz to 0.1 Hz. (c) Comparison of electronic conductivity between PVDF and PPBT system. (d) Illustration of electrochemical doping: PPBT electronic and chemical structure changes during reduction (n-doping).....47

**Figure 3.2.** Effect of PEG coating on the  $\text{Fe}_3\text{O}_4$  surface. (a) Schematics of PEG 1500 coating on the  $\text{Fe}_3\text{O}_4$  surface through an ultrasonic probe. (b) Hansen solubility parameter (HSP) spheres of interaction for PEG and PPBT. (c) SEM images of PEG- $\text{Fe}_3\text{O}_4$  particles compared to bare  $\text{Fe}_3\text{O}_4$  (inset). (d) Optical microscopy (OM) images of PEG- $\text{Fe}_3\text{O}_4$ /PPBT

and Fe<sub>3</sub>O<sub>4</sub>/PPBT composites (inset) prepared by spin coating on the glass substrate. (e) SEM images (cross-sectional view) of PEG-Fe<sub>3</sub>O<sub>4</sub>/carbon/PPBT electrode and Fe<sub>3</sub>O<sub>4</sub>/carbon/PPBT electrode (inset). (f) SEM image (surface view) of PEG-Fe<sub>3</sub>O<sub>4</sub>/carbon/PPBT electrode exhibiting well-dispersion Fe<sub>3</sub>O<sub>4</sub> particles in the carbon mixture.....50

**Figure 3.3.** PEG-Fe<sub>3</sub>O<sub>4</sub> particles: (a) TGA profile of PEG coating, which is carried out in nitrogen in the temperature range of 25–600 °C at a heating rate of 20 °C/min. (b) Dynamic light scattering (DLS) particle size distribution of PEG-Fe<sub>3</sub>O<sub>4</sub> particles. DLS was performed using a Malvern Zetasizer NANO ZS instrument (Malvern instruments). PEG-Fe<sub>3</sub>O<sub>4</sub> particles were dispersed in aqueous medium through bath-type sonication for 30 min (1mg particles/1mL deionized water).....51

**Figure 3.4.** PVDF binder system. The SEM images of (a) surface view and (b) cross-sectional view of Fe<sub>3</sub>O<sub>4</sub>/carbon/PVDF electrode. (c) OM image of carbon/binder composites (50:50 in a mass ratio) prepared by spin coating on the glass substrate.....52

**Figure 3.5.** Electrochemical performance of Fe<sub>3</sub>O<sub>4</sub>-based electrodes. (a) CV profiles of PEG-Fe<sub>3</sub>O<sub>4</sub>/carbon/PPBT electrode in the potential window of 0.01 to 3 V *vs* Li/Li<sup>+</sup> collected at the rate of 0.5 mV s<sup>-1</sup> (the inset shows the galvanostatic charge-discharge profiles in the potential window of 0.01 to 3 V *vs* Li/Li<sup>+</sup> at a constant current density of 80 mA g<sup>-1</sup>, comparable to CV profiles). (b) Cycling performance (=capacity retention as function of cycle number) collected for the current density of 240 mA g<sup>-1</sup> (~0.3 C) between 0.3 and 3 V. (open circles: Li-insertion capacity, filled circles: Li-extraction capacity) (c) The impedance spectra measured at 3 V before cycling (bottom graph) and at open-circuit voltage (OCV) after 50 cycles (upper graph) in the frequency range from 1 MHz to 0.1 Hz. (d) Cycling performance between 0.01 and 3 V. (e) Delithiation rate capability, where cells were lithiated at a constant current density of 80 mA g<sup>-1</sup> and delithiated at different current densities between 0.01 and 3 V. (open symbols: capacity retention, filled symbols: Li-extraction capacity) (f) Cell polarization as a function of the applied current density during the delithiation process.....53

**Figure 3.6.** Spectroscopy characterization of the Fe<sub>3</sub>O<sub>4</sub>, PEG-Fe<sub>3</sub>O<sub>4</sub>, PPBT and electrodes prepared by mixing PEG-Fe<sub>3</sub>O<sub>4</sub> (or Fe<sub>3</sub>O<sub>4</sub>) with PPBT binder. (a) FT-IR spectra of materials (bottom lines: Fe<sub>3</sub>O<sub>4</sub>, PEG-Fe<sub>3</sub>O<sub>4</sub>, PPBT) and electrodes (upper lines: Fe<sub>3</sub>O<sub>4</sub>/PPBT, PEG-Fe<sub>3</sub>O<sub>4</sub>/PPBT). (b) The possible binding modes of complexes on the Fe<sub>3</sub>O<sub>4</sub> surface. (c) and (d) XPS spectra of materials (Fe<sub>3</sub>O<sub>4</sub>, PEG-Fe<sub>3</sub>O<sub>4</sub>, PPBT) and electrodes (Fe<sub>3</sub>O<sub>4</sub>/PPBT, PEG-Fe<sub>3</sub>O<sub>4</sub>/PPBT).....56

**Figure 3.7.** Schematic illustrations depicting electron and ion transport in the electrode.....59

**Figure 3.8.** Effects of material dispersion using chemical/physical dispersion process. (a) OM image of PEG-Fe<sub>3</sub>O<sub>4</sub>/carbon /PPBT composites spin-casted on the glass substrate after probe-type ultra-sonication (physical dispersion). (b) Hansen solubility parameter analysis of PEG 1500, PPBT and carbon: physical affinity of carbon additives were deviated from Hansen sphere of PEG 1500 and PPBT. SDBS surfactant was used for the carbon dispersion (chemical dispersion). (c) Cycling performance (= capacity retention as a function of cycle numbers) of PEG-Fe<sub>3</sub>O<sub>4</sub>/carbon/PPBT, PEG-Fe<sub>3</sub>O<sub>4</sub>/carbon /SDBS/PPBT, and PEG-Fe<sub>3</sub>O<sub>4</sub>/carbon/PPBT prepared by probe-type ultra-sonication. (d) EIS results of coin cell measured before cycling and after 50 cycles. The chemical/physical dispersion process both has largely increase in  $R_{ct}$  before cycling, which affects the resulting poor cycling, especially for the sonication dispersion process.....60

**Figure 3.9.** Surface view SEM images of (a) PEG-Fe<sub>3</sub>O<sub>4</sub>/carbon/PPBT, (b) PEG-Fe<sub>3</sub>O<sub>4</sub>/carbon/SDBS/PPBT and (c) PEG-Fe<sub>3</sub>O<sub>4</sub>/carbon/PPBT prepared by probe-type ultra-sonication.....61

**Figure 4.1.** Materials preparation: effect of PEG coating and PPBT assist on materials dispersion and sFe<sub>3</sub>O<sub>4</sub>-FWNT connection. (a) Schematics of the formation of Fe-carboxylate complex. (b) SEM image of monodispersed Fe<sub>3</sub>O<sub>4</sub> spheres (sFe<sub>3</sub>O<sub>4</sub>). (c) Size distribution of sFe<sub>3</sub>O<sub>4</sub> particles, counted from SEM images. (d) Hansen solubility parameter (HSP) spheres of interaction for PEG and PPBT having 98.3% of the intersection volume portion (% $V_{int}$ ). (e) Optical microscopy (OM) images of PEG-sFe<sub>3</sub>O<sub>4</sub>/PPBT and sFe<sub>3</sub>O<sub>4</sub>/PPBT composites (inset) prepared by spin coating on the glass substrate. (f) FWNT dispersion state after probe-type sonication (top: OM images prepared by spin coating onto a glass substrate, bottom: corresponding suspension images). (g) Electronic conductivities of FWNT and PPBT composite film. The effective weight ratio of FWNT and PPBT was found as 1 to 2 having higher conductivity and good dispersion. (h) SEM and TEM (inset) images demonstrating the dispersion/connection of PEG-sFe<sub>3</sub>O<sub>4</sub> and FWNTs through a PPBT assist in the electrode slurry. The SEM/TEM characterizations were conducted after evaporating water solvent.....71

**Figure 4.2.** Monodispersed Fe<sub>3</sub>O<sub>4</sub> spheres (sFe<sub>3</sub>O<sub>4</sub>). (a) XRD pattern. (b) Galvanostatic charge-discharge profile of Cu foil electrode (sFe<sub>3</sub>O<sub>4</sub>/CB/CBC binder) in the potential window of 0.01 to 3 V vs Li/Li<sup>+</sup> at a constant current density of 0.1C (~90 mA g<sup>-1</sup>). (c) Cycling performance of monodispersed Fe<sub>3</sub>O<sub>4</sub> spheres (sFe<sub>3</sub>O<sub>4</sub>)-based electrode, compared with random-shaped Fe<sub>3</sub>O<sub>4</sub> particles (0.5C rate). sFe<sub>3</sub>O<sub>4</sub> particle system shows much improved capacity retention. (d) Cycling performance of Cu foil electrodes. Half coin cell includes no FEC additive in the electrolyte. PEG coating-PPBT binder system represents higher enhanced electrochemical performance in the Cu foil electrode system.....72

**Figure 4.3.** Dynamic light scattering (DLS) particle size distribution of sFe<sub>3</sub>O<sub>4</sub> particles and PEG-sFe<sub>3</sub>O<sub>4</sub> particles dispersed in water solvent, and sFe<sub>3</sub>O<sub>4</sub> particles and PEG-sFe<sub>3</sub>O<sub>4</sub>



particles dispersed in PPBT solution. DLS was performed using a Malvern Zetasizer NANO ZS instrument (Malvern instruments). The particles were dispersed through bath-type sonication for 30 min (1mg particles/1mL deionized water).....74

**Figure 4.4.** Fabrication of FWNT web electrode. (a) A schematic representation of the overall fabrication procedure for FWNT web electrode, composed of PEG-sFe<sub>3</sub>O<sub>4</sub>/CB/FWNT/PPBT. (b) Photographs of FWNT dispersion and electrode slurry in water solvent after probe-type sonication. (c) Comparison of fabricated electrodes having long-chain FWNTs (sub-mm length) vs short-chain MWNTs (inset). (d) A photograph of a self-standing, flexible FWNT web electrode. (e) Electronic conductivity and porosity of FWNT web electrode, compared with Cu foil electrode (PEG-sFe<sub>3</sub>O<sub>4</sub>/CB/PPBT). (f, g) Cross-sectional and (h) surface-view SEM images of FWNT web electrode.....78

**Figure 4.5.** TGA profiles (a) sFe<sub>3</sub>O<sub>4</sub> and PEG-sFe<sub>3</sub>O<sub>4</sub>, (b) carbon black and FWNT, and (c) PPBT powders and FWNT web electrode, which were carried out in air in the temperature range of 50–900 °C at a heating rate of 10 °C/min.....79

**Figure 4.6.** EDS mapping showing the existence of PPBT component, but no potassium element. This gives more clear evidence that PPBT was attached on the sFe<sub>3</sub>O<sub>4</sub> surface through the Fe-carboxylate bonding.....80

**Figure 4.7.** Spectroscopy characterization. (a) FT-IR spectra of materials (sFe<sub>3</sub>O<sub>4</sub>, PEG-sFe<sub>3</sub>O<sub>4</sub>, PPBT, FWNT) and FWNT web electrode. Peaks were normalized with a peak at 575 cm<sup>-1</sup> associated with the vibration of Fe–O lattice of sFe<sub>3</sub>O<sub>4</sub>. (b) XPS survey spectra of FWNT web electrode with filtration process, in comparison with not-filtrated electrode (solution casting process). (c, d) XPS spectra of materials (sFe<sub>3</sub>O<sub>4</sub>, PEG-sFe<sub>3</sub>O<sub>4</sub>, PPBT, FWNT) and FWNT web electrode.....81

**Figure 4.8.** Electrochemical characterization of FWNT web electrode. (a) Cyclic voltammetry (CV) profiles of FWNT web electrode, Cu foil electrode (PEG-sFe<sub>3</sub>O<sub>4</sub>/CB/PPBT) and FWNT in the potential window of 0.01 to 3 V vs Li/Li<sup>+</sup> collected at the rate of 0.5 mV s<sup>-1</sup>. (b) Galvanostatic charge-discharge profiles in the potential window of 0.01 to 3 V vs Li/Li<sup>+</sup> at a constant current density of 0.1C (~90 mA g<sup>-1</sup>), comparable to CV profiles. (c) Cycling performance (=capacity retention as function of cycle number) collected for the current density of 0.5C (~450 mA g<sup>-1</sup>) between 0.01 and 3 V. (open circle: Coulombic efficiency of FWNT web electrode). (d) Variation of electrode internal resistance ( $R_{ohm}$ ,  $R_{SEI}$ ,  $R_{CT}$ ) after cycling, fitted by EIS results. EIS characterization was conducted at open-circuit voltage (OCV) after 50 and 200 cycles. (e) XPS spectra (C 1s, O 1s, F 1s) of FWNT web electrode and Cu foil electrode (PEG-sFe<sub>3</sub>O<sub>4</sub>/CB/PPBT) after 200 cycles. (f, g) Cycling performance of FWNT web electrodes demonstrating the

effect of (f) PEG coating on the  $\text{sFe}_3\text{O}_4$  surface, and (g) carbon addition into the electrode to acquire more inner pores.....84

**Figure 4.9.** EIS fitting results. The impedance spectra were measured at open-circuit voltage (OCV) in the frequency range from 1 MHz to 0.1 Hz.....87

**Figure 4.10.** SEM images of web electrodes of (a)  $\text{sFe}_3\text{O}_4/\text{FWNT}/\text{PPBT}$ , (b)  $\text{PEG-sFe}_3\text{O}_4/\text{FWNT}/\text{PPBT}$ , (c)  $\text{sFe}_3\text{O}_4/\text{FWNT}$  (SDBS), and (d)  $\text{PEG-sFe}_3\text{O}_4/\text{FWNT}$  (SDBS). SDBS surfactant helps effectively connect  $\text{sFe}_3\text{O}_4$  particles and FWNT, and PPBT for  $\text{PEG-sFe}_3\text{O}_4$  particles and FWNT.....88

**Figure 4.11.** FWNT web electrodes without carbon addition. Increase in FWNT content of the electrodes affected their improved electronic conductivity, but had negatively impact on cycling performance. That might be attributed to covering the pores, thereby preventing ion transport inside electrode.....89

**Figure 4.12.** Rate capability and corresponding electrochemical properties. (a) Lithiation rate capability, where cells were delithiated at a constant current density of 0.1C ( $\sim 90 \text{ mA g}^{-1}$ ) and lithiated at different current densities (0.1–3C, 1C rate =  $900 \text{ mA g}^{-1}$ ) between 0.01 and 3 V. (b) Delithiation rate capability, where cells were lithiated at a constant current density of 0.1C ( $\sim 90 \text{ mA g}^{-1}$ ) and delithiated at different current densities (0.1–3C, 1C rate =  $900 \text{ mA g}^{-1}$ ) between 0.01 and 3 V. (c) Ohmic polarization, and (d) charge transfer polarization as a function of the applied current density during the lithiation and delithiation process. (e, f) Tafel plots:  $\ln(I_{\text{applied}})$  vs  $\Delta E$ , which were plotted from the results of charge transfer polarization in the range from 0.1C to 2C.....90

**Figure 4.13.** Electrochemical characterization: comparison with SDBS surfactant-assisted electrode system of  $\text{sFe}_3\text{O}_4/\text{FWNT}$  (SDBS) and  $\text{sFe}_3\text{O}_4/\text{CB}/\text{FWNT}$  (SDBS). (a) Galvanostatic charge-discharge profiles in the potential window of 0.01 to 3 V vs  $\text{Li}/\text{Li}^+$  at a constant current density of 0.5C ( $\sim 450 \text{ mA g}^{-1}$ ). (b) Cycling performance (=capacity retention as a function of cycle number) collected at the current density of 0.5C ( $\sim 450 \text{ mA g}^{-1}$ ) between 0.01 and 3 V. (c) Electrode internal resistance ( $R_{\text{ohm}}$ ,  $R_{\text{SEI}}$ ,  $R_{\text{CT}}$ ) after 200 cycles, fitted by EIS results. (d) Rate capability (close circles: lithiation rate capability, open circles: delithiation rate capability). (e, f) Tafel plots:  $\ln(I_{\text{applied}})$  vs  $\Delta E$ , which were plotted from the results of charge transfer polarization in the range from 0.1C to 2C.....93

**Figure 4.14.** Surface view SEM images of SDBS surfactant-assisted electrodes of (a)  $\text{sFe}_3\text{O}_4/\text{FWNT}$  (SDBS), and (b)  $\text{sFe}_3\text{O}_4/\text{CB}/\text{FWNT}$  (SDBS).....94

**Figure 4.15.** Analysis of SDBS surfactant-assisted electrode system. Cross-sectional SEM images of (a)  $\text{sFe}_3\text{O}_4/\text{FWNT}$  (SDBS) and (b)  $\text{sFe}_3\text{O}_4/\text{CB}/\text{FWNT}$  (SDBS). (c) Size distribution of  $\text{sFe}_3\text{O}_4$  aggregates observed in the SEM images of each electrode cross-

section. (d) Electronic conductivity and porosity. (e) The impedance spectra measured at open-circuit voltage (OCV) before battery testing in the frequency range from 1 MHz to 0.1 Hz. (f) XPS analysis of SEI layer after 200 cycles.....95

**Figure 4.16.** Cycling performance comparing FWNT web electrode with SDBS surfactant-assisted electrode system including  $\text{sFe}_3\text{O}_4/\text{FWNT}$  (SDBS) and  $\text{sFe}_3\text{O}_4/\text{CB}/\text{FWNT}$  (SDBS). The electrolyte was a solution of 1.2 M  $\text{LiPF}_6$  in EC/DEC (1/1 by volume) without FEC additive. After 200 cycles, EIS measurement was performed in the frequency range from 1 MHz to 0.1 Hz.....97

**Figure 5.1.** Schematic illustration of the preparation of the SWNT-anchored electroactive material with PPBT links. Carboxylate bonds between hydroxylated active particle and PPBT carboxyl substituent, and  $\pi$ - $\pi$  interactions between SWNT and PPBT conjugated backbone, provide for stable electrical linkages.....107

**Figure 5.2.** SWNT-anchored  $\text{sFe}_3\text{O}_4$  with carboxylated polythiophene (PPBT) links. (a) SEM images of SWNT- $\text{sFe}_3\text{O}_4$  particles. (b) FT-IR spectra and (c) XPS spectra of  $\text{sFe}_3\text{O}_4$ , PEG- $\text{sFe}_3\text{O}_4$ , PPBT, SWNT and SWNT-  $\text{sFe}_3\text{O}_4$ . (d) Galvanostatic charge-discharge profiles in the potential window of 0.01 to 3 V vs  $\text{Li}/\text{Li}^+$  at a constant current density of 90  $\text{mA g}^{-1}$  (0.1 C). (e) Cycling performance (=capacity retention as a function of cycle number) collected at the current density of 450  $\text{mA g}^{-1}$  (0.5 C) between 0.01 and 3 V (open circle: Coulombic efficiency of SWNT- $\text{sFe}_3\text{O}_4$  with CMC binder). Inset shows the electrodes' thickness change after 100 cycles as compared with electrodes before cycling. (f) The impedance spectra measured at open-circuit voltage (OCV) after 100 cycles in the frequency range from 1 MHz to 0.1 Hz, and (g) corresponding Warburg plots. The inserted figures are a slope, presenting Warburg coefficient ( $\Omega \text{ s}^{1/2}$ ) associated with ion diffusion resistance in the electrode. (h) Delithiation rate capability, where cells were lithiated at a constant current density of 90  $\text{mA g}^{-1}$  (0.1 C) and delithiated at different current densities between 0.01 and 3 V. (i) Galvanostatic charge-discharge profiles with different delithiation rates of SWNT- $\text{sFe}_3\text{O}_4$  with CMC binder in the potential window of 0.01 to 3 V vs  $\text{Li}/\text{Li}^+$ .....108

**Figure 5.3.** SWNT-anchored  $\text{sFe}_3\text{O}_4$  with carboxylated polythiophene (PPBT) links. (a) Cycling performance (=capacity retention as a function of cycle number) collected for the current density of 450  $\text{mA g}^{-1}$  (0.5C) between 0.01 and 3 V, comparing SWNT anchoring on the  $\text{sFe}_3\text{O}_4$  surface with PPBT carboxylate linkages with SWNT introduction with no PPBT linkages (prepared by sodium dodecylbenzenesulfonate (SDBS) surfactant instead of PPBT component). The electrodes were fabricated with CMC binder. The surface-view SEM images of the electrodes (after 100 cycles) composed of (b)  $\text{sFe}_3\text{O}_4$  with CMC binder, and (c) SWNT- $\text{sFe}_3\text{O}_4$  with CMC binder.....111

**Figure 5.4.** Electrode kinetics interpretation. Cyclic voltammetry (CV) profiles with various scan rates ( $\nu$ ) of the electrodes based on (a) SWNT-sFe<sub>3</sub>O<sub>4</sub> with CMC binder, (b) sFe<sub>3</sub>O<sub>4</sub> with CMC binder, and (c) SWNT-sFe<sub>3</sub>O<sub>4</sub> with PPBT binder. (d, e) Plots of  $\log(I_{pc})$  vs  $\log(\nu)$ , which were plotted from the results of cathodic peak currents and anodic peak currents of CV curves with different scan rates ( $\nu$ ), respectively. (f)  $I_{pc}$  vs  $\nu^{1/2}$  plots, where slopes are the apparent diffusion coefficient ( $\text{cm}^2 \text{s}^{-1}$ ).....113

**Figure 5.5.** SWNT-anchored Si NPs with carboxylated polythiophene (PPBT) links. (a) SEM images of SWNT-Si NPs. (b) FT-IR spectra of PPBT, Si NPs, and SWNT-Si NPs. (c) Cycling performance (=capacity retention as a function of cycle number) collected at the current density of 1250 mA g<sup>-1</sup> (0.5 C) between 0.01 and 1.5 V (open circle: Coulombic efficiency of SWNT-Si NPs with PPBT binder). (d) Galvanostatic charge-discharge profiles with different delithiation rates of SWNT-Si NPs with PPBT binder in the potential window of 0.01 to 1.5 V vs Li/Li<sup>+</sup>. Inset presents charge-discharge profiles. (e) Plots of  $\log(I_{pc})$  vs  $\log(\nu)$ , which were plotted from the results of cathodic peak currents of CV curves with different scan rates ( $\nu$ ). (f) Cycling performance at the current density of 1250 mA g<sup>-1</sup> (0.5 C) between 0.01 and 1.5 V. The electrode comprising SWNT anchoring on the Si NPs surface with PPBT carboxylate linkages was compared with that of SWNT introduction with no PPBT linkages (prepared by SDBS surfactant). The tested electrodes were fabricated with PPBT binder.....116

**Figure 5.6.** XPS spectra of SWNT-anchored Si NPs with carboxylated polythiophene (PPBT) links.....118

**Figure 5.7.** Electrochemical characterization of SWNT-anchored Si NPs with carboxylated polythiophene (PPBT) links. (a) Electronic conductivity of the electrodes composed of Si NPs, carbon black (CB), and PPBT binder. The amount of PPBT binder was fixed at 14 wt % and the electrodes were prepared according to different weight ratio of Si NPs and CB. (b, c) Cycling performance at the current density of 1250 mA g<sup>-1</sup> (0.5C) between 0.01 and 1.5 V, investigating the optimum composition of electrode materials (SWNT-Si NPs/CB/PPBT = 52/34/14 wt%) and SWNT coating amount (10 wt%) realizing better cycling performance. (d) Galvanostatic charge-discharge profiles with different delithiation rates of SWNT-Si NPs with PPBT binder vs Si NPs with CMC binder in the potential window of 0.01 to 3 V vs Li/Li<sup>+</sup>. Si NPs with CMC binder was used as the reference electrode, since the as-prepared electrode of Si NPs with PPBT binder showed poor adhesive and inferior surface. (e) Cycling performance with different charge-discharge rate conditions (0.5C vs 1C). (f) Effect of PPBT linkages for SWNT anchoring on Si NP surfaces. SWNT introduction with no PPBT linkages was prepared by sodium dodecylbenzenesulfonate (SDBS) surfactant instead of carboxylate bearing PPBT component. The electrodes were fabricated using CMC polymeric binder.....119

**Figure 5.8.** SEM images of the surface-view of the electrodes (after 100 cycles) composed of (a) Si NPs with CMC binder, and (b) SWNT-Si NPs with CMC binder. The electrode composed of Si NPs prepared by SWNT anchoring with PPBT carboxylate linkages presents less SEI layer formation, which indicates that SWNT introduction with PPBT links probably contributes to electrode stability that may enable capture pulverized/cracked particles, consequently favorable to forming stable SEI layer.....121

**Figure 5.9.** Proposed schematic illustration of the preparation of the c-SiO<sub>x</sub> comprising SWNT electrical networks with PPBT links.....123

**Figure 5.10.** SWNT-c-SiO<sub>x</sub> with carboxylated polythiophene (PPBT) links. (a) SEM images of SWNT-c-SiO<sub>x</sub> particles vs c-SiO<sub>x</sub> counterpart. (b) XPS spectra of c-SiO<sub>x</sub>, PEG-c-SiO<sub>x</sub>, PPBT, SWNT and SWNT-c-SiO<sub>x</sub>. (c) Cycling performance (=capacity retention as a function of cycle number) collected at the current density of 700 mA g<sup>-1</sup> (0.5 C) between 0.01 and 1.5 V, and (d) corresponding Coulombic efficiency. (e) Surface view SEM images of the electrode with c-SiO<sub>x</sub> (inset) and SWNT-c-SiO<sub>x</sub> active particles after 200 cycles. (f) Delithiation rate capability, where cells were lithiated at a constant current density of 140 mA g<sup>-1</sup> (0.1 C) and delithiated at different current densities between 0.01 and 1.5 V. (g) Cycling performance of the electrode composed of SWNT-c-SiO<sub>x</sub> and PPBT binder with different charge-discharge rate conditions (2 C vs 3 C). (h–j) Effect of carboxylated polythiophene (PPBT) links: Cycling performance of (h) PPBT binder- and (i) CMC binder-based electrodes at a current density of 700 mA g<sup>-1</sup> (0.5 C) between 0.01 and 1.5 V. The electrode comprising SWNT networks on the c-SiO<sub>x</sub> surface with PPBT linkages was compared with that of SWNT introduction with no PPBT linkages (prepared by SDBS surfactant). (j) Plots of log (*I*<sub>pc</sub>) vs log (*v*), which were plotted from the results of cathodic peak currents of CV curves with different scan rates (*v*).....124

**Figure 5.11.** CV profiles with various scan rates (*v*) of the CMC binder-based electrodes based on (a) SWNT-c-SiO<sub>x</sub>, (b) SWNT-c-SiO<sub>x</sub> (prepared by SDBS surfactant), and (c) c-SiO<sub>x</sub>.....126

**Figure 5.12.** Electrochemical evaluation of the electrode comprising c-SiO<sub>x</sub> and PPBT binder. (a) Cycle performance at 700 mA g<sup>-1</sup> (0.5C) between 0.01 and 1.5 V. (b) Corresponding Coulombic efficiency, reflecting SWNT integrated system more stable despite their similar electrochemical performance.....127

**Figure 5.13.** SWNT-c-SiO<sub>x</sub> and graphite blended system (in a mass ratio of 30:70). (a) Cycling performance (=capacity retention as a function of cycle number) collected at the current density of 300 mA g<sup>-1</sup> (0.5 C) between 0.01 and 1.5 V, and (b) corresponding Coulombic efficiency. (c) Variation of electrode internal resistances (*R*<sub>ohm</sub>, *R*<sub>SEI</sub>, *R*<sub>CT</sub>) after cycling, fitted by EIS results. EIS characterization was conducted at open-circuit voltage (OCV) after 50, 100, and 200 cycles. (d) Thickness change of electrodes based on the

CMC/SBR binder after 200 cycles. Inset image exhibits corresponding respective electrode. (e) Delithiation rate capability, where cells were lithiated at a constant current density of 60 mA g<sup>-1</sup> (0.1 C) and delithiated at different current densities between 0.01 and 1.5 V. (f) Charge-discharge profiles according to various rate conditions in the potential window of 0.01 to 1.5 V vs Li/Li<sup>+</sup> .....128

**Figure 5.14.** Cycle performance and Coulombic efficiency of c-SiO<sub>x</sub>/graphite blended electrode with CMC/SBR binder.....130

**Figure 5.15.** EIS fitting results of (a) c-SiO<sub>x</sub>/graphite (3/7) blend with CMC/SBR binder, and (b) SWNT-c-SiO<sub>x</sub>/graphite (3/7) blend with CMC/SBR binder. The impedance spectra measured at open-circuit voltage (OCV) in the frequency range from 1 MHz to 0.1 Hz. (c) Equivalent circuit used to fit EIS data, and (d) results from fitting EIS with equivalent circuit.....131

**Figure 5.16.** Aluminum (Al) pouch-type full cell. The cell is composed of a porous polyethylene (PE) separator.....132

**Figure 5.17.** Coin half-cell results of graphite and LCO. (a) The initial charge-discharge profiles of the electrode comprising graphite, CB, CMC, and SBR binder (95.8:1.7:1.5:1 in a mass ratio) when measured at 34 mA g<sup>-1</sup> (0.1C), observing a reversible capacity of 335 mAh g<sup>-1</sup> and initial efficiency of 88.8 %, and (b) corresponding cycle performance when measured at 170 mA g<sup>-1</sup> (0.5C). (c) The initial charge-discharge profiles of the electrode comprising LiCoO<sub>2</sub> (LCO), CB, and PVDF binder (94:3:3 in a mass ratio) when measured at 15 mA g<sup>-1</sup> (0.1C), observing a reversible capacity of 158 mAh g<sup>-1</sup> and initial efficiency of 96.0 %, and (d) corresponding cycle performance when measured at 75 mA g<sup>-1</sup> (0.5C).....132

**Figure 5.18.** Electrochemical comparison of a pouch-type full cell: LCO/graphite (Gr), LCO/SWNT-c-SiO<sub>x</sub>-Gr blend, and LCO/SWNT-c-SiO<sub>x</sub>-Gr blend. (a) Galvanostatic discharge areal capacities for 3 precycles at 0.05 C and for 100 cycles at 0.5 C in the potential range from 2.5 V to 4.25 V. (b) Capacity retention at various discharge rates from 0.2 C to 3 C with a constant charge rate of 0.2 C. (c, d) Voltage profiles for LCO/SWNT-c-SiO<sub>x</sub>-Gr blend plotted (c) as a function of the number of cycles and (d) as a function of the C-rate for the above cycle life and rate tests, respectively.....134

**Figure 5.19.** Proposed schematic illustration depicting (a) the pulverization of the electrode with the control electroactive particle and its resultant thick SEI layer formation, and (b) the operation of SWNT electrical networks securely anchored/connected on the pulverized particles through PPBT carboxylate bonds, which allows for structural, electrical stability and resulting stable SEI layers.....135

**Figure 5.20.** SWNT-anchored Si microparticles (Si MPs) with carboxylated polythiophene (PPBT) links. (a) SEM images of SWNT-Si MPs (the inset image shows the surface of pristine Si MPs). (b) Cycling performance (=capacity retention as function of cycle number) collected at the current density of  $1500 \text{ mA g}^{-1}$  between 0.01 and 1.5 V. Before the cycling test at  $1500 \text{ mA g}^{-1}$ , the electrodes were pre-cycled at  $300 \text{ mA g}^{-1}$  to measure a reversible capacity and initial efficiency. Si MPs based electrode showed the reversible capacity of  $3750 \text{ mAh g}^{-1}$  with the initial efficiency of 88.7 %, while the capacity of  $2615 \text{ mAh g}^{-1}$  and the initial efficiency of 83.2 % for SWNT-Si MPs. Corresponding (c) capacity retention normalized with the delithiated capacity at the first cycle, and (d) its Coulombic efficiency.....136

**Figure 6.1.** Polyrotaxane (PR)-polyacrylic acid (PAA) binder for Si MP anode.<sup>127</sup> (a, b) Proposed stress dissipation mechanism. (a) The pulley principle to lower the force in lifting an object. (b) Graphical representation of the operation of PR-PAA binder to dissipate the stress during volume changes of Si MPs, together with chemical structure of PR and PAA. (c) Comparison of stress-strain curves of PR-PAA and PAA films. (d) Cycling performance and corresponding Coulombic efficiency of coin half cell. From ref. 127. Reprinted with permission from AAAS.....144

**Figure 6.2.** (a) Proposed SWNT-PPBT networks crosslinked with amino ( $-\text{NH}_2$ ) terminated elastomer. (b) SEM image of SWNT-PPBT networks crosslinked with star PEG terminated with  $\text{NH}_2$ .....146

## SUMMARY

High performance is a major concern for the practical employment of advanced batteries including high energy/power densities associated with smart Internet of Things (IoTs) devices and electric vehicles (EVs). Previous studies provide critical clues for battery electrodes having superior performance. That is the electron and ion transporting behaviors that primarily determine the battery performance. Enhancing the electron/ion transport may result from the perspectives of rational consideration of materials and their systematic, structural design. In this research, systematic approaches to Li-ion battery electrodes considering both factors—electron and ion transport—that enable high electrochemical performance are described. In addition, conjugated polymers were studied as an effective polymeric binder or an electrical linker that facilitates the creation of electronic conduction pathways, coupled with carbonaceous conducting materials such as carbon blacks and carbon nanotube (CNT) networks.

This research comprises four parts: oleic acid capped  $\text{Fe}_3\text{O}_4$  and P3HT-based electrodes (*Study 1*), PEG-coated  $\text{Fe}_3\text{O}_4$  and water-soluble carboxylate polythiophene-based electrodes (*Study 2*), CNT web electrodes with carboxylated polythiophene (PPBT) ‘assist’ (*Study 3*), and SWNT-anchored high-capacity electroactive materials with PPBT ‘links’ (*Study 4*).

The background research, *Study 1*, pertaining to the use of the semiconducting polymer, poly(3-hexylthiophene) (P3HT) in  $\text{Fe}_3\text{O}_4$ -based electrodes to enhance electrode electrical properties, provided fundamental insights into a battery electrode. The results pointed to the necessity that electron transfer as well as ion transport must be considered



in the design of a composite electrode. *Study 2* includes methodical consideration for both ion and electron transport by introducing water-soluble, carboxylate polythiophene binder, poly[3-(potassium-4-butoate) thiophene] (PPBT), and facile polyethylene glycol (PEG) surface treatment. The enhanced performance could prove decisive in consideration of both factors for the electrode design. *Study 3* more focuses on the electrode structure design associated with CNT web frame linked by the carboxylated polythiophene (PPBT), which can afford the fast electron and ion transport during electrochemical testing. This study results demonstrated benefits derived from the rational consideration of electron/ion transport coupled with the surface chemistry of the electrode materials components. Finally, *Study 4* explores the material surface design with respect to high-capacity electroactive particles with SWNT electrical networks anchored/connected by carboxylated polythiophene (PPBT) links. This architecture facilitated the effective capture of cracked/pulverized particles derived from their extensive volume change that occurs during repeated charging-discharging process, consequently, leading to excellent electrochemical performance.

## CHAPTER 1. INTRODUCTION

### 1.1 General understanding of lithium-ion (Li-ion) batteries<sup>1-7</sup>

An electrochemical cell including Li-ion batteries interfaces the external world through two metallic posts: one contacts a negative electrode (the anode) and the other a positive electrode (the cathode). During cell discharge, electrons pass from the anode to the cathode through an external load of resistance and ions flow inside the cell to convert chemical energy into electrical energy. The electronic current delivered by the cell to the external circuit is matched by the ionic current within the cell. During cell charge, electronic current is forced in the opposite direction by an externally applied voltage to convert electrical energy back into chemical energy. The ionic current within an electrochemical cell is carried between the electrodes by an electrolyte, which is ideally an electronic insulator and a good conductor of the working ion of the cell. If a liquid electrolyte is used, a separator is also needed to maintain an even spacing between electrodes while blocking electronic current and passing the ionic current. Common separators are porous electronic insulators permeated by a single liquid electrolyte. The chemical at the anode that is consumed on discharge or produced on charge is the reductant of the chemical reaction; the chemical consumed on discharge or produced on charge at the cathode is the oxidant. The reductant and the oxidant are the two reactants of the cell; the energy of their reaction divided by the electronic charge passed in the reaction gives the maximum discharge voltage available between the positive and negative posts of the cells; it is the minimum voltage required to charge the cell. Therefore, the electrochemical

cells including Li-ion batteries obtain the electrical energy using voltage difference between anode and cathode.

### 1.1.1 Li-ion Batteries

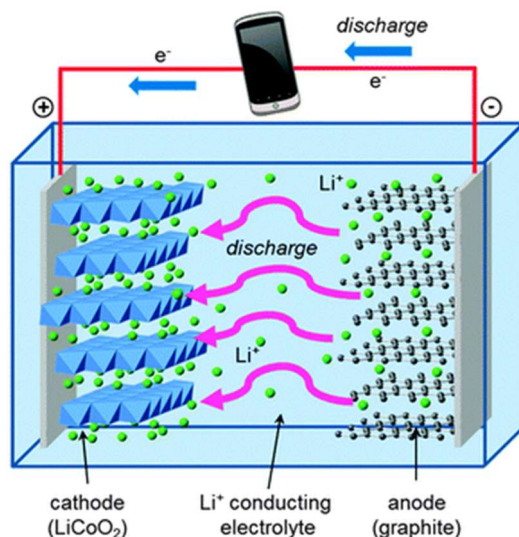
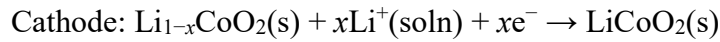
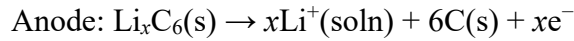


**Figure 1.1.** Schematic diagram of a Li-ion cell. During charging, lithium ions flow to the negative electrode through the electrolyte and electrons flow from the external circuit. During discharge the directions are reversed, generating useful power to be consumed by the device.<sup>3</sup> Published by The Royal Society of Chemistry.

Li-ion batteries use a solid reductant as the anode and a solid oxidant as the cathode. On discharge, the anode supplies  $\text{Li}^+$  ions to the  $\text{Li}^+$  ion electrolyte and electrons to the external circuit; the cathode is an electronically conducting host into which  $\text{Li}^+$  ions are inserted from the electrolyte as guest species and charge-compensated by electrons from the external circuit. The chemical reactions at the anode and cathode of a lithium secondary battery must be reversible; on charge, removal of electrons from the cathode by an external field releases  $\text{Li}^+$  ions back to the electrolyte to restore the parent host structure and the addition of electrons to the anode by the external field attracts charge-compensating  $\text{Li}^+$

ions back into the anode to restore it to its original composition. Simply to explain, Li-ion batteries are charged and discharged through the transport of  $\text{Li}^+$  ions between anode and cathode, with electron exchange as a result of  $\text{Li}^+$  insertion and extraction. Typically, both anode and cathode materials are layered compounds, as a result, the battery reaction is very simple because only  $\text{Li}^+$  ions participate in the charge/discharge reactions.

Specifically, Figure 1.1 shows a representative example of the battery system comprising a graphite (C) anode and  $\text{LiCoO}_2$  cathode where porous polymer film (*i.e.*, separator) separate them to avoid an internal short circuit, contained in a non-aqueous liquid electrolyte, typically  $\text{LiPF}_6$  salt in an carbonate-based organic solvent. The electrode reactions during discharge can be written



During charging, a voltage applied across the electrodes forces lithium ions to be extracted from the layered  $\text{LiCoO}_2$  crystal. These diffuse through the electrolyte, and are intercalated between the graphite sheets in the anode material. During discharge,  $\text{Li}^+$  ions return to the cathode *via* the electronically insulating electrolyte, with electrons passing around the external circuit providing useful power for the device.

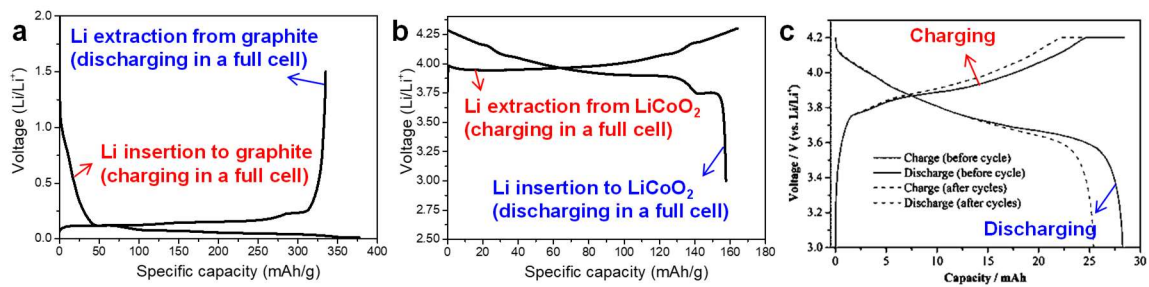


**Figure 1.2.** Galvanostatic charge-discharge voltage profiles of (a) a graphite anode, (b)  $\text{LiCoO}_2$  cathode, and (c) full cell<sup>4</sup> comprising the graphite anode and  $\text{LiCoO}_2$  cathode.

When these electrochemical reactions occur, the anode and cathode show different electrochemical behaviors: during discharging, in each half-cell using a Li metal counter electrode *vs* anode (or cathode) as a working electrode, the voltage of anode tends to elevate (Figure 1.2a) and that of cathode reduces (Figure 1.2b) by following their intrinsic voltage pathways. As a result, the full cell consisting of the graphite anode and  $\text{LiCoO}_2$  cathode exhibits the decreased voltage profile which results from voltage difference between the cathode and the anode (Figure 1.2c), leading to the generation of electrical energy to operate electronic devices. Charge process occurs *vice versa*.

### 1.1.2 Battery Configuration

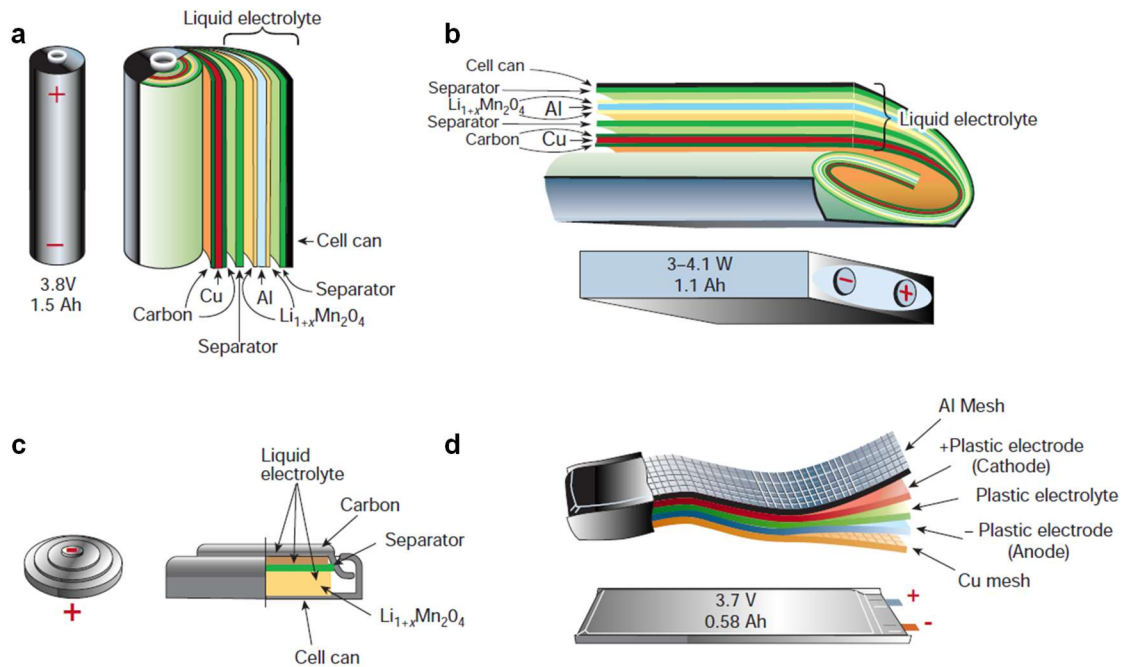


**Figure 1.3.** Schematic illustration of various Li-ion battery configurations: (a) Cylindrical cell, (b) prismatic cell, (c) coin cell, (d) thin and flat cell (or pouch cell).<sup>5</sup> Adapted by permission from Springer Nature: Nature ref.5 Copyright 2001.

Li-ion batteries can be typically divided into four types of configurations: Cylindrical-, prismatic-, coin-, and thin/flat (or pouch)-cell (Figure 1.3). Despite their various configurations, the battery basically consists of an anode, cathode, separator, electrolyte, and packaging unit. As shown in Figure 1.4, the electrode such as the anode and cathode comprises electroactive material (*e.g.* graphite, Si,  $\text{Fe}_3\text{O}_4$  for anode;  $\text{LiCoO}_2$ ,  $\text{LiFePO}_4$  for cathode), conductive agent (*e.g.* carbon black, carbon nanotube), polymeric binder (*e.g.* polyvinylidene fluoride (PVdF), carboxymethyl cellulose (CMC), poly(acrylic acid) (PAA)), and metallic current collector (Cu foil for anode; Al foil for cathode). Thus, regardless of the battery configurations, the research focusing on battery electrodes is likely to be the first step toward developing practical, high-performance, high-capacity battery electrode systems.

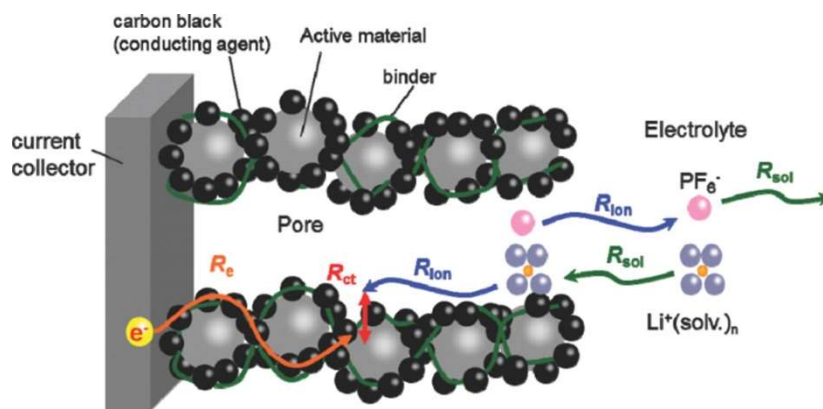


**Figure 1.4.** Schematic illustration of battery electrodes.<sup>6</sup>

In this thesis, we mainly used a coin-type half-cell to evaluate battery electrode performance because of its simplicity and convenience (particularly, in **Chapter 5**, a pouch-type full-cell was fabricated to demonstrate a commercial viability of our concepts/approaches introduced in the dissertation). The specific component of coin-type

half-cell is presented in Figure 1.5. A Li metal was used as a counter/reference electrode and placed in the anode position of the coin-type full-cell (Figure 1.3c), while an electrode of interest (*e.g.* anode or cathode) was a working electrode and placed in the anode position of the coin-type full-cell.

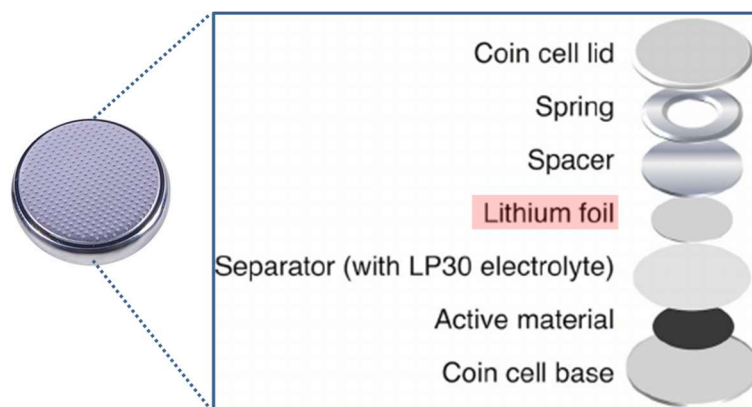


**Figure 1.5.** Coin cell assembly of the electrode half-cells.<sup>7</sup>

## 1.2 Research Motivation

High performance has been a challenge for high energy Li-ion batteries which enable a transition of our imaginations into reality such as smart IT devices, electrical vehicles (EVs), and even flexible/wearable electronics.<sup>8-9</sup> The high energy/power density serves as a driving force for intensive research related to high capacity anode materials. The main obstacles which retard the practical employment of high-capacity electrochemically active particles including Si, Sn, metal oxide and their derivatives, stem from large volume changes associated with Li insertion/extraction and the resultant electrical contact loss, thereby leading to poor cycling performance.<sup>10-15</sup> Efforts have been made to circumvent the breakdown of their electron pathways through the introduction of

electrically conducting functionalities such as carbon coatings<sup>12–18</sup> and conductive polymeric binders onto the surface of the active materials;<sup>11,19,20</sup> or the fabrication of stable battery anodes using an electrically inactive polymeric binder that facilitates retention of electrode integrity.<sup>21–24</sup>

In addition, flexible batteries require the flexible constituents to keep their integrity during mechanical stress.<sup>25, 26</sup> In general, flexible components in the electrode primarily comprise polymeric materials being an electric insulator, deteriorating battery performance in a high rate testing condition due to its increased resistance. To enhance the electrochemical behavior with flexibility, research associated with flexible frame/structure in combination with electrically conductive materials has been investigated: cellulose matrix incorporated with carbon nanotubes (CNTs),<sup>27–29</sup> three-dimensional interconnected graphene networks,<sup>30–31</sup> and CNT/conductive polymer composites.<sup>9</sup> Their resultant high performance is attributed to the fast electron conduction from the carbon material connectivity and the facile ion accessibility through high porous framework. Therefore, that indicates high performance of Li-ion batteries, including high capacity or/and flexibility, would be closely connected to ion and electron transport in their electrode environment.

A standard preparation procedure of Li-ion battery electrode is followed: electroactive powders are mixed with carbon additives and a polymeric binder dissolved in a solvent, and then the as-produced slurry is coated onto the metal current collector, and finally dried. The resultant electrode is composed of electroactive materials, conductive agents, polymeric binder, and current collector. Among them, polymeric binder is typically an electro-inactive insulator. To improve the battery performance, conjugated conductive



polymers appear to be one of the promising solutions to replace an electronically inactive binder component. Additionally, they are of significance in the electronic conductivity enhancement of active materials by forming the conductive layer onto their surface. Apparently, these efforts are quite effective in the battery performance. The important part overlooked, however, is ion conduction within the porous entity of a composite electrode.

In principle, the electrochemical reactions that occur in the electrode when a  $\text{Li}^+$  ion encounters an electron inside an active site reveal its intrinsic energy capacity.<sup>6</sup> Both electron and ion transport are critical factors that determine the battery performance. Despite their importance, research that considers both factors is rarely reported. Our recent studies (*Chapter 2*) pertaining to the use of the semiconducting polymer, poly(3-hexylthiophene) (P3HT), in conjunction with  $\text{Fe}_3\text{O}_4$ -based electrodes to enhance electrode electrical performance, pointed to the necessity that not only electron transfer, but significantly, ion transport must be considered in the design of a composite electrode.<sup>32</sup>

There would be a trade-off: ion transfer generally occurs in the open structure such as pores which allow penetration, whereas electron movement prefers a closely packed structure to maintain the connection of electrode materials. That is, ion transport is associated with the formation of electrode pore structure, while electron conduction is mainly affected by materials' connectivity. Therefore, understanding both factors from the perspective of materials and electrode structures is necessary. This thesis seeks to explore how methodical and structural consideration for both ion and electron transport can contribute to high battery performance, enabling the realization of high capacity and further flexible batteries.

### 1.3 Thesis Overview

This thesis describes systematic approaches to Li-ion battery electrodes enabling high electrochemical performance through adopting conjugated polymers as a conductive binder or an electrical linker, based on materials' surface chemistries. In the beginning research (**Chapter 2**), simple but crucial fundamental criteria have been found while investigating the basic, electrochemical characteristics of the representative conjugated polymer, poly(3-hexylthiophene) (P3HT): both electron and ion transport are critical factors that determine the internal resistance of electrodes, which is the primary influence on electrochemical performance. Two factors must be all considered in the design of a composite electrode. Based on this idea, conjugated polymer electrodes were studied by introducing a water-soluble, carboxylate substituted polythiophene (*i.e.*, poly[3-(potassium-4-butanoate) thiophene] (PPBT)). In particular, the specific molecular interactions originating from PPBT molecular attributes having  $\pi$ -conjugated backbone and carboxylate moieties substituted to its alkyl side chains, played an important role of enhanced battery performance. Those interactions coupled with materials' surface chemistries led to the successful improvement of electrochemical characteristics for following research. **Chapter 3** describes the introduction of PPBT as a new polymeric binder for the formation of a stable battery electrode associated with  $\text{Fe}_3\text{O}_4$  electroactive particles. PPBT with relatively high electrical conductivity further underwent electrochemical doping, which enabled the formation of effective electrical bridges between the carbon and  $\text{Fe}_3\text{O}_4$  components, allowing for more efficient electron transport. Additionally, the PPBT carboxylic moieties afforded a porous structure, and stable electrode performance. **Chapter 4** describes the electrode design of a carbon nanotube

(CNT) web structure comprising  $\text{Fe}_3\text{O}_4$  spheres ( $\text{sFe}_3\text{O}_4$ ) and few-walled carbon nanotubes (FWNTs) linked by the carboxylated conjugated polymer (PPBT). The approach introduces monodispersed spherical  $\text{Fe}_3\text{O}_4$ , owing to structural advantages that lessen the impact of volume changes and facilitate effective particle dispersion; thus supporting uniform  $\text{Li}^+$  ion diffusion during the electrochemical reaction, and a FWNT web electrode frame that affords characteristics of long-ranged electronic pathways and porous networks. **Chapter 5** introduces the high-capacity active materials integrated with single-walled carbon nanotube (SWNT) electrical networks that were securely anchored by PPBT links. Given the promising results obtained from SWNT- $\text{sFe}_3\text{O}_4$  electrodes, the concept was also expanded to alternate high-capacity active materials including silicon nanoparticles (Si NPs) and carbon-coated silicon monoxide (c- $\text{SiO}_x$ ).

## CHAPTER 2. OLEIC ACID CAPPED $\text{Fe}_3\text{O}_4$ AND P3HT-BASED ELECTRODES

### 2.1 Introduction

Identification of effective strategies to reduce electrode resistance and elevate the energy capacity of Li-ion batteries, which are commonly used in mobile devices and electric vehicles (EVs), is of significant interest.<sup>5,33</sup> Nanomaterials are considered to be one promising approach to achieve these goals. Specifically, the use of nanomaterials offers the advantages associated with a short  $\text{Li}^+$  diffusion path that can facilitate the charge transfer process and enhance the utilization of active sites even at high power rates.<sup>34–38</sup>

Despite demonstration of desirable characteristics, the anticipated benefits associated with the use of nanometer-scale materials have yet to be fully realized, and in some cases, composite battery electrode performance has been shown to be inferior for nanomaterials vs their bulk counterparts.<sup>39</sup> Aggregation and materials dispersion have been suggested as leading factors that impact the performance of composite electrode materials. For instance, it has been shown that more uniformly dispersed materials exhibit improved performance attributes.<sup>39–41</sup> Specifically, nano-sized conductive additives tend to readily agglomerate during battery electrode processing, thereby hindering homogeneous current distribution over the electrode and negatively influencing electrochemistry.<sup>36,42</sup> In fact,

---

Adapted with permission from “Kwon, Y. H.; Huie, M. M.; Choi, D.; Chang, M.; Marschilok, A. C.; Takeuchi, K. J.; Takeuchi, E. S.; Reichmanis, E. Toward Uniformly Dispersed Battery Electrode Composite Materials: Characteristics and Performance. *ACS Appl. Mater. Interfaces* **2016**, 8, 3452–3463.” Copyright 2016 American Chemical Society.

mesoscale modeling has shown that both the size of the parent particle (crystallite) and the size of the aggregate must be considered to accurately describe battery performance.<sup>43</sup> Closer inspection of electrode structure offers additional insight. Battery electrodes are generally composite materials, wherein the active materials are mixed with conductive additives to create an interconnected, percolated conductive network. An inactive polymeric binder provides for structural integrity.<sup>36,38</sup> The interconnected conductive pathways are expected to be related to particle dispersion within the polymeric medium which may in turn impact electrochemical performance.

To realize the full potential afforded by nanomaterials, it is necessary to fabricate and characterize composite electrodes with varying degrees of dispersion at the nano-through mesoscales. Here, two approaches are used to gain important perspectives on the impact of dispersity and morphology on composite electrode performance. Investigations focus on i) how to enhance materials dispersity in the battery electrode and ii) how morphological differences link to their electrical properties and performance.

The high surface area and attractive forces (van der Waals) associated with nanomaterials are known to impede their dispersion and from a thermodynamic perspective, facilitate agglomeration. Thus, simple physical techniques such as ultrasonication may be insufficient to achieve stable, homogeneous nanomaterial dispersions and chemical routes may be required.<sup>53</sup> To date, efforts to enhance dispersivity of battery electrode materials have been limited; however, extensive efforts associated with the uniform dispersion of nanomaterials used in photovoltaic devices<sup>46,47</sup> and potential biomedical applications<sup>49,50</sup> have been reported. It has been found that the propensity of nanoparticles such as Au, CdSe, SiO, ZnO, TiO<sub>2</sub>, and Fe<sub>3</sub>O<sub>4</sub> to agglomerate can be reduced

by coating them with suitable capping agents.<sup>44–53</sup> Carbon nanomaterials, including carbon nanotubes (CNTs) and carbon nanofibers (CNFs), can be dispersed effectively by judicious choice of solvent, use of surfactants, surface functionalization, and/or wrapping with conjugated polymers such as poly(9,9-dialkylfluorene) (PF) or regioregular poly(3-alkylthiophene) (P3AT). In the latter case, interactions between the  $\pi$ -conjugated chains and carbon surface, and the presence of alkyl side chains both assist effective dispersion.<sup>54–</sup>

57

Thus, to inhibit the agglomeration process and achieve stable nanomaterials dispersions, surfactant-like moieties can be introduced onto their surface with physical or chemical means. This same fundamental principle may also provide for improved materials dispersion in the case of battery electrode composite materials. To evaluate the impact of nanomaterials dispersion in electrode applications, Fe<sub>3</sub>O<sub>4</sub> nanoparticles (8nm) capped with oleic acid (OA-Fe<sub>3</sub>O<sub>4</sub>) and poly(3-hexylthiophene) (P3HT) were chosen as the active material and conjugated polymer, respectively. Oleic acid (OA) and P3HT provide for surfactant-like functionality for Fe<sub>3</sub>O<sub>4</sub> and carbon additives. Hansen Solubility Parameter (HSP) analysis suggests that OA-Fe<sub>3</sub>O<sub>4</sub> and carbon/P3HT will be well-mixed in the final electrode.

To investigate electrode materials morphology, a spin-coating technique was used to prepare the composite thin-films. Typical coating methods such as blade coating, dip coating, and drop casting form dense, thick film layers that are inappropriate to adequately visualize distinctive morphologies and differentiate the degree of material dispersity in the electrode. The spin coating method affords a thin, uniform film layer, and morphological differences can be easily detected even by optical microscopy (OM) at low magnification.

While battery electrode performance cannot be directly measured using the spin-coating technique, the method is a facile approach to visualize more distinct images of the electrode components in order to judge materials distribution, and help interpret the impact of materials size and distribution on electrical and electrochemical behavior in a dense electrode.

Poly(3-hexylthiophene) (P3HT) is an interesting conductive polymer for a battery cathode material because polythiophenes have relatively small band gaps and high conductivities.<sup>58</sup> Additionally, P3HT has a low reduction potential (0.5 V vs Li/Li<sup>+</sup>)<sup>59</sup> which suggests that this conductive polymer should remain conductive at operating voltages above 0.5 V. Block copolymers of P3HT and poly(ethylene oxide) (P3HT-b-PEO) have been investigated for Li-ion batteries. P3HT-b-PEO block copolymers phase separate to form a lamellar phase which combines the high intrinsic electronic conductivity of P3HT with regions of PEO which are conducive for Li<sup>+</sup> ion diffusion.<sup>60</sup> P3HT-b-PEO has been used as a binder with several cathode materials.<sup>61–63</sup> The block copolymer displayed high electronic and ionic conductivities<sup>60,64,65</sup> as well as mechanical stability.<sup>63</sup> However, electronic conductivity of the LiFePO<sub>4</sub>/P3HT-b-PEO cathode dropped from 10<sup>-4</sup> S/cm to 10<sup>-7</sup> S/cm when the operating voltage dropped below 3.3 V during discharge.<sup>61</sup> P3HT has also been copolymerized with sulfur for use as an additive (not as a binder) in Li-S batteries.<sup>66</sup> The addition of sulfur-P3HT copolymer to the electrode improved battery cycle life and high rate performance which was attributed to the inhibited dissolution of polysulfides.

The dispersing agent used here was oleic acid (C<sub>18</sub>H<sub>34</sub>O<sub>2</sub>), a long organic chain with a carboxylic acid functional group which has been used as a surfactant to promote

nanoparticle formation and reduced nanoparticle agglomeration. Reducing agglomeration is important for electrode performance as it shortens diffusion pathways for ions to reach the crystalline active material. There are some studies of oleic acid-coated active materials, but the electrochemical impact of the coating is still unclear. Oleic acid coated  $\text{Fe}_2\text{O}_3$  in a Li-ion battery displayed better capacity and high rate performance compared to uncoated  $\text{Fe}_2\text{O}_3$ .<sup>67</sup> This result was attributed to the capacitive nature of oleic acid which formed a surface double layer inducing a pseudo-capacitance interfacial charging event. Guo et al. used oleic acid to coat  $\text{Mn}_3\text{O}_4$  for a capacitor and found the oleic acid helped form uniform microspheres with a capacitance improvement.<sup>68</sup> The interaction of oleic acid with conductive polymers is not broadly researched, but one study of oleic acid-stabilized silver nanoparticles with polythiophenes in organic thin-film transistors,<sup>69</sup> found that the presence of oleic acid with polythiophene improved electrical conductivity.

Through investigating the role of an oleic acid capping agent introduced on the magnetite surface in the performance with both conductive and nonconductive polymer binders, the approach presented here aims to provide fundamental insights into the mechanistic foundation for efforts associated with uniform dispersion in battery electrode applications, especially for the efficient incorporation with electroactive nanomaterials components.

## 2.2 Experimental Section

**Materials.**  $\text{Fe}_3\text{O}_4$ , magnetite, was synthesized using a previously reported coprecipitation approach, using aqueous solution of iron(III) chloride hexahydrate, iron(II) chloride hexahydrate, trimethylamine.<sup>70,71</sup> For preparation of  $\text{Fe}_3\text{O}_4$  nanoparticles capped



with oleic acid (OA-Fe<sub>3</sub>O<sub>4</sub>),<sup>53</sup> 4 mL of oleic acid was added to 0.3 g Fe<sub>3</sub>O<sub>4</sub> nanoparticles prepared above and followed by stirring the solution for 24 h. The OA-Fe<sub>3</sub>O<sub>4</sub> powder was extracted after sonication by centrifuge separation with 15 mL acetone with speed of 9000 rpm for 2 min for 3 times. P3HT was purchased from Rieke Metals Inc. The molecular weight of P3HT ( $M_n$  of 19.6 kDa and  $M_w$  of 43.7 kDa) used for the study was measured by gel permeation chromatography (GPC). The head to tail regioregularity (RR) was estimated to be approximately 96% (Bruker DSX 300 <sup>1</sup>H NMR in deuterated chloroform solution at 293K).

**Composite Electrode Fabrication.** The slurries for the P3HT-based electrode were prepared by mixing of OA-Fe<sub>3</sub>O<sub>4</sub>, Super-P carbon additive, and P3HT in a solvent of chloroform, and in case of PVDF-based electrode, NMP solvent was used with the same composition of P3HT-based electrode. The only carbon content was changed with OA-Fe<sub>3</sub>O<sub>4</sub> and Super-P kept constant. Super-P/polymer composite followed the previous procedure, except for OA-Fe<sub>3</sub>O<sub>4</sub>. The solid content was 3.4 wt% for spin coating and mold casting, and 27 wt% for blade coating. The electrodes for the measurements of OM, AFM, FE-SEM, and electronic conductivity were prepared by spin-coating (WS-6500MZ-23NPP, Laurell) the slurries onto substrates at the spin rate of 1500 rpm for 60 sec in air. The electrodes for FE-SEM measurement and electrochemical evaluation were produced by blade coating (doctor blade, MTI corp). Mold casting was conducted using a rectangular mold being put onto the substrate for measuring the electronic conductivity. These prepared electrodes were pre-evaporated at 70 °C for 1 h and completely evaporated at 130 °C for 12 h in a vacuum oven.

**Morphology Characterization.** The optical microscopy (OM) measurements were conducted on the composite films spin-coated on the glass substrate using Olympus MX61 Microscope. The atomic force microscopy (AFM) images were obtained with an ICON dimension scanning probe microscope (Bruker) using tapping mode with a silicon tip (RTESP, Bruker). The field emission-scanning electron microscopy (FE-SEM) images were observed on the top view of the electrodes using Zeiss Ultra-60 FE-SEM.

**Hansen Solubility Parameter (HSP) Characterization.** Polymer (10 mg) such as P3HT and PVDF, Super-P carbon particles (0.5 mg) and OA-Fe<sub>3</sub>O<sub>4</sub> nanoparticles (10 mg) were placed into a vial with 3 mL of a test solvent, respectively.<sup>72–74</sup> The vial was heated at 70 °C for 3 h and sonicated for 60 min and after then the vials were permitted to stand and observed for 6 h in ambient temperature. The dispersion stability was examined by these solutions *via* visual observation. In case of polymer, solvents would be considered as poor if they were unable to dissolve the polymer after dissolving process and good if they were able to dissolve it.<sup>74</sup> For the particles including OA-Fe<sub>3</sub>O<sub>4</sub> and Super-P, solvents would be classified as poor when they were completely deposited on the vial bottom after 60 min sonication, and solvents would be good when sedimentation on the vial bottom required more than 6 h after the sonication step.<sup>72</sup> Based on the visual examination, Hansen solubility parameters ( $\delta_D$ ,  $\delta_P$  and  $\delta_H$ ) and the radius value ( $R_o$ ) of the sphere of interaction were calculated and fitted by HSPiP software (Hansen Solubility Parameters in Practice third edition).

**Electronic Conductivity Measurement.** The electrode devices with two bottom contacts (channel width = 10  $\mu\text{m}$  and length = 50  $\mu\text{m}$ ) were used for electrical characterization, where composite film was deposited *via* spin coating or mold casting on

a silicon wafer with a 300 nm thick SiO<sub>2</sub>. The characterization process is as follows<sup>75</sup>: Au was used for the source and drain contacts which were fabricated using a standard photolithography based on lift-off process, followed by Denton Explorer E-beam evaporation of 3 nm thick Cr as the adhesive layer and sequentially Au contact with 50 nm thickness. Before coating, all devices were exposed in a UV-ozone cleaner (Novascan PSD-UV) for 15 min to completely remove any organic containments. The prepared composite electrodes described in previous section were tested in nitrogen ambient using a semiconductor parameter analyzer (Agilent 4155C).

**Electrochemical Characterization.** Stainless steel coin cells were constructed with Li anodes, polymeric separators and cathodes comprised of composite coatings (15% Super P, 14% polymer binder and 71% Fe<sub>3</sub>O<sub>4</sub>) on copper (Cu) foil. Electrodes used in coin cells were created by coating a slurry mixture onto Cu foil with a doctor blade. After the solvent evaporated, 0.5 inch diameter electrodes were punched from the coating and pressed. Electrolyte consisted of 1 M LiPF<sub>6</sub> salt in a mixture of ethylene carbonate (EC):dimethyl carbonate (DEC) in a volume ratio of 30:70. Coin cells were tested by lithiating Fe<sub>3</sub>O<sub>4</sub> to 0.3 V and then delithiating to 3.0 V at rates of 20 mA per gram of Fe<sub>3</sub>O<sub>4</sub> in the electrode coating at 30°C. After reaching 3.0 V cells were held at constant voltage for 1 h. AC Impedance spectroscopy was measured using a Bio-Logic potentiostat over a frequency range of 1.0 mHz and 1 MHz. Three coin cells were built with each electrode type. All cells showed similar trends in capacity and impedance with respect to electrode type. One representative cell of each electrode type is reported here.

## 2.3 Results and Discussion

### 2.3.1 Materials Morphology

In general, the dense morphology of battery electrodes inhibits the ability to differentiate the degree of materials dispersion within the composite. Using a spin coating technique, well-known but unfamiliar in the battery field, battery electrode materials dispersion was analyzed and evaluated. While indirect, the method enables deposition of a thin, uniform layer of electrode material, which facilitates characterization of the distribution of the individual electrode components. Poly(vinylidene difluoride) (PVDF) and P3HT were used as the binder materials. PVDF is widely used as the binder in Li-ion battery electrodes due to its good electrochemical stability and high binding adhesion to the electrode materials and current collectors.<sup>76</sup> Thus, the PVDF system was used as standard reference; *N*-methyl-2-pyrrolidone (NMP) was the solvent. P3HT is a potentially attractive conducting polymer binder alternative.

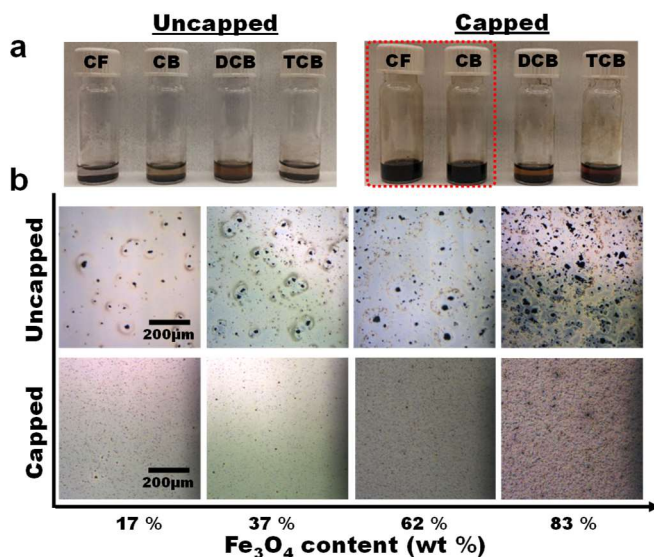


**Figure 2.1.** (a) Dispersion state in different solvents. Capped Fe<sub>3</sub>O<sub>4</sub> is well-dispersed in chloroform and chlorobenzene. (b) OM images of uncapped Fe<sub>3</sub>O<sub>4</sub>/P3HT composites and OA-capped Fe<sub>3</sub>O<sub>4</sub>/P3HT composites. Samples were prepared by spin coating on glass substrates using chloroform solvent.

To minimize agglomeration effects and promote the uniform distribution of active material, Fe<sub>3</sub>O<sub>4</sub> nanoparticles were capped with oleic acid. Oleic acid was selected because previous studies showed that the OA –COOH moieties readily bind to surface -OH functionalities present on many inorganic materials thereby improving their dispersion characteristics.<sup>52,53</sup> The dispersion state of OA-capped and uncapped Fe<sub>3</sub>O<sub>4</sub> nanoparticles was evaluated in a range of solvents known to dissolve the conjugated polymer, P3HT; namely, chloroform (CF), chlorobenzene (CB), dichlorobenzene (DCB), and trichlorobenzene (TCB). As shown in Figure 2.1a, the uncapped nanoparticles failed to disperse and simply precipitated, whereas the OA-capped nanoparticles were well-dispersed in CF and CB. Subsequent studies related to the conjugated polymer-based electrode system focused on chloroform because it solubilizes P3HT more effectively.

To visualize the dispersion state of the capped *vs* uncapped Fe<sub>3</sub>O<sub>4</sub>, Fe<sub>3</sub>O<sub>4</sub>/P3HT composite films were coated onto glass substrates by spin-coating (1500 rpm, 60 sec) and the resultant thin-film morphologies were observed by optical microscopy. Aggregates were observed in all films prepared with uncapped Fe<sub>3</sub>O<sub>4</sub> and aggregate size increased with increased Fe<sub>3</sub>O<sub>4</sub> content. For the proportions investigated here, aggregate size ranged from approximately 2 to 40 μm. Aggregation was not observed for the oleic acid capped materials: OA-Fe<sub>3</sub>O<sub>4</sub> appears uniformly distributed regardless of the proportion of active material. Both OA-Fe<sub>3</sub>O<sub>4</sub> and P3HT are expected to be hydrophobic and may have similar physical affinities, which may in turn facilitate uniform dispersion.

Figure 2.2 presents the observed thin-film morphologies for P3HT- *vs* PVDF-based composites formulated with the respective polymers, carbon and magnetite where the

carbon content of each film was changed. The absolute amount/weight of OA-Fe<sub>3</sub>O<sub>4</sub> and Super-P carbon additives were fixed. The volume percent of carbon was determined from the weight percent using the material density (Fe<sub>3</sub>O<sub>4</sub>: 5.0 g/cc, Super-P carbon additive: 1.85 g/cc, P3HT: 1.10 g/cc, PVDF: 1.78 g/cc). The composite thin-films were prepared by spin-coating (1500 rpm, 60 sec) from chloroform and NMP for the P3HT and PVDF systems, respectively. Coating parameters (*i.e.*, spin speed, colloidal concentration) are known to affect the density and morphology of resultant films; higher spin speeds and lower colloidal concentrations generally afford thinner films that are spread out and have more sparsely dispersed nanoparticles.<sup>77,78</sup> From this perspective, the processing parameters (spin coating: 1500 rpm for 60 sec, solid content: 3.4 wt%) adopted here to explore thin film morphology are expected to provide for the appropriate degree of materials dispersion to be discernible. Furthermore, while substrate and solvent properties (*i.e.*, vapor pressure, boiling point, and evaporation rate) may also affect the evolution of thin-film morphology, the effects will be minimized due to centrifugal forces associated with the spinning process; the deposited material spreads rapidly and solvent quickly evaporates, thereby suppressing solvent evaporation effects and adequately enabling visualization of the physical affinities among component materials.

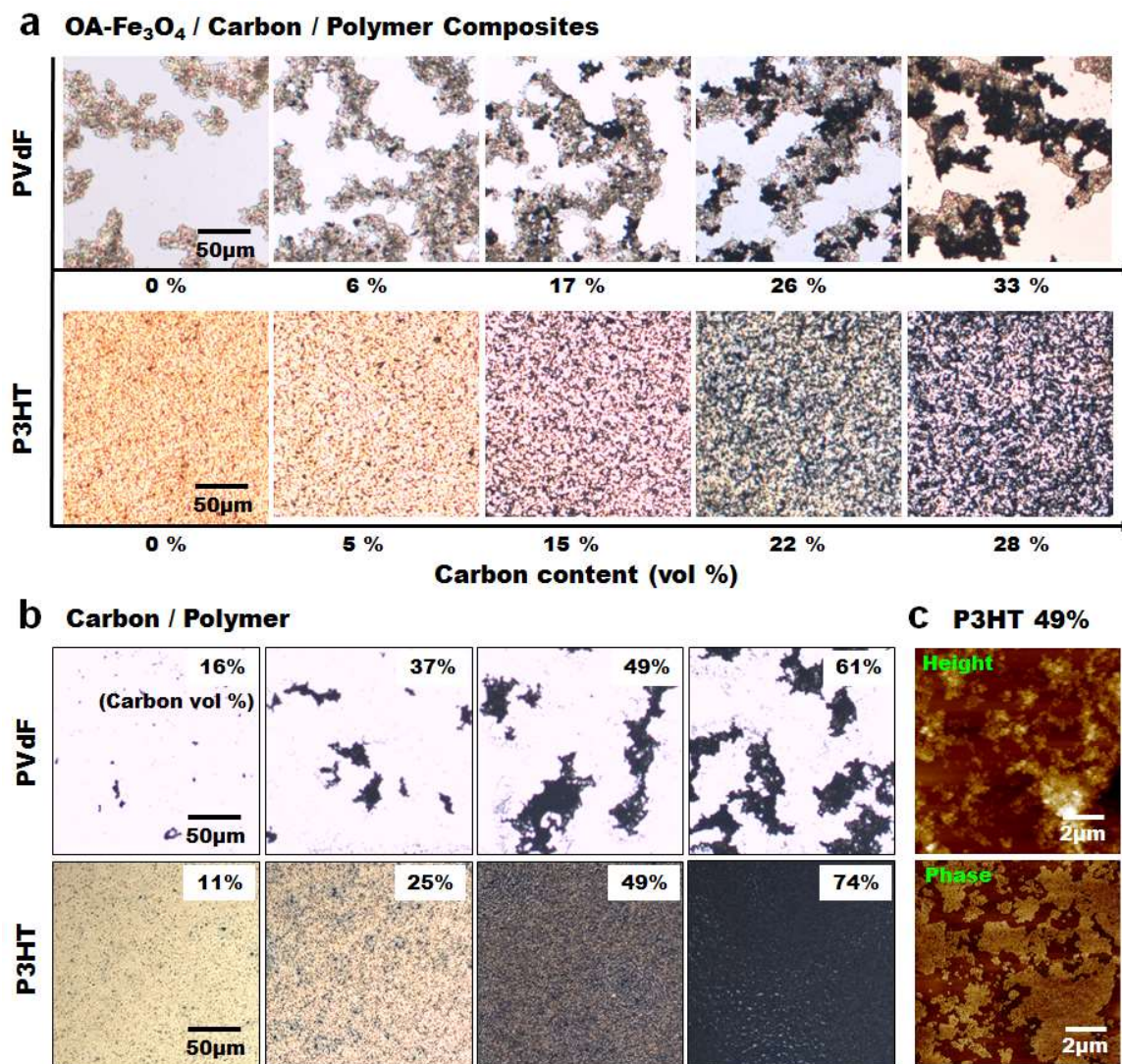


**Figure 2.2.** (a) OM images of OA-Fe<sub>3</sub>O<sub>4</sub>/carbon/polymer composites according to different carbon content. The absolute amount of OA-Fe<sub>3</sub>O<sub>4</sub> and polymer was kept constant. The volume percent of carbon content was converted by material density. (b) OM images of carbon/polymer composites with different carbon content. P3HT system shows much more favorable uniform dispersion than PVDF system. (c) Tapping mode AFM height and phase images of 49 vol. % of carbon/P3HT composite film, demonstrating the conductive percolation networks.

Figures 2.2a and 2.2b present optical microscopic images of OA-Fe<sub>3</sub>O<sub>4</sub>/carbon/polymer and carbon/polymer composite thin-films, respectively. Distinct morphological differences can be discerned between the P3HT and PVDF-based systems.



In PVDF, OA-Fe<sub>3</sub>O<sub>4</sub> nanoparticles appear as brown-colored aggregates and the carbon additive appears black. When the carbon content is increased incrementally, carbon aggregate size also increases and appears to cover the region occupied by OA-Fe<sub>3</sub>O<sub>4</sub>. Further, the desired conductive network appears to be disconnected due to nanoparticle agglomeration. The resulting morphology might be expected to interfere with effective current distribution throughout a PVDF-based composite electrode. In contrast, the P3HT-based system presents a uniformly dispersed morphology irrespective of carbon content. By augmenting the proportion of carbon additive, an apparently percolated, interconnected conductive network was produced. The percolation network formed by the spherical carbon additives (~50nm, 49 vol. %) was readily visualized by atomic force microscopy (AFM) (Figure 2.2c). Moreover, AFM observation (Figure 2.3) provides for the well-connected, electronic carbon additive networks, together with OA-Fe<sub>3</sub>O<sub>4</sub> nanoparticles. The results strongly suggest that the OA-surface treatment of Fe<sub>3</sub>O<sub>4</sub> nanoparticles might also influence the interactions between OA-Fe<sub>3</sub>O<sub>4</sub> and the conductive network due to their similar physical affinities.

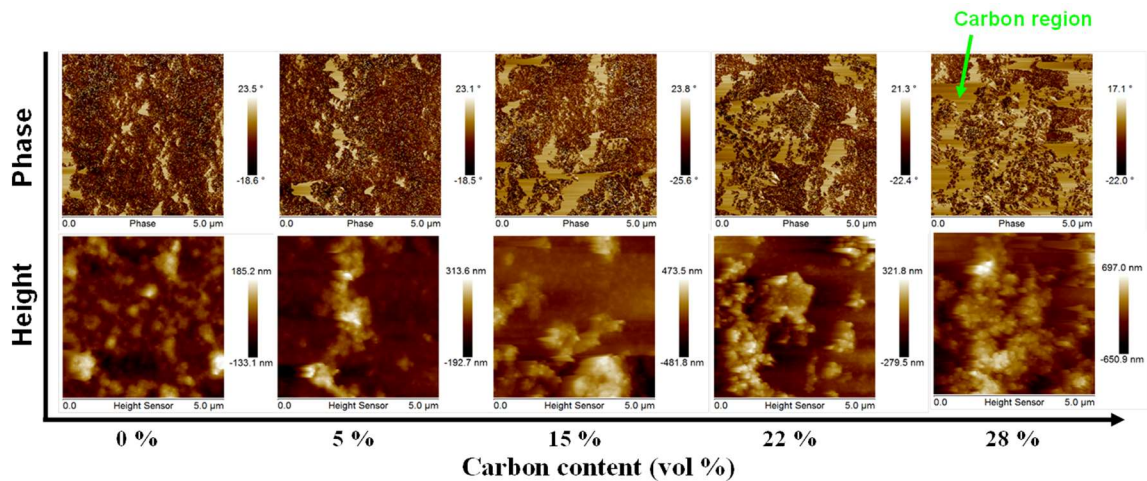


**Figure 2.3.** AFM images of OA-Fe<sub>3</sub>O<sub>4</sub>/carbon/P3HT composites according to different



carbon content. AFM images exhibit the network formation of carbon additives connected with OA-Fe<sub>3</sub>O<sub>4</sub> nanoparticles by the change of carbon content.

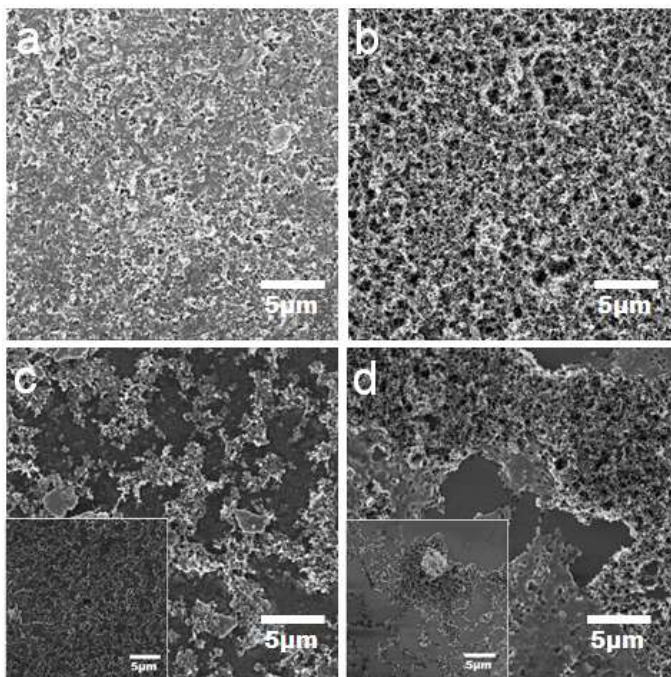


**Figure 2.4.** SEM images of OA-Fe<sub>3</sub>O<sub>4</sub>/carbon/polymer composite electrodes (Top view). (a) P3HT-based electrode (blade coating). (b) PVDF-based electrode (blade coating). (c) P3HT-based electrode (spin coating, inset: carbon/P3HT). (d) PVDF-based electrode (spin coating, inset: carbon/PVDF). The spin coated material shows the distinct morphology associated with the material dispersion state.

Figure 2.4 shows field emission-scanning electron microscopy (FE-SEM) images of OA-Fe<sub>3</sub>O<sub>4</sub>/carbon/P3HT and OA-Fe<sub>3</sub>O<sub>4</sub>/carbon/PVDF battery composite electrodes fabricated by doctor blade (Figure 2.4a, b) and spin coat (Figure 2.4c, d) processes, respectively. Morphological differences between the two systems are difficult to observe from the doctor blade samples (Figure 2.4a, b) due to their thick, dense nature. Alternatively, distinct morphological differences are apparent with the thinner, spin-coated

alternatives (Figure 2.4c, d): the components appear better dispersed within P3HT vs PVDF, which supports the optical imaging results (Figure 2.2).

As shown in Figure 2.2b and the inset image of Figure 2.4c, the spherical, nanosized carbon additives appear relatively well-dispersed within P3HT. Presumably, the  $\pi$ -conjugated regioregular P3HT backbone interacts with carbon  $\pi$ -electrons residing at the surface, while the solubilizing alkyl side chains help to maintain their dispersion state.<sup>55</sup> The dispersion of OA-Fe<sub>3</sub>O<sub>4</sub> nanoparticles in P3HT is likely influenced by similar physical affinities between the hydrophobic tail of the capping agent and the P3HT side chains. The morphology results suggest that in order to achieve uniform and stable battery electrode nanomaterials dispersions, consideration should be given to materials surface physical affinities/interactions. In addition, introduction of a surfactant-like species on the respective nanomaterial surfaces, whether through use of a capping agent or wrapping by a polymer chain, to manipulate that physical affinity in an advantageous manner is especially important.

### 2.3.2 *Physical Affinity Relationship*

Physical compatibility between materials that comprise a battery electrode is expected to greatly influence the materials interfacial properties, as will the degree of material dispersion. One approach to examine the physical affinity between different materials uses Hansen solubility parameter (HSP) analysis. Typically, materials with similar HSP values exhibit high physical affinities or rather, compatibility.<sup>79</sup> The extent of the similarity can serve as a measure of the extent of interaction. Thus, a comparison of

electrode composite material HSPs can provide insight into the physical interactions between the components and thereby provide a quantitative view of materials dispersion.

Using the solubility and/or dispersivity of the component materials in a range of solvents with known HSPs, materials HSPs can be calculated by Hansen software (Hansen Solubility Parameters in Practice third edition). HSPs ( $\delta_D$ ,  $\delta_P$  and  $\delta_H$ ) and the radius ( $R_o$ ) of the sphere of interaction for the materials can be obtained, wherein solvents within  $R_o$  can be expected to dissolve/disperse the solute. The parameters,  $\delta_D$ ,  $\delta_P$  and  $\delta_H$ , are related to the (atomic) dispersion forces, (molecular) permanent dipole-permanent dipole forces and (molecular) hydrogen bonding, respectively.<sup>72-74,79</sup> Furthermore, to evaluate whether or not a solvent belongs to a sphere of high physical affinity, the distance  $R_a$  between the solvent and the material is calculated by Eq. 1,

$$(R_a)^2 = 4(\delta_{D1} - \delta_{D2})^2 + (\delta_{P1} - \delta_{P2})^2 + (\delta_{H1} - \delta_{H2})^2 \quad (1)$$

where the subscripts 1 and 2 represent the solute and solvent, respectively. The relative energy difference ( $RED=R_a/R_o$ ) provides an estimate of whether two materials will be miscible (miscible when  $RED < 1$ , partially miscible when  $RED = 1$  and immiscible when  $RED > 1$ ).<sup>74</sup> In this investigation, nanoparticles were judged to be dispersible when  $RED$  was less than 1.

As shown in Figure 2.5,  $RED$  was calculated for OA-Fe<sub>3</sub>O<sub>4</sub> and Super-P carbon additives with respect to PVDF and P3HT. For OA-Fe<sub>3</sub>O<sub>4</sub>, the  $RED$  of PVDF and P3HT is 1.86 and 1.04, respectively; for Super-P, the PVDF value is 0.82 and that of P3HT is 0.85. The calculated OA-Fe<sub>3</sub>O<sub>4</sub>  $RED$  values support the optical microscopy observations (*vide supra*). The  $RED$  value calculated for Super-P with PVDF is unexpected, and suggests that

carbon additives should be dispersible in PVDF. Examination of the RED with different solvents, chloroform has a value of 0.63 for Super-P, whereas NMP exhibits an RED of 1.00 (note: OA-Fe<sub>3</sub>O<sub>4</sub>: chloroform 1.04, NMP 1.86). Thus, solvent-electrode component interactions during electrode processing also play an important role in determining the material dispersion state. In other words, the carbon aggregates seen in the PVDF system (Figure 2.2) might be ascribed to poor/inferior physical affinity between the Super-P carbon additive and NMP solvent inducing poor dispersion, even though carbon and PVDF have good physical affinity. On a cautionary note, this investigation is limited to estimating the physical interaction between just two materials; the gross physical interactions present among active nanoparticles, carbon additives, polymeric binder, and even solvent could significantly impact final processed morphology.

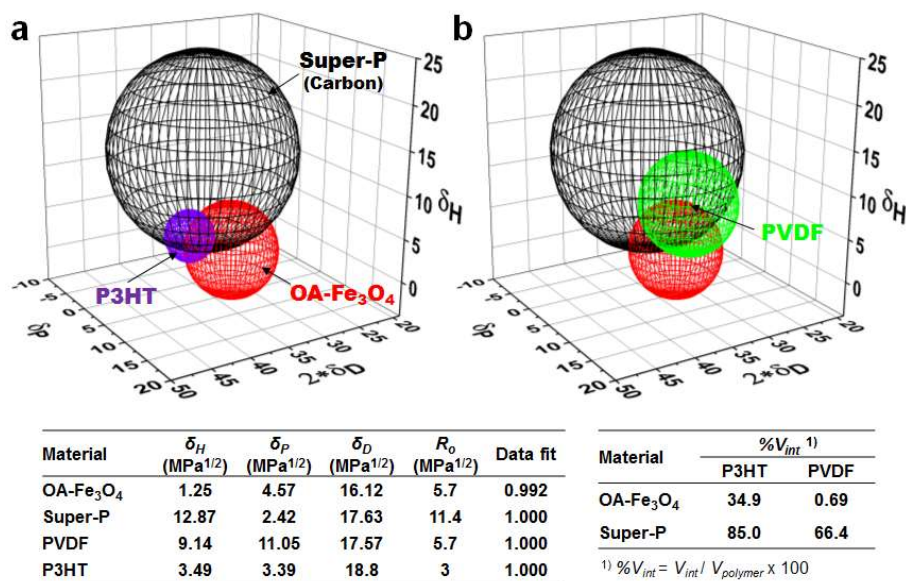


**Figure 2.5.** Hansen solubility parameter (HSP) spheres of interaction for (a) OA-Fe<sub>3</sub>O<sub>4</sub>/carbon/P3HT and (b) OA-Fe<sub>3</sub>O<sub>4</sub>/carbon/PVDF. Tables show HSPs of the composite battery electrode components and superimposed volume portions (%V<sub>int</sub>) for each polymer volume (V<sub>polymer</sub>).

The Hansen spheres in Figure 2.5 show the regional relationship of interactions for OA-Fe<sub>3</sub>O<sub>4</sub>/carbon/P3HT and OA-Fe<sub>3</sub>O<sub>4</sub>/carbon/PVDF. Generally, when regions of affinity/solubility for different materials are superimposed, the components are expected to experience very high physical attraction.<sup>72</sup> Together with the RED value, in order to confirm the extent of overlap between two spheres of interaction, the sphere intersection volume ( $V_{int}$ ) was calculated and the superimposed volume portion ( $\%V_{int}$ ) for each polymer volume ( $V_{polymer}$ ) was obtained by  $V_{int} / V_{polymer}$  as shown in the table in Figure 2.5.<sup>80</sup> The results of this analysis strongly suggest that OA-Fe<sub>3</sub>O<sub>4</sub> and Super-P carbon additives have more favorable physical affinity with P3HT vs PVDF. The insights gained from evaluation of the sphere intersection volume appear more suitable than RED to predict the dispersivity of battery electrode materials.

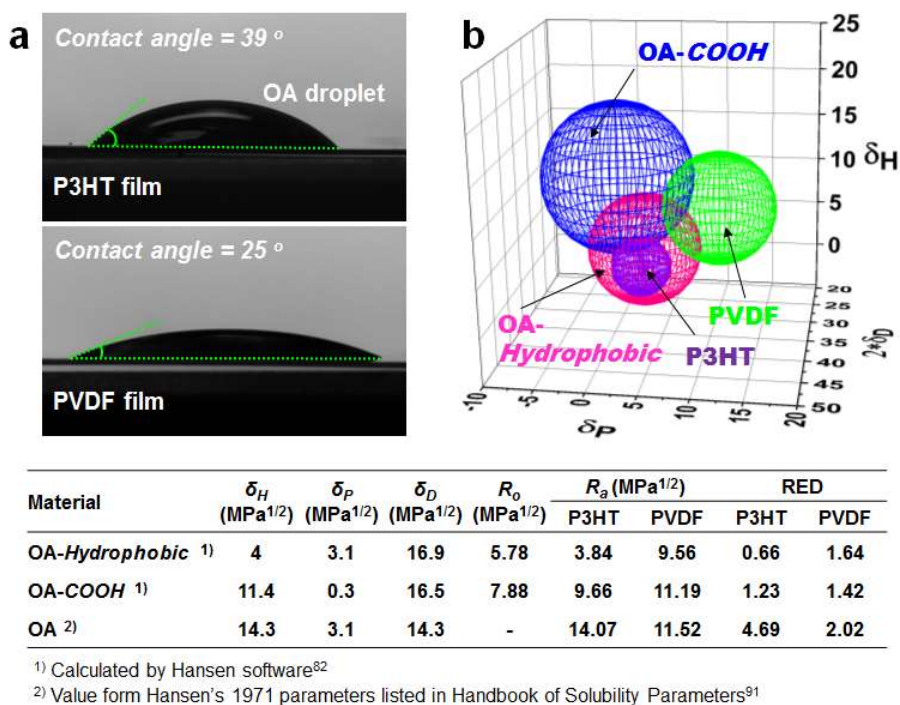


**Figure 2.6.** Surface physical affinities between oleic acid (OA) and polymer (P3HT & PVDF): (a) contact angle measurement (OA droplet on polymer film) and (b) HSP spheres of interaction. Table represents the values of HSP,  $R_a$  and RED. The RED of unsaturated

hydrocarbon part of OA (OA-Hydrophobic) with P3HT is less than 1, predicting they are miscible.

The propensity of OA-Fe<sub>3</sub>O<sub>4</sub> to disperse uniformly within P3HT might also result from surface interactions. The contact angle of an OA droplet on the surface of the polymer film provides one measure of the physical interactions between the two materials. Typically, the contact angle decreases when the extent of physical attraction increases.<sup>81</sup> As shown in Figure 2.6a, OA exhibits a lower contact angle on PVDF than P3HT, which implies good physical affinity with PVDF. These results concur with estimates of RED for OA with P3HT (4.69) and PVDF (2.02) (see table in Figure 2.6; a smaller RED suggests better miscibility); however, they contradict experimental OA-Fe<sub>3</sub>O<sub>4</sub>-based composite observations.

Considering OA-Fe<sub>3</sub>O<sub>4</sub> nanoparticle structure, only the hydrophobic OA tail is relevant, because the capping agent's -COOH groups would be chemically bound to the Fe<sub>3</sub>O<sub>4</sub> surface. Accordingly, the measured contact angle may not be a fully reflective measure to judge the physical affinity between the capped nanoparticles and polymer binders. Alternatively, the HSP approach may be predictive. As illustrated in Figure 2.6b, OA exhibits two HSP spheres<sup>82</sup>; one associated with the unsaturated hydrocarbon tail (OA-Hydrophobic), the second for the carboxylic acid moiety (OA-COOH). For OA-Hydrophobic, the RED and intersection volume portion (% $V_{int}$ ) for PVDF and P3HT are 1.64/4.2% and 0.66/87.5%, respectively. In the case of OA-Hydrophobic and P3HT, the two spheres are almost superimposed indicating the close nature of the HSP regions. Consequently, their physical affinities towards other materials are expected to be

comparable.<sup>72</sup> Thus, in order to effectively evaluate the physical affinities/interactions between materials comprising a composite, all aspects of molecular structure must be considered. HSP analysis provides an effective strategy to evaluate interactions between components which can then suggest approaches to modify relevant surfaces. Taken together, the approach might prove powerful to aid identification of strategies to improve materials dispersity in battery electrodes.

### 2.3.3 *Electrical Properties*

It has been demonstrated that composite materials morphology influences electrode performance.<sup>83–85</sup> In particular, the dispersion of active materials and carbon additives can affect the current distribution over the composite electrode during electrochemical testing. The current distribution directly impacts battery performance. Thus, it would be anticipated that the material dispersion state would also be connected to battery electrode electrical properties such as electronic conductivity. The development of reliable and robust experimental techniques that can directly measure electronic conductivity without interference from the metal foil substrate, however, is a challenge. Existing techniques such as electrochemical impedance spectroscopy (EIS) and point probe measurement have some limitations. For instance, for EIS, it is difficult to separate electronic and ionic resistances in the presence of electrolyte, while for the point probe method, it is difficult to maintain sufficient contact with porous, composite films without damage as well as to keep the applied pressure of the probe constant.<sup>86,87</sup> Hence here, a newly designed electrode device for measuring electronic conductivity of composite battery electrode materials is introduced; the device is similar to a field-effect transistor (FET).<sup>75,88</sup>

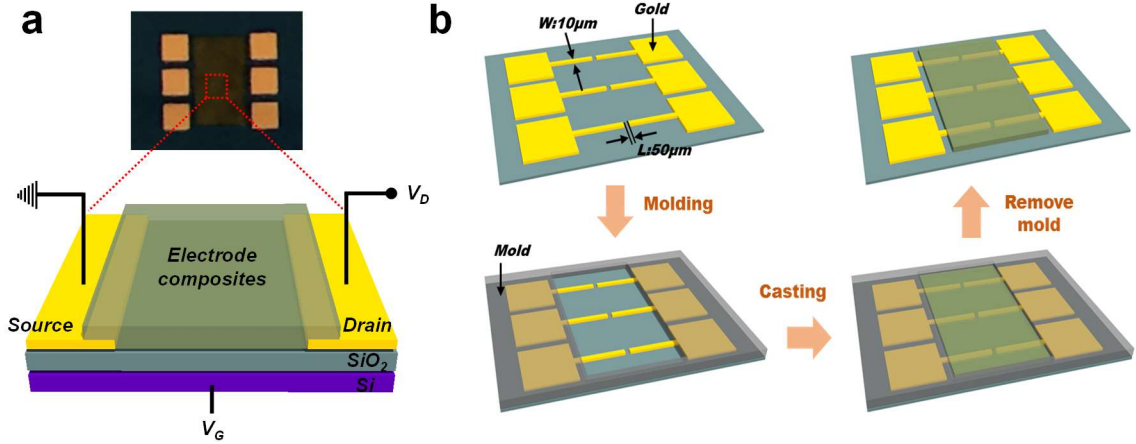


**Figure 2.7.** (a) Schematic structure and photo-image of bottom contact electrode device. (b) Schematic diagram of mold casting process showing fabrication of the electrode devices for measuring the electronic conductivity. The respective composite slurries were mold-casted onto the device substrates (channel width = 10 μm and length = 50 μm). The thickness of composite films was approx. 4~10 μm.

For the electrical measurements, we adopted the newly designed configuration (channel width = 10 μm and length = 50 μm) (Figure 2.7a) with two bottom contacts, allowing for measurements of contact resistance. Composite electrode electronic conductivity is measured simultaneously at three different points, thereby providing insight as to the uniformity of the distribution of the electronically conductive channels. Two voltage probes between the source and drain electrodes monitor the potential along the conductive channel, consequently inducing mobile charge carriers.<sup>88</sup> The resulting electronic conductivity was calculated by Eq.2

$$\sigma = \frac{L}{W \times t} \frac{I_D}{V_D} \quad (2)$$

where  $W$  (10 μm),  $L$  (50 μm) and  $t$  are the channel width, length and film thickness, respectively.  $V_D$  is the drain voltage, and  $I_D$  is the drain current.



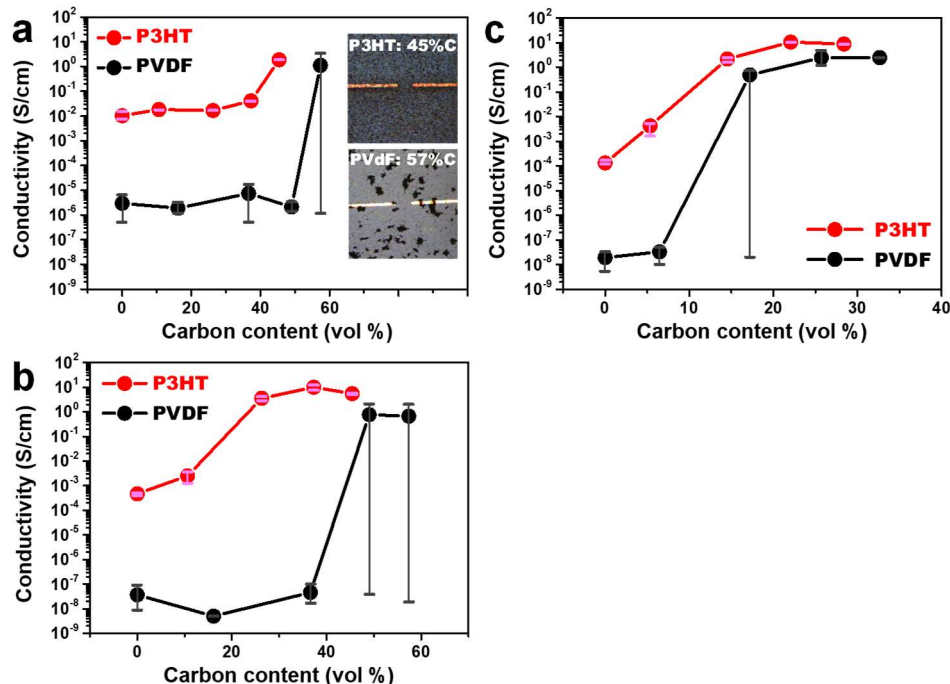


**Figure 2.8.** Electronic conductivities of (a) carbon/polymer composites (spin-coating method): inset figures showing the OM images of 45 vol. % of carbon/P3HT and 57% vol. % of carbon/PVDF which are considered the percolation threshold concentration in spin-coated electrodes, (b) carbon/polymer composites (mold-casting method) and (c) OA-Fe<sub>3</sub>O<sub>4</sub>/carbon/polymer composites (mold-casting method) with constant amount of OA-Fe<sub>3</sub>O<sub>4</sub> and polymer. The graph has the sphere symbols expressing the average conductivity, together with the upper bar for the largest value and the lower bar for the smallest value.

The composite film layers were prepared by spin coating and mold casting. The electronic conductivity associated with spin coating, as shown in Figure 2.8a, correlates with the OM observation results in Figure 2.2b; P3HT with uniformly dispersed carbon additives exhibits electronic conductivities having no deviation, whereas carbon obviously aggregates in the PVDF counterpart and large deviations are observed, notably at about 57 vol. % carbon. The results strongly suggest that the improved electrical properties derive from the more uniformly dispersed P3HT system. The electronic conductivity of devices fabricated by the two methods, however, differs (Figure 2.8a, b), particularly for the

percolation threshold concentration. Although the electrode prepared by spin coating has the advantage of facilitating differentiation of the material dispersion state *via* readily accessible techniques such as optical microscopy and accurately representing the enhanced electrical properties associated with the respective morphologies, the percolation networks generated between two channels (10  $\mu\text{m}$ ) vary from the more representative dense electrodes. Most likely, this results from the spread-out morphology of spin-coated electrodes (inset images in Figure 2.8a). Thus, mold casting was used as the electrode fabrication method, whereby a rectangular mold was used to make the dense electrode, as depicted in Figure 2.7b. Specifically, after a mold is placed on the patterned electrode device, the as-prepared slurry was cast into the mold and then solvent was evaporated. The photo-image in Figure 2.7a represents the electrode device coated by mold casting (green rectangle). For the carbon/polymer composite electrodes (Figure 2.8b), the P3HT system exhibits a conductive percolation threshold at about 26 vol. % carbon, while that for the PVDF counterpart is about 45 vol. %. In addition, the P3HT system conductivity shows almost no deviation, whereas PVDF requires over 48 vol. % carbon and the composite has many fewer conductive regions despite exhibiting percolation behavior. For the OA-Fe<sub>3</sub>O<sub>4</sub>/carbon/polymer composites (Figure 2.8c), even though both systems have similar percolation thresholds, the electronic conductivity of the PVDF-17 vol. % carbon electrode exhibits the same small value,  $\sim 10^{-8}$  S/cm, as that prepared with under 7 vol. % carbon. These results provide further evidence that the dispersion state of the electrode materials has a significant effect on properties such as electronic conductivity; more well-dispersed battery materials provide for enhanced electrical characteristics. Accordingly, it might be expected that P3HT-based electrodes will experience more homogeneous current

distribution over the uniformly dispersed components of a composite electrode *vs* PVDF-based counterparts with uneven current distribution.

#### 2.3.4 *Electrochemical Evaluation*

Four combinations of electrode components were tested in an experimental two electrodes coin cell configuration *vs* lithium metal: 1) P3HT with uncapped  $\text{Fe}_3\text{O}_4$ , 2) PVDF with uncapped  $\text{Fe}_3\text{O}_4$ , 3) P3HT with OA- $\text{Fe}_3\text{O}_4$  and 4) PVDF with OA- $\text{Fe}_3\text{O}_4$ . Each electrode was lithiated from open-circuit potential to 0.3 V then delithiated to 3.0 V *vs*  $\text{Li}/\text{Li}^+$ . The lithiation and delithiation voltage profiles for each electrode type are shown in Figure 2.9. During lithiation, electrodes with uncapped  $\text{Fe}_3\text{O}_4$  produced 1,334 mAh/g with P3HT binder and a similar 1,300 mAh/g with PVDF. Samples with uncapped  $\text{Fe}_3\text{O}_4$  with either binder operated at similar operating voltages with plateaus of 1.63, 1.18 and 0.90 V. The sample with uncapped  $\text{Fe}_3\text{O}_4$  and PVDF demonstrated 830 mAh/g on delithiation while the capacity for the P3HT sample was 739 mAh/g. Cells with OA- $\text{Fe}_3\text{O}_4$  and PVDF binder delivered 600 mAh/g and those with P3HT binder delivered 125 mAh/g. Additionally, the cell with P3HT and oleic acid-capped magnetite showed a lower lithiation voltage ( $\sim 0.5$  V).

Electrodes fabricated with oleic acid-capped  $\text{Fe}_3\text{O}_4$  showed better particle dispersion and worse electrochemical performance than cells with uncapped  $\text{Fe}_3\text{O}_4$ . It was hypothesized that evenly distributed particles would expose more surface area of the active material to the electrolyte and shorten  $\text{Li}^+$  ion diffusion pathways. There can be slow diffusion paths to the center of large particle agglomerates which limit gravimetric capacity as some active material is isolated in the agglomerate center and inaccessible to  $\text{Li}^+$

ions.<sup>36,43,89</sup> As depicted in Figure 2.9, both P3HT and PVDF displayed significant agglomeration with uncapped  $\text{Fe}_3\text{O}_4$  but they outperformed electrodes with OA-capped  $\text{Fe}_3\text{O}_4$ . These results suggest that oleic acid has an additional, significant impact on electrochemical performance beyond particle dispersivity. The use of oleic acid decreased capacity which is likely due to poor electron transport or  $\text{Li}^+$  ion diffusion through the layer of oleic acid surrounding the active particles. It is possible that oleic acid acted as an insulating shell around the active material. Poor electron or ion transport through the electrode can be visualized as an increase in electrode electrical resistance. AC impedance was measured to investigate differences in resistances of the assembled coin cells.

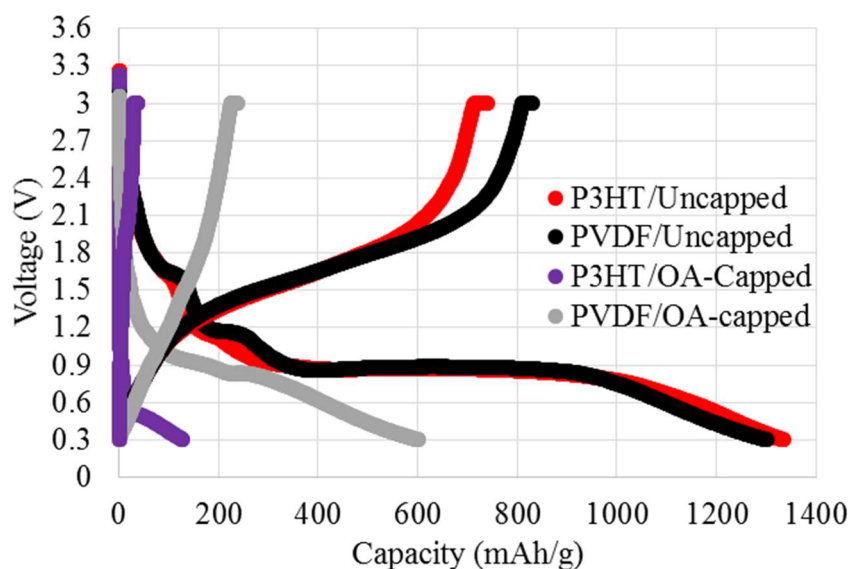


**Figure 2.9.** Voltage profiles for  $\text{Fe}_3\text{O}_4$  half-cells.

AC impedance spectroscopy of the coin cells was performed prior to operation, as shown in Figure 2.10. AC impedance spectroscopy can be used to measure a battery's ionic and electronic conductivities. P3HT/uncapped  $\text{Fe}_3\text{O}_4$ , PVDF/uncapped  $\text{Fe}_3\text{O}_4$  and PVDF/OA- $\text{Fe}_3\text{O}_4$  samples displayed AC responses showing a depressed semicircle at

higher frequencies followed by a long linear tail at lower frequencies. This type of Nyquist plot can be fit with the equivalent circuit shown in Figure 2.10d. In this model,  $R_s$  is the ohmic series resistance,  $R_{ct}$  is related to the charge-transfer resistance the Warburg element is related to ionic diffusion. The P3HT and OA-Fe<sub>3</sub>O<sub>4</sub> showed significantly larger impedance. Absolute impedance  $Z'$  is plotted against frequency in Figure 2.10c. All samples responded similarly to higher frequencies, but differed greatly at low frequencies. At 0.01 Hz the absolute impedance of P3HT/OA-Fe<sub>3</sub>O<sub>4</sub> is more than 100 times greater than both samples with uncapped magnetite while the sample with PVDF/OA-Fe<sub>3</sub>O<sub>4</sub> had an absolute impedance more than 15 times the impedance of the uncapped samples. Results from the equivalent circuit fits are displayed in Figure 2.10e. The Warburg coefficient was taken as the slope of the relationship between absolute impedance ( $Z'$ ) and the inverse square root of angular frequency ( $\omega^{-1/2}$ ) at low frequencies.

Each cell showed similar  $R_s$  values as expected. Comparing the two samples with uncapped Fe<sub>3</sub>O<sub>4</sub> show that the electrode with P3HT exhibited nearly double the charge-transfer resistance and a larger Warburg coefficient compared to PVDF. The electrodes with PVDF indicate that the presence of oleic acid increases charge-transfer resistance and significantly increases the Warburg coefficient. The Warburg coefficient in the P3HT/OA-Fe<sub>3</sub>O<sub>4</sub> sample is large which indicates that ion diffusion is limited in this electrode.

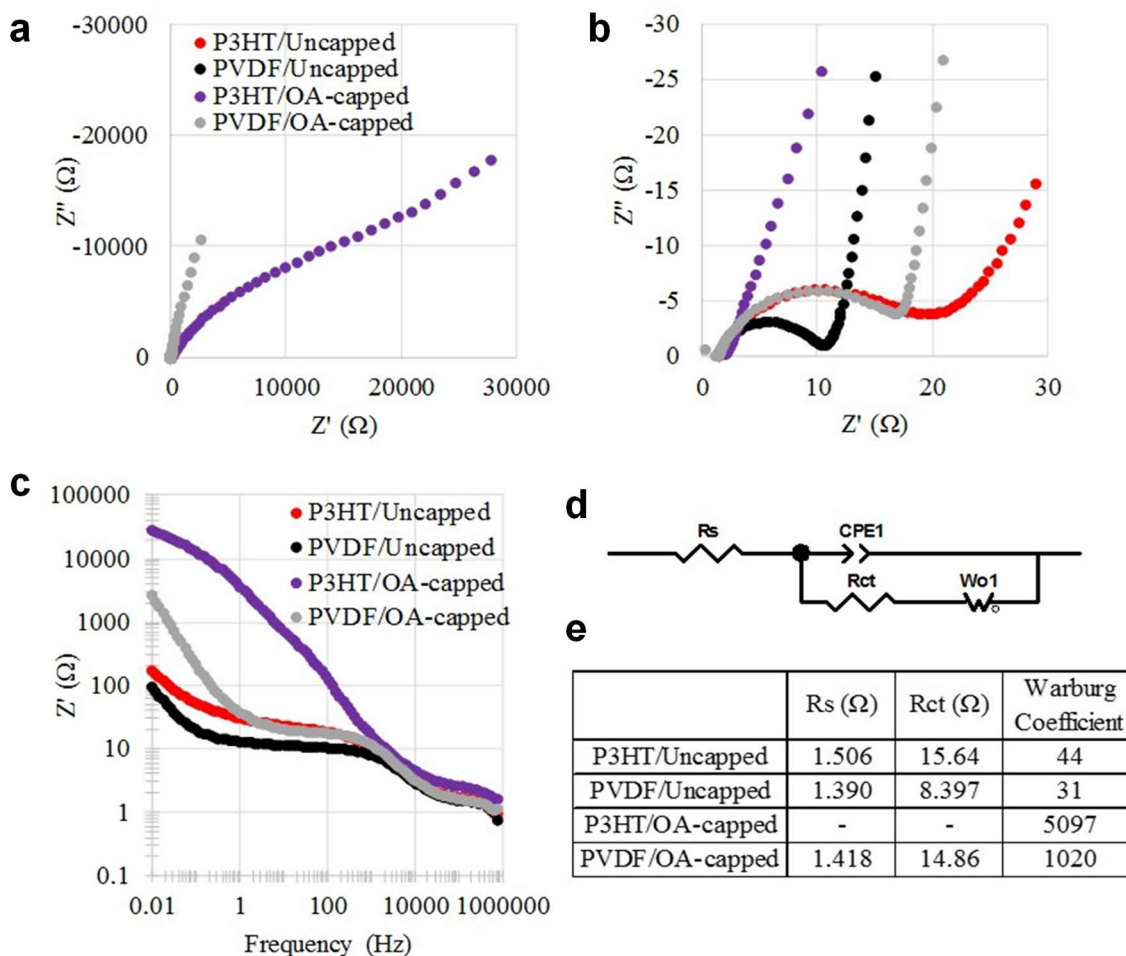


**Figure 2.10.** Electrochemical Impedance Spectroscopy (EIS) results for coin cells before cycling. (a) Nyquist plot of EIS results, (b) Nyquist plot of EIS results with smaller axes values, (c) Bode plot of EIS results, (d) equivalent circuit used to fit EIS data, and (e) results from fitting EIS with equivalent circuit.

The delivered capacities of uncapped magnetite ( $\text{Fe}_3\text{O}_4$ ) electrodes prepared with P3HT or PVDF binders were similar. These results are consistent with the impedance results for the two systems, which are also similar. The capacities of the electrodes containing OA- $\text{Fe}_3\text{O}_4$  were significantly lower than those using pristine  $\text{Fe}_3\text{O}_4$ . As oleic acid coats the  $\text{Fe}_3\text{O}_4$  particles it interferes with the electrochemical activity of magnetite in the electrode coating. Oleic acid as a capping agent improves particle dispersion, but

capping agents can also negatively influence electrochemical results by restricting ion and possibly electron transport. The cells containing P3HT and OA-capped  $\text{Fe}_3\text{O}_4$  displayed the poorest electrochemical performance of the group. This cathode combination produced the lowest capacity and lowest operating voltage.

Previously, oleic acid capped  $\text{Fe}_3\text{O}_4$  nanoparticles dispersed on a glassy carbon electrode surface were evaluated electrochemically.<sup>90</sup> Cyclic voltammetry of the coated electrodes was performed in acidic aqueous media and demonstrated that while the  $\text{Fe}_3\text{O}_4$  was electrochemically active, the delivered current was lower than anticipated based on estimates from the film thickness. It was noted that a significant fraction of magnetite was not electrochemically accessible; the cause was broadly assigned to nanoparticle aggregation, limited transport through the Nafion film that was used or the presence of oleic acid.

The electrochemical results here provide several findings. In comparison to the performance of cells prepared with PVDF and uncapped magnetite, the P3HT counterparts exhibit somewhat higher charge-transfer resistance. The similar lithiation and lower delithiation capacity of the P3HT cells are consistent with the impedance results. The combined EIS and constant current cycling results indicate that the electrochemical behavior of uncapped  $\text{Fe}_3\text{O}_4$  is superior to that of OA- $\text{Fe}_3\text{O}_4$ . The presence of the oleic acid capping agent increases the charge-transfer resistance in both polymeric binder environments. The impact on electrochemistry of oleic acid is much more significant when P3HT serves as the binder vs PVDF. As evidenced by the increased Warburg coefficient, oleic acid appears to severely limit ion transport in both systems. The effect is more significant in the P3HT environment.

The results presented in this investigation show that capping agents can effectively stabilize and promote improved nanoparticle dispersion; however that dispersivity is highly system dependent. With respect to composite battery electrodes, the active material, conductor and binder all play a role in performance. Through studies using capped and uncapped  $\text{Fe}_3\text{O}_4$ , and two alternative binder polymers, it was demonstrated that materials dispersivity cannot be used in isolation to predict electrochemical performance. For instance, separate previous studies strongly suggested that oleic acid coated active materials would positively impact electrode performance and/or conjugated polymer electronic conductivity. Here, it was shown that capping agents can be detrimental to electrochemical performance. Electronic conductivity, electron transfer as well as ion transport impact electrochemical behavior and must all be considered in the design of active material environments. This report provides insight for future studies pertaining to dispersion of active nanomaterials, surface modifications, and compatibility with polymeric binders.

## **2.4 Conclusion**

Surface modification of nanoparticles used for composite battery electrode applications has been shown to be an effective strategy to achieve remarkably enhanced materials dispersivity. Effective approaches include the introduction of surfactant-like functionalities onto electroactive materials *via* organic capping agents and wrapping of carbon additives with conjugated polymers. In addition, deliberate consideration of particle surface physical affinities/interactions aided by Hansen solubility parameter analysis helps to illuminate component surface characteristics, and thereby facilitate the design of compatible architectures. A simple spin coating process which affords a thin-film can



simplify characterization of the component materials dispersion state *via* optical, atomic force and scanning electron microscopies.

It is anticipated that the use of physical affinity relationships will enable the design and fabrication of more uniformly dispersed composites for battery electrode applications; improved dispersion characteristics are expected to enhance both electrical and electrochemical properties. Notably, electronic conductivity, electron transfer as well as ion transport impact electrochemical behavior and must all be considered in the design of active material environments. The approaches described herein are expected to provide fundamental insights into the mechanisms and impact of uniform dispersion in battery electrode applications, especially for the effective incorporation and utilization of electroactive nanomaterials components.

# **CHAPTER 3. ELECTRON AND ION TRANSPORT ENHANCER: PEG-COATED $\text{Fe}_3\text{O}_4$ AND PPBT WATER- SOLUBLE CARBOXYLATE POLYTHIOPHENE- BASED ELECTRODES**

## **3.1 Introduction**

The high energy/power density associated with Li-ion batteries serves as a driving force for intensive research related to high capacity anode materials. The main obstacles which retard the practical implementation of high-capacity electrochemically active particles including metal oxides, Si, Sn and their derivatives (Table 3.1), stem from large volume changes associated with Li insertion/extraction and the resultant electrical contact loss, thereby leading to poor cycling performance.<sup>10–15</sup> Efforts have been made to circumvent the breakdown of electronic pathways through the introduction of electrically conducting functionalities such as carbon coatings<sup>12–18</sup> and conductive polymeric binders onto the surface of the active materials,<sup>11,19,20</sup> or the fabrication of stable battery anodes using an electrically inactive polymeric binder that facilitates retention of electrode integrity.<sup>21–24</sup> While these approaches are quite effective, consideration should also be given to ion transport. In that regard, a composite electrode designed with porous ion

---

Adapted with permission from “Kwon, Y. H.; Minnici, K.; Huie, M. M.; Takeuchi, K. J.; Takeuchi, E. S.; Marschilok, A. C.; Reichmanis, E. Electron/Ion Transport Enhancer in High Capacity Li-Ion Battery Anodes. *Chem. Mater.* **2016**, 28, 6689–6697.” Copyright 2016 American Chemical Society.

transport channels in addition to electron transport pathways should afford improved performance.

**Table 3.1.** Comparison of electroactive anode materials for Li-ion batteries

Material	Theoretical capacity <sup>92</sup> (mAh g <sup>-1</sup> )	Reaction potential <sup>a</sup> (V vs. Li/Li <sup>+</sup> )	Volume change <sup>b</sup> (%)
Graphite	372	0.05 – 0.25 <sup>93</sup>	10 <sup>94</sup>
Si	4200	0.05 – 0.5 <sup>93</sup>	420 <sup>94</sup>
Sn	994	0.4 – 0.8 <sup>93</sup>	260 <sup>94</sup>
Metal oxides (Fe <sub>3</sub> O <sub>4</sub> )	500 – 1000 (926)	- (0.5 – 2 <sup>15,17</sup> )	- (200 <sup>38,95,96</sup> )

<sup>a</sup> Based on lithiation/delithiation peaks in the cyclic voltammetry.

<sup>b</sup> Volume change during lithiation/delithiation processes.

In principle, the electrochemical reactions that occur in an electrode when a Li ion encounters an electron within an active site determine the electrode's intrinsic energy capacity.<sup>6</sup> Both electron and ion transport are critical factors that determine the internal resistance of electrodes, which is the primary influence on electrochemical performance. Despite their importance, research that considers both factors is rarely reported.

Here, we report a facile strategy to enhance both electron and ion transport within high capacity anode systems. Magnetite (Fe<sub>3</sub>O<sub>4</sub>) was used as the electroactive component because it is readily available and has a high theoretical capacity (~926 mAh g<sup>-1</sup>), which derives from the possibility to induce the transfer of multiple electrons from the lithiation and conversion processes.<sup>97,98</sup> Fe<sub>3</sub>O<sub>4</sub> also exhibits low conductivity that induces poor cycling.<sup>18</sup> Further, studies pertaining to the use of the semiconducting polymer, poly(3-hexylthiophene) (P3HT), in conjunction with Fe<sub>3</sub>O<sub>4</sub>-based electrodes to enhance electrode

electrical performance, demonstrated that in addition to electron transfer, consideration of ion transport in the design of a composite electrode was essential.<sup>32</sup>

The approach presented here introduces poly[3-(potassium-4-butanoate) thiophene] (PPBT) — a water-soluble, carboxylate substituted polythiophene — as a binder component and a polyethylene glycol (PEG) surface coating for the active material. Conjugated polythiophenes have relatively high electronic conductivity ( $10^{-2} - 10^{-4} \text{ S cm}^{-1}$ ; *i.e.*, P3HT)<sup>32</sup> and undergo electrochemical doping — provided that the applied potential drives the reduction of the conjugated polymers within the operating voltage of anode applications<sup>59,61,99</sup> — enabling more rapid electron transport and developing electrical bridges between the active materials and carbon additives. Additionally, the side chain carboxylic moieties present in PPBT could facilitate the formation of porous, stable electrodes. PPBT is soluble in water, which has high surface tension and thus may be expected to inhibit perfect coverage of the material surface.<sup>100</sup> In turn, this may support pore formation during the evaporation process. Chemical interactions between the PPBT COO- moieties and metal oxide surface (–OH) are expected to favorably impact electrode stability.<sup>21–24,101</sup> The PEG coating on the Fe<sub>3</sub>O<sub>4</sub> surface is likely to reduce the size of aggregates, improve their dispersion,<sup>102</sup> and thereby shorten the Li ion diffusion path and enable homogeneous current distribution over the electrode.<sup>43</sup> In addition, PEG is expected to facilitate Li ion conduction to the active sites from the surrounding electrolyte.<sup>103</sup>

The introduction of PPBT as a binder and PEG as a coating on the Fe<sub>3</sub>O<sub>4</sub> active particle surface demonstrates the opportunities afforded by consideration of both electron and ion transport processes in the design of high performance composite electrode materials. Synergetic effects derived from using a conjugated polymer for enhanced

electron transport with the PEG surface coating that supports ion transport lead to reduced electrode resistance, stable cycling performance and improved rate capabilities.

### 3.2 Experimental Section

**Materials.**  $\text{Fe}_3\text{O}_4$  nanoparticles ( $\sim 10$  nm) were synthesized by a previously reported co-precipitation process, using aqueous solution of iron (III) chloride hexahydrate, iron (II) chloride hexahydrate, and triethylamine.<sup>70,71</sup> For preparation of  $\text{Fe}_3\text{O}_4$  particles coated with PEG (PEG- $\text{Fe}_3\text{O}_4$ ), 1 g of  $\text{Fe}_3\text{O}_4$  powders in 10 g water were sonicated for 1.5 min at room temperature with an ultrasonic probe (3 pulse of 30 sec each, operated at around 3–5 W). 2 mL of PEG 1500 solution (50 % w/v, Sigma-Aldrich) was added with sonication for 30 sec, and this process was repeated four times until that the total amount of PEG 1500 is 8 mL. The PEG- $\text{Fe}_3\text{O}_4$  powders were washed and extracted by centrifuge separation using acetone with speed of 6000 rpm for 5 min for 3 times. PPBT ( $M_w$ : 16 kDa, polydispersity: 2.2, the head to tail regioregularity: 89%) was purchased from Rieke Metals Inc..

**Electrode Fabrication.** The slurries for the PPBT-based electrode were prepared by mixing of  $\text{Fe}_3\text{O}_4$  (or PEG- $\text{Fe}_3\text{O}_4$ ), carbon additives, and PPBT in a solvent of water, and in case of PVDF-based electrode, *N*-methyl-2-pyrrolidone (NMP) solvent was used (weight ratio of  $\text{Fe}_3\text{O}_4$ :carbon:polymer = 71.4:14.3:14.3). The solid content was 3.4 wt% for spin coating, and 27 wt% for blade coating. The composite films for the measurement of optical microscopy (OM) were prepared by spin-coating (WS-6500MZ-23NPP, Laurell) the slurries onto substrates at the spin rate of 1500 rpm for 60 sec in air. The electrodes for field-emission scanning electron microscopy (FE-SEM) measurement, electrochemical evaluation and spectroscopy characterization were produced by blade coating (doctor blade,

MTI corp). These prepared electrodes were pre-evaporated at the room temperature for 2 h and completely evaporated at 110 °C for 12 h in a vacuum oven. In case of PVDF-based electrode, NMP solvent was pre-evaporated at 70 °C for 1 h, and the other fabrication procedures were the same as that of PPBT-based electrodes.

**Electrochemistry.** 2032-type coin cells were used for electrochemical measurements. Lithium metal was used as a counter electrode and 1M LiPF<sub>6</sub> in ethylene carbonate (EC) and diethylene carbonate (DEC) (1:1 by volume) was adopted as electrolyte. Before electrochemical testing, all the coin cells were charging and discharging with the current density of 40 mA g<sup>-1</sup> (~0.05 C) to confirm their capacity. The tests were then proceeded for cycling and rate capability. Cyclic voltammetry (CV) was performed in the potential range of 0.01–3 V at the rate of 0.5 mV s<sup>-1</sup> and electrochemical impedance spectroscopy (EIS) measurements were conducted in the frequency range from 1 MHz to 0.1 Hz.

**Microscopic Characterization.** OM measurements were conducted on the composite films spin-coated on the glass substrate using Olympus MX61 Microscope. FE-SEM images were observed on the surface/cross-sectional view of the electrodes using Zeiss Ultra-60 FE-SEM with an accelerating voltage of 5–10 kV using the high vacuum mode at room temperature.

**Spectroscopic Characterization.** The electrode samples for the spectroscopic measurements were prepared by scraping powder samples from the prepared electrodes to closely investigate the chemical interactions between Fe<sub>3</sub>O<sub>4</sub> and PPBT inside the electrodes. Fourier transform infrared (FT-IR) spectra were recorded using KBr pellets of the materials

and a Nicolet 8700 FTIR spectrometer. X-ray photoelectron spectroscopy (XPS) characterization was performed using a Thermo K-Alpha XPS system. The instrument was equipped with a monochromatic Al-K X-ray source (1468 eV). Spectra were collected using the flood gun and an X-ray spot size of 400  $\mu\text{m}$ . Survey scans were collected with pass energy of 200 eV with 1 eV increments. High resolution scans (for specific elements) were collected with pass energy of 50 eV with 0.1 eV increments

**Solubility tests for Hansen solubility parameter (HSP).** 5 mg of polymer such as PEG and PPBT were placed into a vial with 2 mL of a test solvent. The vial was heated at 70 °C for 3 h and sonicated for 60 min and after then the vials were permitted to stand and observed for 6 h in ambient temperature. The solubility was examined by these solutions *via* visual observation. In case of polymer, solvents would be considered as poor if they were unable to dissolve the polymer after dissolving process and good if they were able to dissolve it. Based on the visual examination, HSPs ( $\delta_D$ ,  $\delta_P$  and  $\delta_H$ ) and the radius value ( $R_o$ ) of the sphere of interaction were calculated and fitted by HSPiP software (Hansen Solubility Parameters in Practice third edition).

### 3.3 Results and Discussion

#### 3.3.1 Electrochemical properties of PPBT

To characterize the basic electrochemical behavior of poly[3-(potassium-4-butanoate) thiophene] (PPBT), cyclic voltammetry (CV) experiments were performed in the potential window of 0.01 V to 3 V *vs* Li/Li<sup>+</sup> (Figure 3.1a). An electrode fabricated with a thin polymer film for electrochemical testing was prepared by spin coating the solution onto a Cu foil substrate. Thick polymer films tend to respond more slowly due to ion

transport limitations, which lead to resultant lower capacities and energy/power density.<sup>59,99</sup> Poly(vinylidene difluoride) (PVDF) was used as the standard reference, owing to its wide utilization as a binder in Li-ion battery electrodes. The first CV profile of PPBT shows two distinctive reduction peaks at 0.32 V and 1.1 V and two oxidation peaks at about 1.1 V and 2.2 V. After the 2nd cycle, one reduction peak at ~1.5 V and broad reduction region below 1 V in contrast with PVDF were observed, and one oxidation peak appears at ~1.1 V. This result indicates electrochemical doping could take place within the operating potential window, possibly boosting electron transport along the PPBT backbone and building the requisite electrical bridge between active particles, carbon additives, and current collector.

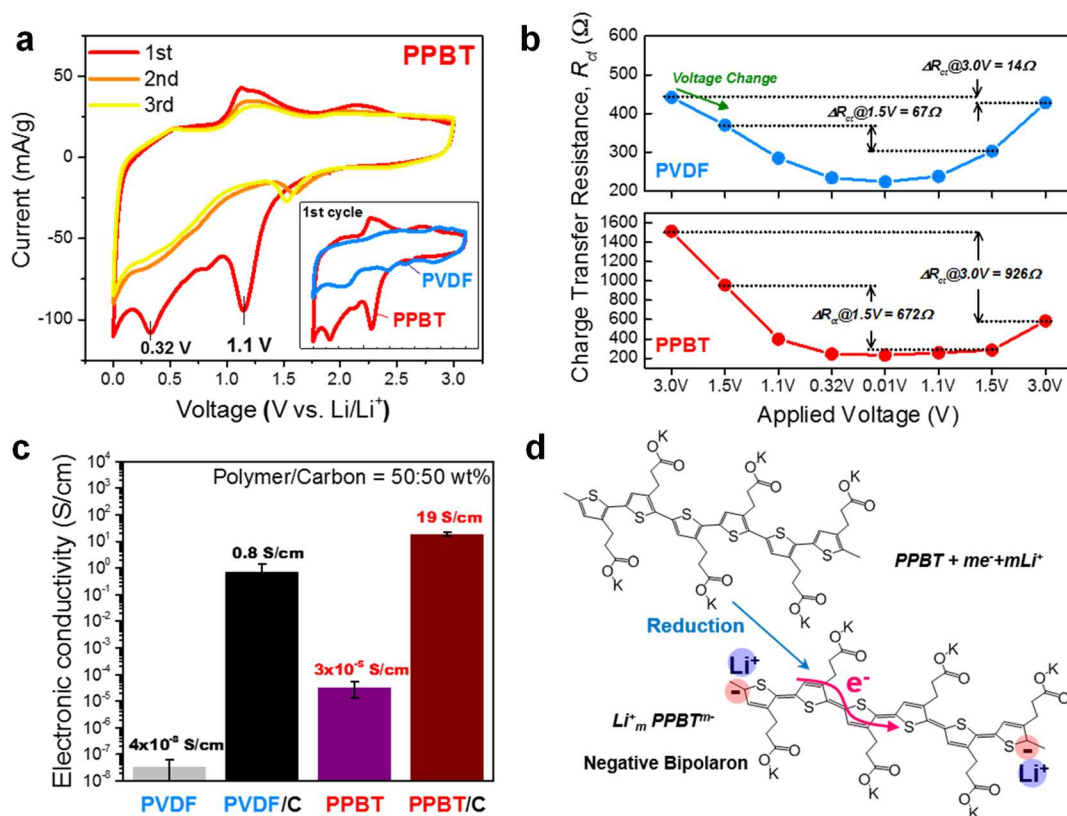


**Figure 3.1.** Electrochemical characterization of PPBT binder. (a) CV profiles of PPBT binder in the potential window of 0.01 to 3 V vs Li/Li<sup>+</sup> collected at the rate of 0.5 mV s<sup>-1</sup>



(inset: PPBT vs PVDF at the first cycle). (b) Trend of charge-transfer resistance with the change of applied voltage measured by EIS in the frequency range from 1 MHz to 0.1 Hz. (c) Comparison of electronic conductivity between PVDF and PPBT system. (d) Illustration of electrochemical doping: PPBT electronic and chemical structure changes during reduction (n-doping).

As shown in Figure 3.1b, electrochemical impedance spectroscopy (EIS) studies were performed with different applied voltages to confirm the possibility of electrochemical doping of PPBT. Typically, the semi-circle in the EIS response profile corresponds to the charge-transfer resistance ( $R_{ct}$ ) at the electrode/electrolyte interface. The electronic resistance and ionic resistance have direct influence on the behavior of  $R_{ct}$ .<sup>104</sup> The electronic resistance reflects the resistance to bring electrons to the surface reaction sites and the ionic resistance is associated with the transfer of ions across the polymer/electrolyte interface. The investigation of  $R_{ct}$  with a change of applied voltage might suggest the existence of electrochemical doping in the PPBT backbone during electrochemical testing. In Figure 3.1b, applied potential was sequentially lowered from 3 V to 0.01 V, and then sequentially increased to 1.5 V and 3 V. When the applied voltage decreased,  $R_{ct}$  of both PPBT and PVDF decreased. Notably, the hysteresis in  $R_{ct}$  at 1.5 V and 3 V was distinctly different for PPBT and PVDF.  $R_{ct}$  of PVDF almost recovered to the initial value at each applied voltage step, whereas  $R_{ct}$  of PPBT showed large hysteresis, with a difference of 672  $\Omega$  at 1.5 V and 926  $\Omega$  at 3 V between the initial and final measurements at those voltages. PVDF itself is an electronic/ionic insulator ( $\sim 10^{-8}$  S cm<sup>-1</sup>, Figure 3.1c), but well-known to possess high ionic conductivity in the electrolyte environment ( $\sim 10^{-3}$  S cm<sup>-1</sup>).<sup>105</sup> Considering  $R_{ct}$  recovery and low initial resistance at 3V in the PVDF system, ionic conducting properties would be a dominant factor for determining

its  $R_{ct}$  value. PPBT, however, might be primarily governed by the electronic characteristics and its distinctive behavior could be ascribed to electrochemical doping.

In addition, PPBT and PPBT composites with carbon exhibit relatively high electronic conductivity compared to the PVDF system (Figure 3.1c). Though PPBT binder is not intrinsically conductive in a pristine state, electrochemical doping enables the formation of electron pathways along its backbone, therefore leading to enhanced electron transport under the reducing environment for anodes. Figure 3.1d illustrates a proposed PPBT doping mechanism during reduction (n-doping).<sup>99</sup> In the case of electrochemical doping, an applied potential induces reduction of the conjugated polymer. Diffusion of a dopant counterion ( $\text{Li}^+$ ) into PPBT from the surrounding electrolyte compensates for the formal negative charge (negative polaron) created on the polymer backbone.<sup>61</sup> Furthermore, the formation of a lamellar structure *via*  $\pi$ - $\pi$  interchain stacking of polythiophenes could facilitate intermolecular charge transport, leading to enhanced electron conduction within the PPBT binder in the composite electrode.<sup>106,107</sup>

### 3.3.2 Effect of PEG coating on the $\text{Fe}_3\text{O}_4$ surface

In an effort to reduce aggregate size and improve particle dispersion within the electrode, polyethylene glycol (PEG) was physically introduced onto the  $\text{Fe}_3\text{O}_4$  particle surface (Figure 3.2a). PEG was selected as a coating material because it is known to be permeable to ions and it has high physical affinity to the PPBT binder. Hansen solubility parameter (HSP) analysis and estimation of the Hansen spheres of interaction provided supporting evidence<sup>32</sup>: 98.3% of the intersection volume portion ( $\%V_{int}$ ) indicates high physical compatibility between the two components (Figure 3.2b). Closer physical affinity

induces better mixing or dispersion. It is anticipated that the resultant electrodes may experience more homogeneous current distribution over the composite electrode during electrochemical testing.

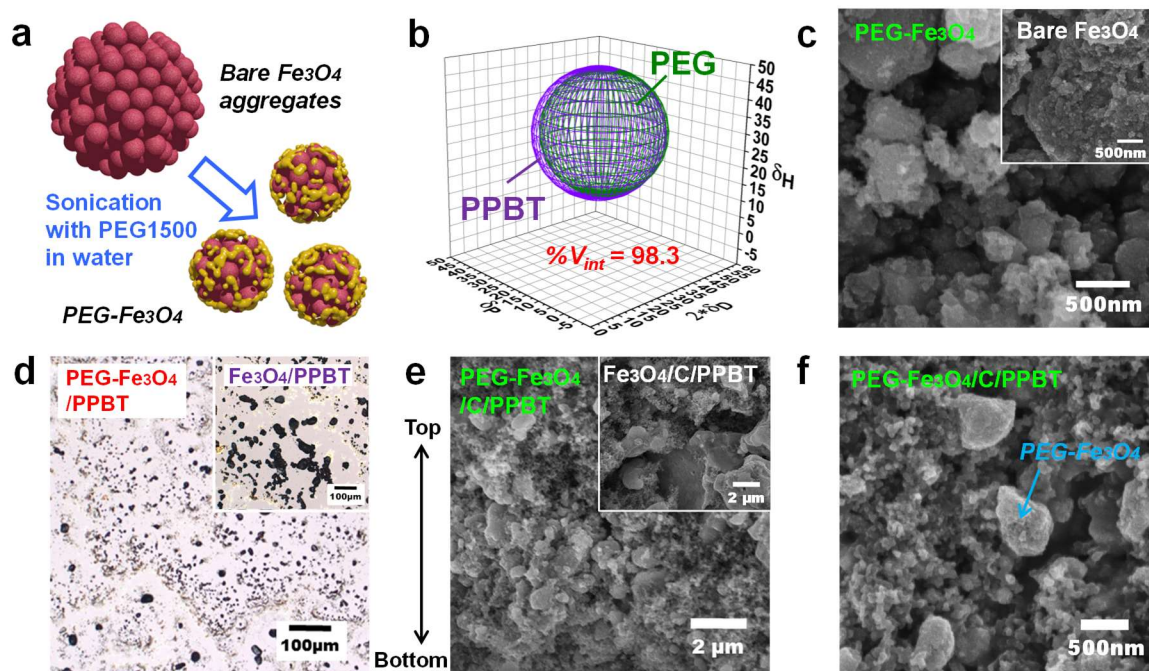


**Figure 3.2.** Effect of PEG coating on the Fe<sub>3</sub>O<sub>4</sub> surface. (a) Schematics of PEG 1500 coating on the Fe<sub>3</sub>O<sub>4</sub> surface through an ultrasonic probe. (b) Hansen solubility parameter (HSP) spheres of interaction for PEG and PPBT. (c) SEM images of PEG-Fe<sub>3</sub>O<sub>4</sub> particles compared to bare Fe<sub>3</sub>O<sub>4</sub> (inset). (d) Optical microscopy (OM) images of PEG-Fe<sub>3</sub>O<sub>4</sub>/PPBT and Fe<sub>3</sub>O<sub>4</sub>/PPBT composites (inset) prepared by spin coating on the glass substrate. (e) SEM images (cross-sectional view) of PEG-Fe<sub>3</sub>O<sub>4</sub>/carbon/PPBT electrode and Fe<sub>3</sub>O<sub>4</sub>/carbon/PPBT electrode (inset). (f) SEM image (surface view) of PEG-Fe<sub>3</sub>O<sub>4</sub>/carbon/PPBT electrode exhibiting well-dispersion Fe<sub>3</sub>O<sub>4</sub> particles in the carbon mixture.

As illustrated in Figure 3.2a, Fe<sub>3</sub>O<sub>4</sub> particles were coated with PEG 1500 in aqueous medium *via* a simple probe-type ultra-sonication process without any stringent control over the conditions.<sup>102</sup> The sonication-assisted PEG coating process limited the growth of aggregates (Figure 3.2c) which is expected to facilitate access to active sites by both Li

ions and electrons. Thermogravimetric analysis (TGA) showed that the PEG-Fe<sub>3</sub>O<sub>4</sub> particles were comprised of 10 wt% PEG, and dynamic light scattering (DLS) analysis demonstrated that the average particle size was ~303 nm (Figure 3.3). To visualize PEG-Fe<sub>3</sub>O<sub>4</sub> particle dispersion within the PPBT binder, optical microscopic (OM) characterization was performed as shown in Figure 3.2d. The uniform morphologies induced by spin-coating demonstrate that the PEG-Fe<sub>3</sub>O<sub>4</sub> particles with smaller aggregate dimensions were well-dispersed in the PPBT binder medium with no apparent re-aggregation.

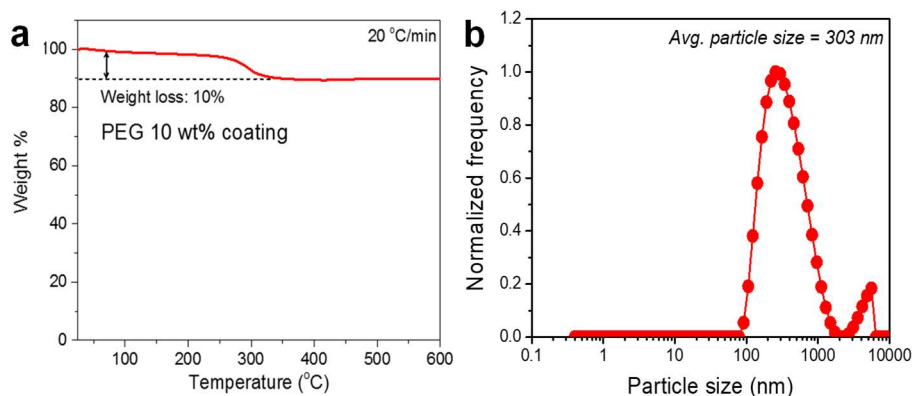


**Figure 3.3.** PEG-Fe<sub>3</sub>O<sub>4</sub> particles: (a) TGA profile of PEG coating, which is carried out in nitrogen in the temperature range of 25–600 °C at a heating rate of 20 °C/min. (b) Dynamic light scattering (DLS) particle size distribution of PEG-Fe<sub>3</sub>O<sub>4</sub> particles. DLS was performed using a Malvern Zetasizer NANO ZS instrument (Malvern instruments). PEG-Fe<sub>3</sub>O<sub>4</sub> particles were dispersed in aqueous medium through bath-type sonication for 30 min (1mg particles/1 mL deionized water).

A standard electrode preparation procedure was followed: Fe<sub>3</sub>O<sub>4</sub> powders were mixed with carbon additives and a polymeric binder dissolved in a solvent, and then the as-produced slurry was blade-coated onto the Cu foil current collector, and finally dried. The resultant electrodes were characterized with field-emission scanning electron

microscopy (FE-SEM) to confirm materials dispersion in a vertical/horizontal direction. The SEM images (Figure 3.2e,f) show that PEG-Fe<sub>3</sub>O<sub>4</sub> with relatively small aggregate size (~0.5–1  $\mu\text{m}$ ) was well mixed and connected with the carbon additives in the PEG-Fe<sub>3</sub>O<sub>4</sub>/carbon/PPBT electrode, compared to a Fe<sub>3</sub>O<sub>4</sub>/carbon/PPBT electrode with large aggregates over ~5  $\mu\text{m}$  (the inset of Figure 3.2e). The PVDF-based electrode exhibits similar morphology to the PPBT-based system with no PEG coating (Figure 3.4). In addition, SEM characterization demonstrates that the water-soluble PPBT binder system might be favorable to pore formation within the electrode during solvent evaporation, which is expected to facilitate ion transport from the liquid electrolyte environment.

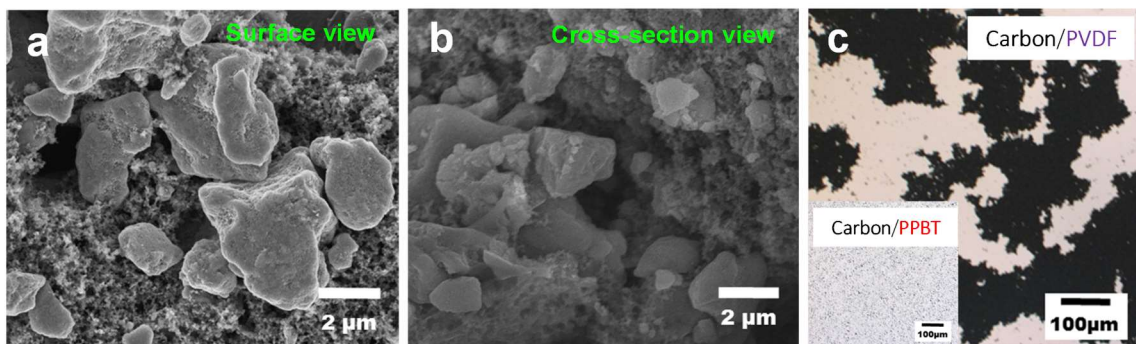


**Figure 3.4.** PVDF binder system. The SEM images of (a) surface view and (b) cross-sectional view of Fe<sub>3</sub>O<sub>4</sub>/carbon/PVDF electrode. (c) OM image of carbon/binder composites (50:50 in a mass ratio) prepared by spin coating on the glass substrate.

### 3.3.3 Electrochemical Performance

To evaluate the electrochemical performance, coin cells with a Li metal counter electrode were utilized and all of the electrodes were prepared with Fe<sub>3</sub>O<sub>4</sub>-based active particles, carbon additives, and a polymeric binder in a 71.4:14.3:14.3 mass ratio. The Fe<sub>3</sub>O<sub>4</sub> mass loading in the present study was typically 2–3  $\text{mg cm}^{-2}$ . The electrolyte was a solution of 1 M LiPF<sub>6</sub> in EC/DEC (1 : 1 by volume).

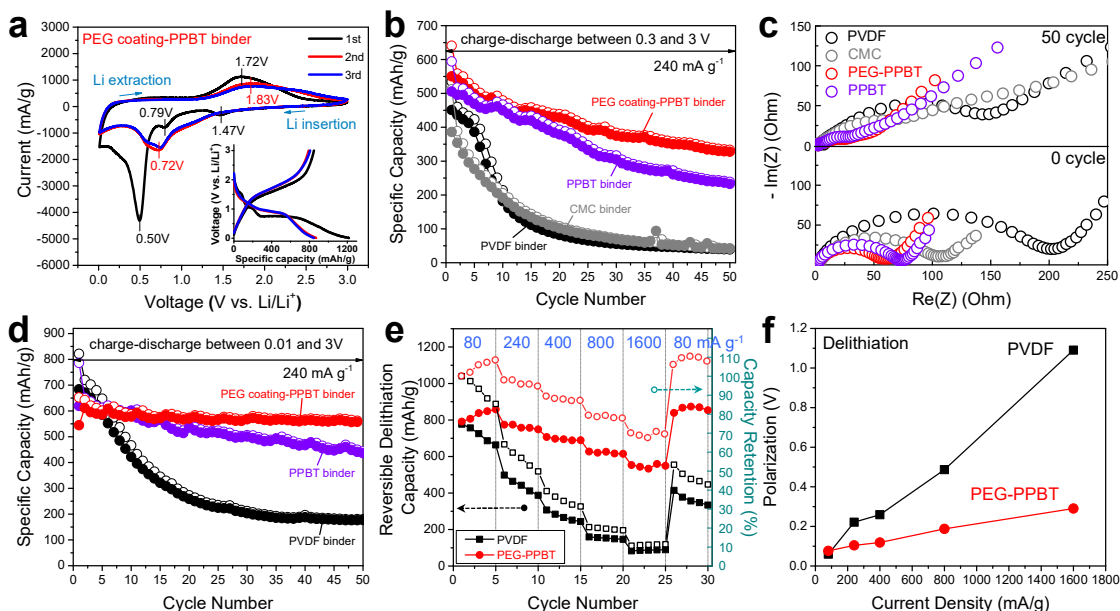


**Figure 3.5.** Electrochemical performance of Fe<sub>3</sub>O<sub>4</sub>-based electrodes. (a) CV profiles of PEG-Fe<sub>3</sub>O<sub>4</sub>/carbon/PPBT electrode in the potential window of 0.01 to 3 V vs Li/Li<sup>+</sup> collected at the rate of 0.5 mV s<sup>-1</sup> (the inset shows the galvanostatic charge-discharge profiles in the potential window of 0.01 to 3 V vs Li/Li<sup>+</sup> at a constant current density of 80 mA g<sup>-1</sup>, comparable to CV profiles). (b) Cycling performance (=capacity retention as a function of cycle number) collected for the current density of 240 mA g<sup>-1</sup> (~0.3 C) between 0.3 and 3 V. (open circles: Li-insertion capacity, filled circles: Li-extraction capacity) (c) The impedance spectra measured at 3 V before cycling (bottom graph) and at open-circuit voltage (OCV) after 50 cycles (upper graph) in the frequency range from 1 MHz to 0.1 Hz. (d) Cycling performance between 0.01 and 3 V. (e) Delithiation rate capability, where cells were lithiated at a constant current density of 80 mA g<sup>-1</sup> and delithiated at different current densities between 0.01 and 3 V. (open symbols: capacity retention, filled symbols: Li-extraction capacity) (f) Cell polarization as a function of the applied current density during the delithiation process.

CV analysis was performed to elucidate electrochemical behavior of the PEG-Fe<sub>3</sub>O<sub>4</sub>/PPBT binder-based electrode (Figure 3.5a). In the reduction process at the first cycle, the cathodic peaks at 1.47 V and 0.79 V correspond to the structure transition induced by lithium intercalation ( $\text{Fe}_3\text{O}_4 + x\text{Li}^+ + xe^- \rightarrow \text{Li}_x\text{Fe}_3\text{O}_4$ ) and the cathodic peak at 0.5 V is attributed to further reduction by the conversion reaction ( $\text{Li}_x\text{Fe}_3\text{O}_4 + (8-x)\text{Li}^+ + (8-x)e^- \rightarrow 3\text{Fe}^0 + 4\text{Li}_2\text{O}$ ) along with formation of the SEI layer.<sup>16,18,108–110</sup> The region below 0.5 V

has a significant contribution from lithiation of the carbon additives.<sup>111</sup> The subsequent oxidation process at the first cycle shows a broad anodic peak at ~1.72 V, ascribed to oxidation of Fe to Fe<sup>2+</sup>/Fe<sup>3+</sup>. In the subsequent cycles, a broad peak between ~0.72 V and ~1.83 V appeared during the reduction and oxidation process, respectively, due to the electrochemical redox reaction (Fe<sub>3</sub>O<sub>4</sub> ↔ Fe<sup>0</sup>) through Li insertion/extraction.<sup>16</sup> The results obtained for the PEG-Fe<sub>3</sub>O<sub>4</sub>/PPBT binder-based electrode are in close agreement with previous studies for Fe<sub>3</sub>O<sub>4</sub>/PVDF systems.<sup>108,109</sup>

Charging-discharging cycling (Figure 3.5b) at the current density of 240 mA g<sup>-1</sup> (~0.3 C) demonstrated that the PPBT binder system allowed for noticeably improved capacity retention, and that the PEG coating on the Fe<sub>3</sub>O<sub>4</sub> surface afforded more stable cycling than that obtained with only PPBT as a binder. These results are in contrast to Fe<sub>3</sub>O<sub>4</sub> anodes fabricated with either PVDF or carboxymethyl cellulose (CMC) binders. EIS analysis in Figure 3.5c supports this observation. The coin cells used in the EIS study correspond to those cycled between 0.3 V and 3 V as shown in Figure 3.5b. This impedance test was performed in the frequency range of 1 MHz to 0.1 Hz before cycling at 3.0 V and after 50 cycles at their open-circuit voltage (OCV). The superior battery performance associated with the PEG coated active material and PPBT binder system may originate from decreased electrode resistance: in comparison to the PVDF standard, PEG coating/PPBT binder system charge transfer resistance ( $R_{ct} \approx$  estimated diameter of the semicircle) was effectively reduced both before cycling and after 50 cycles. This strongly points to positive synergistic effects associated with using both the PEG coating and conjugated polymer binder to improve electron and ion transport phenomena in the electrode. Coating the Fe<sub>3</sub>O<sub>4</sub> active material surface with PEG to limit growth of aggregates

and facilitate their dispersion is expected to enhance ion transport. With respect to electron transport, the semiconducting PPBT binder may function as an ‘electrical bridge’ between  $\text{Fe}_3\text{O}_4$  active particles and carbon additives (or current collector), thereby facilitating electron transport *via* the PPBT pathway induced by electrochemical doping during battery cycling (Figure 3.1d).

In order to investigate PPBT binder electrochemical doping effects, newly fabricated coin cells were further lithiated by lowering the cut-off voltage from 0.3 V to 0.01 V. In other words, the cycling test was performed between 0.01 V and 3 V. Figure 3.5d presents the charging-discharging performance at a current density of  $240 \text{ mAh g}^{-1}$  ( $\sim 0.3 \text{ C}$ ). Despite the harsher lithiation conditions, both PEG- $\text{Fe}_3\text{O}_4$ /PPBT binder- and PPBT binder-based electrode capacity retention appeared more stable than observed under the 0.3 V cut-off conditions. The PEG coating/PPBT binder system, in particular, exhibited 91.2 % capacity retention at 50 cycles, compared to the PVDF control showing only 25.9 % retention.

Conceivably, electrochemical doping positively impacts the low voltage region – recall the PPBT CV profile which exhibited a broad reduction peak at about 0.32 V that is believed to be due to electrochemical doping (Figure 3.1a). Moreover, the beneficial effect of the PEG/PPBT approach was also seen in the rate capability experiments (Figure 3.5e). Under a constant lithiation current density of  $80 \text{ mA g}^{-1}$  ( $\sim 0.1 \text{ C}$ ), a PEG- $\text{Fe}_3\text{O}_4$ /PPBT binder-based electrode shows much higher delithiated capacity than the PVDF control over a wide range of delithiation current densities ( $80\text{--}1600 \text{ mA g}^{-1}$ ) at a voltage range of 0.01–3 V, which conveys its superior rate capability. Figure 3.5f summarizes a quantitative analysis of the ohmic polarization as a function of the applied current density, where the



polarization was examined by measuring the difference in initial voltage between the current density of 80 mA g<sup>-1</sup> (~0.1 C) and a given current density.<sup>28</sup> A comparison of voltage profiles provides for a cell polarization which provides an indication of the electrochemical kinetics taking place in the electrode. Specifically, in the PEG/PPBT system, PPBT and conductive carbon-mediated electron networks and PEG-induced Li ion accessibility are, presumably, the crucial factors determining the kinetics. The PEG/PPBT approach exhibited a polarization value that was noticeably lower than that of the control, resulting in improved battery performance.

### 3.3.4 Surface Analysis

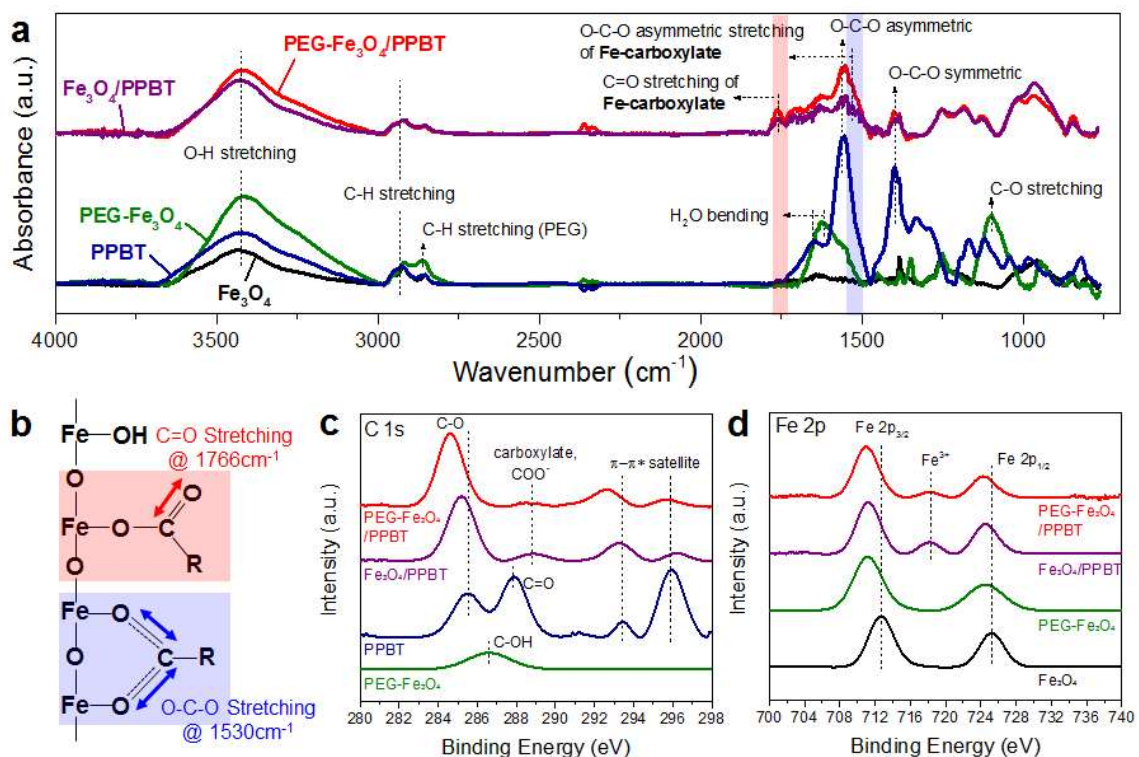


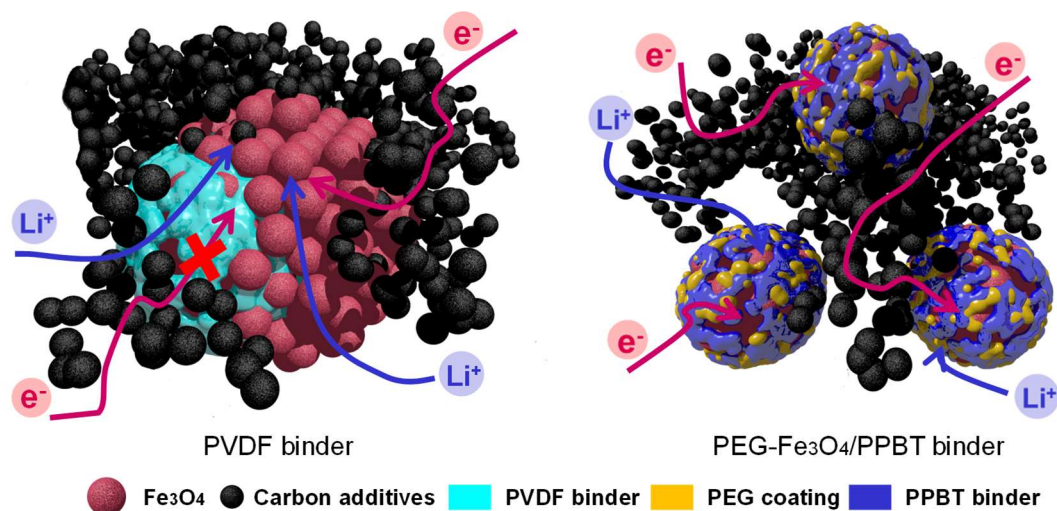
**Figure 3.6.** Spectroscopy characterization of the Fe<sub>3</sub>O<sub>4</sub>, PEG-Fe<sub>3</sub>O<sub>4</sub>, PPBT and electrodes prepared by mixing PEG-Fe<sub>3</sub>O<sub>4</sub> (or Fe<sub>3</sub>O<sub>4</sub>) with PPBT binder. (a) FT-IR spectra of materials (bottom lines: Fe<sub>3</sub>O<sub>4</sub>, PEG-Fe<sub>3</sub>O<sub>4</sub>, PPBT) and electrodes (upper lines: Fe<sub>3</sub>O<sub>4</sub>/PPBT, PEG-Fe<sub>3</sub>O<sub>4</sub>/PPBT). (b) The possible binding modes of complexes on the Fe<sub>3</sub>O<sub>4</sub> surface. (c, d) XPS spectra of materials (Fe<sub>3</sub>O<sub>4</sub>, PEG-Fe<sub>3</sub>O<sub>4</sub>, PPBT) and electrodes (Fe<sub>3</sub>O<sub>4</sub>/PPBT, PEG-Fe<sub>3</sub>O<sub>4</sub>/PPBT).

From a mechanistic perspective, molecular interactions between the PPBT carboxyl group and either  $\text{Fe}_3\text{O}_4$  or PEG- $\text{Fe}_3\text{O}_4$  particles may enable electron and ion transport. Fourier transform infrared (FT-IR) spectroscopy studies (Figure 3.6a) revealed sharp C–H and C–O stretching bands at  $1105\text{ cm}^{-1}$  and  $2860\text{ cm}^{-1}$ , respectively for PEG- $\text{Fe}_3\text{O}_4$  powders, which confirmed  $\text{Fe}_3\text{O}_4$  surface modification with PEG.<sup>102</sup> PPBT carboxylic moieties exhibit peaks at  $1556\text{ cm}^{-1}$  and  $1400\text{ cm}^{-1}$  which correspond respectively to O–C–O asymmetric and symmetric stretching.<sup>24</sup> After electrode formation, FT-IR test samples were prepared by scraping powdered samples from the electrodes. In comparison to the raw materials, all PPBT-based electrodes, fabricated with either  $\text{Fe}_3\text{O}_4$  or PEG- $\text{Fe}_3\text{O}_4$  particles, showed strong bands centered at  $1556\text{ cm}^{-1}$  and  $1400\text{ cm}^{-1}$  associated with free carboxylate anions. In addition, new, lower intensity peaks that were not apparent in the parent samples were observed at  $1530\text{ cm}^{-1}$  and  $1766\text{ cm}^{-1}$ . As depicted in Figure 3.6b, the peak at  $1766\text{ cm}^{-1}$  is associated with Fe-carboxylate bond C=O stretching. The shoulder observed at about  $1530\text{ cm}^{-1}$  (split from the  $1556\text{ cm}^{-1}$  band) suggests coordination of carboxylate functionalities with  $\text{Fe}_3\text{O}_4$  surface: the shift to lower frequency arises from weakening of the O–C–O vibration due to Fe-carboxylate bonding.<sup>101,112–114</sup> The FT-IR results provide evidence of PPBT- $\text{Fe}_3\text{O}_4$  chemical interactions. Spectroscopically, the PEG- $\text{Fe}_3\text{O}_4$ /PPBT and  $\text{Fe}_3\text{O}_4$ /PPBT electrodes are very similar, strongly suggesting that the PEG coating on  $\text{Fe}_3\text{O}_4$  is readily displaced by PPBT carboxylate groups which can chemically bond with  $\text{Fe}_3\text{O}_4$  surface hydroxyl functionalities.<sup>115,116</sup> While such strong interactions between a binder and the surface of high capacity active materials have been

reported to be one of the most critical factors influencing electrode stability, previous experimental results have been limited to Si anodes.<sup>21–24</sup>

The X-ray photoelectron spectroscopy (XPS) spectra of the C 1s and Fe 2p core levels further substantiate the presence of chemical interaction between PPBT and the Fe<sub>3</sub>O<sub>4</sub> surface. In Figure 3.6c, the C 1s peaks at ~285 eV are ascribed to carbon atoms associated with the C-O bond; note the chemical shift to lower binding energy with an increase in interatomic distance which results from additional bonding between PPBT and Fe<sub>3</sub>O<sub>4</sub>.<sup>117,118</sup> The C 1s peak at 287.88 eV for PPBT is indicative of a C=O bond. The remaining C 1s peaks for PPBT at 293.48 eV and 295.88 eV are associated with satellite peaks, which result from the extended delocalized electrons in the sample and provide evidence of interchain PPBT  $\pi$ - $\pi^*$  stacking.<sup>119</sup> This molecular packing formation may induce charge transport along the  $\pi$ - $\pi$  stacking direction and improve the electrical properties of the PPBT binder system. C 1s peaks at 288.78 eV for Fe<sub>3</sub>O<sub>4</sub>/PPBT and PEG-Fe<sub>3</sub>O<sub>4</sub>/PPBT are attributed to carboxylate (COO<sup>-</sup>),<sup>117</sup> as seen in the proposed chemical structure in Figure 3.6b. When analyzing the Fe 2p core-level peaks (Figure 3.6d), the binding energy shifts to about 712 eV and 724 eV for Fe<sub>3</sub>O<sub>4</sub>/PPBT and PEG-Fe<sub>3</sub>O<sub>4</sub>/PPBT might be attributed to the Fe-carboxylate bond.<sup>120</sup> In addition, the Fe<sup>3+</sup> associated with both systems exhibits a distinct satellite peak at ~718 eV.<sup>121</sup> Their absence for Fe<sub>3</sub>O<sub>4</sub> and PEG-Fe<sub>3</sub>O<sub>4</sub> confirms a pure magnetite phase. The presence of the satellite peak for Fe<sub>3</sub>O<sub>4</sub>/PPBT and PEG-Fe<sub>3</sub>O<sub>4</sub>/PPBT, further illustrates the chemical interaction between PPBT carboxylic moieties and the hydroxylated Fe<sub>3</sub>O<sub>4</sub> surface.

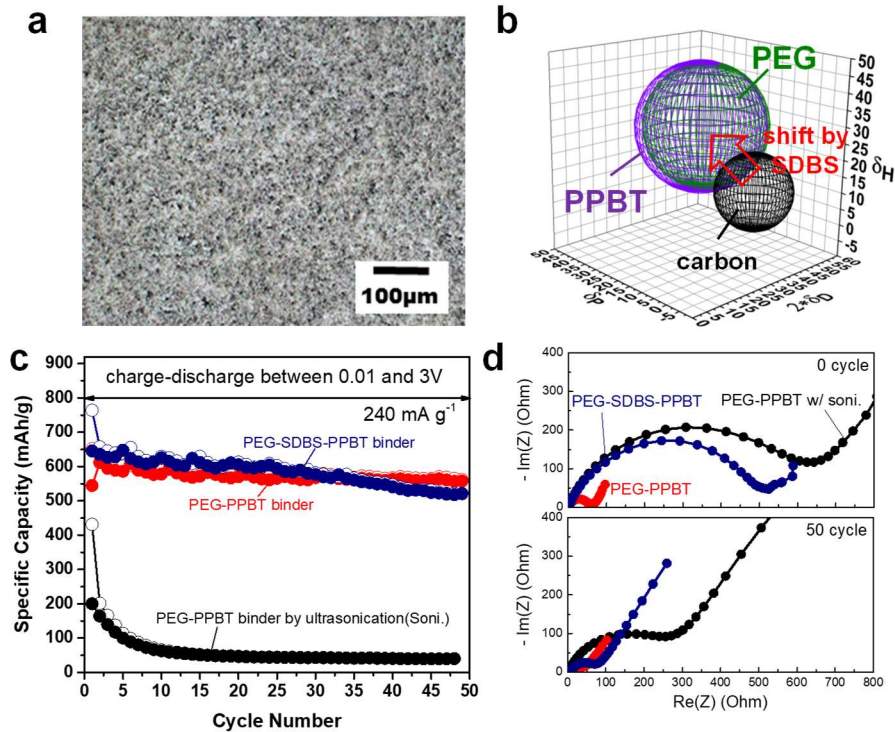
### 3.3.5 Proposed Mechanism



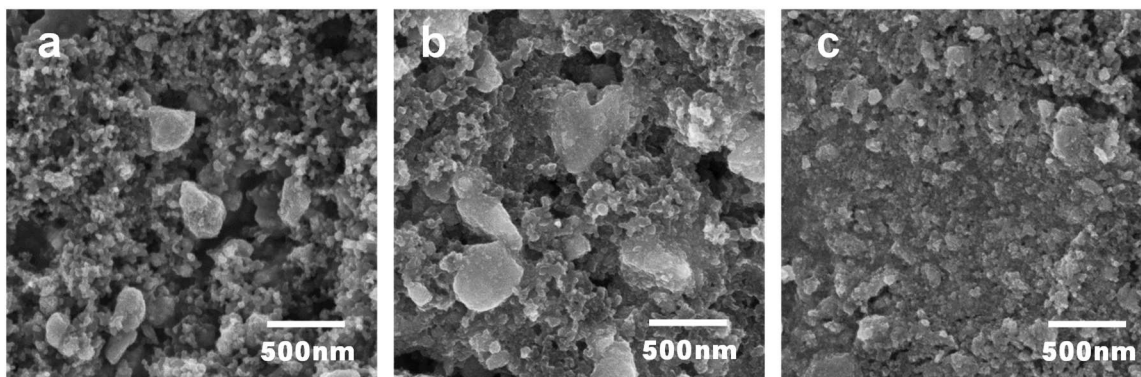
**Figure 3.7.** Schematic illustrations depicting electron and ion transport in the electrode.

Figure 3.7 presents a schematic diagram that elucidates the electron and ion transport phenomena associated with the PEG/PPBT based electrode *vs* its PVDF counterpart. Within the PVDF control, the individual components (including active materials, carbon additives, and even the PVDF binder) comprising the electrode are expected to exhibit a significant level of aggregation due to their different physical affinities<sup>32</sup> (Figure 3.4). PVDF is an electronic insulator, thus blocking electron transport between active materials and carbon additives (or current collector). The PEG/PPBT system, however, enables the creation of electron and ion pathways in the Fe<sub>3</sub>O<sub>4</sub> surroundings to enhance the conducting characteristics which help battery performance. Moreover, the smaller-sized aggregates arising from the introduction of PEG onto the Fe<sub>3</sub>O<sub>4</sub> surface are also expected to contribute positively to the electrochemical processes, which may be facilitated by improved dispersion between the active material and carbon additives.<sup>122</sup>

Importantly, however, when considering materials dispersion within a polymer composite electrode, a porous structure must be maintained if a given binder is not permeable to electrolyte molecules.<sup>24</sup> In other words, a binder should either cover only a portion of active material surface or remain permeable to Li ions. In this work, since PPBT is not permeable to Li ions, polymer wrapping on a carbon or active particle through the use of chemical or physical methods, may expedite the process whereby pores become blocked, yielding poor electrochemical results (Figure 3.8 and Figure 3.9). Therefore, it is critical to consider transport processes in conjunction with molecular/chemical structure and possible physical or chemical interactions. Here, the possible synergies obtained from the combined use of the semiconducting polymer, PPBT as a binder and PEG as a surface coating for Fe<sub>3</sub>O<sub>4</sub> active particles were considered in terms of the above requisites, effecting improved electrochemical behavior.



**Figure 3.8.** Effects of material dispersion using chemical/physical dispersion process. (a) OM image of PEG-Fe<sub>3</sub>O<sub>4</sub>/carbon /PPBT composites spin-casted on the glass substrate after probe-type ultra-sonication (physical dispersion). (b) Hansen solubility parameter analysis of PEG 1500, PPBT and carbon: physical affinity of carbon additives were deviated from Hansen sphere of PEG 1500 and PPBT. SDBS surfactant was used for the carbon dispersion (chemical dispersion). (c) Cycling performance (= capacity retention as a function of cycle numbers) of PEG-Fe<sub>3</sub>O<sub>4</sub>/carbon/PPBT, PEG-Fe<sub>3</sub>O<sub>4</sub>/carbon /SDBS/PPBT, and PEG-Fe<sub>3</sub>O<sub>4</sub>/carbon/PPBT prepared by probe-type ultra-sonication. (d) EIS results of coin cell measured before cycling and after 50 cycles. The chemical/physical dispersion process both has largely increase in  $R_{ct}$  before cycling, which affects the resulting poor cycling, especially for the sonication dispersion process.



**Figure 3.9.** Surface view SEM images of (a) PEG-Fe<sub>3</sub>O<sub>4</sub>/carbon/PPBT, (b) PEG-Fe<sub>3</sub>O<sub>4</sub>/carbon/SDBS/PPBT and (c) PEG-Fe<sub>3</sub>O<sub>4</sub>/carbon/PPBT prepared by probe-type ultra-sonication. The electrodes with no treatment show the well-constructed porous structure, whereas the electrodes with SDBS surfactant and the electrodes prepared by ultra-sonication appear covered with PPBT binder. These morphologies might be attributed to substantially high degree of reaction of PPBT carboxylic moieties with hydroxyl group of Fe<sub>3</sub>O<sub>4</sub> and carbon, inducing the polymer wrapping/covering. This strongly indicates the material dispersion by polymer wrapping on the surface of Fe<sub>3</sub>O<sub>4</sub> active materials enables the prevention of the pore formation during the solvent evaporation, which rather hinders ion and electron transport.

### 3.4 Conclusion

We demonstrated methodical consideration for both ion and electron transport by introducing a carboxylated PPBT binder and facile PEG surface treatment, which

remarkably enhanced the performance of  $\text{Fe}_3\text{O}_4$  high-capacity anodes. PPBT with pendant carboxylic moieties facilitated electron transport along the polymer backbone *via* electrochemical doping, building necessary electrical linkages between carbon and  $\text{Fe}_3\text{O}_4$  particles. Additionally, Fe-carboxylate bonding positively affected high-capacity anode stability. Generally, the poor cycling performance of high-capacity electrode materials lies in difficulties related to substantial volume changes in the active material and resultant loss of electron transport pathways. The results and mechanistic insight presented here suggest a new approach that can provide for high-capacity energy materials with feasible process methodologies for their practical use in the near future.

# **CHAPTER 4. CARBON NANOTUBE WEB WITH CARBOXYLATED POLYTHIOPHENE “ASSIST” FOR HIGH-PERFORMANCE BATTERY ELECTRODES**

## **4.1 Introduction**

Achieving close to theoretical performance is an ongoing challenge for high energy Li-ion batteries, which enable a transition from our imagination into reality for technologies such as smart Internet of Things (IoT) devices, electrical vehicles (EVs), and even flexible/wearable electronics.<sup>8,9,33</sup> In theory, electrochemical performance is largely dominated by electrode resistance during operation, coupled with electron/ion transport in the electrode.<sup>6</sup> In the case of high-capacity anode materials which undergo conversion upon electrochemical (dis)charge including metal oxides, Si, Sn, and their derivatives, however, severe volume changes can occur that lead to crack formation and pulverization resulting in electrical contact loss during electrochemical testing, thereby exacerbating electrode resistance and degrading battery performance.<sup>93</sup> Thus, designing electrode materials and/or materials architectures to alleviate those properties is the first step toward developing high performance battery systems.

---

Adapted with permission from “Kwon, Y. H.; Park, J. J.; Housel, L. M.; Minnici, K.; Zhang, G.; Lee, S. R.; Lee, S. W.; Chen, Z.; Noda, S.; Takeuchi, E. S.; Takeuchi, K. J.; Marschilok, A. C.; Reichmanis, E. Carbon Nanotube Web with Carboxylated Polythiophene “Assist” for High-Performance Battery Electrodes. *ACS Nano* **Article ASAP** DOI: 10.1021/acsnano.7b08918.” Copyright 2018 American Chemical Society.



A typical electrode comprises electroactive materials, conductive carbon additives and a polymeric binder that are blade-coated onto a metal foil substrate. Among those components, most studies have been focused on the electroactive powders, including investigations related to controlling their morphology<sup>10,123,124</sup> or modifying their surface<sup>13,15,125</sup> to benefit  $\text{Li}^+$  ion diffusion or electron transfer. Also, new polymeric binders have been introduced that facilitate the formation of a stable electrode.<sup>24,126,127</sup> While these material-oriented approaches were quite effective, the resultant electrodes continued to have inherent limitations originating from the inorganic/organic composite matrix. Specifically, discontinuities in electron pathways and blockage of porous ion transport passages by the polymeric binder can impede electron/ion movement.

To address these obstacles, systematic approaches that introduce three-dimensionally (3-D) interconnected porous electrode designs in conjunction with highly electrical conductive functionalities including conductive polymers,<sup>20,128–130</sup> carbon nanotubes (CNTs),<sup>28,29,132,133</sup> graphene,<sup>30,31</sup> or even metallic ingredients,<sup>134,135</sup> have been suggested. The resultant electrodes possessed high porosity and well-developed electrical channels, which positively influenced their performance. Interestingly, a CNT network-based concept demonstrated high-rate capability, without sacrificing performance associated with losses of volumetric and gravimetric electrode capacity; and a 3-D interconnected architecture using either a graphene—<sup>30,31</sup> or electrodeposited Ni—frame<sup>134,135</sup> exerted less impact on these same characteristics owing to a large inner pore volume. Still, the expected performance enhancements were not fully realized. For instance, the CNT networks required a mechanical support in the form of an integrated electrically inert polymer,<sup>28,29,133</sup> or an underlying metal foil substrate.<sup>132</sup> Further, the

networks were simply physically interconnected with electrode components. In the absence of interactions facilitated by surface chemistry, intimate contact between components was likely absent, thereby adversely impacting electrical conductivity/connectivity and electrode stability. To date, efforts to develop CNT network-based electrodes have not fully considered materials dispersion; neither have mechanisms to ensure effective electrical connectivity between electroactive particles and those networks been contemplated. Notably, current distribution and charge transfer kinetics are critically dependent on both.

Here, we report that carbon nanotube web electrodes, assisted by a carboxylate substituted polythiophene yielded stable, high-performance battery electrodes. To maximize electron/ion transport, the conjugated, carboxylate bearing polymer was introduced as a physical/chemical linker to render the electroactive spheres and CNT networks well-connected through molecular interactions. The approach uses poly[3-(potassium-4-butoate) thiophene] (PPBT) as a water-soluble, carboxylated polythiophene, polyethylene glycol (PEG) coated monodispersed  $\text{Fe}_3\text{O}_4$  spheres (PEG- $\text{sFe}_3\text{O}_4$ ), introduction of carbon nanoparticles (*e.g.* carbon black) to assure inner pores due to their bulky attributes, and few-walled carbon nanotubes (FWNTs)<sup>136,137</sup> having sub-millimeter length for building a porous, self-standing web as a long-chain CNT component.

High-capacity  $\text{Fe}_3\text{O}_4$  powders ( $\sim 925 \text{ mAh g}^{-1}$ ) — readily synthesized in spherical form with controlled size allowing for uniform  $\text{Li}^+$  ion diffusion — were used as a model metal oxide active material: the metal oxide surface ( $-\text{OH}$ ) presents a well-defined chemistry that is easily probed.<sup>18,138</sup> PPBT, having a conjugated backbone and carboxylated side chain moieties, plays a very important role, whereby it contributes both to effective FWNT dispersion and to bond formation between the carboxylate substituent and available

surface  $\text{-OH}$  moieties present on the  $\text{sFe}_3\text{O}_4$  active material. The  $\pi$ -conjugated polythiophene backbone physically interacts with the two-dimensional, graphene-like  $\pi$ -electron rich nanotube surface; and the solubilizing carboxylated alkyl side chains assist in FWNT debundling and effective dispersion in water.<sup>55</sup> Chemical interactions between PPBT carboxylic moieties and the hydroxylated  $\text{sFe}_3\text{O}_4$  surface favorably affected electrode stability, and facilitated electron transport by creating electrical linkages between the FWNTs and  $\text{Fe}_3\text{O}_4$  spheres through electrochemical doping during battery operation.<sup>139</sup> Thus, unlike typical electrodes where the polymer simply acts as a binding component, the carboxylated polythiophene supports facile formation of substantial electrical pathways through both physical and importantly, chemical interactions. To allow for PPBT  $\text{COO-}$  functionalities to deliver FWNTs onto the  $\text{sFe}_3\text{O}_4$  metal oxide surface, the physical affinity between the carboxylated polymer and the  $\text{sFe}_3\text{O}_4$  surface is of importance. By introducing a PEG coating on the metal oxide, the carboxylated polythiophene is attracted to the active component drawing FWNTs along to successfully bring the nanotubes into intimate contact with the metal oxide while still dispersed in the aqueous solvent prior to electrode fabrication.

Successful fabrication of a high-performance FWNT web electrode using PPBT that assists not only with physical but importantly, chemical coupling between the active material and nanotube surface demonstrates the significant need to consider surface chemistry and surface chemical interactions in the design of composite electrodes. Appropriate choice of surface chemistry can provide for effective dispersion of the components and induce formation of critical electrical transport pathways. Here, binding between PPBT carboxylate and  $\text{sFe}_3\text{O}_4$  surface hydroxyl groups,  $\pi$ -electron surface

interactions (FWNT and PPBT backbone), and the physical affinity between the materials surfaces (PEG and PPBT) were considered advantageously. Consequently, stable connections between electrode materials were successfully created through linkages with the carboxylated polythiophene, which led to reduced electrode resistance and enhanced charge transfer kinetics. In turn, electrode specific capacity even at a high rate was improved, as were cycle stability and rate capabilities.

## 4.2 Experimental Section

**Materials.** Monodispersed spherical  $\text{Fe}_3\text{O}_4$  particles (~500 nm in diameter) were synthesized by a solvothermal method reported by Fan *et al.*<sup>138</sup> The precursor solution was prepared by dissolution of  $\text{FeCl}_3 \cdot 6\text{H}_2\text{O}$  (2.16 g) and  $\text{CH}_3\text{COONa} \cdot 3\text{H}_2\text{O}$  (5.76 g) into 40 mL of ethylene glycol (EG) to form a homogeneous solution with stirring for 24 h. The resultant solution was then sealed in a Teflon lined stainless steel autoclave (45 mL capacity), in which the concentration of  $\text{FeCl}_3 \cdot 6\text{H}_2\text{O}$  was  $0.200 \text{ mol L}^{-1}$ . The autoclave was heated to  $200^\circ\text{C}$  for 8 h, and then cooled to room temperature. After sequentially washing several times with deionized water and ethanol using a centrifuge, monodispersed  $\text{Fe}_3\text{O}_4$  spheres (s $\text{Fe}_3\text{O}_4$ ) were produced. For the preparation of s $\text{Fe}_3\text{O}_4$  particles coated with PEG (PEG-s $\text{Fe}_3\text{O}_4$ ), 1 g of s $\text{Fe}_3\text{O}_4$  powders in 10 g ethanol adding 8 mL of PEG 1500 solution (50 % w/v, Sigma-Aldrich) were sonicated for 30 min in an ice bath with an ultrasonic probe. The PEG-s $\text{Fe}_3\text{O}_4$  powders were washed and extracted by centrifuge separation using acetone at a speed of 6000 rpm for 10 min. The process was repeated 3 times. FWNTs with submillimeter length were synthesized using fluidized-bed chemical vapor deposition method, as a conductive substrate owing to its high electrical conductivity and high aspect

ratio.<sup>136,137</sup> PPBT ( $M_w$ : 16 kDa, polydispersity: 2.2, head to tail regioregularity: 89%) was purchased from Rieke Metals Inc..

**Electrode Fabrication and Characterization.** For the fabrication of the FWNT web electrode, the mixture of FWNT (3.5 mg) in PPBT solution (7 mg of PPBT, 4mL of deionized water) was sonicated for 15 min in an ice bath with an ultrasonic probe. After adding PEG-sFe<sub>3</sub>O<sub>4</sub> (25 mg) and carbon black (CB, 5mg) into the FWNT dispersion, the suspension was subjected to ultrasonication for 3 min. The FWNT suspension for a mechanical support layer was prepared by dispersing FWNT (2 mg) with probe-type ultrasonication in 10 mL of SDBS solution (concentration = 1.0 wt % in water). The resultant FWNT suspension and the electrode slurry were sequentially vacuum-filtrated onto a membrane filter (PVDF membrane filter with pore size of 0.22  $\mu$ m, EMD Millipore). To remove residual SDBS surfactant and excessive PPBT, the electrode was washed by vacuum filtration adding sufficient water. To promote the development of a porous structure in the FWNT web electrode, the wet-state electrode was subjected to vacuum filtration by pouring ethanol (20 mL) followed by acetone (20 mL) through the electrode and it was then placed in a freeze dryer (Labconco, Freeze drying system/Freezone 4.5 L) overnight (solvent exchange-assisted freeze-drying method). The electrode was finally vacuum-dried overnight at 110 °C, eventually fabricating self-standing FWNT web electrodes. The SDBS surfactant-assisted FWNT web electrodes were prepared by the same process mentioned above, except for the electrode slurry preparation using SDBS surfactant solution (concentration = 1.0 wt % in water) instead of PPBT solution. The electrode of sFe<sub>3</sub>O<sub>4</sub>/FWNT (SDBS) was produced from 25 mg of sFe<sub>3</sub>O<sub>4</sub> and 3.5 mg of FWNT in 10 mL of SDBS solution, and sFe<sub>3</sub>O<sub>4</sub>/CB/FWNT (SDBS) electrode for 25 mg of

sFe<sub>3</sub>O<sub>4</sub>, 5 mg of CB, and 3.5 mg of FWNT in 10 mL of SDBS solution. The reference electrode including PEG-sFe<sub>3</sub>O<sub>4</sub>/CB/PPBT and sFe<sub>3</sub>O<sub>4</sub>/CB/PVDF (weight ratio = 71.4/14.3/14.3) was blade-coated on the Cu foil substrate.<sup>32,139</sup> These prepared electrodes were pre-dried at 65 °C for 3 h and completely dried at 110 °C for 12 h in a vacuum oven. The electronic conductivity of the electrodes was measured using a standard four-point probe configuration (Signatone). For measuring the electronic conductivity of the FWNT/PPBT composite film (Figure 4.1g), mold casting was conducted using a rectangular mold being put onto the substrate. These prepared electrodes were pre-dried at 65 °C for 1 h and completely dried at 110 °C for 12 h in a vacuum oven. The porosity of the electrodes was calculated by measuring the thickness and mass loading (mg cm<sup>-2</sup>) of each electrode disc (1 cm in diameter) and using the density of each materials component (sFe<sub>3</sub>O<sub>4</sub>: 5.17 g cm<sup>-3</sup>; FWNT: 2.1 g cm<sup>-3</sup>; carbon black: 1.89 g cm<sup>-3</sup>; PPBT: 1.1 g cm<sup>-3</sup>).<sup>140</sup>

**Electrochemistry.** 2032-type coin cells (MTI corp.) were used for electrochemical measurements. Lithium metal was used as a counter electrode and 1.2 M LiPF<sub>6</sub> in ethylene carbonate (EC) and diethyl carbonate (DEC) (1:1 by volume) with 10 wt % fluoroethylene carbonate (FEC) for long cycle stability, was utilized as an electrolyte. Before electrochemical testing, all the coin cells were charged and discharged with the current density of 0.1 C (~90 mA g<sup>-1</sup>) to confirm their capacity and initial Coulombic efficiency. The tests then proceeded for cycling performance and rate capability. Cyclic voltammetry (CV) was performed in the potential range of 0.01–3 V at the rate of 0.5 mV s<sup>-1</sup> and electrochemical impedance spectroscopy (EIS) measurements were conducted in the frequency range from 1 MHz to 0.1 Hz.

**Spectroscopic Characterization.** The electrode samples for spectroscopic measurements were prepared by grinding powder samples from the as-prepared FWNT web electrodes to closely investigate the chemical interactions between  $\text{sFe}_3\text{O}_4$  and PPBT inside the electrodes. Fourier-transform infrared spectroscopy (FT-IR) spectra were recorded using KBr pellets of the materials and a Nicolet 8700 FTIR spectrometer. X-ray photoelectron spectroscopy (XPS) characterization was performed using a Thermo K-Alpha XPS system. The instrument was equipped with a monochromatic Al-K X-ray source (1468 eV). Spectra were collected using the flood gun and an X-ray spot size of 400  $\mu\text{m}$ . Survey scans were collected with pass energy of 200 eV with 1 eV increments. High-resolution scans (for specific elements) were collected with the pass energy of 50 eV with 0.1 eV increments. For XPS analysis of the electrodes after 200 cycles, the delithiated electrodes were extracted from cycled coin cells and carefully rinsed with DEC three times (5mL in total) to remove residual electrolyte and then dried in a vacuum oven (80 °C, 10 h).

**Microscopic Characterization.** The optical microscopy (OM) measurements were conducted using an Olympus MX61 Microscope. The composite films optical microscopy (OM) were prepared by spin-coating (WS-6500MZ-23NPP, Laurell) the slurries onto substrates at the spin rate of 1500 rpm for 60 sec in air.<sup>32</sup> The field-emission scanning electron microscopy (FE-SEM) images were observed in surface and cross-sectional view of the electrodes using a Zeiss Ultra-60 FE-SEM with an accelerating voltage of 10 kV using the high vacuum mode at room temperature. Ion milling system (IM4000, Hitachi) was used for preparing the cross-sections of the electrodes.

### 4.3 Results and Discussion

### 4.3.1 Materials Preparation

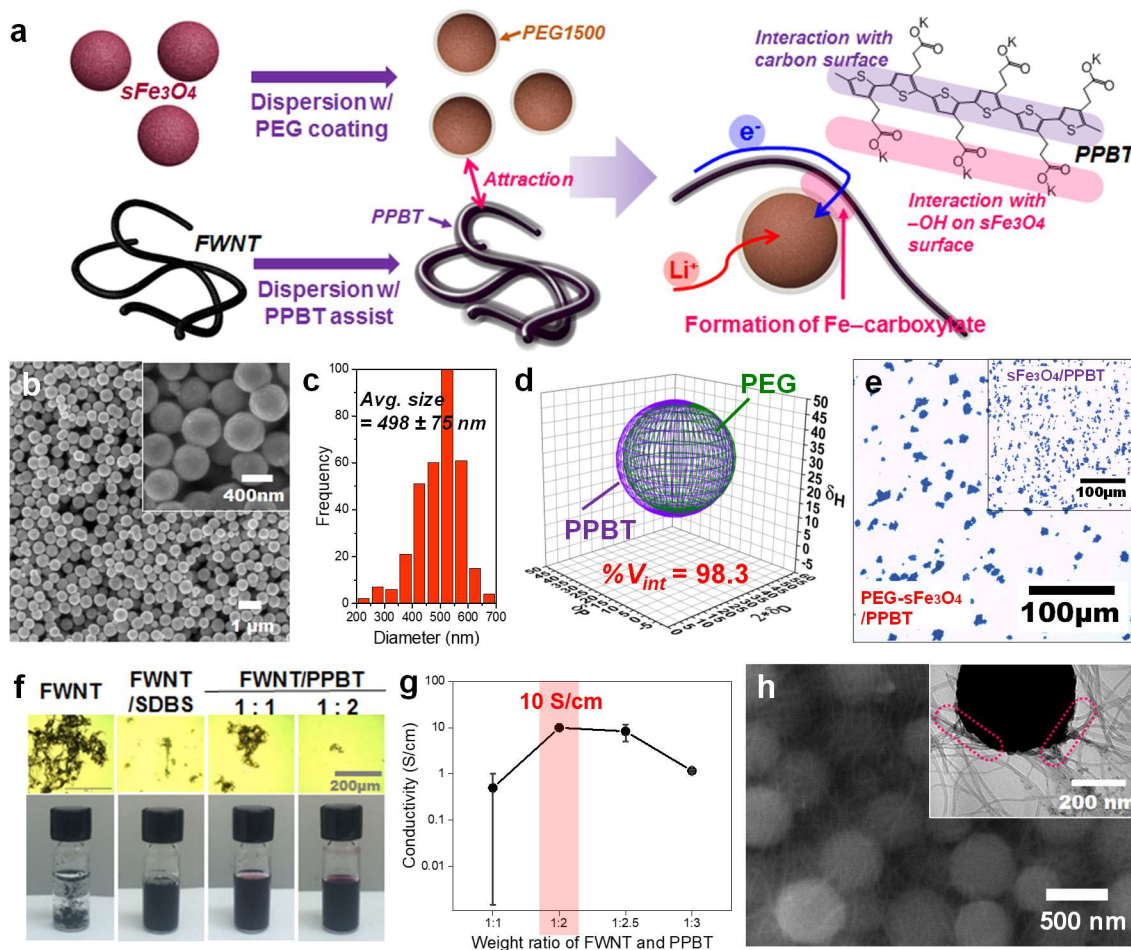


**Figure 4.1.** Materials preparation: effect of PEG coating and PPBT assist on materials dispersion and  $s\text{Fe}_3\text{O}_4$ -FWNT connection. (a) Schematics of the formation of Fe-carboxylate complex. (b) SEM image of monodispersed  $\text{Fe}_3\text{O}_4$  spheres ( $s\text{Fe}_3\text{O}_4$ ). (c) Size distribution of  $s\text{Fe}_3\text{O}_4$  particles, counted from SEM images. (d) Hansen solubility parameter (HSP) spheres of interaction for PEG and PPBT having 98.3% of the intersection volume portion ( $\%V_{\text{int}}$ ).<sup>139</sup> Adapted with permission from ref. 139. Copyright 2016 American Chemical Society. (e) Optical microscopy (OM) images of PEG- $s\text{Fe}_3\text{O}_4$ /PPBT and  $s\text{Fe}_3\text{O}_4$ /PPBT composites (inset) prepared by spin coating on the glass substrate. (f) FWNT dispersion state after probe-type sonication (top: OM images prepared by spin coating onto a glass substrate, bottom: corresponding suspension images). (g) Electronic conductivities of FWNT and PPBT composite film. The effective weight ratio of FWNT and PPBT was found as 1 to 2 having higher conductivity and good dispersion. (h) SEM and TEM (inset) images demonstrating the dispersion/connection of PEG- $s\text{Fe}_3\text{O}_4$  and FWNTs through a PPBT assist in the electrode slurry. The SEM/TEM characterizations were conducted after evaporating water solvent.



An effective, stable link between magnetite based electroactive materials and CNT surfaces enables rapid electron transport, possibly contributing to a battery electrode that exhibits high performance. To build such stable networks, understanding the surface chemistry, which dominates effective materials dispersion through physical/chemical interactions, is imperative. This approach, which introduces a PEG coating onto the surface of  $\text{sFe}_3\text{O}_4$  and uses PPBT as an electrical linker connecting the metal oxide with the carbon nanotube surface, relies primarily on the materials' surface chemistries; the PEG coating induces favorable molecular interactions between the carboxylate moieties of PPBT to attract the coated magnetite into a water medium, while the PPBT conjugated backbone physically interacts with FWNT surfaces. Those interactions led to the formation of a Fe-carboxylate complex at the interface, which positively impacted electrode stability (Figure 4.1a).

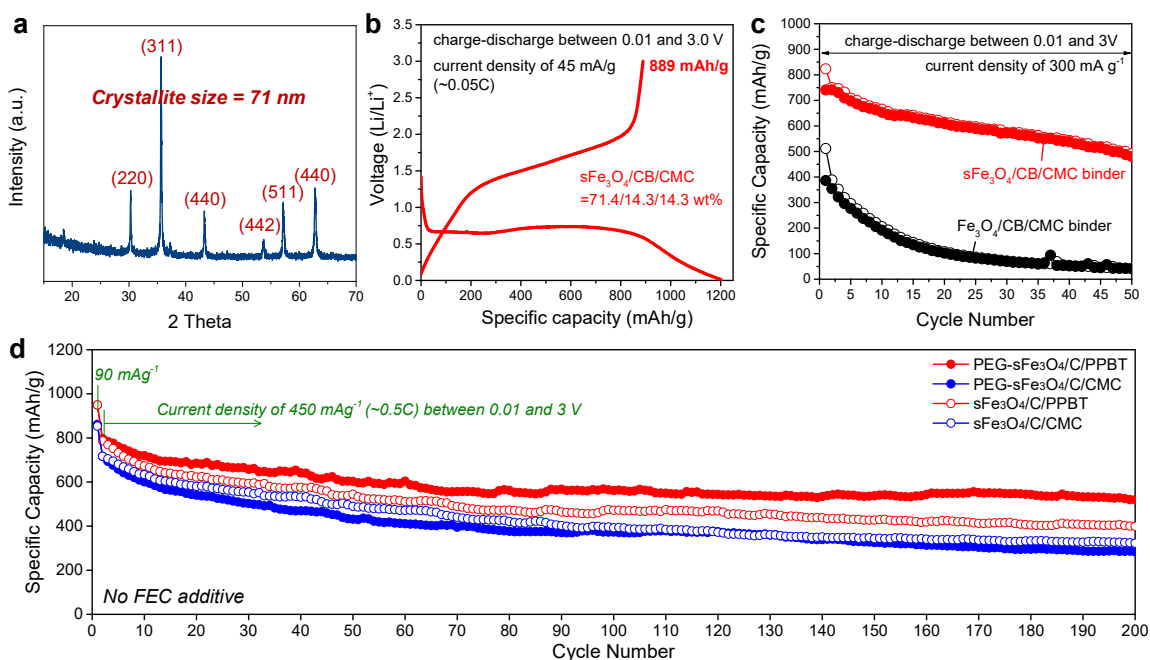


**Figure 4.2.** Monodispersed  $\text{Fe}_3\text{O}_4$  spheres ( $\text{sFe}_3\text{O}_4$ ). (a) XRD pattern. (b) Galvanostatic charge-discharge profile of Cu foil electrode ( $\text{sFe}_3\text{O}_4/\text{CB}/\text{CMC}$  binder) in the potential window of 0.01 to 3 V vs  $\text{Li/Li}^+$  at a constant current density of 0.1C ( $\sim 90 \text{ mA g}^{-1}$ ). (c)

Cycling performance of monodispersed  $\text{Fe}_3\text{O}_4$  spheres ( $\text{sFe}_3\text{O}_4$ )-based electrode, compared with random-shaped  $\text{Fe}_3\text{O}_4$  particles (0.5C rate). The  $\text{sFe}_3\text{O}_4$  particle system shows much improved capacity retention. (d) Cycling performance of Cu foil electrodes. Half coin cell includes no FEC additive in the electrolyte. PEG coating-PPBT binder system represents higher enhanced electrochemical performance in the Cu foil electrode system.

The electrode system described herein used monodispersed spherical  $\text{Fe}_3\text{O}_4$  particles ( $\text{sFe}_3\text{O}_4$ ) that have structural advantages to facilitate particle dispersion and thus support uniform  $\text{Li}^+$  ion diffusion during the electrochemical reaction. Monodispersed  $\text{sFe}_3\text{O}_4$  with tunable particle size ranging from 100 to 400 nm were readily fabricated through a solvothermal method by varying the concentration of a single iron source,  $\text{FeCl}_3 \cdot 6\text{H}_2\text{O}$ .<sup>138</sup> We targeted a particle size over 400 nm to acquire a large interstitial volume to facilitate ion transport within inner pores. Figure 4.1b presents scanning electron microscope (SEM) images of as synthesized  $\text{sFe}_3\text{O}_4$  particles having an average size of 498 nm. The X-ray diffraction (XRD) pattern (Figure 4.2a) indicates that the particles possess a typical spinel structure composed of a well-crystallized cubic magnetite phase ( $\text{Fe}_{2.933}\text{O}_4$  in JCPDS No. 86-1354),<sup>138</sup> with a crystallite size of 71 nm. This result implies that  $\text{sFe}_3\text{O}_4$  is a cluster of small  $\text{Fe}_3\text{O}_4$  crystallites. While the large crystallite structure might be expected to negatively impact  $\text{sFe}_3\text{O}_4$  electrochemistry,<sup>36</sup> studies pertaining to the use of a PEG coating to reduce  $\text{Fe}_3\text{O}_4$  aggregate size suggested that aside from crystallite size, perhaps more importantly, secondary particle size (or agglomerate size) significantly influenced battery electrode performance.<sup>139</sup> In addition, spherical nanoparticle clusters experience less exposure to the electrolyte, due to their effectively reduced surface area compared with randomly agglomerated nanoparticles. In turn, decreased exposure to the electrolyte is expected to contribute to formation of a stable solid-electrolyte interphase

(SEI) layer, leading to enhanced  $\text{Fe}_3\text{O}_4$  electrochemical behavior.<sup>111</sup> Notably, results from coin cell testing (Figure 4.2c) demonstrated that  $\text{sFe}_3\text{O}_4$  exhibited more favorable cycling performance than uncontrolled  $\text{Fe}_3\text{O}_4$  aggregated particles<sup>70,139</sup> comprised of 8nm crystallites, which supports the premise that overall aggregate surface area is a critical determining factor to be considered in the design of composite electrodes. Given the positive coin cell results, monodispersed  $\text{sFe}_3\text{O}_4$  was adopted here as a model high capacity metal oxide in the design of an ideal geometric configuration for battery electrodes to have high electrochemical characteristics.

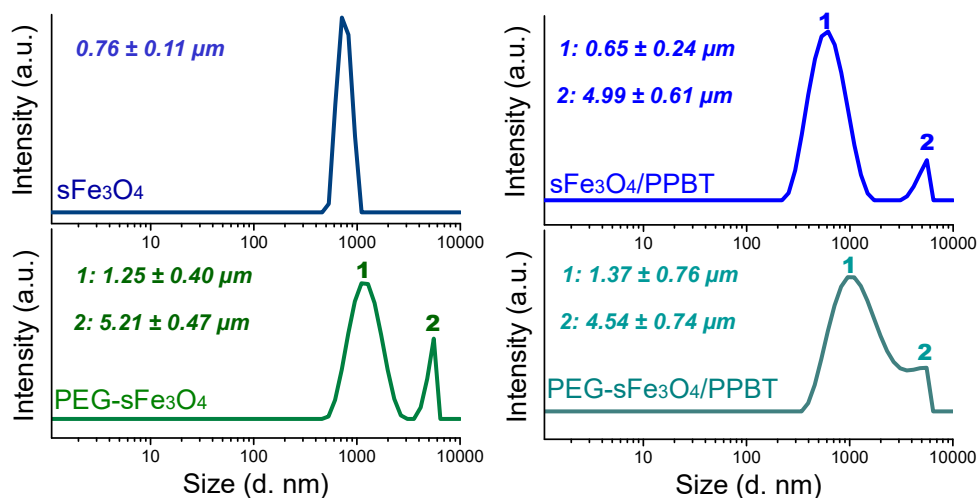


**Figure 4.3.** Dynamic light scattering (DLS) particle size distribution of  $\text{sFe}_3\text{O}_4$  particles and  $\text{PEG-sFe}_3\text{O}_4$  particles dispersed in water solvent, and  $\text{sFe}_3\text{O}_4$  particles and  $\text{PEG-sFe}_3\text{O}_4$  particles dispersed in PPBT solution. DLS was performed using a Malvern Zetasizer NANO ZS instrument (Malvern instruments). The particles were dispersed through bath-type sonication for 30 min (1mg particles/1mL deionized water).

Since PEG has a high physical affinity to PPBT (Figure 4.1d), it was anticipated that their physical attraction might drive the formation of  $\text{sFe}_3\text{O}_4$ –FWNT linkages through Fe-carboxylate chemical bonding. Optical microscopic (OM) characterization (Figure

4.1e), however, shows that the presence of a PEG coating on the  $\text{sFe}_3\text{O}_4$  surface induced the growth of aggregates in the water solvent. Dynamic light scattering (DLS) supported this observation (Figure 4.3): for dispersion in water, the average size of  $\text{sFe}_3\text{O}_4$  aggregates is  $0.76\ \mu\text{m}$ , whereas PEG- $\text{sFe}_3\text{O}_4$  exhibited bimodal peaks with  $1.25$  and  $5.21\ \mu\text{m}$  (for dispersion in PPBT solution,  $\text{sFe}_3\text{O}_4$  aggregates were  $0.65$  and  $4.99\ \mu\text{m}$ , while the PEG- $\text{sFe}_3\text{O}_4$  counterparts were  $1.37$  and  $4.54\ \mu\text{m}$  in average aggregate size). Counter to the expectation that PEG would facilitate particle dispersion, the PEG coating induced an increased level of  $\text{sFe}_3\text{O}_4$  aggregation, which might derive from a decrease in their surface energy in the aqueous solvent.

The dispersion of FWNTs into the aqueous PPBT solution was readily accomplished because of the carboxylate substituent:  $\pi$ - $\pi$  interactions between the polythiophene  $\pi$ -conjugated backbone and the  $\pi$ -electron surface of the carbon nanotubes promoted wrapping of PPBT around the FWNTs, while the side chain carboxylate moieties efficiently debundled and helped disperse the FWNT aggregates in the water medium.<sup>55,141</sup> Despite these favorable properties, the conjugated semiconducting polymer, PPBT is intrinsically an electronic insulator, and thus addition of too large a quantity of PPBT during FWNT dispersion was expected to negatively impact electrode electronic conductivity. To identify the optimal PPBT:FWNT ratio that allows for effective dispersion while maximizing electrical properties, the materials dispersion state of spin coated samples was examined using OM characterization (Figure 4.1f) and electronic conductivity of drop cast electrodes was measured (Figure 4.1g) for different weight ratio of the two components. When the weight ratio of FWNT to PPBT was 1 to 2, the electrode components appeared well dispersed, and comparable to FWNT dispersion (Figure 4.1f)

using sodium dodecylbenzenesulfonate (SDBS), a well-known surfactant.<sup>28,29,132</sup> Importantly, drop cast films of PPBT dispersed FWNTs at this ratio also exhibited higher conductivity.

As confirmed by SEM and TEM characterization, using the combination of PEG and PPBT to enable the dispersion of  $\text{sFe}_3\text{O}_4$  and FWNT, respectively, in the aqueous medium, coupled with subsequent chemical interactions facilitated interconnectivity between the electroactive components. Figure 4.1h presents SEM and TEM images of a well dispersed dried electrode slurry comprising PEG- $\text{sFe}_3\text{O}_4$  and FWNT dispersed in PPBT solution on an as-prepared TEM grid. The TEM image (inset image of Figure 4.1h) suggests that PEG- $\text{sFe}_3\text{O}_4$  and FWNT are well-connected at their interface, most likely due to the role of the carboxylated conjugated polymer (PPBT) linking the two components through chemical/physical interactions at their respective surfaces.

#### 4.3.2 Fabrication of FWNT Web Electrode

The FWNT web electrode was fabricated *via* a vacuum-assisted filtration process followed by a solvent exchange-assisted freeze-drying method that allowed for well-dispersed materials and well-developed porous electrode structure.<sup>28,29</sup> First, as illustrated in Figure 4.4a, the electrode slurry was prepared by a sonication process using an ultrasonic probe to sequentially disperse (i) FWNTs, and (ii) carbon black (CB)/PEG- $\text{sFe}_3\text{O}_4$  particles in PPBT solution. PPBT helped to effectively disperse FWNTs and carbon particles in the aqueous solution, thereby ensuring a well-dispersed electrode slurry (Figure 4.4b). Prior to depositing the slurry, a FWNT mechanical support layer was prepared by dispersing FWNTs with probe-type ultrasonication in water using SDBS surfactant (concentration =

1.0 wt % in water). The resultant FWNT suspension was poured onto a membrane filter (pore size  $\sim 0.22\ \mu\text{m}$ ) and then subjected to vacuum filtration. Subsequently, the electrode slurry consisting of PEG-s $\text{Fe}_3\text{O}_4$ , carbon black and FWNT in PPBT aqueous solution was placed on the top surface of FWNT support layer using the same filtration process. To remove residual SDBS surfactant and excess PPBT assumed not to be involved in carboxylate bonding with the metal oxide surface, the as prepared electrode was washed with water by vacuum filtration. Then, a solvent (ethanol followed by acetone) exchange-assisted freeze-drying treatment<sup>28</sup> was employed to facilitate development of a more porous structure within the electrodes in order to compensate for residual PPBT that surrounds the FWNT surface that could cover inner porous structures. Finally, the electrode was vacuum-dried overnight at  $110\ ^\circ\text{C}$  to afford the self-supported FWNT web-electrode (Figure 4.4c, d).

As indicated in Figure 4.4c, in comparison to a multi-walled carbon nanotube (MWNT) CNT web, sub-millimeter, long-chain FWNTs (diameter: 6–10 nm, length:  $\sim 0.4\ \text{mm}$ )<sup>137</sup> afforded a free-standing web with high mechanical strength and long-range conducting networks, while that derived from MWNTs with a diameter  $< 8\ \text{nm}$  and length of 10–30  $\mu\text{m}$  failed to produce free-standing web electrodes, because of electrode shrinkage after solvent evaporation (inset Figure 4.4c). Similar to previous observations,<sup>9</sup> super-long CNTs are essential to secure mechanical superiority of a CNT web-based electrode. Also, the resultant FWNT system presented improved electronic conductivity and higher porosity than a corresponding Cu foil electrode consisting of PEG-s $\text{Fe}_3\text{O}_4$ , carbon black (CB), and PPBT binder control (Figure 4.4e). While the Cu foil reference electrodes exhibited electronic conductivity of  $0.99\ \text{S cm}^{-1}$  and 64.9 % porosity, FWNT web electrode

conductivity and porosity were  $25 \text{ S cm}^{-1}$  and 77.8 %, respectively. These improved values ensured higher electron/ion transport properties, which may contribute to battery electrodes with higher performance attributes. The results most likely derive from the well-developed electronic networks associated with FWNTs intimately connected with electrode active materials through PPBT linkages, and removal of excess PPBT not involved in Fe-carboxylate bonding which could block pores.

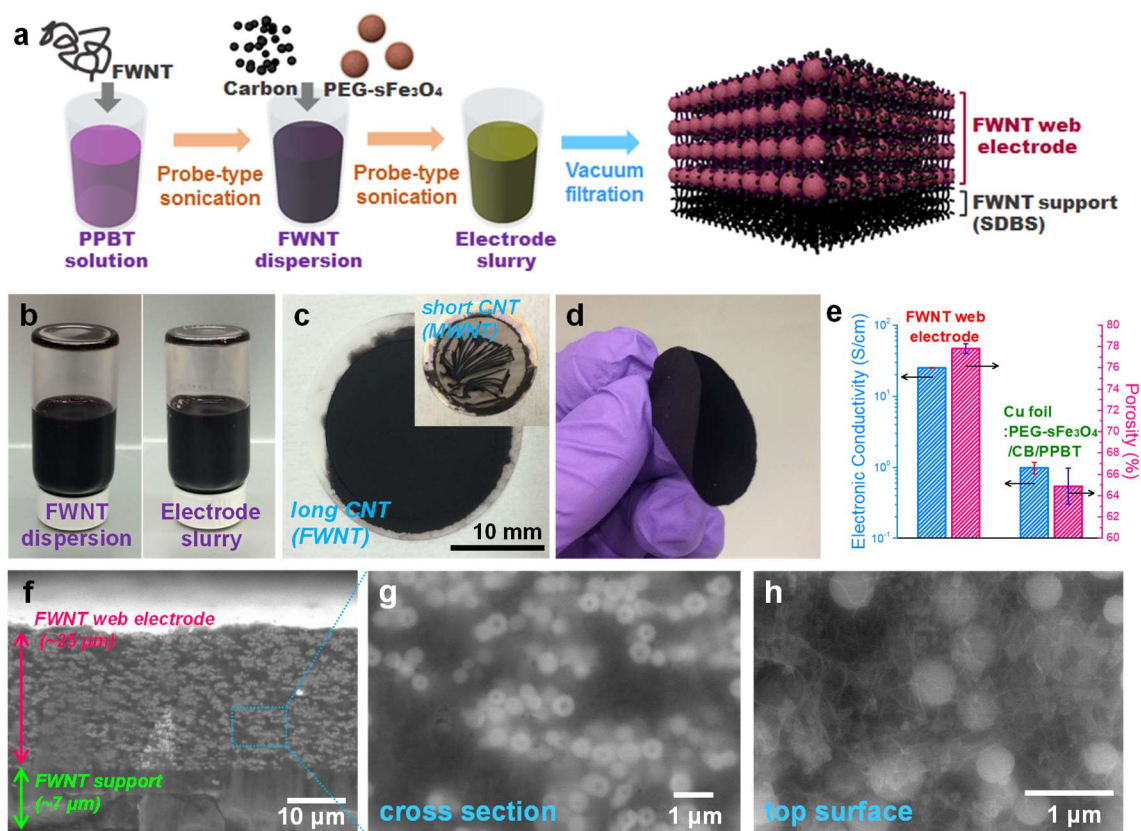
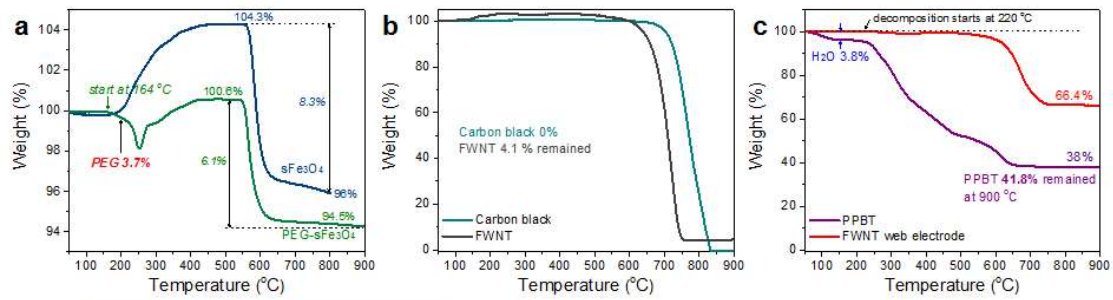


**Figure 4.4.** Fabrication of FWNT web electrode. (a) A schematic representation of the overall fabrication procedure for FWNT web electrode, composed of PEG-sFe<sub>3</sub>O<sub>4</sub>/CB/FWNT/PPBT. (b) Photographs of FWNT dispersion and electrode slurry in water solvent after probe-type sonication. (c) Comparison of fabricated electrodes having long-chain FWNTs (sub-mm length) vs short-chain MWNTs (inset). (d) A photograph of a self-standing, flexible FWNT web electrode. (e) Electronic conductivity and porosity of FWNT web electrode, compared with Cu foil electrode (PEG-sFe<sub>3</sub>O<sub>4</sub>/CB/PPBT). (f, g) Cross-sectional and (h) surface-view SEM images of FWNT web electrode.

SEM images (Figure 4.4f–h) confirmed the well-constructed FWNT web electrode morphology, comprised of a FWNT web composite layer (~25  $\mu\text{m}$ ) and FWNT mechanical support layer (~7  $\mu\text{m}$ ). Although the observation of small  $\text{sFe}_3\text{O}_4$  particle aggregates (~1.7  $\mu\text{m}$ ) points out that each magnetite particle (~500 nm in diameter) was not perfectly dispersed, overall, the electrode presented a well-dispersed structure with well-developed carbon/FWNT channels which can enhance electron/ion transport. The carbon particles (CB) attached along the FWNT surface in particular, allowed for more porous attributes of carbon/FWNT channels owing to their spherical, bulky structure. When designing Li-ion batteries, apparently, those aspects including the high porosity of the FWNT web electrodes could adversely influence critical battery characteristics such as a volumetric energy density ( $\text{Wh L}^{-1}$ ), despite their advantageous effect on a gravimetric energy density ( $\text{Wh kg}^{-1}$ ) owing to the metallic current collector-free system. Thus, for the practical standard, considering/finding an optimum porosity by controlling electrode thickness would be further necessary.



Materials	FWNT web electrode	
	Before TGA	After TGA
$\text{sFe}_3\text{O}_4$ <sup>1)</sup>	24.075 mg	23.579 mg
CB	5.0 mg	0 mg
FWNT	5.5 mg	0.2255 mg
PPBT	X mg	0.418*X mg

<sup>1)</sup> Assumed that PEG was completely exchanged with PPBT in the vacuum filtration process.

$$\begin{aligned}
 & \frac{(m_{\text{Fe}_3\text{O}_4} + m_{\text{CB}} + m_{\text{FWNT}} + m_{\text{PPBT}})_{\text{after TGA}}}{(m_{\text{Fe}_3\text{O}_4} + m_{\text{CB}} + m_{\text{FWNT}} + m_{\text{PPBT}})_{\text{before TGA}}} \times 100\% \\
 &= \text{Wt}\%_{\text{after TGA}} \\
 & \frac{23.579 \text{ mg} + 0.2255 \text{ mg} + 0.418x \text{ mg}}{24.075 \text{ mg} + 5 \text{ mg} + 5.5 \text{ mg} + x \text{ mg}} = 0.664 \\
 & m_{\text{PPBT before TGA}} (x \text{ mg}) = 3.44 \text{ mg}
 \end{aligned}$$



**Figure 4.5.** TGA profiles (a)  $\text{sFe}_3\text{O}_4$  and PEG- $\text{sFe}_3\text{O}_4$ , (b) carbon black and FWNT, and (c) PPBT powders and FWNT web electrode, which were carried out in air in the temperature range of 50–900 °C at a heating rate of 10 °C/min. Table represents the weight change of materials in FWNT web electrode and the remained amount of PPBT after filtration that was calculated by TGA results.  $\text{sFe}_3\text{O}_4$  particles were oxidized by 4.3 % during TGA and had acetate—an electrostatic stabilization agent and reduction assistant agent for  $\text{sFe}_3\text{O}_4$  synthesis—on their surface with the amount of ~8.3 %. PEG- $\text{sFe}_3\text{O}_4$  particles were composed of 3.7 % PEG that starts decomposition at 164 °C and 6.1% acetate on them. Based on the fact that FWNT web electrode exhibits no decomposition at 164 °C, it was assumed that PEG was completely exchanged with PPBT component during the electrode fabrication. As a result, the amount of PPBT remained as the form of Fe-carboxylate complex was calculated into 3.44 mg (9.05 %).

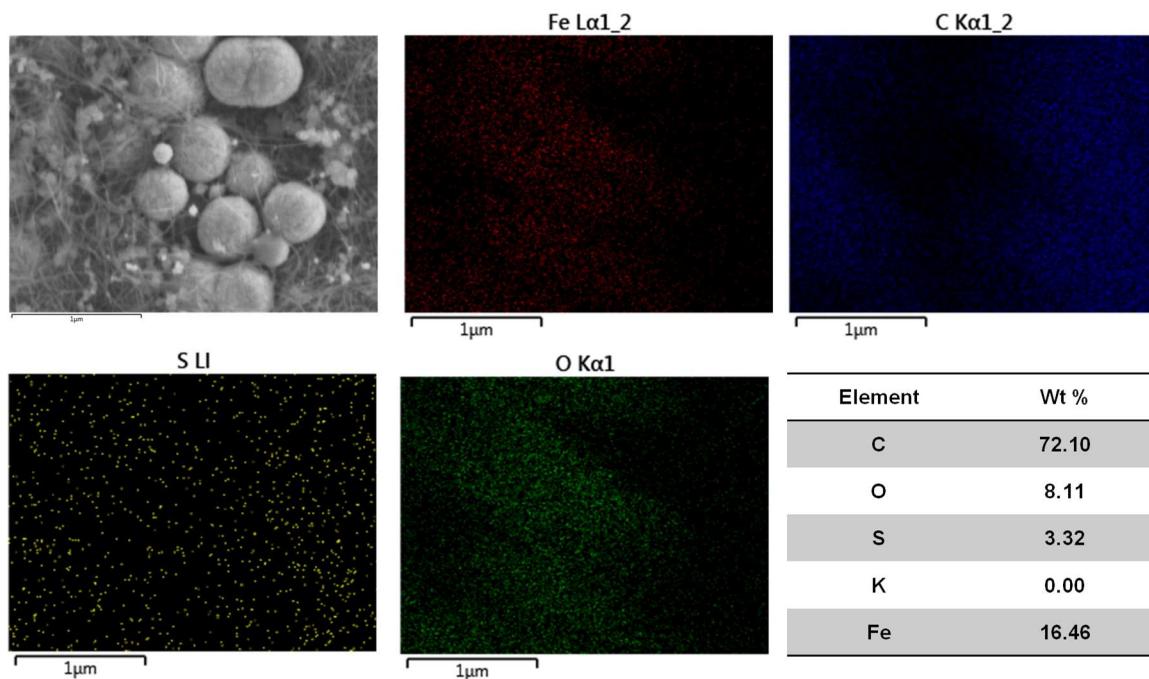


**Figure 4.6.** EDS mapping showing the existence of PPBT component, but no potassium element. This gives more clear evidence that PPBT was attached on the  $\text{sFe}_3\text{O}_4$  surface through the Fe-carboxylate bonding.

To calculate the specific capacity ( $\text{mAh g}^{-1}$ ) based on the active material content, the precise weight of PPBT remaining in the FWNT web electrode through Fe-carboxylate

bonding is necessary. Thermogravimetric analysis (TGA) demonstrated that the electrode was composed of 9.0 wt % PPBT, which in turn results in 63.3 wt % of electroactive particles ( $\text{sFe}_3\text{O}_4$ ) (Figure 4.5). According to TGA analysis, no PEG component remained in the FWNT web electrode, which implies that PEG was completely exchanged with PPBT and removed during vacuum filtration. In addition, elemental mapping using energy-dispersive X-ray spectroscopy (EDS) (Figure 4.6) illustrated that while sulfur (S) was present in the composite electrode, the element potassium (K) was absent. These results further support the premise that PPBT remained in the FWNT web electrode through Fe-carboxylate complex bond formation and is involved in providing connective pathways between the  $\text{sFe}_3\text{O}_4$  and FWNTs.

#### 4.3.3 Surface Analysis

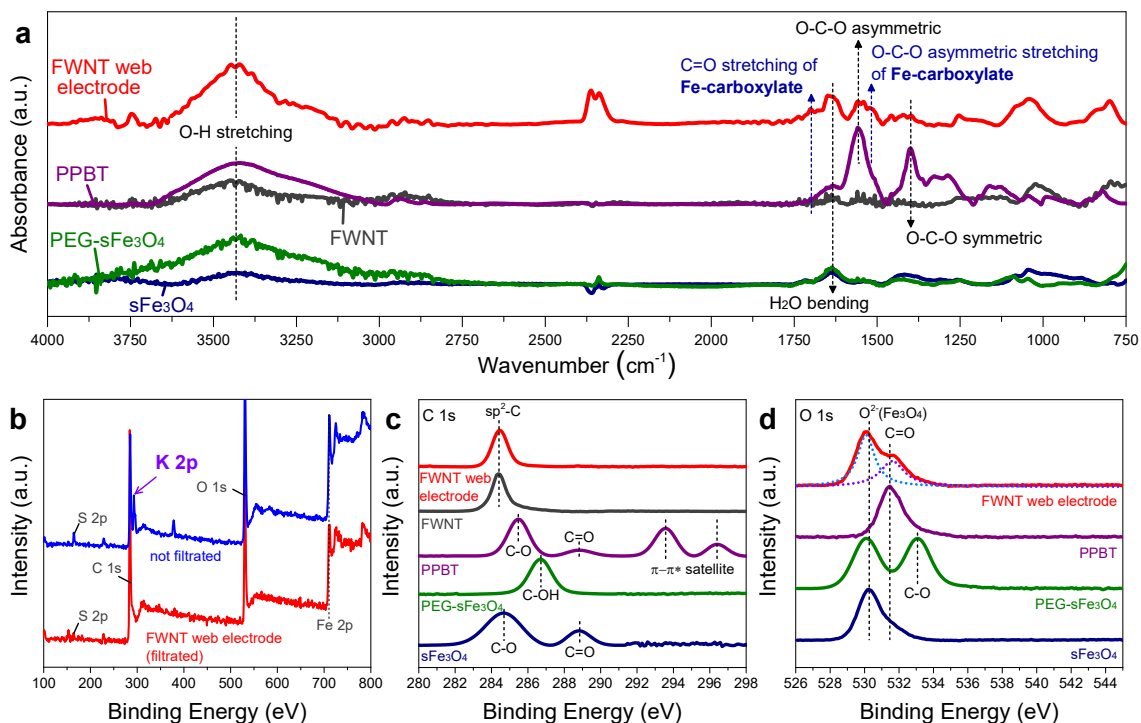


**Figure 4.7.** Spectroscopy characterization. (a) FT-IR spectra of materials ( $\text{sFe}_3\text{O}_4$ , PEG- $\text{sFe}_3\text{O}_4$ , PPBT, FWNT) and FWNT web electrode. Peaks were normalized with a

peak at  $575\text{ cm}^{-1}$  associated with the vibration of Fe–O lattice of  $\text{sFe}_3\text{O}_4$ .<sup>138</sup> (b) XPS survey spectra of FWNT web electrode with filtration process, in comparison with not-filtrated electrode (solution casting process). (c, d) XPS spectra of materials ( $\text{sFe}_3\text{O}_4$ , PEG- $\text{sFe}_3\text{O}_4$ , PPBT, FWNT) and FWNT web electrode.

Fourier transform infrared (FT-IR) spectroscopy (Figure 4.7a) provided evidence for the formation of an Fe-carboxylate complex where carboxylate moieties were chemically bound to hydroxyl groups on the metal oxide surface.<sup>139</sup> The FWNT web electrode exhibited peaks at  $\sim 1699\text{ cm}^{-1}$  and  $\sim 1517\text{ cm}^{-1}$  corresponding to C=O stretching and O–C–O asymmetric stretching (the shoulder was split from  $\sim 1560\text{ cm}^{-1}$  band), respectively, which are associated with an Fe-carboxylate bond. Vibrational bands at  $\sim 1560\text{ cm}^{-1}$  and  $\sim 1397\text{ cm}^{-1}$  correspond to PPBT O–C–O asymmetric and symmetric stretching, respectively.

X-ray photoelectron spectroscopy (XPS) provided further evidence for chemical interactions between the PPBT carboxylate functionalities and the metal oxide surface. In Figure 4.7b, the disappearance of the K 2p peak at 293.1 eV which appears in the unwashed/filtered composite, in the FWNT web electrode indicates that only PPBT chemically interacting with  $\text{sFe}_3\text{O}_4$  –OH groups remained in the fabricated material. In addition, O 1s spectrum of the FWNT web electrode displayed a peak at 531.6 eV for C=O, substantiating the existence of PPBT in the form of carboxylate. C 1s peaks at 284.68 eV and 288.8 eV corresponding to C–O and C=O bonds, respectively were retained by  $\text{sFe}_3\text{O}_4$ . These are carboxylate bonds originating from sodium acetate placed on the  $\text{sFe}_3\text{O}_4$  surface and used as an electrostatic stabilization and reduction assistant agent for  $\text{sFe}_3\text{O}_4$  synthesis.<sup>138</sup> TGA analysis indicated that 8.3 wt % of acetate remained in the  $\text{sFe}_3\text{O}_4$

powders (Figure 4.5) prior to coating the active material with PEG. When the PEG coating was introduced onto the  $\text{sFe}_3\text{O}_4$  surface, a C–OH peak associated with PEG was observed in XPS at 286.7 eV, while the acetate bands were not visible. Based on TGA analysis (Figure 4.5), however, PEG only partially displaced with acetate: the weight of acetate was 6.1 wt %, while that of PEG was 3.7 wt %. This suggests that the PEG coating relies more on physical interactions and that acetate chemically bonded onto the  $\text{sFe}_3\text{O}_4$  surface impedes the approach of PEG onto its surface, leading to insufficient coverage with PEG. This may, in turn, stimulate  $\text{sFe}_3\text{O}_4$  aggregation in order to reduce particle surface energy in water (Figure 4.3). Furthermore, the absence of an O 1s peak at 533.1 eV associated with the C–O bond of PEG- $\text{sFe}_3\text{O}_4$  in XPS spectra of the FWNT web electrode (Figure 4.7d), suggest that PEG detached from the metal oxide surface during the filtration process. Thus, in this study, PEG most likely contributed to attracting the PPBT component of the conjugated polymer wrapped FWNTs, thereby helping to disperse and connect  $\text{sFe}_3\text{O}_4$  hydroxyl groups with the FWNT surface *via* PPBT carboxylate linkages, rather than assisting in the uniform dispersion of  $\text{sFe}_3\text{O}_4$  particles.

#### 4.3.4 *Electrochemical Evaluation*

To evaluate the electrochemical performance, coin cells with a Li metal counter electrode and a solution of 1.2 M  $\text{LiPF}_6$  in ethylene carbonate (EC)/diethyl carbonate (DEC) (1/1 by volume) with 10 wt % fluoroethylene carbonate (FEC) as electrolyte were fabricated. The  $\text{sFe}_3\text{O}_4$  mass loading in the present study was typically 2.1–2.5  $\text{mg cm}^{-2}$ .

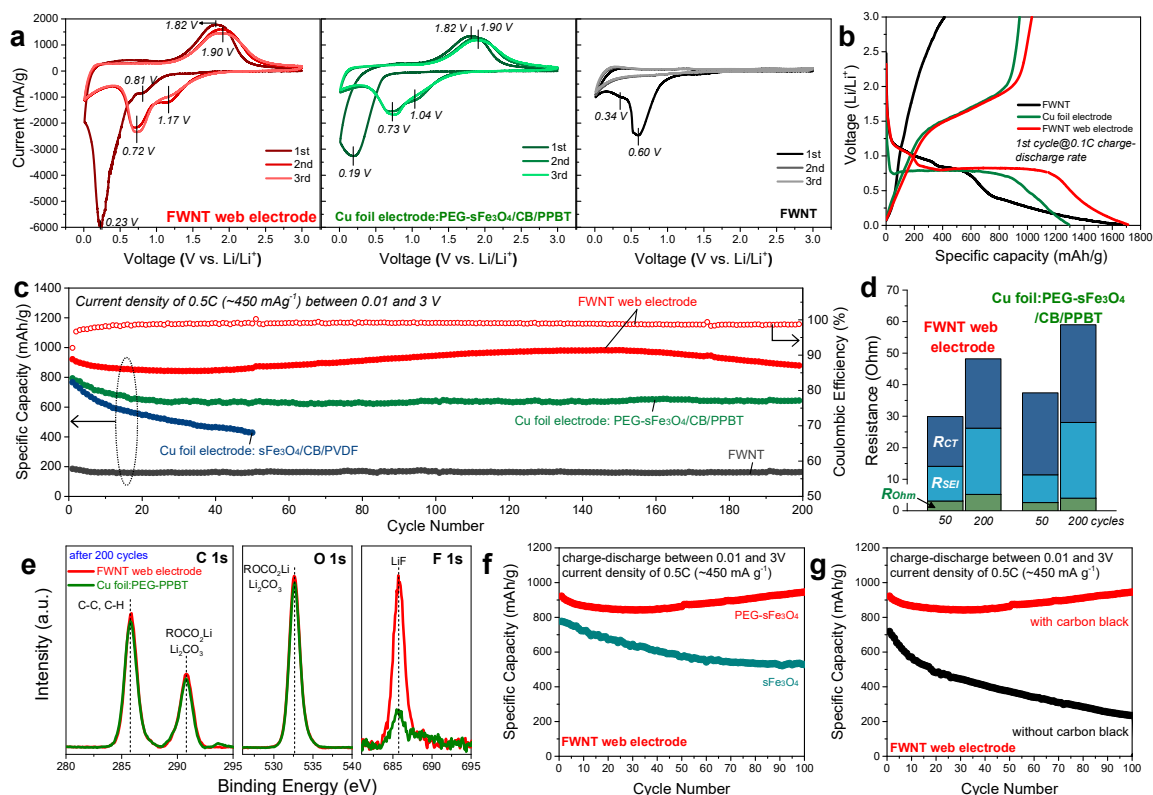


**Figure 4.8.** Electrochemical characterization of FWNT web electrode. (a) Cyclic voltammetry (CV) profiles of FWNT web electrode, Cu foil electrode (PEG-sFe<sub>3</sub>O<sub>4</sub>/CB/PPBT) and FWNT in the potential window of 0.01 to 3 V vs Li/Li<sup>+</sup> collected at the rate of 0.5 mV s<sup>-1</sup>. (b) Galvanostatic charge-discharge profiles in the potential window of 0.01 to 3 V vs Li/Li<sup>+</sup> at a constant current density of 0.1C (~90 mA g<sup>-1</sup>), comparable to CV profiles. (c) Cycling performance (=capacity retention as function of cycle number) collected for the current density of 0.5C (~450 mA g<sup>-1</sup>) between 0.01 and 3 V. (open circle: Coulombic efficiency of FWNT web electrode). (d) Variation of electrode internal resistance ( $R_{ohm}$ ,  $R_{SEI}$ ,  $R_{CT}$ ) after cycling, fitted by EIS results. EIS characterization was conducted at open-circuit voltage (OCV) after 50 and 200 cycles. (e) XPS spectra (C 1s, O 1s, F 1s) of FWNT web electrode and Cu foil electrode (PEG-sFe<sub>3</sub>O<sub>4</sub>/CB/PPBT) after 200 cycles. (f, g) Cycling performance of FWNT web electrodes demonstrating the effect of (f) PEG coating on the sFe<sub>3</sub>O<sub>4</sub> surface, and (g) carbon addition into the electrode to acquire more inner pores.

Cyclic voltammetry (CV) characterization was performed to investigate the lithiation and delithiation behavior of the FWNT web electrode, compared to a Cu foil reference electrode and pure FWNT electrode (Figure 4.8a). The Cu foil electrode was

comprised of PEG-sFe<sub>3</sub>O<sub>4</sub>, CB, and PPBT that were blade-coated onto the Cu foil substrate. For electrochemical testing, a pure FWNT electrode was prepared by vacuum filtration after dispersion in an aqueous solution with 1.0 wt % SDBS surfactant. In principle, Fe<sub>3</sub>O<sub>4</sub> is known to follow two reaction steps: (1) lithium intercalation that induces structure transition, considered to be irreversible ( $\text{Fe}_3\text{O}_4 + x\text{Li}^+ + x\text{e}^- \rightarrow \text{Li}_x\text{Fe}_3\text{O}_4$ ), and (2) conversion reaction, responsible for the theoretical reversible capacity of ~925 mAh g<sup>-1</sup> ( $\text{Li}_x\text{Fe}_3\text{O}_4 + (8-x)\text{Li}^+ + (8-x)\text{e}^- \rightarrow 3\text{Fe}^0 + 4\text{Li}_2\text{O}$ ).<sup>16,18,139</sup> Figure 4.8a shows CV results with three initial cycles at the scan rate of 0.5 mV s<sup>-1</sup>. The FWNT web electrode has similar CV behavior to the Cu foil electrode, except for increased peak current and double layer capacitance (non-Faradaic reaction), ascribed to FWNT characteristics. At the first cycle, the cathodic peak at 0.81 V corresponds to lithium intercalation, the cathodic peak at 0.23 V is attributed to further reduction by the conversion reaction including SEI layer formation, and the broad anodic peak at 1.82 V is associated with oxidation of Fe to Fe<sup>2+</sup>/Fe<sup>3+</sup>. In the subsequent cycles, the cathodic Li<sup>+</sup> insertion mainly occurs at 1.17 V and 0.72 V, and the anodic Li<sup>+</sup> extraction takes place at 1.90 V, appearing highly reversible, due to the electrochemical redox reaction ( $\text{Fe}_3\text{O}_4 \leftrightarrow \text{Fe}^0$ ) through Li insertion/extraction.<sup>128</sup>

CNTs tend to undergo non-Faradaic reaction at their interface where Li<sup>+</sup> might be accumulated, which points out the double layer capacitance in the CV profiles.<sup>28,132,142</sup> At a voltage below 1.0 V (vs Li<sup>+</sup>/Li), Li<sup>+</sup> intercalation/deintercalation may arise in CNTs. They behave as electrochemically active materials, which enable the improvement of battery capacity, although their contribution is not large. Having a large surface area, however, CNTs tend to be more involved in the formation of the SEI layer associated with Li<sup>+</sup> loss, impacting their low Coulombic efficiency and large irreversible capacity at the first cycle.

This behavior was observed at 0.60 V, the cathodic peak in the pure FWNT electrode (Figure 4.8a). Galvanostatic charge-discharge profiles (Figure 4.8b) show FWNT has a specific capacity of 413 mAh g<sup>-1</sup> with an initial efficiency of 24.8 % at a constant current density of ~20 mA g<sup>-1</sup>. This attribute is directly reflected in the electrochemical characteristics of the FWNT web electrode, which results in increased electrode capacity (1031 mAh g<sup>-1</sup> vs. 944 mAh g<sup>-1</sup> of Cu foil electrode) but reduced initial efficiency (60.2 % vs 73.0 % of Cu foil electrode) at the low rate condition, current density of 0.1C (~90 mA g<sup>-1</sup>).

Despite this drawback, with respect to battery performance, the FWNT web electrode is very effective. Figure 4.8c demonstrates the superiority of the FWNT web electrode in cycling performance at the constant current density of 0.5C (~450 mAh g<sup>-1</sup>) in a potential range of 0.01–3 V (vs Li<sup>+</sup>/Li), as compared to Cu foil electrodes including PEG coating/PPBT binder system and no PEG coating/PVDF binder system as control experiments. The FWNT web electrode reveals higher capacity even at the high rate condition, a gain in energy capacity of approximately 120–230 mAh g<sup>-1</sup> vs the Cu foil electrode having PEG-sFe<sub>3</sub>O<sub>4</sub> and PPBT binder. After 200 cycles, the reversible capacity of the FWNT web electrode was 880 mAh g<sup>-1</sup> vs 921 mAh g<sup>-1</sup> at the 1st cycle, and the electrode exhibited a very stable capacity retention of 95.5 %, while the Cu foil counterpart with PEG-sFe<sub>3</sub>O<sub>4</sub>/CB/PPBT retained only 81.2 % of its capacity (793 mAh g<sup>-1</sup> at 1st cycle to 644 mAh g<sup>-1</sup> at 200th cycle).

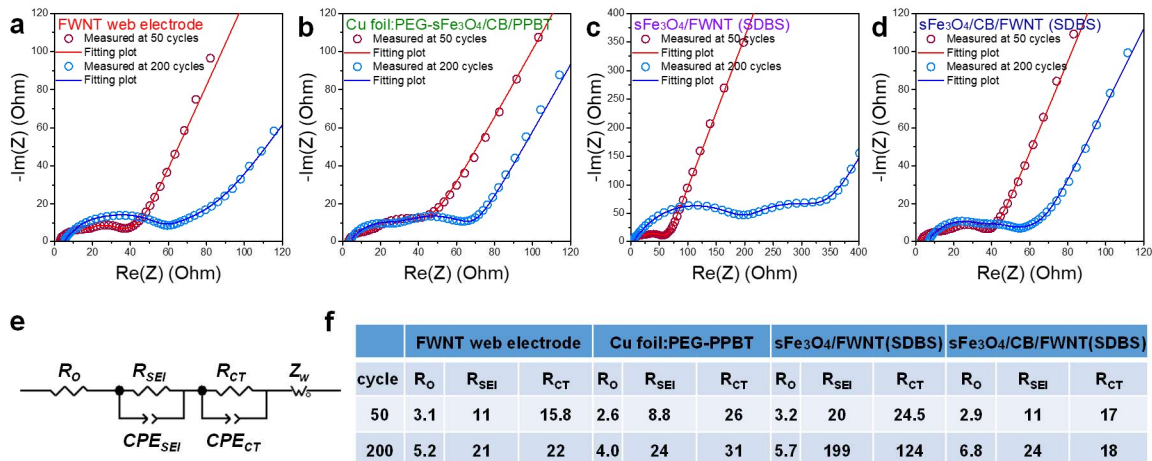


**Figure 4.9.** EIS fitting results. The impedance spectra were measured at open-circuit voltage (OCV) in the frequency range from 1 MHz to 0.1 Hz.

Although the PEG coating–PPBT binder system improved electrode electrochemical performance (Figure 4.2d), consistent with previous studies,<sup>139</sup> the FWNT web electrode provides for further enhancement. The improved electrochemical performance in the present case might be attributed to improved electrochemical kinetics associated with the interconnected, stable FWNT electron networks having carboxylated polythiophene (PPBT) linkages connecting the FWNT and sFe<sub>3</sub>O<sub>4</sub> surfaces, coupled with a well-developed porous structure that ensures facile Li<sup>+</sup> ion accessibility from the surrounding electrolyte. During cycling, the internal resistance is effectively reduced, especially charge transfer resistance, which provides supporting evidence for improved kinetics (Figure 4.8d and 4.9). Moreover, XPS spectra of the FWNT web electrode after 200 cycles, Figure 4.8e, showed distinctly different features from that of the Cu foil electrode consisting of PEG-sFe<sub>3</sub>O<sub>4</sub> and PPBT binder; specifically, the former exhibited a substantially larger amount of LiF component. The XPS points to the formation of a



thinner, more dense SEI layer, reflecting the enhanced stability of the SEI layer of the FWNT web electrode system.<sup>127,143</sup>

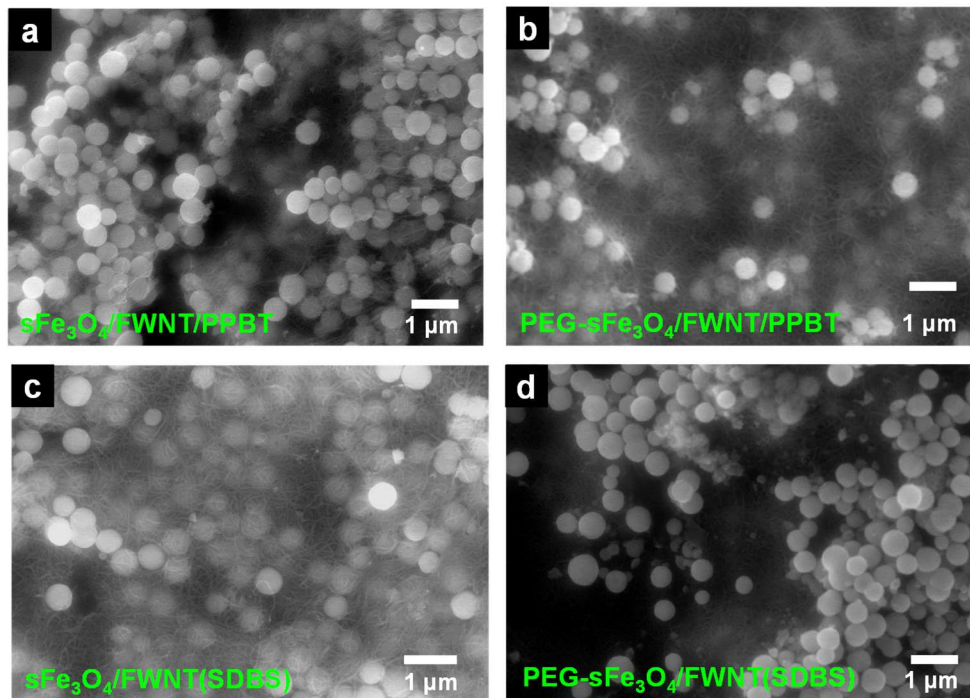


**Figure 4.10.** SEM images of web electrodes of (a) sFe<sub>3</sub>O<sub>4</sub>/FWNT/PPBT, (b) PEG-sFe<sub>3</sub>O<sub>4</sub>/FWNT/PPBT, (c) sFe<sub>3</sub>O<sub>4</sub>/FWNT (SDBS), and (d) PEG-sFe<sub>3</sub>O<sub>4</sub>/FWNT (SDBS). SDBS surfactant helps effectively connect sFe<sub>3</sub>O<sub>4</sub> particles and FWNT, and PPBT for PEG-sFe<sub>3</sub>O<sub>4</sub> particles and FWNT.

The introduction of PEG and carbon particles (*i.e.*, carbon black), in particular, contributed to the high performance of the FWNT web electrode (Figure 4.8f, g). The physical affinity between PEG and PPBT is so similar that the attractive forces probably lead to the PEG coated sFe<sub>3</sub>O<sub>4</sub> moving to interact with PPBT covering the  $\pi$ -conjugated FWNT surface, which facilitated successful materials dispersion (Figure 4.10) and consequently induced Fe-carboxylate bond formation between the PPBT carboxylate moieties and the sFe<sub>3</sub>O<sub>4</sub> hydroxyl group. Meanwhile, addition of carbon into the electrode

composite is also key to the observed improvement in electrochemistry. In the absence of added carbon, the FWNT web electrode exhibited poor cycling performance. Also, increasing FWNT content that enhanced the electronic conductivity, provoked degradation in cyclability.

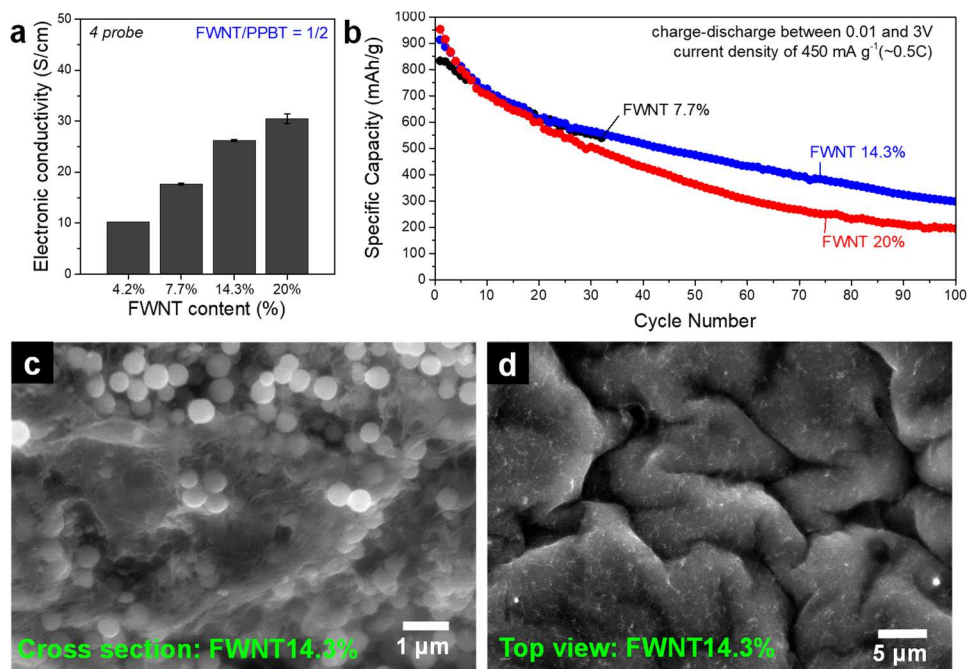


**Figure 4.11.** FWNT web electrodes without carbon addition. Increase in FWNT content of the electrodes affected their improved electronic conductivity, but had negatively impact on cycling performance. That might be attributed to covering the pores, thereby preventing ion transport inside electrode.

Based on SEM characterization (Figure 4.11), the FWNT–PPBT component covered the inner pores and the top surface of the electrode, impeding electrolyte accessibility. Supposedly, this observation is ascribed to strong physical interactions between the PPBT conjugated backbone and readily available FWNT surface, that is able to then build the thick blanket. Carbon particles, however, help to alleviate these issues. The carbon surface is itself able to interact with the PPBT  $\pi$ -conjugated backbone thereby

reducing the degree of physical interactions taking place between the PPBT and FWNT surfaces. As a result, the pores created in the web electrode are less likely to be blocked. In addition, the morphology (Figure 4.4h) where carbon particles were attached along the z-axial direction of FWNT surface confirmed that they facilitate formation of a more porous structure.

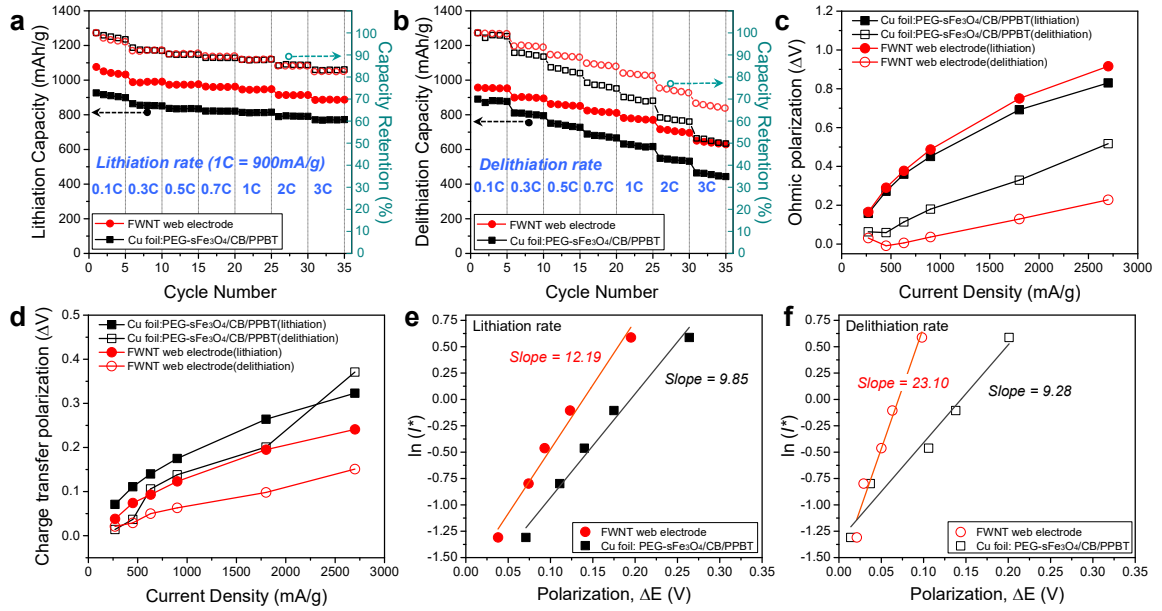


**Figure 4.12.** Rate capability and corresponding electrochemical properties. (a) Lithiation rate capability, where cells were delithiated at a constant current density of 0.1C ( $\sim 90 \text{ mA g}^{-1}$ ) and lithiated at different current densities (0.1–3C, 1C rate =  $900 \text{ mA g}^{-1}$ ) between 0.01 and 3 V. (b) Delithiation rate capability, where cells were lithiated at a constant current density of 0.1C ( $\sim 90 \text{ mA g}^{-1}$ ) and delithiated at different current densities (0.1–3C, 1C rate =  $900 \text{ mA g}^{-1}$ ) between 0.01 and 3 V. (c) Ohmic polarization, and (d) charge transfer polarization as a function of the applied current density during the lithiation and delithiation process. (e, f) Tafel plots:  $\ln(I_{\text{applied}})$  vs  $\Delta E$ , which were plotted from the results of charge transfer polarization in the range from 0.1C to 2C.

Rate capability experiments demonstrate the beneficial effects of the FWNT web electrode system. For the lithiation rate capability (Figure 4.12a), under a constant

delithiation current density of 0.1 C ( $\sim 90 \text{ mA g}^{-1}$ ), the cells were lithiated over a wide range of current densities of 0.1–3.0 C ( $\sim 90$ – $2700 \text{ mA g}^{-1}$ ) in a voltage range of 0.01–3 V. In the delithiation test (Figure 4.12b), the cells were lithiated at a constant current density of 0.1 C ( $\sim 90 \text{ mA g}^{-1}$ ) and delithiated in the range of 0.1–3.0 C ( $\sim 90$ – $2700 \text{ mA g}^{-1}$ ) between 0.01–3 V. Both conditions illustrate that the FWNT web electrode retains a much higher capacity than its Cu foil control, presenting its superior rate capability. From the perspective of capacity retention which is normalized with the lithiated, or delithiated capacity at the 1st cycle, however, while the FWNT web electrode still shows improvement at the different delithiation rate conditions, surprisingly, the lithiation rate capability appears very similar to the control: seemingly, the electrode configuration does not affect performance during the lithiation process. This result implies that the poor  $\text{sFe}_3\text{O}_4$  electroactive material electrochemistry most likely originates from the delithiation process rather than the lithiation process. Those are closely associated with the intrinsic properties of metal oxides following a conversion reaction: large voltage hysteresis in charge/discharge profiles, which results from different electrochemical reaction paths related to respective lithiation and delithiation process.<sup>144</sup> The additional formation of an intermediate phase that only occurs during the delithiation might delay the electrochemical reaction by lowering ionic mobility among interdiffusing species in a metal oxide compound. Those lead to slow reaction kinetics and resultant inferior electrochemistry in the delithiation process. Thus, the results obtained for the different delithiation rate conditions support the structural superiority of the FWNT web electrode.

A comparison of lithiation/delithiation voltage profiles at the different current densities, which provides for a cell polarization, is of importance for understanding the

electrochemical behavior in the electrode. As depicted in Figures 4.12c and 4.12d, the FWNT web electrode with improved electrochemistry exhibited polarization values that were noticeably lower than the reference, except for showing a similar value in ohmic polarization during the lithiation process. Ohmic polarization (Figure 4.12c) as a function of the applied current density was examined by measuring the difference in initial voltage between the current density of 0.1 C ( $\sim 90 \text{ mA g}^{-1}$ ) and a given current density.<sup>28</sup> In addition, measuring the voltage difference in the middle of the sloping plateau between the current density of 0.1 C ( $\sim 90 \text{ mA g}^{-1}$ ) and a given current density can determine the cell polarization that includes ohmic and charge transfer polarization.<sup>123</sup> In electrochemically active materials such as  $\text{Fe}_3\text{O}_4$  that undergo a conversion reaction, the charge transfer process (occurring at the interface of the active material and electrolyte) is the rate-determining step for the conversion reaction.<sup>123</sup> Thus, assuming that the effect of ohmic polarization becomes negligible at a relatively low rate, this cell polarization can be approximated into the charge transfer polarization as summarized in Figure 4.12d. The value for the charge transfer polarization was plotted according to a Tafel plot ( $\ln I_{\text{applied}}$  vs  $\Delta E$ ), resulting in a quasi-linear correlation which accounts for the electrochemical kinetics: FWNT web electrode having a larger slope is indicative of improved kinetics, compared to the control. From a mechanistic perspective, the Fe-carboxylate linkages resulting from chemical interactions between PPBT  $\text{COO}^-$  functionalities and  $-\text{OH}$  on the electroactive particle surface, serve to electrically connect FWNTs to the  $\text{sFe}_3\text{O}_4$  surface and in turn very positively impacting electrode electrical connectivity and stability, thereby assisting in the enhanced kinetics. Thus, this result demonstrates that PPBT-mediated FWNT porous

networks allowing for better electron and ion transport are, presumably, the decisive factor for determining the enhancement in kinetics.

#### 4.3.5 Comparison with SDBS Surfactant-Assisted Electrode System

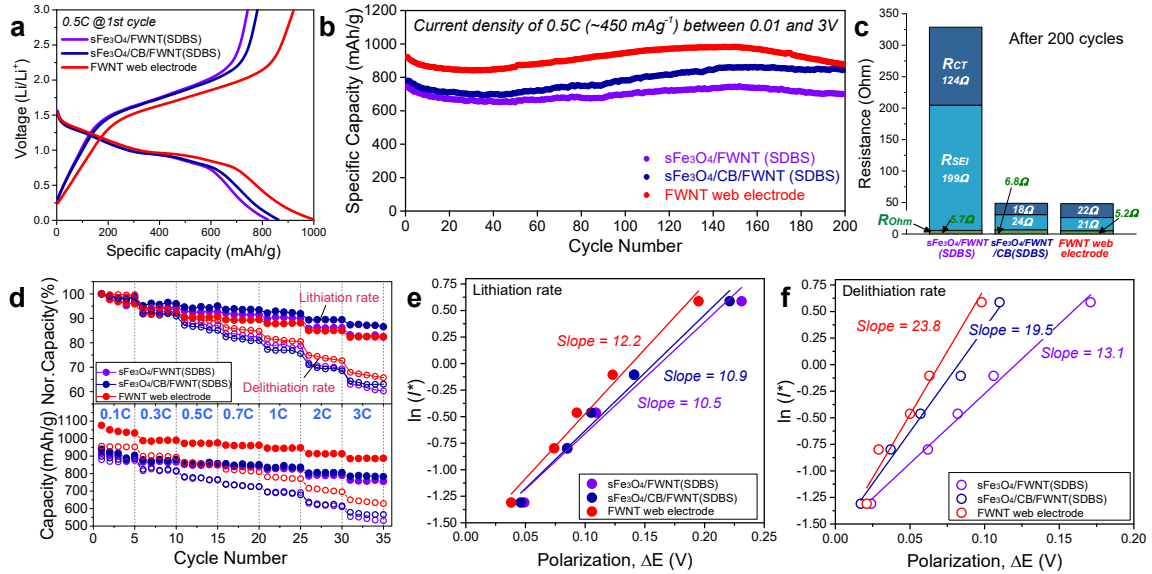


**Figure 4.13.** Electrochemical characterization: comparison with SDBS surfactant-assisted electrode system of sFe<sub>3</sub>O<sub>4</sub>/FWNT (SDBS) and sFe<sub>3</sub>O<sub>4</sub>/CB/FWNT (SDBS). (a) Galvanostatic charge-discharge profiles in the potential window of 0.01 to 3 V vs Li/Li<sup>+</sup> at a constant current density of 0.5C (~450 mA g<sup>-1</sup>). (b) Cycling performance (=capacity retention as function of cycle number) collected at the current density of 0.5C (~450 mA g<sup>-1</sup>) between 0.01 and 3 V. (c) Electrode internal resistance ( $R_{ohm}$ ,  $R_{SEI}$ ,  $R_{CT}$ ) after 200 cycles, fitted by EIS results. (d) Rate capability (close circles: lithiation rate capability, open circles: delithiation rate capability). (e, f) Tafel plots:  $\ln(I_{applied})$  vs  $\Delta E$ , which were plotted from the results of charge transfer polarization in the range from 0.1C to 2C.

A comparison of the current FWNT web electrode with a previously reported SDBS surfactant-assisted electrode system including sFe<sub>3</sub>O<sub>4</sub>/FWNT (SDBS)<sup>132</sup> and sFe<sub>3</sub>O<sub>4</sub>/CB/FWNT (SDBS) shows the importance of considering carboxylated polythiophene (*i.e.*, PPBT) and carbon particle (*i.e.*, carbon black (CB)) addition, which

are expected to build stable electron pathways between the FWNT and  $\text{sFe}_3\text{O}_4$  surfaces and facilitate formation of a more porous morphology, respectively. A PEG coating that prevented  $\text{Fe}_3\text{O}_4$  particle dispersion in SDBS solution (Figure 4.10) was not introduced in the SDBS surfactant-assisted system. The fabrication of the surfactant-assisted electrode followed the same process as that of FWNT web electrode, except for the use of SDBS (concentration = 1.0 wt %) to disperse electrode materials rather than PPBT solution. The resultant electrode exhibited a well-dispersed structure, observed in the surface-view SEM images (Figure 4.14).

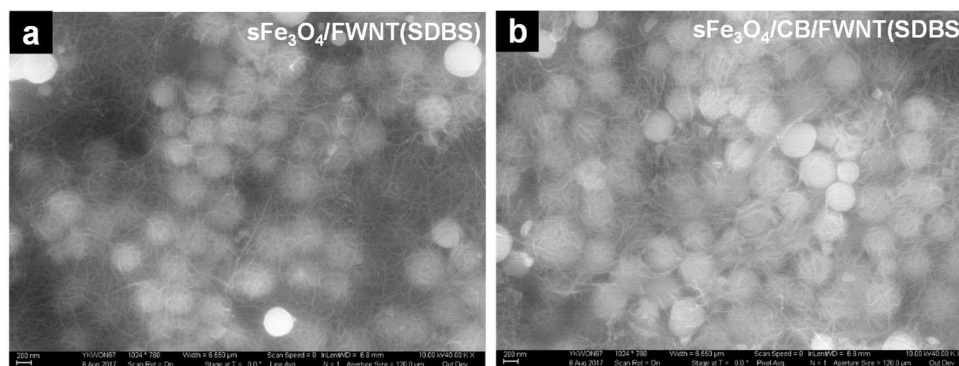


**Figure 4.14.** Surface view SEM images of SDBS surfactant-assisted electrodes of (a)  $\text{sFe}_3\text{O}_4/\text{FWNT}$  (SDBS), and (b)  $\text{sFe}_3\text{O}_4/\text{CB}/\text{FWNT}$  (SDBS).

Figure 4.13a presents the galvanostatic charge-discharge voltage profiles at the 1st cycle of the cycling performance as described in Figure 4.13b, where the cells were lithiated/delithiated at a constant current density of 0.5 C ( $\sim 450 \text{ mAh g}^{-1}$ ) in the potential range of 0.01–3 V. To our surprise, the FWNT web electrode shows a much higher delithiated capacity at a rate of 0.5 C, presenting the specific capacity of  $920 \text{ mAh g}^{-1}$  at the 1st cycle, as compared to  $742 \text{ mAh g}^{-1}$  for  $\text{sFe}_3\text{O}_4/\text{FWNT}$  (SDBS) and  $780 \text{ mAh g}^{-1}$  for  $\text{sFe}_3\text{O}_4/\text{CB}/\text{FWNT}$  (SDBS). Note, when comparing only SDBS-assisted electrodes, carbon



addition favorably impacted the capacity aspects and retention during cycling. Electrode internal resistance (Figure 4.13c) including ohmic, SEI, and charge-transfer resistance ( $R_{Ohm}$ ,  $R_{SEI}$ ,  $R_{CT}$ ), fitted by EIS results after 200 cycles (Figure 4.9), supports this observation, where the FWNT web electrode and surfactant-assisted system with carbon particles tend to have similar resistance while  $R_{SEI}$  and  $R_{CT}$  in the system with no carbon addition remained much larger. Rate capability (Figure 4.13d) and Tafel plots that account for the electrochemical kinetics (Figure 4.13e,f), also show comparable tendencies to the above electrochemical testing results: FWNT web electrode > sFe<sub>3</sub>O<sub>4</sub>/CB/FWNT (SDBS) > sFe<sub>3</sub>O<sub>4</sub>/FWNT (SDBS).

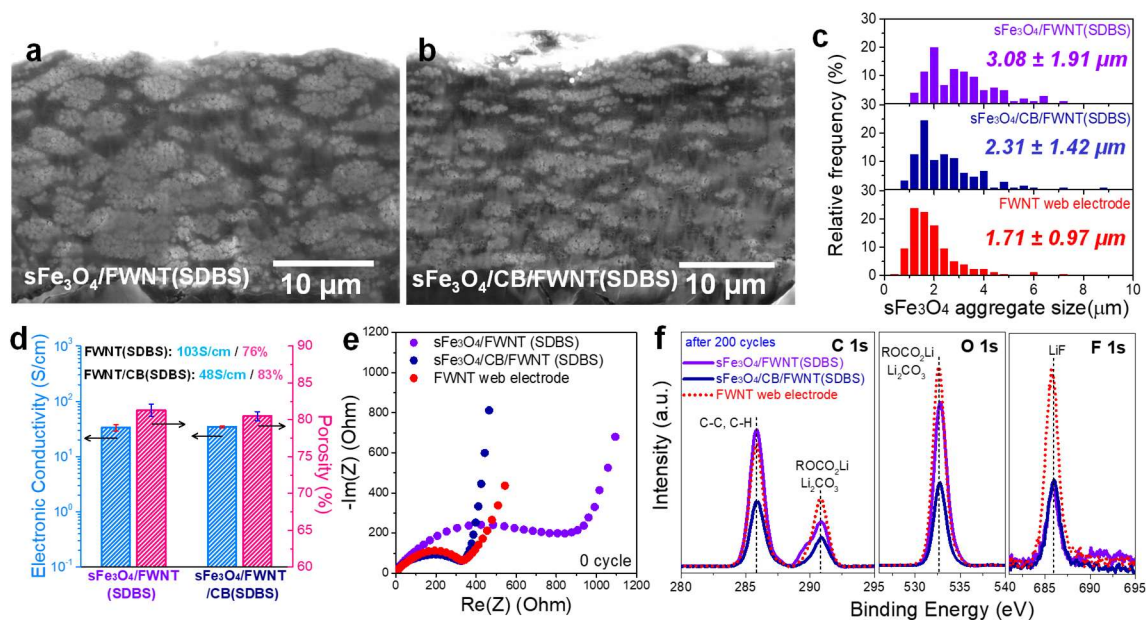


**Figure 4.15.** Analysis of SDBS surfactant-assisted electrode system. Cross-sectional SEM images of (a) sFe<sub>3</sub>O<sub>4</sub>/FWNT (SDBS) and (b) sFe<sub>3</sub>O<sub>4</sub>/CB/FWNT (SDBS). (c) Size distribution of sFe<sub>3</sub>O<sub>4</sub> aggregates observed in the SEM images of each electrode cross-section. (d) Electronic conductivity and porosity. (e) The impedance spectra measured at open-circuit voltage (OCV) before battery testing in the frequency range from 1 MHz to 0.1 Hz. (f) XPS analysis of SEI layer after 200 cycles.



Insights into the origins of the differences in electrochemistry can be derived from the cross-sectional SEM images depicting morphologies of electrodes with different  $\text{sFe}_3\text{O}_4$  aggregate size (Figure 4.4f and Figure 4.15a–c). Aggregate size within FWNT web electrodes assisted by PEG and PPBT carboxylic groups was  $\sim 1.71 \mu\text{m}$ , whereas that for  $\text{sFe}_3\text{O}_4/\text{CB}/\text{FWNT}$  (SDBS) and  $\text{sFe}_3\text{O}_4/\text{FWNT}$  (SDBS) was 2.31 and  $3.08 \mu\text{m}$ , respectively, demonstrating the ability of PEG and PPBT to improve materials dispersion. Interestingly, the addition of carbon particles also appears to facilitate reduction in the size of  $\text{sFe}_3\text{O}_4$  aggregates. Moreover, although electronic conductivity and porosity (Figure 4.15d;  $33.7 \text{ S cm}^{-1}$  and 81.3 %) of  $\text{sFe}_3\text{O}_4/\text{CB}/\text{FWNT}$  (SDBS) electrodes exhibit no difference from those of  $\text{sFe}_3\text{O}_4/\text{FWNT}$  (SDBS) ( $34.5 \text{ S cm}^{-1}$  and 80.5 %),  $\text{CB}/\text{FWNT}$  web (porosity = 83 %) exhibited improved porosity vs the pure FWNT web (porosity = 76%), which might help to explain why  $\text{CB}/\text{FWNT}$  networks appear to possess more facile ion transport channels. This hypothesis is consistent with EIS results (Figure 4.15e), where only the  $\text{sFe}_3\text{O}_4/\text{FWNT}$  (SDBS) electrode system exhibits a much larger semi-circle, indicating larger charge-transfer resistance. Conceivably, the physical characteristics of carbon particles (i) are more favorable to dispersion than FWNTs and prone to placement at the interspace between  $\text{sFe}_3\text{O}_4$  particles, thereby preventing  $\text{sFe}_3\text{O}_4$  aggregation, and (ii) are attached on FWNT surfaces to restrict their bundling, both of which contribute to more porous FWNT networks.

As presented in Figure 4.15f, XPS analysis of the electrodes after 200 cycles provides additional evidence that PPBT-assisted FWNT web electrode stability was derived from formation of a stable SEI layer having a higher fraction of LiF.<sup>143</sup> Specifically, when the FEC additive — a source for LiF in the stable SEI layer — was

excluded from the electrolyte, SDBS surfactant-assisted systems experienced substantial cycle degradation, whereas the FWNT web electrode exhibited relatively stable cycling performance (Figure 4.16).

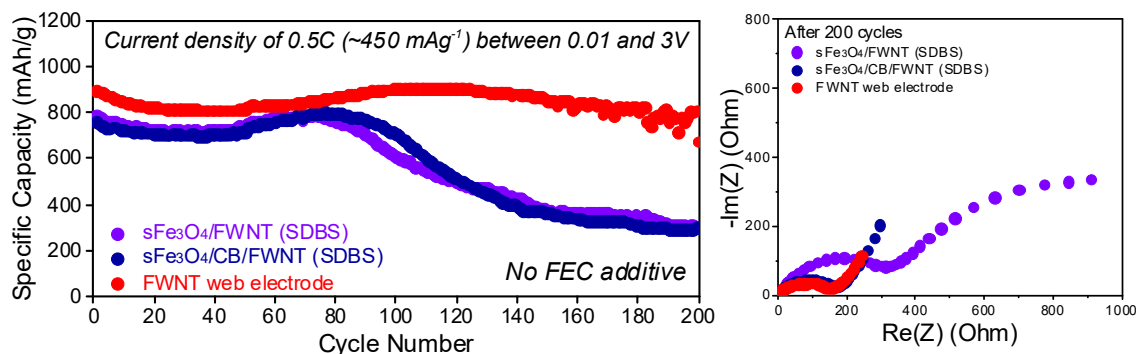


**Figure 4.16.** Cycling performance comparing FWNT web electrode with SDBS surfactant-assisted electrode system including  $s\text{Fe}_3\text{O}_4/\text{FWNT}$  (SDBS) and  $s\text{Fe}_3\text{O}_4/\text{CB}/\text{FWNT}$  (SDBS). The electrolyte was a solution of 1.2 M  $\text{LiPF}_6$  in EC/DEC (1/1 by volume) without FEC additive. After 200 cycles, EIS measurement was performed in the frequency range from 1 MHz to 0.1 Hz.

Thus, FWNT web electrode SEI layer stability appears positively influenced by the stable connections formed between the electrode components by PPBT linkages, and the smaller  $s\text{Fe}_3\text{O}_4$  aggregates that result in smaller volume changes during the charging/discharging process. Meanwhile, as evidenced by the C 1s and O1s XPS spectra,  $s\text{Fe}_3\text{O}_4/\text{FWNT}$  (SDBS) manifested a relatively larger proportion of organic compounds within the SEI layer than  $s\text{Fe}_3\text{O}_4/\text{CB}/\text{FWNT}$  (SDBS), which may explain the dramatic increase in SEI resistance ( $R_{\text{SEI}}$ ) for the former during cycling (Figure 4.13c). This observation also demonstrates the effectiveness of carbon particle introduction into FWNT web electrode systems.

#### 4.4 Conclusion

We demonstrated that FWNT web electrodes fabricated with carboxylate substituted polythiophene (PPBT) ‘assists’ enabled the formation of electrical bridges between FWNT and  $\text{sFe}_3\text{O}_4$  surfaces. These bridges improved electrode electrochemical kinetics and reduced electrode resistance with respect to control electrodes, which directly translated into significantly improved battery performance. The effort to design a composite electrode structure that facilitates electron/ion transport, took advantage of an electrode frame composed of a FWNT web having long-range electron pathways and a network of porous passages, and monodispersed electroactive spheres (*i.e.*,  $\text{sFe}_3\text{O}_4$ ) possessing uniform  $\text{Li}^+$  diffusion paths. The latter were integrated into the FWNT web by means of an electrical linker (*i.e.*, PPBT) using chemical/physical interactions that took advantage of the materials’ surface chemistries. Introduction of the PEG coating on  $\text{sFe}_3\text{O}_4$  enabled favorable physical attraction to PPBT carboxylic moieties, consequently stimulating the formation of a Fe-carboxylate bond at their interface that contributed to formation of a stable connection. Notably, the addition of carbon particles into the web electrode proved effective for improving battery performance through creation of added porosity and impeding further  $\text{sFe}_3\text{O}_4$  aggregation. The approach mediated by electrode component surface chemistries led to significant performance improvements associated with the FWNT web electrodes. The results and fundamental insight described herein suggest a feasible approach — inspired by consideration of surface chemistries in conjunction with electron and ion transport — that can provide for practical, high-performance, high-capacity battery electrode systems.

## CHAPTER 5. SWNT ANCHORING ON HIGH-CAPACITY ANODE MATERIALS WITH CARBOXYLATED POLYTHOPHENE ‘LINKS’

### 5.1 Introduction

High-capacity electroactive materials that assure high performance are a prerequisite for ubiquitous adoption of technologies that require high energy/power density lithium (Li)-ion batteries, such as smart Internet of Things (IoT) devices and electric vehicles (EVs).<sup>8,33</sup> While high-capacity anode materials including Si, Sn, metal oxide and their derivatives have been identified; they undergo massive volume changes and resultant poor electrochemistry, which is arguably the major impediment delaying their practical implementation.<sup>93</sup> Specifically, crack formation and pulverization during volume expansion contribute substantially to breakage of electronic pathways in electrodes and in turn degradation of battery performance.

Efforts have been made to suppress the electrical breakdown through introduction of electrically conducting functionalities (*e.g.* carbon coatings,<sup>12,13,15,23</sup> carbon nanotubes (CNTs),<sup>145–147</sup> or graphene<sup>148–150</sup>) onto the active material surface. Despite improvements in performance, these approaches are not solely capable of maintaining electrical connectivity between cracked/pulverized active particles during repeated charge-discharge

---

Adapted with permission from “Kwon, Y. H.; Minnici, K.; Park, J. J.; Lee, S. R.; Zhang, G.; Takeuchi, E. S.; Takeuchi, K. J.; Marschilok, A. C.; Reichmanis, E. SWNT Anchored with Carboxylated Polythiophene ‘Links’ on High-Capacity Li-Ion Battery Anode Materials. *J. Am. Chem. Soc.* DOI: 10.1021/jacs.8b00693.” Copyright 2018 American Chemical Society.

cycles because of weak van der Waals interactions between carbon and active material surface. Thus, it is imperative to link the carbonaceous conducting agent with the high-capacity active particles with a binding component. Studies pertaining to new polymeric binders that impact electrode stability pointed to the importance of surface chemistry stimulating desirable molecular interactions. For instance, formation of a carboxylate bond between a carboxylate substituted polymeric binder and the hydroxylated surface of electroactive particles led to highly enhanced cycle life.<sup>23,24,127,139,151,152</sup> These fundamental insights provide critical clues for the design of high-capacity anode materials with superior electrochemical performance. Specifically, introducing electronically conductive carbon nanotube (CNT) networks onto the active material surface, in conjunction with the formation of carboxylate bonds to afford stable links between the CNT networks and active materials *via* a binding component might be favorable. Such a construct may allow for dimensional stability and electrical continuity in the active materials during volume expansion, thereby leading to improved performance. Identification of a polymeric binding component able to connect the CNT networks with the electroactive material surface, nevertheless, remains a challenge. Polymers bearing carboxylic moieties including poly(acrylic acid) (PAA) and sodium carboxymethyl cellulose (CMC), utilized as binders in Li-ion battery electrodes, are intrinsically electrical insulators and would be expected to eventually increase electrode resistance. Furthermore, since PAA and CMC have poor affinity with the CNT surface, it would additionally be necessary to effectively disperse and debundle the CNTs.

Alternatively, carboxylate substituted polythiophenes, such as poly[3-(potassium-4-butoate) thiophene] (PPBT), have apparently impressive potential to serve as a

polymeric binder or physical/chemical linker to render electroactive particles and carbon additives well-connected through specific molecular interactions, thereby yielding stable, high-performance battery electrodes.<sup>139,151,152</sup> The carboxylate bearing conjugated polymer, PPBT, has relatively high electronic conductivity of  $\sim 10^{-5}$  S cm<sup>-1</sup> when compared with polyvinylidene fluoride (PVDF; conductivity  $\sim 10^{-8}$  S cm<sup>-1</sup>); and further, electrochemical doping where the conjugated polymer undergoes reduction within the operating voltage of anode applications, enables more rapid electron transport.<sup>59,61,99,139</sup> In addition, PPBT, with its conjugated backbone and side chain carboxylic moieties, has been shown to contribute to CNT dispersion and the formation of carboxylate bonds through interactions with surface –OH groups on the electroactive particles. In particular, the  $\pi$ -conjugated polythiophene backbone physically interacts with the two-dimensional, graphene-like electron rich nanotube surface while the solubilizing carboxylate substituted alkyl side chains support CNT debundling and dispersion in water.<sup>55,152</sup> Covalent interactions between PPBT COO– functionalities and –OH on the electroactive particle surface are presumed to provide for electrode stability and the ability to withstand severe volume changes. These factors in turn, facilitate electron transport through electrical linkages between the CNTs and the electroactive particles.<sup>139,151,152</sup>

Here, we introduce the use of carboxylated polythiophene to fabricate anchored, single-walled carbon nanotube (SWNT) - high-capacity active anode materials. To explore the proof of concept and its feasibility for anchoring SWNTs with PPBT links, monodispersed Fe<sub>3</sub>O<sub>4</sub> spheres (sFe<sub>3</sub>O<sub>4</sub>, theoretical capacity: 925 mAh g<sup>-1</sup>, volume expansion: 200 %),<sup>139</sup> silicon nanoparticles (Si NPs, theoretical capacity: 4200 mAh g<sup>-1</sup>, volume expansion: 420 %)<sup>94</sup> and carbon-coated silicon monoxide (c-SiO<sub>x</sub> with  $x \approx 1$ ,

theoretical capacity: 2600 mAh g<sup>-1</sup>,<sup>153</sup> volume expansion: ~200 %<sup>154</sup>) were used as representative high-capacity active materials.

Initially, Fe<sub>3</sub>O<sub>4</sub> spheres (sFe<sub>3</sub>O<sub>4</sub>) were utilized as a model high capacity metal oxide active material owing to their well-defined chemistry with surface hydroxyl (–OH) functionalities that facilitate elucidation of molecular interactions.<sup>138,139,151,152</sup> This preliminary study provided supportive evidence for the importance of surface chemistry, whereby interfacial interactions between the metal oxide surface and SWNT networks could be enabled through incorporation of PPBT. Specifically, the polythiophene carboxylate group can chemically bind to the metal oxide surface to impart stability and robust electronic connectivity of the sFe<sub>3</sub>O<sub>4</sub> surface with the SWNT networks, providing improved rate capabilities and long-term cycle life performance. To further demonstrate the superiority of SWNT anchoring *via* PPBT linkages, we expanded the concept to other electroactive materials with much higher capacity, such as silicon nanoparticles (Si NPs) and carbon-coated silicon monoxide (c-SiO<sub>x</sub>) that are more susceptible to pulverization during volume expansion. Consequently, the design presented here allowed for exceptional advances in electrochemical performance that can be ascribed to improved electrode stability and robust electrical connections enabled by PPBT  $\pi$ - $\pi$  interactions and carboxylate linkages. The physical and chemical interactions led to effective capture of cracked/pulverized particles, contributing to suppressed thickness change of electrodes, formation of stable solid electrolyte interface (SEI) layers, reduced electrode internal resistance and enhanced electrode kinetics.

## 5.2 Experimental Section

**Materials.** Monodispersed spherical  $\text{Fe}_3\text{O}_4$  particles ( $\sim 500$  nm in diameter) were synthesized by a solvothermal method reported by Fan *et al.*<sup>138</sup> The precursor solution was prepared by  $\text{FeCl}_3 \cdot 6\text{H}_2\text{O}$  (2.16 g) and  $\text{CH}_3\text{COONa} \cdot 3\text{H}_2\text{O}$  (5.76 g) dissolved in 40 mL of ethylene glycol (EG) to form homogeneous solution with stirring for 24 h, and then sealed in a Teflon lined stainless autoclave (45 mL capacity), in which the concentration of  $\text{FeCl}_3 \cdot 6\text{H}_2\text{O}$  was  $0.200 \text{ mol L}^{-1}$ . The autoclave was heated to  $200^\circ\text{C}$  for 8 h, and then cooled to room temperature. After sequentially washing several times with deionized water and ethanol using a centrifuge, monodispersed  $\text{Fe}_3\text{O}_4$  spheres ( $\text{sFe}_3\text{O}_4$ ) were produced. As synthesized  $\text{sFe}_3\text{O}_4$  particles, composed of small  $\text{Fe}_3\text{O}_4$  crystallites ( $\sim 71$  nm), have an average size of 498 nm.<sup>152</sup> For the preparation of  $\text{sFe}_3\text{O}_4$  particles coated with PEG (PEG- $\text{sFe}_3\text{O}_4$ ), 1 g of  $\text{sFe}_3\text{O}_4$  powders in 10 g ethanol adding 8 mL of PEG 1500 solution (50 % w/v, Sigma-Aldrich) were sonicated for 30 min in the ice bath with an ultrasonic probe. The PEG- $\text{sFe}_3\text{O}_4$  powders were washed and extracted by centrifuge separation using acetone with speed of 6000 rpm for 10 min for 3 times. PPBT (Mw: 16 kDa, polydispersity: 2.2, the head to tail regioregularity: 89%) was purchased from Rieke Metals Inc.. For the preparation of SWNT- $\text{sFe}_3\text{O}_4$ , the mixture of SWNT (10 mg, Sigma-Aldrich) in PPBT solution (20 mg of PPBT, 4mL of deionized water) was sonicated for 15 min in the ice bath with an ultrasonic probe. After adding PEG- $\text{sFe}_3\text{O}_4$  (100 mg) into the SWNT dispersion, the mixture suspension was subjected to further ultrasonication for 3 min. The resultant SWNT/PEG- $\text{sFe}_3\text{O}_4$  suspension was vacuum-filtrated onto a membrane filter (PVDF membrane filter with pore size of  $0.22 \mu\text{m}$ , EMD Millipore) adding sufficient water, ethanol and acetone for washing. As-filtrated powders were finally vacuum-dried at  $110^\circ\text{C}$  for overnight, eventually producing SWNT- $\text{sFe}_3\text{O}_4$  electroactive particles. The SWNT-



sFe<sub>3</sub>O<sub>4</sub> particles assisted by SDBS surfactant (no PPBT linkage sample) were prepared by the same process mentioned above, except for the SWNT suspension preparation using SDBS surfactant solution (concentration = 1.0 wt % in water) instead of PPBT solution. In case of Si NPs (50–70 nm, US Research Nanomaterials, Inc.) and c-SiO<sub>x</sub> (KSC1064, Shin-Etsu Chemical Co., Ltd.), material preparation for SWNT anchoring with PPBT links followed the same procedure with SWNT-sFe<sub>3</sub>O<sub>4</sub> preparation.

**Electrochemical Characterization.** Working electrodes were made by blade-coating electrode slurry on the Cu foil substrate with active material (sFe<sub>3</sub>O<sub>4</sub>, SWNT-sFe<sub>3</sub>O<sub>4</sub>, Si NPs, SWNT-Si NPs, c-SiO<sub>x</sub>, SWNT-c-SiO<sub>x</sub>, c-SiO<sub>x</sub>/graphite blend, SWNT-c-SiO<sub>x</sub>/graphite blend), carbon black (CB) and binder (PPBT, sodium carboxymethyl cellulose (CMC), CMC/styrene butadiene rubber (SBR)). The electrode comprising SWNT-sFe<sub>3</sub>O<sub>4</sub> (or sFe<sub>3</sub>O<sub>4</sub>), CB, and binder (CMC or PPBT) was 71.4:14.3:14.3 in a mass ratio, whereas 52:34:14 for the electrode consisting of active material (Si NPs, SWNT-Si NPs, c-SiO<sub>x</sub>, SWNT-c-SiO<sub>x</sub>), CB, and binder (CMC or PPBT). In the graphite-blended systems with PPBT or CMC binder, the mass ratio of SWNT-c-SiO<sub>x</sub>/graphite blend, CB, and binder was 52:34:14. When fabricating CMC/SBR binder-based electrodes, active material (c-SiO<sub>x</sub>/graphite blend, SWNT-c-SiO<sub>x</sub>/graphite blend), CB, CMC, and SBR were 95.8:1.7:1.5:1 in a mass ratio. In the graphite-blended system, the active material was prepared by blending SWNT-c-SiO<sub>x</sub> with graphite in a mass ratio of 30:70. These prepared electrodes were pre-evaporated at 65 °C for 3 h and completely evaporated at 110 °C for 12 h in a vacuum oven, and then pressed until the density of the electrode became ~0.7–0.9 g cm<sup>-3</sup>. 2032-type coin cells (MTI corp.) were used for electrochemical measurements. Lithium metal was used as a counter electrode and 1.2 M LiPF<sub>6</sub> in ethylene carbonate (EC)

and diethyl carbonate (DEC) (1:1 by volume) with 10 wt % fluoroethylene carbonate (FEC) for long cycle stability, was utilized as an electrolyte. When testing coin cells comprising  $\text{sFe}_3\text{O}_4$ -based electrodes, only constant current (CC) condition was used (*i.e.*, lithiated to 0.01 V and delithiated to 3.0 V at the set value of current density), whereas when measuring coin cells comprising Si NPs (or  $\text{c-SiO}_x$ )-based electrodes, a constant current (CC)–constant voltage (CV) technique was applied: the coin cell was lithiated to 0.01 V at the set value of current density under constant CC condition and then maintained at CV of 0.01 V until the current density became 0.05 C. In turn, the cell was delithiated to 1.5 V at the set value of current density under CC condition. Before electrochemical testing, all the coin cells were charging and discharging with the current density of 0.1 C to confirm their capacity and initial efficiency. The tests were then proceeded for cycling performance and rate capability. Cyclic voltammetry (CV) was performed in the potential range of 0.01–3 V for  $\text{sFe}_3\text{O}_4$ -based electrodes (0.01–1.5 V for Si NPs and  $\text{c-SiO}_x$ -based electrodes) with various scan rates. Electrochemical impedance spectroscopy (EIS) measurements were conducted in the frequency range from 1 MHz to 0.1 Hz.

**Full-Cell Fabrication and Characterization.** A prototype full cell sealed with an aluminumized polymer pouch was fabricated with a negative/positive (*n/p*) ratio of  $\sim 1.08$ ; the anode and cathode areal capacities were  $3.15 \text{ mAh cm}^{-2}$  and  $2.93 \text{ mAh cm}^{-2}$ . The cathode was prepared by blade-coating electrode slurry on an aluminum (Al) foil substrate with commercialized lithium cobalt oxide ( $\text{LiCoO}_2$ , or LCO), CB, and polyvinylidene difluoride (PVDF) binder in a mass ratio of 94:3:3 using *N*-methyl-2-pyrrolidone (NMP) as the solvent and dried at  $110^\circ\text{C}$  for 1 h, and then pressed until the density of the electrode became  $\sim 3.8 \text{ g cm}^{-3}$ . The aluminumized polymer pouch-type full cells, composed of a

porous polyethylene (PE) separator sandwiched between anode and cathode, were assembled. The electrolyte comprising 1.2 M LiPF<sub>6</sub> in EC/DEC (1:1 by volume) with 10 wt % FEC was injected and the pouch was completely sealed. The pouch-type cells were fabricated in a globe box filled with argon gas. The prepared full cells were pre-cycled in the first three cycles over the potential range of 2.5–4.25 V at 0.05 C under CC/CV mode for charging to 4.25 V and maintained 4.25 V until the current density became 0.03 C, and then CC mode for discharging to 2.5 V. The tests were then proceeded for cycling performance and rate capability.

**Physicochemical Characterization.** Fourier-transform infrared spectroscopy (FT-IR) spectra were recorded using KBr pellets of the materials and a Nicolet 8700 FTIR spectrometer. The field-emission scanning electron microscopy (FE-SEM) images were observed on the surface view of the electrodes using Zeiss Ultra-60 FE-SEM with an accelerating voltage of 10 kV using the high vacuum mode at room temperature.

## 5.3 Results and Discussion

### 5.3.1 Approach

Stable SWNT electronic networks on the surface of electroactive materials through PPBT carboxylate links would provide fast electron transport and help seize cracked/pulverized particles created during repeated charge-discharge cycling, thereby delivering battery electrode stability which could impact electrochemical performance.

As depicted in Figure 5.1, successful introduction of a polyethylene glycol (PEG) coating on the surface of an active particle coupled with PPBT as an electrical linker to

connect the active particle to the SWNT surface critically depends on the materials' surface chemistries. The PEG coating induces attractive molecular interactions with PPBT carboxylate moieties in water, while the PPBT conjugated backbone physically interacts with the SWNT surface through noncovalent  $\pi$ - $\pi$  interactions.<sup>139,152</sup> Combined, those interactions led to the successful preparation of structurally and electrically stable, anchored SWNT – high-capacity electroactive materials through the formation of carboxylate bonds, which influenced the ability of the active material to tolerate the repeated volume changes that occur during battery operation.

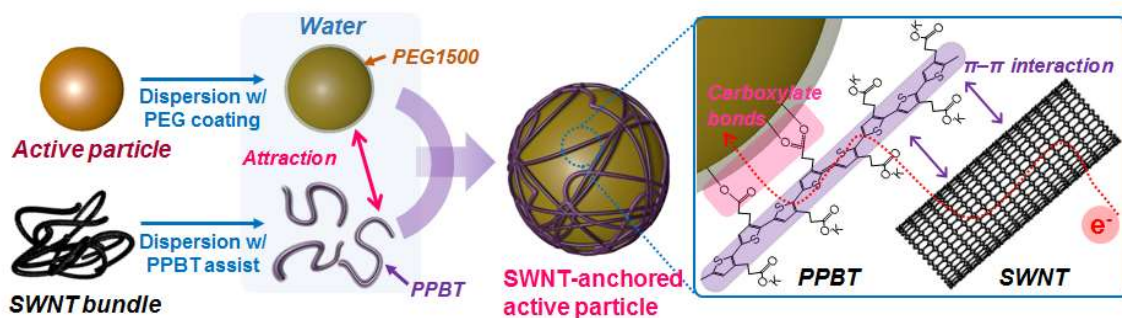


**Figure 5.1.** Schematic illustration of the preparation of the SWNT-anchored electroactive material with PPBT links. Carboxylate bonds between hydroxylated active particle and PPBT carboxyl substituent, and  $\pi$ - $\pi$  interactions between SWNT and PPBT conjugated backbone, provide for stable electrical linkages.

### 5.3.2 SWNT-Anchored $s\text{Fe}_3\text{O}_4$ with Carboxylated Polythiophene (PPBT) Links.

Monodispersed spherical  $\text{Fe}_3\text{O}_4$  particles ( $s\text{Fe}_3\text{O}_4$ )<sup>152</sup> with an average size of ~500 nm was used as the high capacity iron oxide because of structural advantages that lessen the impact of volume changes and facilitate effective particle dispersion; thus supporting uniform  $\text{Li}^+$  ion diffusion during the electrochemical reaction. Prior to SWNT anchoring with PPBT links, a PEG coating on the  $s\text{Fe}_3\text{O}_4$  surface was introduced to increase the

physical affinity of  $s\text{Fe}_3\text{O}_4$  particles to PPBT component.<sup>139</sup> Then, anchored SWNT- $s\text{Fe}_3\text{O}_4$  particles (denoted as SWNT- $s\text{Fe}_3\text{O}_4$ ) were prepared by a probe sonication process to sequentially disperse SWNTs and PEG-coated  $s\text{Fe}_3\text{O}_4$  (PEG- $s\text{Fe}_3\text{O}_4$ ) particles in PPBT solution, followed by a vacuum filtration step to collect the as-prepared SWNT- $s\text{Fe}_3\text{O}_4$  powders. Figure 5.2a presents scanning electron microscope (SEM) images of SWNT- $s\text{Fe}_3\text{O}_4$ , confirming that SWNTs are well-connected at the PEG- $s\text{Fe}_3\text{O}_4$  surface, most likely due to the role of the carboxylated conjugated polymer (PPBT) linking the two components through chemical/physical interactions at the respective surfaces.<sup>152</sup>

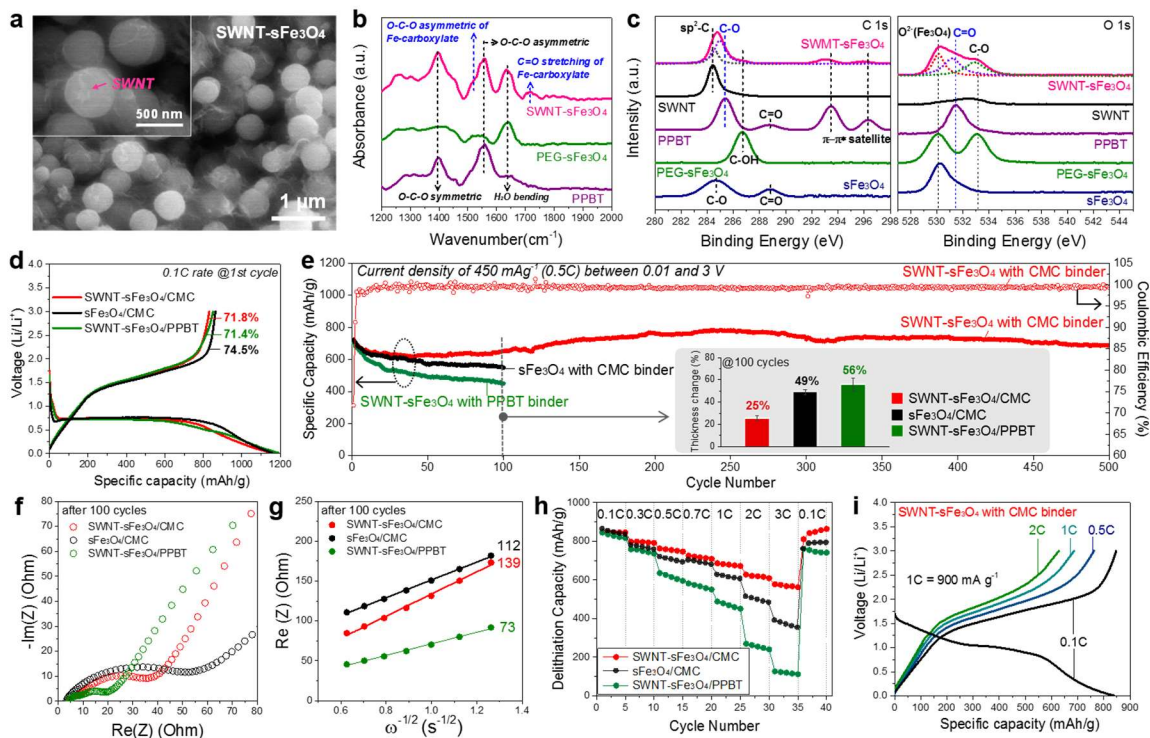


**Figure 5.2.** SWNT-anchored  $s\text{Fe}_3\text{O}_4$  with carboxylated polythiophene (PPBT) links. (a) SEM images of SWNT- $s\text{Fe}_3\text{O}_4$  particles. (b) FT-IR spectra and (c) XPS spectra of  $s\text{Fe}_3\text{O}_4$ , PEG- $s\text{Fe}_3\text{O}_4$ , PPBT, SWNT and SWNT- $s\text{Fe}_3\text{O}_4$ . (d) Galvanostatic charge-discharge profiles in the potential window of 0.01 to 3 V vs Li/Li<sup>+</sup> at a constant current density of 90  $\text{mA g}^{-1}$  (0.1 C). (e) Cycling performance (=capacity retention as a function of cycle number) collected at the current density of 450  $\text{mA g}^{-1}$  (0.5 C) between 0.01 and 3 V (open circle: Coulombic efficiency of SWNT- $s\text{Fe}_3\text{O}_4$  with CMC binder). Inset shows the

electrodes' thickness change after 100 cycles as compared with electrodes before cycling. (f) The impedance spectra measured at open-circuit voltage (OCV) after 100 cycles in the frequency range from 1 MHz to 0.1 Hz, and (g) corresponding Warburg plots. The inserted figures are a slope, presenting Warburg coefficient ( $\Omega \text{ s}^{-1/2}$ ) associated with ion diffusion resistance in the electrode. (h) Delithiation rate capability, where cells were lithiated at a constant current density of 90 mA g<sup>-1</sup> (0.1 C) and delithiated at different current densities between 0.01 and 3 V. (i) Galvanostatic charge-discharge profiles with different delithiation rates of SWNT-sFe<sub>3</sub>O<sub>4</sub> with CMC binder in the potential window of 0.01 to 3 V vs Li/Li<sup>+</sup>.

Fourier transform infrared (FT-IR) spectroscopy (Figure 5.2b) provides strong evidence of the specific interactions between the PPBT carboxylate group and sFe<sub>3</sub>O<sub>4</sub> particles, namely, the formation of a Fe-carboxylate complex where PPBT carboxylate substituents were chemically bound to hydroxyl groups present on the metal oxide surface.<sup>139,151,152</sup> SWNT-sFe<sub>3</sub>O<sub>4</sub> presents a peak at  $\sim 1716 \text{ cm}^{-1}$  for C=O stretching and a peak at  $\sim 1520 \text{ cm}^{-1}$  for O–C–O asymmetric stretching where the shoulder was slit from  $\sim 1558 \text{ cm}^{-1}$  band, associated with the Fe-carboxylate bond. A peak of SWNT-sFe<sub>3</sub>O<sub>4</sub> at  $\sim 1558 \text{ cm}^{-1}$  and  $\sim 1396 \text{ cm}^{-1}$  corresponds to O–C–O asymmetric and symmetric stretching of PPBT, respectively. The X-ray photoelectron spectroscopy (XPS) spectra (Figure 5.2c) of the C 1s and O 1s core levels further substantiate the presence of chemical interactions between PPBT and the sFe<sub>3</sub>O<sub>4</sub> surface. The C 1s peak of SWNT-sFe<sub>3</sub>O<sub>4</sub> at 284.97 eV is indicative of carbon atoms associated with the C-O bond of PPBT, shifted from a peak at 285.36 eV; note the chemical shift to lower binding energy with an increase in interatomic distance which results from additional bonding between PPBT and sFe<sub>3</sub>O<sub>4</sub>.<sup>117,139</sup> In addition, the O 1s spectrum of SWNT-sFe<sub>3</sub>O<sub>4</sub> displayed a peak at 531.1 eV for C=O which was slightly shifted to lower bonding energy from a peak at 531.5 eV for the C=O bond of PPBT, suggesting the existence of PPBT in the form of carboxylate.

To evaluate electrochemical performance, coin-type half cells with a Li metal counter electrode and electrolyte solution of 1.2 M LiPF<sub>6</sub> in ethylene carbonate (EC)/diethyl carbonate (DEC) (1/1 by volume) with 10 wt % fluoroethylene carbonate (FEC) were used. The sFe<sub>3</sub>O<sub>4</sub> mass loading in the present study was typically ~1.9–3.0 mg cm<sup>-2</sup>. Galvanostatic charge-discharge profiles (Figure 5.2d) show the electrode composed of SWNT-sFe<sub>3</sub>O<sub>4</sub> with either CMC or PPBT binder exhibited comparable initial performance at a constant current density of 90 mA g<sup>-1</sup> (0.1 C), where the specific capacity and efficiency were 831 mAh g<sup>-1</sup> and 71.8 % vs 850 mAh g<sup>-1</sup> and 71.4 %, respectively. The electrode fabricated with sFe<sub>3</sub>O<sub>4</sub> and CMC binder presented with a specific capacity of 862 mAh g<sup>-1</sup> and initial efficiency of 74.5 %. The reduced initial efficiency associated with the SWNT systems is attributed to intrinsic properties of CNTs; the large surface area is more involved in SEI layer formation associated with Li<sup>+</sup> ion loss, leading to low Coulombic efficiency and large irreversible capacity at the first cycle.<sup>132,152</sup>

Excellent cycling stability and otherwise improved electrochemical behavior compensate for the above drawbacks. A comparison of SWNT-sFe<sub>3</sub>O<sub>4</sub> vs sFe<sub>3</sub>O<sub>4</sub> control electrodes where both are fabricated with CMC binder, aptly demonstrates that introduction of PPBT carboxylate linkages to anchor the SWNTs to the active material allowed for noticeably improved capacity retention with stable long-term cycling, and superior rate capabilities. Figure 5.2e presents advantages of SWNT-sFe<sub>3</sub>O<sub>4</sub> with CMC binder in cycling performance at the constant current density of 450 mAh g<sup>-1</sup> (0.5 C) in the potential range of 0.01–3 V (vs Li<sup>+</sup>/Li). After 500 cycles, the reversible capacity of the SWNT-sFe<sub>3</sub>O<sub>4</sub>/CMC binder electrode decreased from 710 mAh g<sup>-1</sup> at the 1st cycle to 687 mAh g<sup>-1</sup> after 500 cycles, which represents very stable capacity retention of 96.8 %.

Notably, PPBT carboxylate linkages that serve to anchor SWNTs to the  $\text{sFe}_3\text{O}_4$  particle surface contribute much favorably to electrochemical cycling (Figure 5.3a). After 100 cycles, the SWNT- $\text{sFe}_3\text{O}_4$ /CMC binder electrode underwent a volume change of 25 %, while the control electrode based on  $\text{sFe}_3\text{O}_4$  with CMC binder underwent a relatively larger volume change of 49 %. These differences may derive from the thick SEI layer observed at the  $\text{sFe}_3\text{O}_4$ /CMC binder electrode surface, *vs* that observed for the SWNT- $\text{sFe}_3\text{O}_4$ /CMC binder system (Figure 5.3b, c).

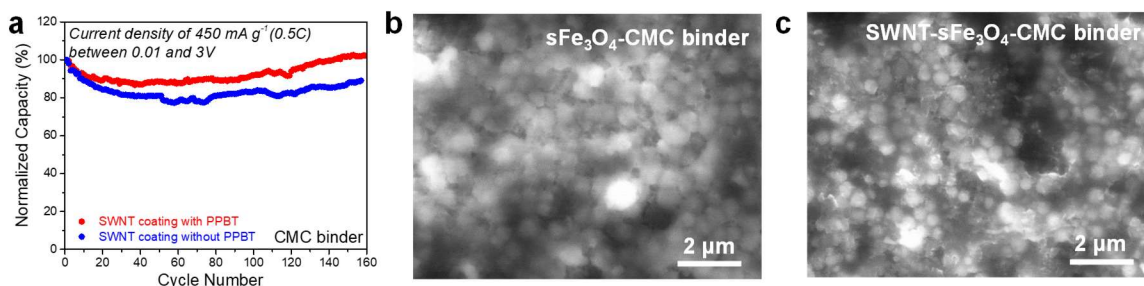


**Figure 5.3.** SWNT-anchored  $\text{sFe}_3\text{O}_4$  with carboxylated polythiophene (PPBT) links. (a) Cycling performance (=capacity retention as function of cycle number) collected for the current density of  $450 \text{ mA g}^{-1}$  (0.5C) between 0.01 and 3 V, comparing SWNT anchoring on the  $\text{sFe}_3\text{O}_4$  surface with PPBT carboxylate linkages with SWNT introduction with no PPBT linkages (prepared by sodium dodecylbenzenesulfonate (SDBS) surfactant instead of PPBT component). The electrodes were fabricated with CMC binder. The surface-view SEM images of the electrodes (after 100 cycles) composed of (b)  $\text{sFe}_3\text{O}_4$  with CMC binder, and (c) SWNT- $\text{sFe}_3\text{O}_4$  with CMC binder.

Electrochemical impedance spectroscopy (EIS) analysis in Figure 5.2f supports this observation: note the decreased size of the semi-circle ( $\approx$  reduced electrode internal resistance including SEI and charge transfer resistance) of the of SWNT- $\text{sFe}_3\text{O}_4$ /CMC binder electrode compared to that of the  $\text{sFe}_3\text{O}_4$ /CMC control. The beneficial effect of PPBT induced anchoring of SWNTs was also seen in the rate capability experiments (Figure 5.2h, i). Under a constant lithiation current density of  $90 \text{ mA g}^{-1}$  (0.1 C), the



SWNT-sFe<sub>3</sub>O<sub>4</sub>/CMC electrode exhibits much higher delithiated capacity over a wide range of delithiation current densities of 90–2700 mA g<sup>-1</sup> (0.1 C–3 C) at a voltage range of 0.01–3 V, which conveys its superior rate capability. Given that the PPBT binder provided for stable electrodes,<sup>139,151,152</sup> improved cyclability was also anticipated. Contrary to that expectation, the SWNT-sFe<sub>3</sub>O<sub>4</sub>/PPBT binder electrode exhibited poor cycling (Figure 5.2e) and inferior rate capability (Figure 5.2h). These results were not correlated with its lower internal resistance ( $\approx$  small semi-circle size) observed in the EIS (Figure 5.2f) and lower Warburg coefficient of 73  $\Omega$  s<sup>-1/2</sup> (Figure 5.2g) vs the SWNT-sFe<sub>3</sub>O<sub>4</sub>/CMC (139  $\Omega$  s<sup>-1/2</sup>) and sFe<sub>3</sub>O<sub>4</sub>/CMC (112  $\Omega$  s<sup>-1/2</sup>) counterparts. Specifically, the observed value points to impedance in the low frequency range that can be attributed to ion diffusion resistance within the electrode.<sup>129</sup> To gain fundamental insight into the observed differences in electrode performance that derive from differences in binder chemistry, we investigated the electrode reaction kinetics and apparent lithium ion diffusion coefficients in SWNT-sFe<sub>3</sub>O<sub>4</sub> and sFe<sub>3</sub>O<sub>4</sub> fabricated with different binders including CMC and PPBT (Figure 5.4).

Cyclic voltammetry (CV) investigations provided information surrounding electrode reaction kinetics.<sup>155–158</sup> The kinetic data were characterized by analyzing the voltammetric response of an electrode-active material at various scan rates according to

$$I_{pc} = av^b \quad (1)$$

where the measured peak current ( $I_{pc}$ ) obeys a power-law relationship with the potential scan rate ( $v$ ). The value of  $b$  is positively correlated with the corresponding Li<sup>+</sup> diffusion, which is determined from the slope of the plot of  $\log(I_{pc})$  vs  $\log(v)$  and provides insight

into the charge storage mechanism. With respect to reaction kinetics, it also offers a means to compare systems, where a higher  $b$  value suggests faster kinetics.<sup>158</sup> For a redox reaction limited by semi-infinite diffusion, the peak current ( $I_{pc}$ ) varies by  $v^{1/2}$  ( $b = 0.5$ ); for a capacitive process, it varies with  $v$  ( $b = 1$ ). Over a wide range of sweep rates ( $v$ ), it has been demonstrated that well-known battery materials (e.g. LiFePO<sub>4</sub>, LiCoO<sub>2</sub>, LiMn<sub>2</sub>O<sub>4</sub>, graphite) have  $b \approx 0.5$ , consistent with slow kinetics, whereas  $b \approx 1.0$  for the pseudocapacitor materials (e.g. MnO<sub>2</sub>, Nb<sub>2</sub>O<sub>5</sub>) showing fast kinetics.<sup>156,157</sup> Therefore, low  $b$  might imply sluggish kinetics.

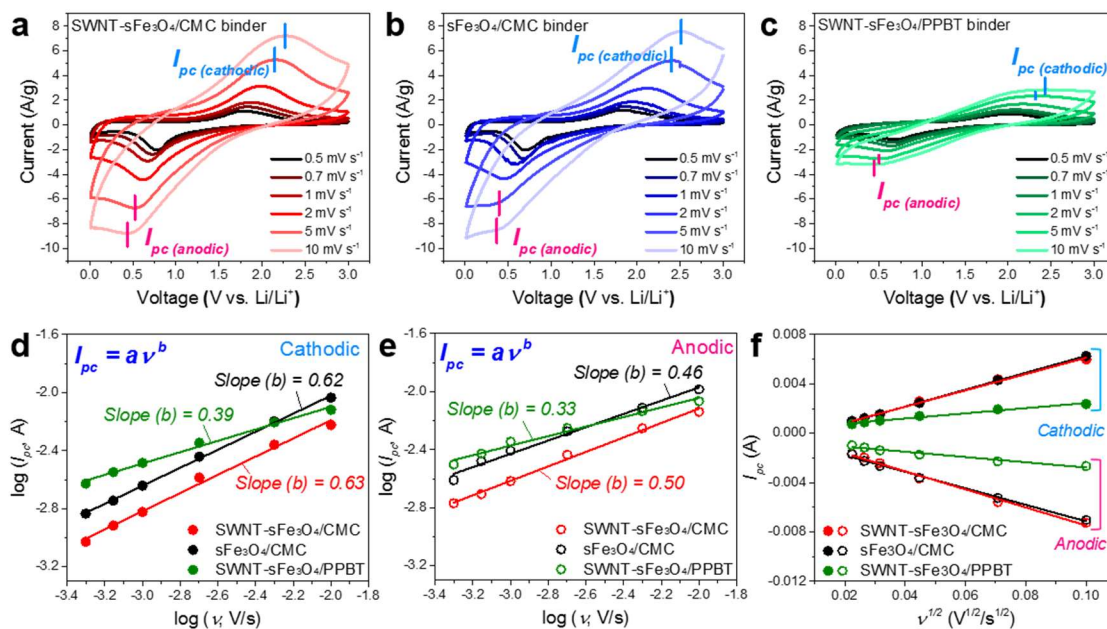


**Figure 5.4.** Electrode kinetics interpretation. Cyclic voltammetry (CV) profiles with various scan rates ( $v$ ) of the electrodes based on (a) SWNT-sFe<sub>3</sub>O<sub>4</sub> with CMC binder, (b) sFe<sub>3</sub>O<sub>4</sub> with CMC binder, and (c) SWNT-sFe<sub>3</sub>O<sub>4</sub> with PPBT binder. (d, e) Plots of log( $I_{pc}$ ) vs log( $v$ ), which were plotted from the results of cathodic peak currents and anodic peak currents of CV curves with different scan rates ( $v$ ), respectively. (f)  $I_{pc}$  vs  $v^{1/2}$  plots, where slopes are the apparent diffusion coefficient (cm<sup>2</sup> s<sup>-1</sup>).

**Table 5.1.** Electrochemical kinetic parameters obtained from CV analysis with various scan rates: transfer coefficient ( $\alpha$ ) and apparent lithium-ion diffusion coefficient ( $D_{Li}$ ).

	$\alpha$	$D_{Li}$ (cathodic) [ $\text{cm}^2 \text{s}^{-1}$ ]	$D_{Li}$ (anodic) [ $\text{cm}^2 \text{s}^{-1}$ ]
SWNT-sFe <sub>3</sub> O <sub>4</sub> /CMC binder	0.012	$2.11 \times 10^{-9}$	$2.57 \times 10^{-9}$
sFe <sub>3</sub> O <sub>4</sub> /CMC binder	0.010	$2.88 \times 10^{-9}$	$2.75 \times 10^{-9}$
SWNT-sFe <sub>3</sub> O <sub>4</sub> /PPBT binder	0.014	$1.69 \times 10^{-11}$	$1.73 \times 10^{-11}$

Figure 5.4d and 5.4e summarizes the fitting results to equation (1) for cathodic and anodic peak currents, respectively. All  $b$  values appeared close to 0.5, which indicates that the kinetics follow the diffusion-limited redox reaction. The SWNT-sFe<sub>3</sub>O<sub>4</sub>/CMC electrode exhibited a slightly larger value of  $b$  than the control sFe<sub>3</sub>O<sub>4</sub>/CMC electrode, suggesting that SWNT anchoring to the active material through PPBT  $\pi$ - $\pi$  interactions and carboxylate bonds enabled enhanced kinetics. Surprisingly, the SWNT-sFe<sub>3</sub>O<sub>4</sub>/PPBT electrode exhibited a very low  $b$  value,  $\sim 0.3$ – $0.4$ , possibly due to sluggish electrode kinetics. Moreover, as shown in Figure 5.4f and Table 5.1, the apparent lithium-ion (Li-ion) diffusion coefficient ( $D_{Li}$ ) for the SWNT-sFe<sub>3</sub>O<sub>4</sub>/PPBT electrode is much lower than that for the other systems, providing insight into the origins of poor battery performance, specifically cycle life and rate capability.

The apparent Li-ion diffusion coefficient was estimated by using the results from Figure 5.4a–c and considering the irreversible system using the following equations<sup>129, 159–</sup>

161

$$I_{PC} = (2.69 \times 10^5)(\alpha n)^{1/2} A \Delta C_{Li} D_{Li}^{1/2} \nu^{1/2} \quad (2)$$

$$|E_p - E^0| = \left(\frac{RT}{\alpha n F}\right) \left\{ 0.780 + \ln\left(\frac{D_{Li}^{1/2}}{k^0}\right) + \ln\left(\frac{\alpha n F v}{RT}\right)^{1/2} \right\} \quad (3)$$

where  $E_p$  is the peak potential and  $E^0$  is the formal potential. The values of  $|E_p - E^0|$  were calculated as half of the difference between the peak potential values at the anodic and cathodic sides,  $\alpha$  is the transfer coefficient,  $n$  is the number of electrons in the charge-transfer step ( $n = 8$  for  $\text{Fe}_3\text{O}_4$ ),  $F$  is the Faraday constant,  $R$  is the gas constant,  $T$  is the absolute temperature,  $D_{Li}$  is the apparent Li-ion diffusion coefficient ( $\text{cm}^2 \text{s}^{-1}$ ) in  $\text{Fe}_3\text{O}_4$  at 298 K,  $k^0$  is the standard rate constant,  $v$  is the scan rate ( $\text{V s}^{-1}$ ),  $I_{pc}$  is the peak current (A),  $A$  is the surface area of the electrode ( $\text{cm}^2$ ), and  $\Delta C_{Li}$  is the concentration of lithium ions ( $\Delta C_{Li} = 2.25 \times 10^{-2} \text{ mol cm}^{-3}$ ).<sup>160</sup> The values of the apparent Li-ion diffusion coefficient ( $D_{Li}$ ) can be obtained from the slope of the plot where the peak current ( $I_{pc}$ ) is in linear response to the square root of the scan rate ( $v^{1/2}$ ) with the knowledge of  $\alpha$  derived from equation (3) using the plot of  $|E_p - E^0|$  vs  $\ln(v)$ . The results are summarized in Figure 5.4f and Table 1.

The calculated average cathodic and anodic diffusion coefficients for the SWNT-s $\text{Fe}_3\text{O}_4$ /CMC electrode were  $2.11 \times 10^{-9}$  and  $2.57 \times 10^{-9} \text{ cm}^2 \text{s}^{-1}$ , respectively, which are very similar to those found for the s $\text{Fe}_3\text{O}_4$ /CMC control ( $D_{Li}$  (cathodic) =  $2.88 \times 10^{-9}$  and  $D_{Li}$  (anodic) =  $2.75 \times 10^{-9} \text{ cm}^2 \text{s}^{-1}$ ).  $D_{Li}$ 's for the SWNT-s $\text{Fe}_3\text{O}_4$ /PPBT counterpart are about 150 times lower: the average cathodic and anodic diffusion coefficients were  $1.69 \times 10^{-11}$  and  $1.73 \times 10^{-11} \text{ cm}^2 \text{s}^{-1}$ , respectively. The CV and electrode kinetics studies revealed that the SWNT-s $\text{Fe}_3\text{O}_4$ /PPBT binder-based electrodes suffered inferior electrochemical performance due to slow lithium ion diffusion within the whole electrode and resultant sluggish kinetics. Conceivably, the high affinity of PPBT to the carbon surface of SWNTs anchored onto s $\text{Fe}_3\text{O}_4$  leads to the full coverage of the active particle surface by the

conjugated polymer binder. Consequently, lithium ion transport into electroactive sites may be blocked, thereby negatively influencing Li-ion diffusivity and electrode kinetics. Note that the density of the unpressed electrode fabricated with CMC as the binder was  $0.50 \text{ g cm}^{-3}$ , whereas in the presence of PPBT binder, the density was almost twice as high ( $0.95 \text{ g cm}^{-3}$ ). Presumably, the high electrode density results from strong interactions between PPBT and SWNT-sFe<sub>3</sub>O<sub>4</sub> electrode active materials. Thus, the positive effect of PPBT likely derives from its ability to both interact with SWNTs through its conjugated backbone and then serve to anchor the nanotubes to the active material surface *via* carboxylate linkages — features that very positively impacted electrode structural and electrical stability, while electrode kinetics were only modestly affected (PPBT anchored SWNTs exhibited slightly improved kinetics when CMC was used as the binder). These aspects very effectively led to the observed suppressed volume change, stable SEI layer formation, and reduced electrode resistance *vs* control electrodes, thereby significantly improving battery performance.

### 5.3.3 SWNT-Anchored Si NPs with Carboxylated Polythiophene (PPBT) Links.

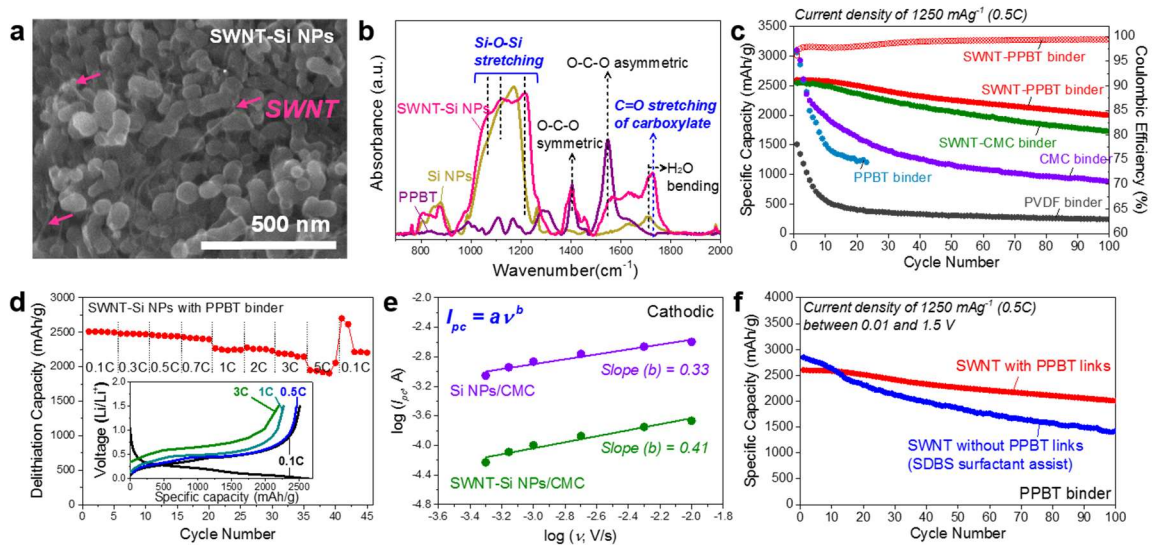


**Figure 5.5.** SWNT-anchored Si NPs with carboxylated polythiophene (PPBT) links. (a) SEM images of SWNT-Si NPs. (b) FT-IR spectra of PPBT, Si NPs, and SWNT-Si NPs. (c) Cycling performance (=capacity retention as a function of cycle number) collected at the current density of  $1250 \text{ mA g}^{-1}$  (0.5 C) between 0.01 and 1.5 V (open circle: Coulombic efficiency of SWNT-Si NPs with PPBT binder). (d) Galvanostatic charge-discharge profiles with different delithiation rates of SWNT-Si NPs with PPBT binder in the potential window of 0.01 to 1.5 V vs Li/Li<sup>+</sup>. Inset presents charge-discharge profiles. (e) Plots of  $\log(I_{pc})$  vs  $\log(v)$ , which were plotted from the results of cathodic peak currents of CV curves with different scan rates ( $v$ ). (f) Cycling performance at the current density of  $1250 \text{ mA g}^{-1}$  (0.5 C) between 0.01 and 1.5 V. The electrode comprising SWNT anchoring on the Si NPs surface with PPBT carboxylate linkages was compared with that of SWNT introduction with no PPBT linkages (prepared by SDBS surfactant). The tested electrodes were fabricated with PPBT binder.

Given the promising results obtained for SWNT-sFe<sub>3</sub>O<sub>4</sub> electrodes, the concept was expanded to alternate high capacity active materials. Using Si nanoparticles (Si NPs), we demonstrated that PPBT could also effectively anchor SWNTs to Si NP surfaces and enable the fabrication of highly stable Si anodes for high-capacity Li-ion battery applications. The well-dispersed/connected morphology of the Si NPs anchored to the SWNTs is presented in the SEM image of Figure 5.5a, and the presence of PPBT carboxylate bonds linking Si NPs to SWNT surfaces was confirmed through FT-IR investigations (Figure 5.5b). SWNT-Si NPs exhibited a broad Si–O–Si stretching vibration at  $\sim 1000\text{--}1240 \text{ cm}^{-1}$ ,<sup>162</sup> which represents a peak shift and change in intensity relative to pure Si NPs and indicates the creation of new chemical bonds. Peaks at  $1547 \text{ cm}^{-1}$  and  $1404 \text{ cm}^{-1}$  associated with the PPBT carboxylate group correspond respectively to O–C–O asymmetric and symmetric stretching. A newly observed strong peak at  $1726 \text{ cm}^{-1}$  is assigned to a C=O stretch, and is indicative carboxylate bond formation.<sup>139,151,152</sup> Additionally, XPS spectra (Figure 5.6) support the presence of chemical interactions between PPBT and the Si NPs surface.

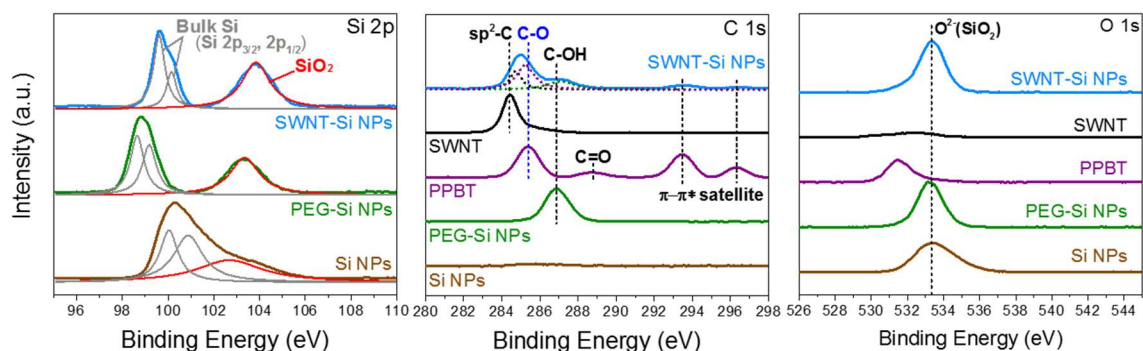


**Figure 5.6.** XPS spectra of SWNT-anchored Si NPs with carboxylated polythiophene (PPBT) links. In the high-energy resolved XPS spectrum of Si 2p core-level spectrum, Si NPs displays the deconvolution of Si 2p peak: first two peaks at ~100 eV (composed of 2p<sub>3/2</sub> and 2p<sub>1/2</sub> due to spin-orbit coupling) assigned to bulk silicon (gray line) and a peak at 102.7 eV assigned to surface oxide SiO<sub>2</sub> (red line).<sup>163</sup> The chemical shift to lower binding energy of the bulk Si peaks reflects an increase in interatomic distance which results from additional bonding between PPBT and bulk Si surface. The C 1s peak of SWNT-Si NPs at 285.22 eV is indicative of carbon atoms associated with the C-O bond of PPBT, shifted to lower binding energy from a peak at 285.38 eV. Those peak shifts substantiate the presence of chemical interaction between PPBT carboxylic moieties and hydroxyl surface of bulk Si. No change in O 1s peaks at 533.3 eV with respect to SiO<sub>2</sub><sup>163</sup> further provides evidence that the formation of carboxylate bonds would be involved in hydroxyl species on the bulk Si surfaces.

Coin-type half cells were fabricated to evaluate the electrochemical performance of Si NPs-based electrodes anchored to SWNTs using PPBT. The half cells were fabricated with a Li metal counter electrode, 1.2 M LiPF<sub>6</sub> in EC/DEC (1/1 by volume) with 10 wt % FEC electrolyte, and a Si NPs mass loading of ~0.8–1.9 mg cm<sup>-2</sup>. The optimal composition of Si-based electrode materials was determined by evaluating the performance of electrodes fabricated with different weight ratios of SWNT-Si NPs and carbon black (CB) while fixing the PPBT binder component at 14 wt %. The effective weight ratio of Si NPs, CB, and PPBT was 52:34:14 (Figure 5.7a, b); and 10 wt % of SWNT per Si NPs weight

was observed to be the optimal ratio of SWNTs anchored to the Si NPs surface using PPBT links for improved battery performance (Figure 5.7c).

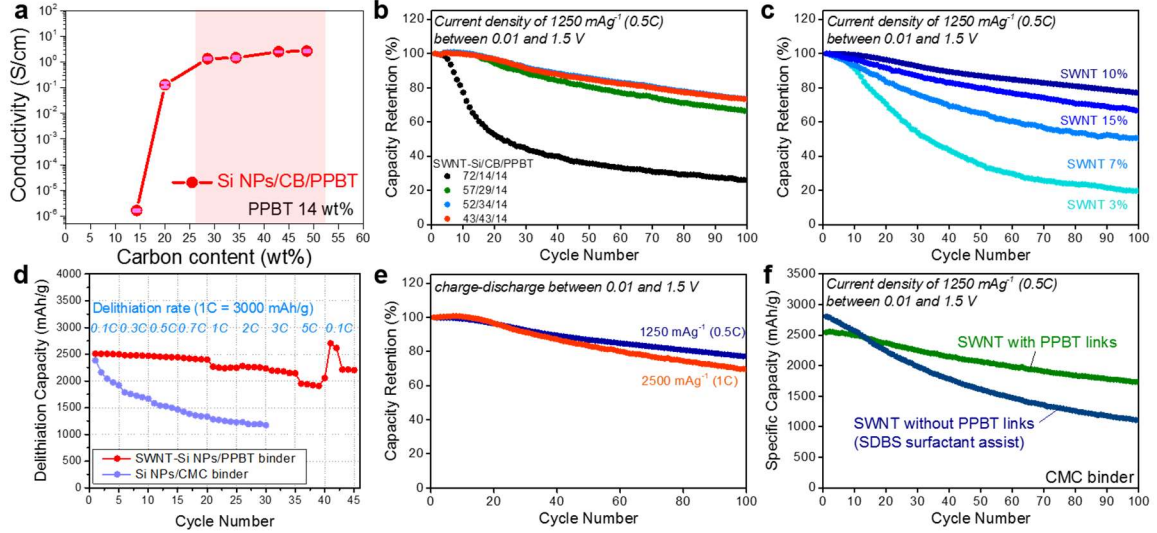


**Figure 5.7.** Electrochemical characterization of SWNT-anchored Si NPs with carboxylated polythiophene (PPBT) links. (a) Electronic conductivity of the electrodes composed of Si NPs, carbon black (CB), and PPBT binder. The amount of PPBT binder was fixed at 14 wt % and the electrodes were prepared according to different weight ratio of Si NPs and CB. (b, c) Cycling performance at the current density of  $1250 \text{ mA g}^{-1}$  (0.5C) between 0.01 and 1.5 V, investigating the optimum composition of electrode materials (SWNT-Si NPs/CB/PPBT = 52/34/14 wt%) and SWNT coating amount (10 wt%) realizing better cycling performance. (d) Galvanostatic charge-discharge profiles with different delithiation rates of SWNT-Si NPs with PPBT binder vs Si NPs with CMC binder in the potential window of 0.01 to 3 V vs Li/Li<sup>+</sup>. Si NPs with CMC binder was used as the reference electrode, since the as-prepared electrode of Si NPs with PPBT binder showed poor adhesive and inferior surface. (e) Cycling performance with different charge-discharge rate conditions (0.5C vs 1C). (f) Effect of PPBT linkages for SWNT anchoring on Si NP surfaces. SWNT introduction with no PPBT linkages was prepared by sodium dodecylbenzenesulfonate (SDBS) surfactant instead of carboxylate bearing PPBT component. The electrodes were fabricated using CMC polymeric binder.

Examination of Figure 5.5c demonstrates that the SWNT-Si NPs electrode exhibited far better cycling performance at 0.5 C ( $1250 \text{ mA g}^{-1}$ ) than its pure Si NPs



counterpart. Further, distinct from the magnetite case, the PPBT binder facilitated significantly improved cycling. Since Si undergoes a much larger volume change (420 %) during Li-ion insertion, it is conceivable that volume change is sufficient to disrupt the PPBT binder surrounding the Si NPs, leading to the creation of passageways that facilitate ion transport into the electroactive material. The electrode comprised of SWNT-Si NPs and PPBT binder exhibited reduced reversible capacity of 2604 mAh g<sup>-1</sup> and decreased initial efficiency of 77.0% during pre-cycling at 0.1 C (30 mA g<sup>-1</sup>), which is due to the large irreversible electrochemistry associated with the SWNT component. Under the same conditions, the Si NPs-CMC binder control electrode presented a reversible capacity of 3357 mAh g<sup>-1</sup> and initial efficiency of 85.6%. Nevertheless, the approach using PPBT to anchor SWNTs to the active material benefited the electrochemistry of the Si-based electrodes. The SWNT-Si NPs/PPBT binder-based electrode with an initial capacity of 2600 mAh g<sup>-1</sup> preserved 2003 mAh g<sup>-1</sup> after 100 cycles, corresponding to 77.0% capacity retention; whereas the initial capacity of the control electrode was 3108 mAh g<sup>-1</sup> faded to only 887 mAh g<sup>-1</sup> after 100 cycles (28.5% capacity retention). Top-view SEM images of the electrodes after cycling (Figure 5.8) are consistent with the cycling results. Due to the inferior surface of the Si NPs/PPBT electrode, CMC binder-based electrodes were characterized after cycling. While the Si NPs/CMC electrode suffered from the growth of thick SEI layers with cracked surfaces, the SWNT-Si NPs/CMC electrode experienced less SEI layer formation and the resultant electrode surface appeared less cracked. In other words, the former is highly susceptible to volume changes during repeated charge-discharge cycles, while the latter is much more stable. This observation suggests that PPBT facilitated anchoring of SWNTs to the Si NP surface may provide for effective connectivity

between cracked/pulverized particles, leading to improved electrode stability and relatively stable SEI layer formation. In addition, the SWNT-Si NPs/PPBT system exhibited significantly enhanced rate capability (Figure 5.5d and Figure 5.7d).

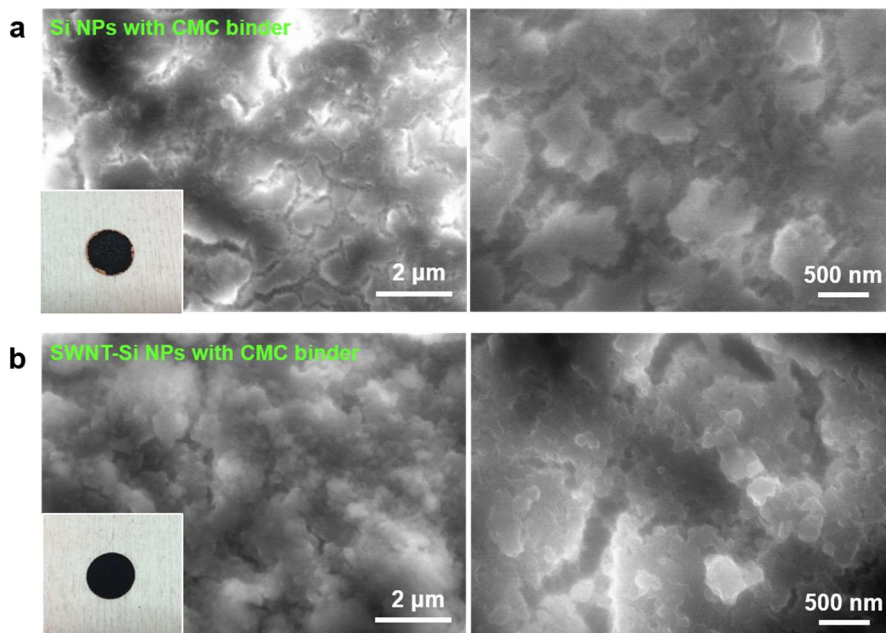


**Figure 5.8.** SEM images of the surface-view of the electrodes (after 100 cycles) composed of (a) Si NPs with CMC binder, and (b) SWNT-Si NPs with CMC binder. The electrode composed of Si NPs prepared by SWNT anchoring with PPBT carboxylate linkages presents less SEI layer formation, which indicates that SWNT introduction with PPBT links probably contributes to electrode stability that may enable capture pulverized/cracked particles, consequently favorable to forming stable SEI layer.

Examination of electrode kinetics can provide further insight into electrode performance characteristics. As depicted in Figure 5.5e, the calculated value of  $b$  for a SWNT-Si NPs electrode fabricated with CMC as the binder is 0.41 vs only 0.33 for pure Si NPs in CMC: note a larger  $b$  value indicates faster electrode kinetics. In addition, PPBT facilitated SWNT anchoring to the Si NPs surface played a critical role. When the SWNTs were dispersed using an aqueous solution of the well-known surfactant, sodium

dodecylbenzensulfonate (SDBS) rather than aqueous PPBT, the resultant SWNT-Si NPs (SDBS) electrode with no PPBT anchoring exhibited much faster cycling degradation (Figure 5.5f). This result emphasizes the importance of PPBT anchoring the SWNTs to the Si NPs' hydroxyl surface, which may be the predominant contributor to stable electrical connection and electrode robustness.

#### 5.3.4 SWNT-Anchored $c\text{-SiO}_x$ with Carboxylated Polythiophene (PPBT) Links.

For further demonstrate the advantages and broad applicability of anchoring SWNTs to the surface of active materials *via* PPBT linkages, their impact on carbon-coated silicon monoxide ( $c\text{-SiO}_x$ ,  $x \approx 1$ ) based electrodes was evaluated. Silicon monoxide has captured the interest of industry and has been recently adopted because of its relatively low volume expansion ( $\sim 200\%$ ) originating from structural characteristics –  $\text{SiO}_y$  ( $y \approx 2$ ) background matrix can buffer the volume expansion of embedded Si nanodomains.<sup>154,164</sup>  $\text{SiO}_x$  particles, however, have low electronic conductivity, with low cycling efficiency and large irreversible capacity due to the formation of fatal irreversible products ( $\text{Li}_2\text{O}$  and  $\text{Li}_4\text{SiO}_4$ ) affecting  $\text{Li}^+$  loss. Thus, surface carbon-coating layers, which lead to fewer side reactions with electrolytes and high capacity retention during electrochemical cycling, are required.<sup>164–167</sup> Nevertheless, such approaches introducing amorphous carbon layers that are not elastic but rather subjected to fracture<sup>168</sup> and resultant breakdown of electrical passages during lithiation process, continue to present significant challenges. To suppress the breakage of electrical pathways resulting from the pulverized particles during charging/discharging, we introduce the use of a carboxylated polythiophene linker to securely construct single-walled carbon nanotube (SWNT) electrical networks onto the

surface of the carbon-coated silicon monoxide (denoted as c-SiO<sub>x</sub>), ensuring the electrical and structural stability of the silicon monoxide electrode (Figure 5.9).

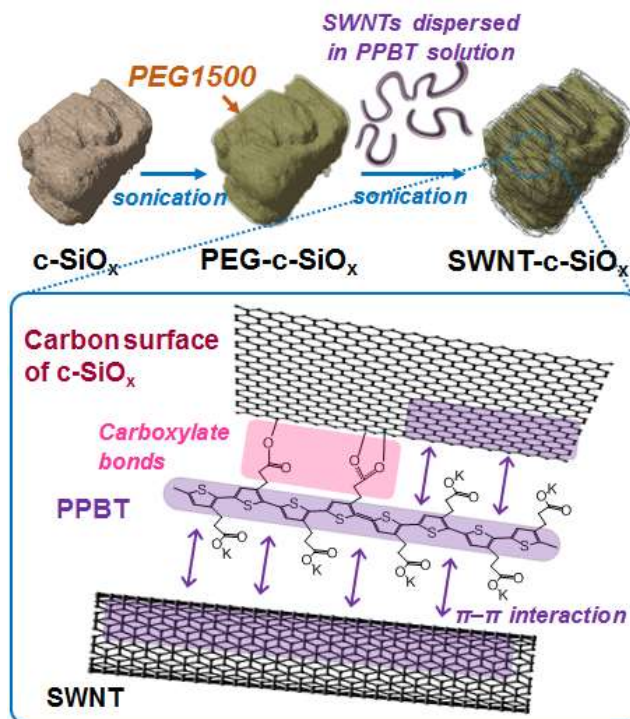


**Figure 5.9.** Proposed schematic illustration of the preparation of the c-SiO<sub>x</sub> comprising SWNT electrical networks with PPBT links. Carboxylate bonds between hydroxylated active particle and PPBT carboxyl substituent, and  $\pi$ - $\pi$  interactions between SWNT/c-SiO<sub>x</sub>'s carbon surface and PPBT conjugated backbone, provide for stable electrical linkages.

Carbon-coated SiO<sub>x</sub> which retains a small portion of -OH on the carbon surface, naturally oxidized, can be modified with SWNTs through the formation of carboxylate bonds with the PPBT component. Figure 5.10a displays successful preparation of SWNT-c-SiO<sub>x</sub> active particles and XPS analysis (Figure 5.10b) confirms the generation of carboxylate bonds connecting SWNTs to c-SiO<sub>x</sub> surfaces through corresponding peak shifts associated with C-O and C=O bonds of PPBT.<sup>139,151,152</sup> In detail, the C 1s peak of

SWNT-c-SiO<sub>x</sub> at 285.05 eV indicates the C-O bond of PPBT; note the shift from the corresponding PPBT peak at 285.38 eV to lower binding energy. O 1s spectrum of SWNT-c-SiO<sub>x</sub> exhibited a peak at 531.27 eV for C=O which was also slightly shifted to lower binding energy from the PPBT C=O bond at 531.44 eV. The observed peak shifts confirm the development of chemical interactions between the PPBT carboxylate substituent and hydroxylated c-SiO<sub>x</sub>. A broad peak at the binding energy of ~532.3 eV that corresponds to hydroxyl species<sup>169</sup> on the carbon-coated SiO<sub>x</sub> surface confirms the presence of surface –OH species on c-SiO<sub>x</sub> that would be engaged in the carboxylate bonding.

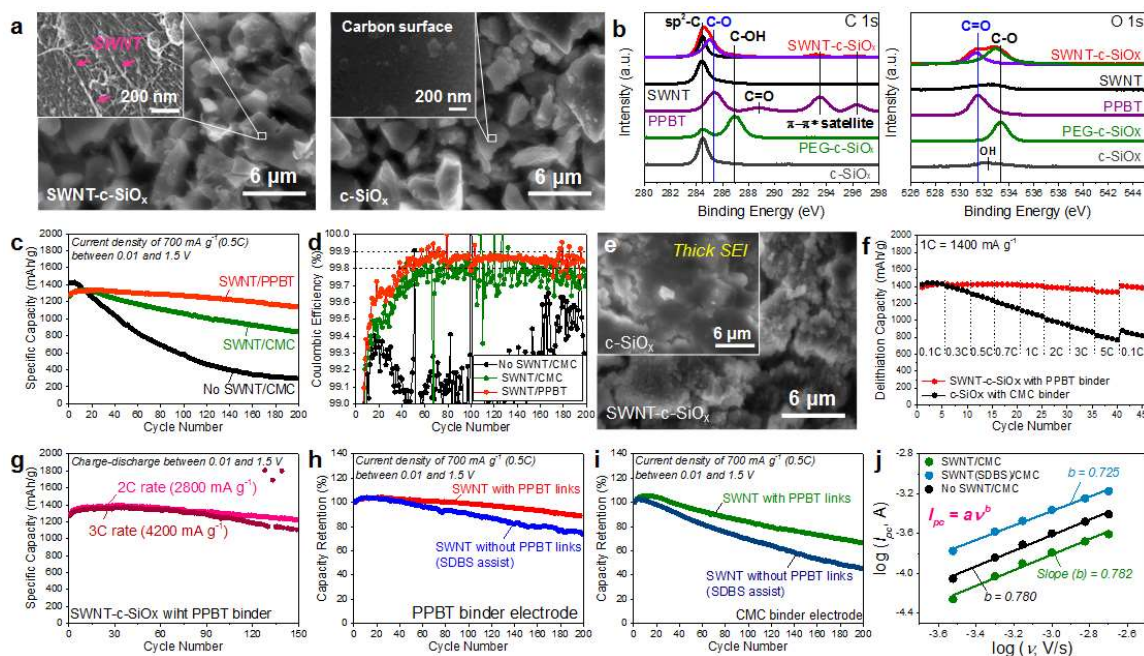


**Figure 5.10.** SWNT-c-SiO<sub>x</sub> with carboxylated polythiophene (PPBT) links. (a) SEM images of SWNT-c-SiO<sub>x</sub> particles vs c-SiO<sub>x</sub> counterpart. (b) XPS spectra of c-SiO<sub>x</sub>, PEG-c-SiO<sub>x</sub>, PPBT, SWNT and SWNT-c-SiO<sub>x</sub>. (c) Cycling performance (=capacity retention as a function of cycle number) collected at the current density of 700 mA g<sup>-1</sup> (0.5 C) between 0.01 and 1.5 V, and (d) corresponding Coulombic efficiency. (e) Surface view SEM images of the electrode with c-SiO<sub>x</sub> (inset) and SWNT-c-SiO<sub>x</sub> active particles after 200 cycles. (f) Delithiation rate capability, where cells were lithiated at a constant current density of 140 mA g<sup>-1</sup> (0.1 C) and delithiated at different current densities between 0.01 and 1.5 V. (g) Cycling performance of the electrode composed of SWNT-c-SiO<sub>x</sub> and PPBT binder with

different charge-discharge rate conditions (2 C vs 3 C). (h–j) Effect of carboxylated polythiophene (PPBT) links: Cycling performance of (h) PPBT binder- and (i) CMC binder-based electrodes at a current density of 700 mA g<sup>-1</sup> (0.5 C) between 0.01 and 1.5 V. The electrode comprising SWNT networks on the c-SiO<sub>x</sub> surface with PPBT linkages was compared with that of SWNT introduction with no PPBT linkages (prepared by SDBS surfactant). (j) Plots of log ( $I_{pc}$ ) vs log ( $v$ ), which were plotted from the results of cathodic peak currents of CV curves with different scan rates ( $v$ ).

Coin-type half cells were fabricated to evaluate electrochemical performance. The half cells were fabricated with a Li metal counter electrode, 1.2 M LiPF<sub>6</sub> in EC/DEC (1/1 by volume) with 10 wt % FEC electrolyte. Each electrode consisted of active materials, carbon black (CB), and binder in a mass ratio of 52:34:14. The c-SiO<sub>x</sub> mass loading of as-prepared electrodes was typically ~1.3–2.0 mg cm<sup>-2</sup>.

The introduction of SWNTs with PPBT links improved electrode performance and the PPBT binder brought along the synergistic effects on much enhanced electrochemical characteristics, although SWNTs caused a decrease in initial efficiency. Whereas the initial efficiency of the c-SiO<sub>x</sub>/CMC binder system was 72%, that of the SWNT-c-SiO<sub>x</sub>/CMC and SWNT-c-SiO<sub>x</sub>/PPBT binder electrodes were 66 % and 65 %, respectively. Nonetheless, the cycling stability and corresponding Coulombic efficiency was much improved (Figure 5.10c, d): SWNT-c-SiO<sub>x</sub>/PPBT binder > SWNT-c-SiO<sub>x</sub>/CMC binder > c-SiO<sub>x</sub>/CMC binder. After 200 cycles, the reversible capacity of the SWNT-c-SiO<sub>x</sub>/PPBT binder electrode changed from 1284 mAh g<sup>-1</sup> at the 1st cycle to 1137 mAh g<sup>-1</sup> at 200 cycles, leading to a far better capacity retention of 88.6 % (SWNT-c-SiO<sub>x</sub>/CMC binder and c-SiO<sub>x</sub>/CMC binder electrodes retained only 66.5 % and 21.0 % of their initial capacity after 200 cycles, respectively). Importantly, Coulombic efficiency of the SWNT-c-SiO<sub>x</sub>/PPBT system, close to ~99.8–99.9%, appeared pronounced, which might be attributed to the



beneficial effects of stable SWNT networks securely connected onto the electroactive particles being able to capture pulverized c-SiO<sub>x</sub> particles and suppress volume changes, resulting in stable, thin SEI layer formation and excellent electrode integrity (Figure 5.10e). Besides, the rate capability of electrode based on SWNT-c-SiO<sub>x</sub> and PPBT binder appeared very stable even at the high rate condition of 5C (7000 mA g<sup>-1</sup>) (Figure 5.10f). At the high charge-discharge rates of 2C (2800 mA g<sup>-1</sup>) and 3C (4200 mA g<sup>-1</sup>), as shown in Figure 5.10g, the SWNT-c-SiO<sub>x</sub>/PPBT electrodes presented cycling stability, even with similar capacity with that of 0.5C (700 mA g<sup>-1</sup>) charge-discharge condition.

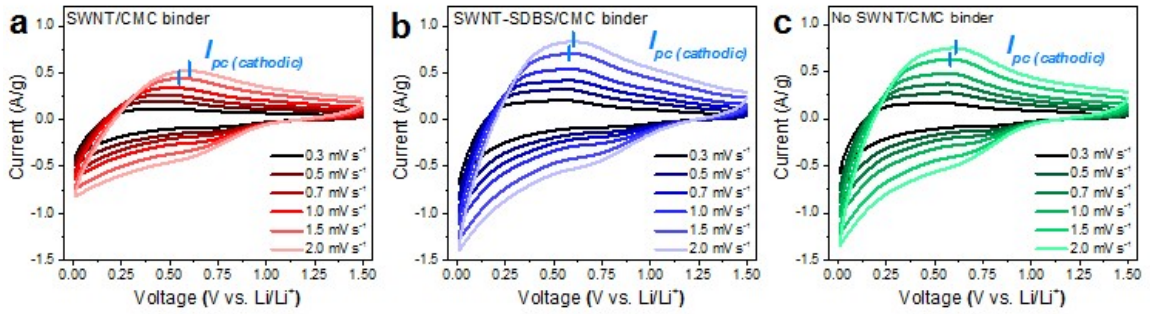


**Figure 5.11.** CV profiles with various scan rates ( $v$ ) of the CMC binder-based electrodes based on (a) SWNT-c-SiO<sub>x</sub>, (b) SWNT-c-SiO<sub>x</sub> (prepared by SDBS surfactant), and (c) c-SiO<sub>x</sub>.

In addition, the effect of PPBT linking SWNT to the c-SiO<sub>x</sub> surface played a critical role: When the SWNTs were dispersed in an aqueous solution using SDBS surfactant instead of aqueous PPBT solution, the resultant electrode comprising SWNT networks with no PPBT links showed much rapid cycle fading (Figure 5.10h, i). Figure 5.10j summarizes the fitting results for cathodic peak currents observed in the CV profiles (Figure 5.11) to investigate electrode reaction kinetics: note that a higher  $b$  value indicates faster kinetics. The CMC binder-based electrodes were characterized to minimize binder

effect and maximize the effect of SWNT integration combined with PPBT electrical linkages. The SWNT-c-SiO<sub>x</sub> with PPBT links electrode ( $b = 0.782$ ) presented a slightly larger value of  $b$  than that of the control c-SiO<sub>x</sub> electrode ( $b = 0.780$ ), but much improved  $b$  value than that of SWNT-c-SiO<sub>x</sub> (SDBS) with no PPBT links counterpart ( $b = 0.725$ ), substantiating that SWNT networks connecting to the active material through incorporation of PPBT  $\pi$ - $\pi$  interactions and carboxylate bonds enabled enhanced kinetics.

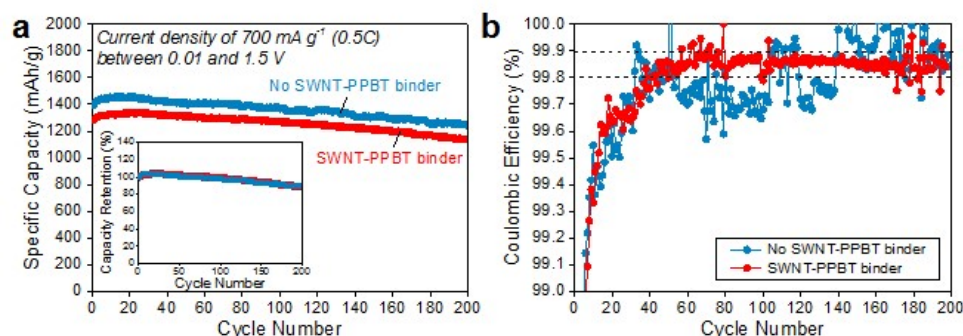


**Figure 5.12.** Electrochemical evaluation of the electrode comprising c-SiO<sub>x</sub> and PPBT binder. (a) Cycle performance at 700 mA g<sup>-1</sup> (0.5C) between 0.01 and 1.5 V. (b) Corresponding Coulombic efficiency, reflecting SWNT integrated system more stable despite their similar electrochemical performance

Notably, high-capacity energy materials tend to critically depend on polymeric binders to allow for electrode stability.<sup>23,24,127,148</sup> Similarly, using PPBT as a binder also improved the cyclability of c-SiO<sub>x</sub>, almost to the level of the SWNT-c-SiO<sub>x</sub> system (Figure 5.12a), most likely due to the carbon coating, which might be analogous to SWNT networks enabling electrical continuity and the PPBT binder providing electrode stability sufficient to seize pulverized particles. Seemingly, the benefit of SWNT networks would be negligible, unless its Coulombic efficiency appeared more stable (Figure 5.12b). Nevertheless, the approach using SWNT electrical networks with PPBT linkages allows



significant improvements when the practical implementation utilizing an electrode system blended with graphite and adopting only a small amount of binding materials, less than 3 wt% of sodium carboxymethyl cellulose (CMC) and styrene butadiene rubber (SBR), is taken into account.

### 5.3.5 SWNT-Anchored *c*-SiO<sub>x</sub> and Graphite Blended Electrode System.

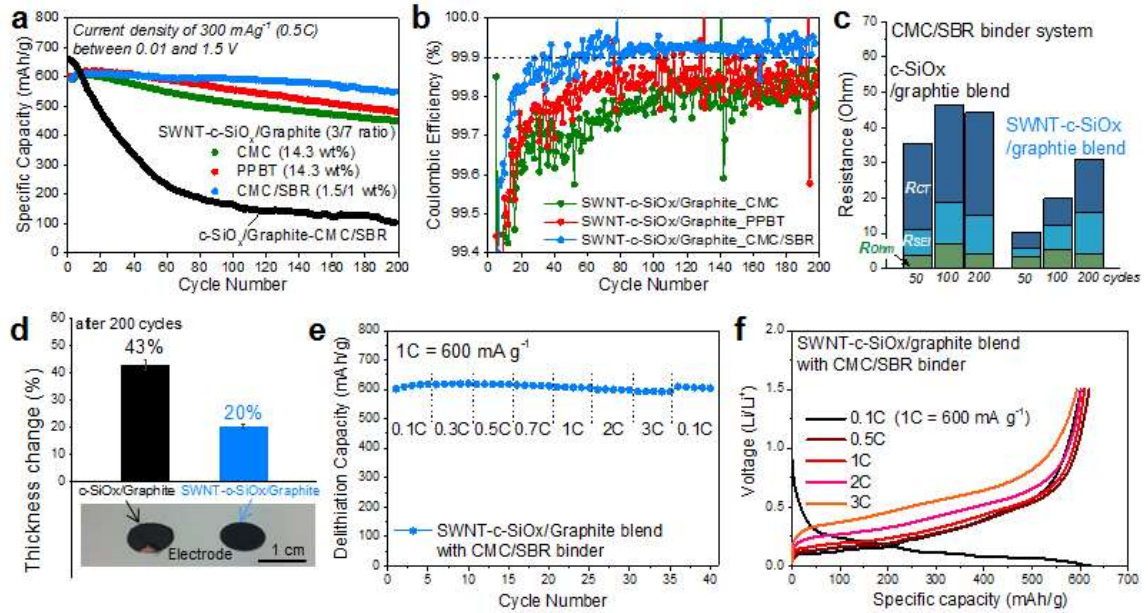


**Figure 5.13.** SWNT-*c*-SiO<sub>x</sub> and graphite blended system (in a mass ratio of 30:70). (a) Cycling performance (=capacity retention as a function of cycle number) collected at the current density of 300 mA g<sup>-1</sup> (0.5 C) between 0.01 and 1.5 V, and (b) corresponding Coulombic efficiency. (c) Variation of electrode internal resistances (*R*<sub>ohm</sub>, *R*<sub>SEI</sub>, *R*<sub>CT</sub>) after cycling, fitted by EIS results. EIS characterization was conducted at open-circuit voltage (OCV) after 50, 100, and 200 cycles. (d) Thickness change of electrodes based on the CMC/SBR binder after 200 cycles. Inset image exhibits corresponding respective electrode. (e) Delithiation rate capability, where cells were lithiated at a constant current density of 60 mA g<sup>-1</sup> (0.1 C) and delithiated at different current densities between 0.01 and 1.5 V. (f) Charge-discharge profiles according to various rate conditions in the potential window of 0.01 to 1.5 V vs Li/Li<sup>+</sup>.

The electrode comprising SWNT-*c*-SiO<sub>x</sub> and graphite blend (in a mass ratio of 30:70) with the CMC/SBR binder provided unprecedented advances in the electrochemical

performance including enhanced cycle life (Figure 5.13a), high Coulombic efficiency over 99.9 % close to that of graphite-based electrode (Figure 5.13b), and superior rate capability (Figure 5.13e, f). In case of the CMC and PPBT binder systems, each electrode comprised active material, CB, and binder in a mass ratio of 52:34:14. When fabricating CMC/SBR binder-based electrodes, active material, CB, CMC, and SBR were 95.8:1.7:1.5:1 in a mass ratio.<sup>154</sup> The active materials were prepared by blending SWNT-c-SiO<sub>x</sub> with graphite in a mass ratio of 30:70, the mass loading of which was ~5.8–8.9 mg cm<sup>-2</sup>.

Prior to a cycling test, coin-type half-cells comprising as-prepared electrodes were precycled at 0.1 C for the formation of SEI layers. The CMC/SBR binder electrode retained a higher initial efficiency. The CMC binder electrode with SWNT-c-SiO<sub>x</sub>/graphite blend had a reversible capacity of 578 mAh g<sup>-1</sup> with an initial efficiency of 72.3 %, while the PPBT binder based SWNT-c-SiO<sub>x</sub>/graphite blend electrode exhibited a reversible capacity of 609 mAh g<sup>-1</sup> with an initial efficiency of 68.7 %. CMC/SBR electrode fabricated with SWNT-c-SiO<sub>x</sub>/graphite blend retained a reversible capacity of 586 mAh g<sup>-1</sup> with an initial efficiency of 78.9 %, while when used with a c-SiO<sub>x</sub>/graphite blend had a reversible capacity of 650 mAh g<sup>-1</sup> with initial efficiency of 81.9 % (an electrode comprised of only graphite with CMC/SBR binder: 335 mAh g<sup>-1</sup> capacity, 88.8 % initial efficiency). With the half-cells cycled at 0.5 C (300 mA g<sup>-1</sup>) shown in Figure 5.13a and b, CMC/SBR binder electrode with SWNT-c-SiO<sub>x</sub>/graphite blend with the initial capacity of 592 mAh g<sup>-1</sup> preserved 549 mAh g<sup>-1</sup> after 200 cycles, showed 92.7 % capacity retention and 99.86 % average Coulombic efficiency. In contrast, when measured under the same conditions, CMC/SBR binder based electrode fabricated with the c-SiO<sub>x</sub>/graphite blend began to

rapidly lose its capacity from the first cycle and exhibited only 15.8 % of its initial capacity after 200 cycles, presenting poor average Coulombic efficiency of 99.03 % (Figure 5.14).

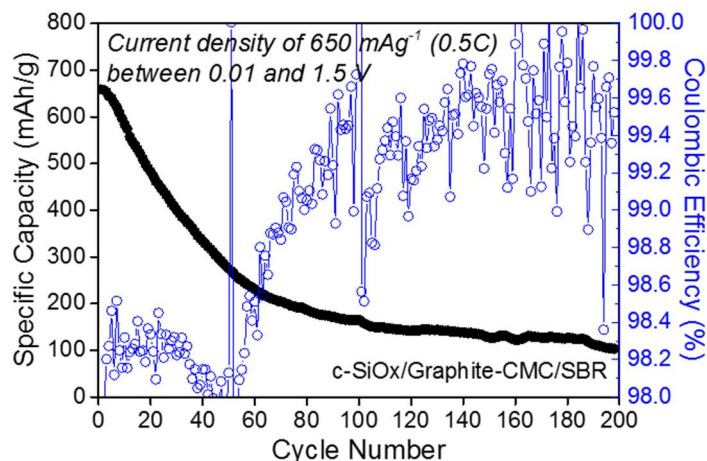


**Figure 5.14.** Cycle performance and Coulombic efficiency of c-SiO<sub>x</sub>/graphite blended electrode with CMC/SBR binder.

Surprisingly, when characterizing SWNT-c-SiO<sub>x</sub>/graphite blend-based electrodes, the cycling stability and Coulombic efficiency of the CMC/SBR binder system appeared much improved in comparison to the electrodes using either CMC or PPBT binders, in spite of using such a small amount of polymeric binder (< 3 wt %). Figure 5.13b demonstrates that the concept of introducing SWNT electrical networks stably connected onto the high-capacity active materials with PPBT linkages, led to a rapid increase of Coulombic efficiency of greater than 99.5 % after only 8 cycles including the first formation cycle. This is indicative of SWNT-c-SiO<sub>x</sub> benefitting from the mitigation of electrolyte decomposition, such as the formation of the SEI layer, presumably due to less area of lithium consumption.<sup>127,154</sup> Those results might be ascribed to SWNT electrical networks securely linked on the c-SiO<sub>x</sub> surface through PPBT linkages which might tightly

capture the pulverized particles, leading to reduced charge-transfer resistance (Figure 5.13c and Figure 5.15) and suppressed volume change of the SWNT-c-SiO<sub>x</sub> particle. The thickness change of the electrodes after 200 cycles was found to be only 20% for the CMC/SBR binder electrode with a SWNT-c-SiO<sub>x</sub>/graphite blend, whereas the c-SiO<sub>x</sub>/graphite blend counterpart underwent change in thickness of 43 % (Figure 5.13d).

Additionally, the advantageous effect of the SWNT electrical networks with PPBT links is also remarkable in rate capability experiments (Figure 5.13e, f). Under a constant lithiation current density of 60 mA g<sup>-1</sup> (0.1 C), CMC/SBR binder electrode with SWNT-c-SiO<sub>x</sub>/graphite blend exhibited almost no variation of delithiated capacity over a wide range of delithiation current densities (= 60–1800 mA g<sup>-1</sup>) at a voltage range of 0.01–1.5 V, which demonstrates its excellent rate capability performance.

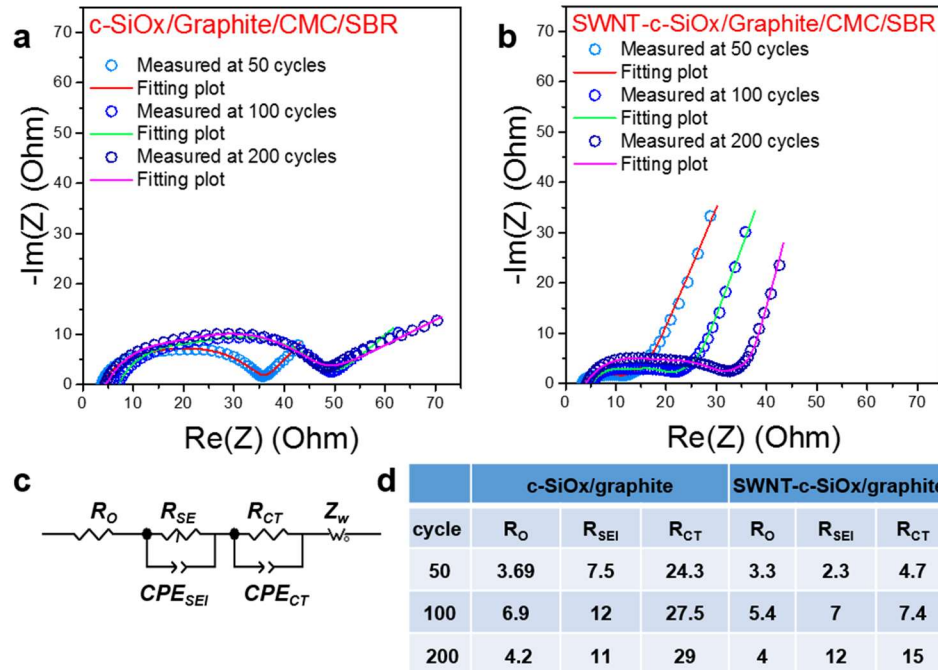


**Figure 5.15.** EIS fitting results of (a) c-SiO<sub>x</sub>/graphite (3/7) blend with CMC/SBR binder, and (b) SWNT-c-SiO<sub>x</sub>/graphite (3/7) blend with CMC/SBR binder. The impedance spectra measured at open-circuit voltage (OCV) in the frequency range from 1 MHz to 0.1 Hz. (c)

Equivalent circuit used to fit EIS data, and (d) results from fitting EIS with equivalent circuit.

### 5.3.6 Pouch-Type Full-Cell Evaluation

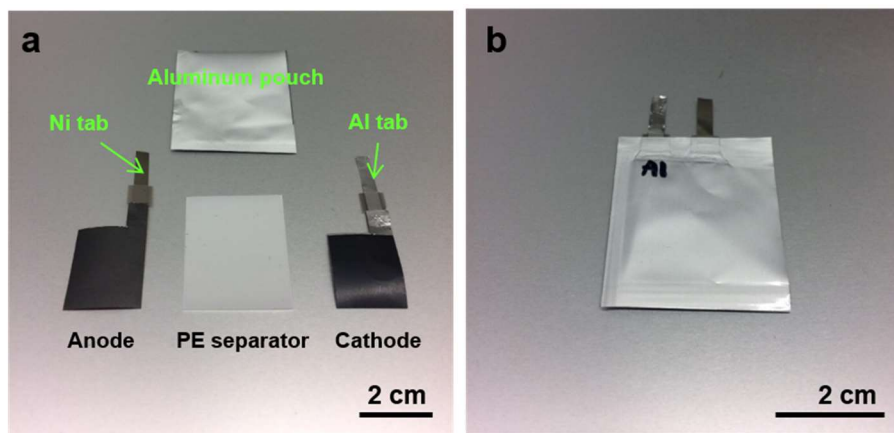


**Figure 5.16.** Aluminumized (Al) polymer pouch-type full cell. The cell is composed of a porous polyethylene (PE) separator.

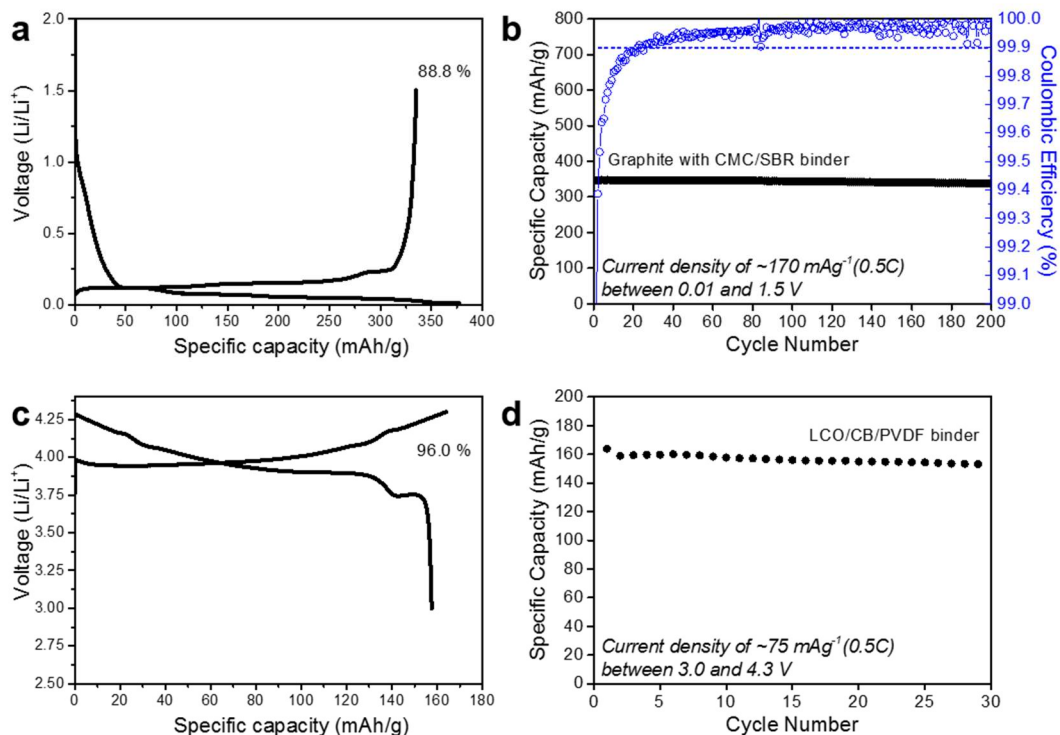


**Figure 5.17.** Coin half-cell results of graphite and LCO. (a) The initial charge-discharge

profiles of the electrode comprising graphite, CB, CMC, and SBR binder (95.8:1.7:1.5:1 in a mass ratio) when measured at  $34 \text{ mA g}^{-1}$  (0.1 C), observing a reversible capacity of  $335 \text{ mAh g}^{-1}$  and initial efficiency of 88.8 %, and (b) corresponding cycle performance when measured at  $170 \text{ mA g}^{-1}$  (0.5 C). (c) The initial charge-discharge profiles of the electrode comprising  $\text{LiCoO}_2$  (LCO), CB, and PVDF binder (94:3:3 in a mass ratio) when measured at  $15 \text{ mA g}^{-1}$  (0.1 C), observing a reversible capacity of  $158 \text{ mAh g}^{-1}$  and initial efficiency of 96.0 %, and (d) corresponding cycle performance when measured at  $75 \text{ mA g}^{-1}$  (0.5 C).

A prototype full cell completely sealed with a battery-grade aluminumized polymer pouch (Figure 5.16) was fabricated to demonstrate the commercial feasibility of a high-energy Li-ion battery which was composed of a lithium cobalt oxide ( $\text{LiCoO}_2$ , or LCO) cathode (half-cell data in Figure 5.17c, d) and the SWNT-c- $\text{SiO}_x$ /graphite blend anode including the CMC/SBR binder (SWNT-c- $\text{SiO}_x$ -Gr blend). The full cell was designed with a negative/positive (*n/p*) ratio of  $\sim 1.08$ ; the anode and cathode areal capacities were  $3.15 \text{ mAh cm}^{-2}$  and  $2.93 \text{ mAh cm}^{-2}$ . When tested at 0.05 C, the full cell comprising SWNT-c- $\text{SiO}_x$ -Gr blend/LCO exhibited an areal capacity of  $2.28 \text{ mAh cm}^{-2}$ . The SWNT-c- $\text{SiO}_x$ -Gr blend/LCO full cell was compared with a commercial graphite anode (half-cell data in Figure 5.17a, b)/LCO full cell and c- $\text{SiO}_x$ -Gr blend/LCO full cell in the potential range of 2.5–4.25 V at 25 °C at 0.05 C with three precycles for the formation of stable SEI layers, and then 0.5 C for a cycling test (Figure 5.18a). The fabricated SWNT-c- $\text{SiO}_x$ -Gr blend/LCO full-cell device demonstrated 85 % capacity retention after 100 cycles, comparable to the cycling performance of the graphite/LCO full cell (91 % capacity retention), while c- $\text{SiO}_x$ -Gr blend/LCO full cell exhibited fast degradation of its capacity, retaining an areal capacity of only  $0.11 \text{ mAh cm}^{-2}$  after 100 cycles when observing the capacity of  $2.17 \text{ mAh cm}^{-2}$  in the first precycle at 0.05 C. In addition, the cell with SWNT-



c-SiO<sub>x</sub>-Gr blend/LCO showed a quickly stabilized efficiency with a rapid increase upwards of 99.5 % over only 3 cycles at a discharge rate of 0.5 C (not including the three precycles at 0.05 C).

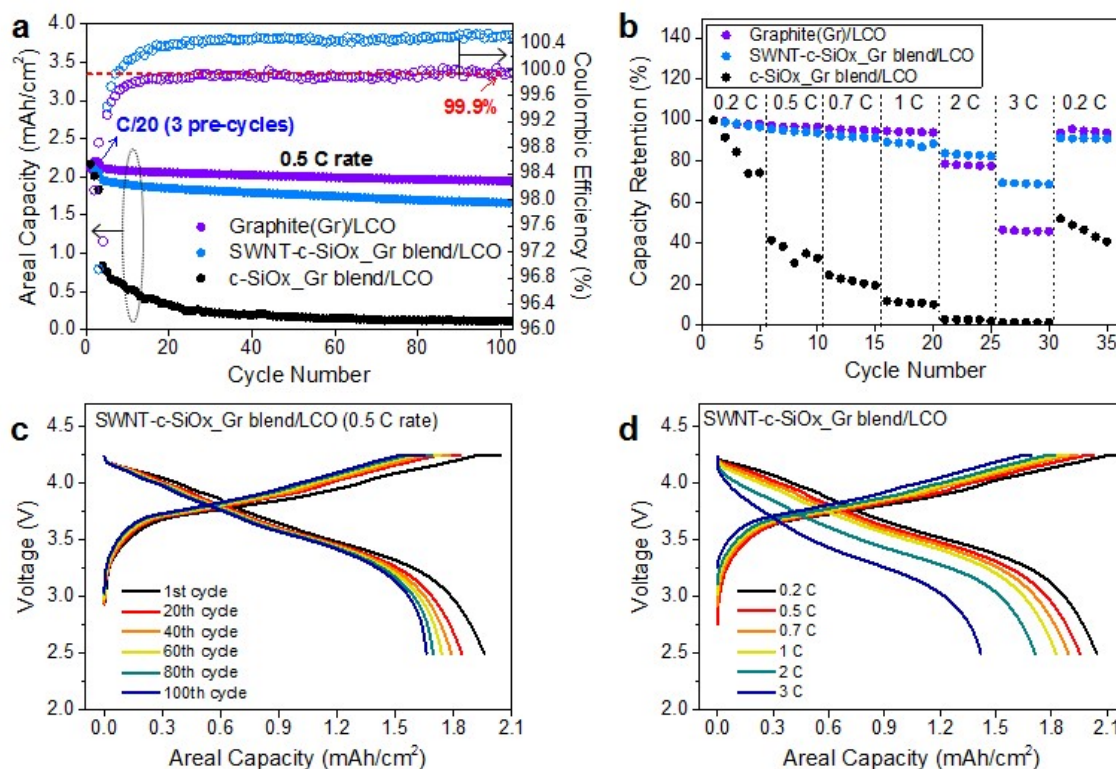


**Figure 5.18.** Electrochemical comparison of a pouch-type full cell: graphite (Gr)/LCO, SWNT-c-SiO<sub>x</sub>-Gr blend/LCO, and SWNT-c-SiO<sub>x</sub>-Gr blend/LCO. (a) Galvanostatic discharge areal capacities for 3 precycles at 0.05 C and for 100 cycles at 0.5 C in the potential range from 2.5 V to 4.25 V. (b) Capacity retention at various discharge rates from 0.2 C to 3 C with a constant charge rate of 0.2 C. (c, d) Voltage profiles for SWNT-c-SiO<sub>x</sub>-Gr blend/LCO plotted (c) as a function of the number of cycles and (d) as a function of the C-rate for the above cycle life and rate tests, respectively.

Capacity retention tests at various discharge rates from 0.2–3 C were performed following the capacity normalization with an areal capacity at the first cycle (Figure 5.18b). Surprisingly, at the high rate conditions of 2 C and 3 C, the measured values of the full cell comprising SWNT-c-SiO<sub>x</sub>-Gr blend/LCO were much enhanced in comparison to the

graphite/LCO full cell. Even though the rate capability is limited by the high areal capacity mass loading ( $2.93 \text{ mAh cm}^{-2}$ , or  $18.4 \text{ mg cm}^{-2}$ ) of the LCO cathode,<sup>154</sup> the exceptional performance decisively demonstrated the advantages associated with PPBT assisted linkages of SWNT networks to the c-SiO<sub>x</sub> that allows for the formation of robust electrical networks.

### 5.3.7 Proposed Mechanism

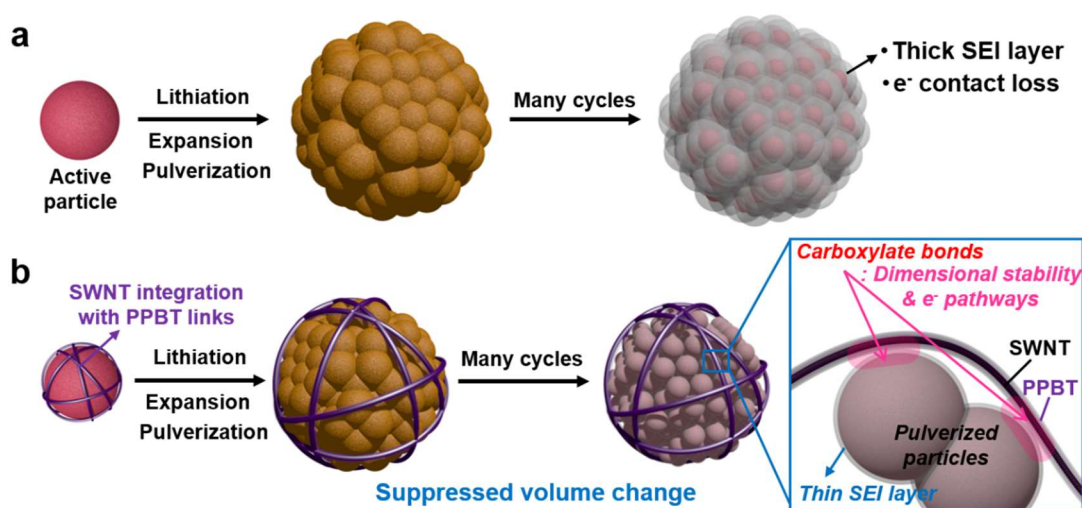


**Figure 5.19.** Proposed schematic illustration depicting (a) the pulverization of the electrode with the control electroactive particle and its resultant thick SEI layer formation, and (b) the operation of SWNT electrical networks securely anchored/connected on the pulverized particles through PPBT carboxylate bonds, which allows for structural, electrical stability and resulting stable SEI layers.

Figure 5.19 presents a schematic diagram of the proposed mechanism to elucidate the effect of SWNT electrical networks securely anchored/connected on a high-capacity electroactive material through PPBT linkages vs a pristine counterpart. In principle, as shown in Figure 5.19a, high-capacity energy materials experience large volume expansion and subsequent pulverization during Li insertion, and pulverized active particles remain



apart, thereby promoting the growth of SEI layers in the interparticle space.<sup>127</sup> With prolonged cycling, SEI layers become much thicker, resulting in breakdown of electron pathways between the pulverized particles. However, stable electrical networks strongly anchored on the surface of the high-capacity materials using PPBT with its carboxylate substituent can accommodate for the volume expansion through PPBT-mediated carboxylate bonds interconnecting between the pulverized particle and SWNT surface. This connection may assist in strongly capturing the pulverized particles and allow for suppressed volume change, improved electrical continuity, and the formation of stable SEI layers, leading to reduced electrode internal resistance and even enhanced electrode kinetics.

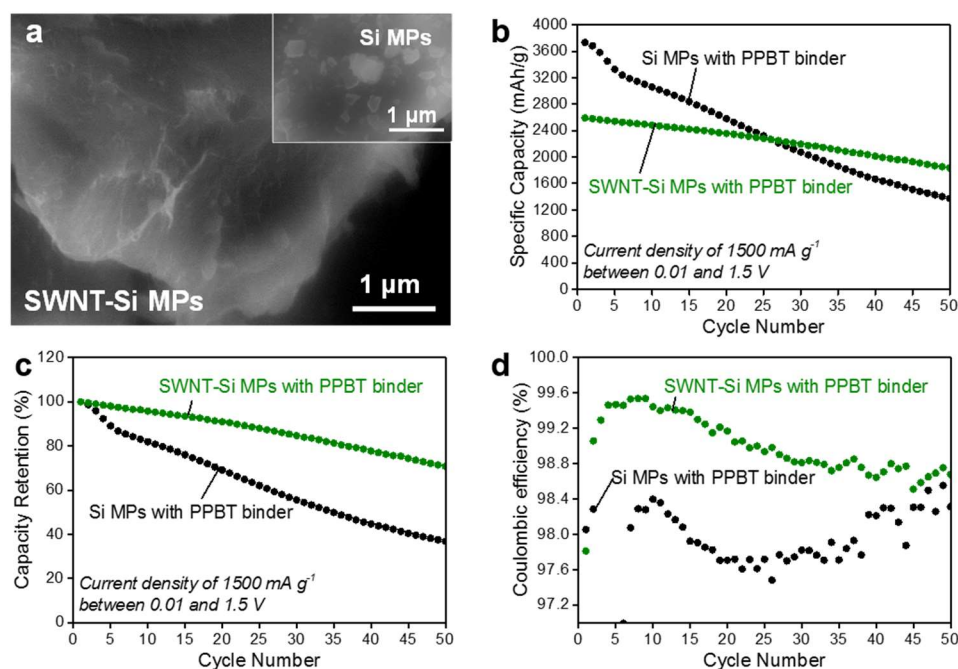


**Figure 5.20.** SWNT-anchored Si microparticles (Si MPs) with carboxylated polythiophene (PPBT) links. (a) SEM images of SWNT-Si MPs (the inset image shows the surface of pristine Si MPs). (b) Cycling performance (=capacity retention as a function of cycle number) collected at the current density of 1500  $\text{mA g}^{-1}$  between 0.01 and 1.5 V. Before the cycling test at 1500  $\text{mA g}^{-1}$ , the electrodes were pre-cycled at 300  $\text{mA g}^{-1}$  to measure a reversible capacity and initial efficiency. Si MPs based electrode showed the reversible

capacity of 3750 mAh g<sup>-1</sup> with the initial efficiency of 88.7 %, while the capacity of 2615 mAh g<sup>-1</sup> and the initial efficiency of 83.2 % for SWNT-Si MPs. Corresponding (c) capacity retention normalized with the delithiated capacity at the first cycle, and (d) its Coulombic efficiency.

Notably, this approach may have more impact on high-capacity electroactive materials with relatively moderate volume expansion (~200 %), although we demonstrated silicon nanoparticles with large volume change (420 %) were also effective in their performance. When examined for Si microparticles (Si MPs) that are more susceptible to pulverization during the volume expansion as compared with their nanoparticle counterpart,<sup>127</sup> SWNT-Si MPs showed enhanced cycling performance with better Coulombic efficiency (Figure 5.20). However, the effect was not as significant as that for Si NPs. After 10 cycles, the gradual decrease in Coulombic efficiency reflecting increased irreversible lithium losses was observed, which indicates that additional electrode design using binders with highly elastic properties<sup>126,127</sup> is necessary for practical Si MP anodes, together with our approach using SWNT networks with PPBT links, which is capable of sufficiently capturing the pulverized particles despite their repeated extremely large volume change.

## 5.4 Conclusion

We demonstrated that high-capacity energy materials including sFe<sub>3</sub>O<sub>4</sub>, Si NPs, and c-SiO<sub>x</sub> anchored by SWNT electrical networks using carboxylate substituted polythiophene (PPBT) ‘links’ contributed to electrode stability and secure electron transport pathways through capturing cracked/pulverized particles that can form during repeated battery cycling, thereby resulting in suppressed volume change, formation of

stable SEI layers, reduced electrode resistance, and enhanced electrode kinetics. This, in turn, afforded the remarkable enhancement in the representative electrochemical cycling and rate capability characteristics. Importantly, considering materials' surface chemistries to predict their attractive interactions led to the successful connection between electroactive particles and SWNT surface through PPBT linkages. Introduction of the PEG coating on the surface of high-capacity active materials allowed for favorable attraction to PPBT carboxylic moieties, which encouraged the formation of carboxylate bonds at their interface. PPBT conjugated backbone that physically interacts with SWNT  $\pi$ -electron rich assisted in SWNTs debundling and their spontaneous anchoring onto the active material surface. Surface analysis and following electrochemical results proved this concept to be plausible, and showed its versatility that would be applicable to a variety of high-capacity anode materials in improving battery performance. In particular, blending 30 wt % of c-SiO<sub>x</sub> with graphite including CMC/SBR binder (< 3 wt %) in the full-cell system demonstrated the commercial validity of the PPBT-mediated SWNT network integration for advanced high-energy battery systems.

## CHAPTER 6. CONCLUSIONS

### 6.1 Summary

The primary objective of this thesis was to elucidate how methodical and structural consideration for both ion and electron transport coupled with electrode materials' surface chemistries can contribute to high battery performance, enabling the realization of high-capacity Li-ion battery applications.

At first, when considering that battery electrodes are complex mesoscale systems comprised of electroactive components, conductive additives, and binders, we started our investigation in *Chapter 2* pertaining to methods for processing electrodes with dispersion of the components. To investigate the degree of material dispersion, a spin coating technique was adopted to provide a thin, uniform layer which enabled observation of the morphology. Distinct differences in the distribution profile of the electrode components arising from individual materials physical affinities were readily identified. Hansen solubility parameter (HSP) analysis revealed pertinent surface interactions associated with materials dispersivity. Further studies demonstrated that HSPs can provide an effective strategy to identify surface modification approaches for improved dispersions of battery electrode materials. Specifically, introduction of surfactant-like functionality such as oleic acid (OA) capping and P3HT conjugated polymer wrapping, on the surface of nanomaterials significantly enhanced material dispersity over the composite electrode. The approach to the surface treatment on the basis of HSP study can facilitate design of composite electrodes with uniformly dispersed morphology, and may contribute to enhancing their electrical and electrochemical behaviors. In this study, it was anticipated

that the use of physical affinity relationships will enable the design and fabrication of more uniformly dispersed composites for battery electrode applications; improved dispersion characteristics are expected to enhance both electrical and electrochemical properties. As a result, however, material dispersion impacted on the improvement of electronic conductivity of composite electrodes, but not resulting in electrochemical enhancement. Through studies using capped and uncapped  $\text{Fe}_3\text{O}_4$ , and two alternative binder polymers, it was demonstrated that materials dispersivity cannot be used in isolation to predict electrochemical performance. Therefore, the study results strongly suggest the importance of considering electronic conductivity, electron transfer as well as ion transport in the design of environments incorporating active nanomaterials.

Based on the insights obtained from *Chapter 2* study, *Chapter 3* then investigated the composite electrode design considering both electron and ion transport. The conjugated polymer, poly[3-(potassium-4-butanoate) thiophene] (PPBT), was introduced as a binder component, while polyethylene glycol (PEG) was coated onto the surface of  $\text{Fe}_3\text{O}_4$  nanoparticles. The introduction of PEG reduced aggregate size, enabled effective dispersion of the active materials and facilitated ionic conduction. As a binder for the composite electrode, PPBT underwent electrochemical doping which enabled the formation of effective electrical bridges between the carbon and  $\text{Fe}_3\text{O}_4$  components, allowing for more efficient electron transport. Additionally, the PPBT carboxylic moieties effect a porous structure, and stable electrode performance. The methodical consideration of both enhanced electron and ion transport by introducing a carboxylated PPBT binder and PEG surface treatment led to effectively reduced electrode resistance, which improved cycle life performance and rate capabilities. Importantly, *Chapter 3* provided us with

fundamental insights and clues for following studies to improve battery performance using PPBT surface chemistries.

*Chapter 4* explored the electrode structure design including a carbon nanotube (CNT) web frame comprising magnetite spheres and few-walled carbon nanotubes (FWNTs) linked by the carboxylated conjugated polymer, poly[3-(potassium-4-butanoate) thiophene] (PPBT). This structure was devised to demonstrate benefits derived from the rational consideration of electron/ion transport coupled with the surface chemistry of the electrode materials components. To maximize transport properties, the approach introduces monodispersed spherical  $\text{Fe}_3\text{O}_4$  (s $\text{Fe}_3\text{O}_4$ ) for uniform  $\text{Li}^+$  diffusion and a FWNT web electrode frame that affords characteristics of long-ranged electronic pathways and porous networks. The s $\text{Fe}_3\text{O}_4$  particles were used as a model high-capacity energy active material, owing to their well-defined chemistry with surface hydroxyl ( $-\text{OH}$ ) functionalities that provide for facile detection of molecular interactions. Poly[3-(potassium-4-butanoate) thiophene] (PPBT), having a  $\pi$ -conjugated backbone and alkyl side chains substituted with carboxylate moieties, interacted with the FWNT  $\pi$ -electron rich and hydroxylated s $\text{Fe}_3\text{O}_4$  surfaces, which enabled the formation of effective electrical bridges between the respective components, contributing to efficient electron transport and electrode stability. Similar to *Chapter 2*, to further induce interactions between PPBT and the metal hydroxide surface, polyethylene glycol (PEG) was coated onto the s $\text{Fe}_3\text{O}_4$  particles, allowing for facile materials dispersion and connectivity. Additionally, the introduction of carbon particles into the web electrode minimized s $\text{Fe}_3\text{O}_4$  aggregation and afforded more porous FWNT networks. As a consequence, the design of composite electrodes with rigorous consideration of specific molecular interactions induced by the

surface chemistries favorably influenced electrochemical kinetics and electrode resistance, which afforded high performance electrodes for battery applications.

Finally, **Chapter 5** demonstrated that conjugated polymers possessing polar functionalities (*i.e.*, PPBT) were shown to effectively anchor single-walled carbon nanotubes (SWNTs) to the surface of high-capacity anode materials, and enable the formation of electrical networks. Specifically, PPBT served as a bridge between SWNT networks and various anode materials, including monodispersed  $\text{Fe}_3\text{O}_4$  spheres ( $\text{sFe}_3\text{O}_4$ ), silicon nanoparticles (Si NPs), and carbon-coated silicon monoxide ( $\text{c-SiO}_x$ ,  $x \approx 1$ ). SWNT anchoring onto the active material surface was also achieved through consideration of materials surface chemistry and resultant physical/chemical bonding mediated by favorable molecular interactions: The PPBT  $\pi$ -conjugated backbone and carboxylate ( $\text{COO}^-$ ) substituted alkyl side chains, respectively, attracted the SWNT  $\pi$ -electron surface and chemically interacted with active material surface hydroxyl ( $-\text{OH}$ ) species to a form of carboxylate bond. Beneficially, this architecture effectively captured cracked/pulverized particles that typically form as a result of repeated active material volume changes that occur during charging and discharging. Thus, changes in electrode thickness were suppressed substantially, stable SEI layers were formed, electrode resistance was reduced, and enhanced electrode kinetics was observed. Together, these factors led to excellent electrochemical performance. Moreover, electrodes fabricated by blending 30 wt % of  $\text{c-SiO}_x$  with graphite using < 3 wt % binder material exhibited remarkable performance in both coin-type half-cell and pouch-type full-cell systems to demonstrate its commercial validity.

In summary, this thesis explored systematic approaches to Li-ion battery electrodes considering both factors, electron/ion transport, that provides for high electrochemical performance. The approaches commonly introduced the carboxylate substituted polythiophene as a new polymeric binder in a composite electrode, or an electrical linker effectively connecting CNT networks to active material surfaces, coupled with materials' surface chemistries. Apparently, this approach is, seemingly, very simple, but remarkably effective and efficient in battery performance enhancement. In addition, the expansion of the results obtained from  $\text{Fe}_3\text{O}_4$  study to alternate high-capacity active materials including Si NPs and c-SiO<sub>x</sub> further demonstrated the versatility of the concept introducing robust SWNT electrical networks with PPBT carboxylate linkages. Consequently, the results and fundamental insight described here suggest a feasible approach to achieving practical, high-performance, and high-capacity battery electrode applications, which could be an expected breakthrough for the next-generation electronic devices.

## 6.2 Future Works

### 6.2.1 *Elastomeric components*

As described in **Chapter 5**, SWNT-Si microparticles (Si MPs) showed enhanced cycling performance with better Coulombic efficiency, but the effect was not significant, since Si MPs are much prone to pulverization during the volume expansion when compared with silicon nanoparticles. This indicates that additional electrode or material design adopting highly elastic components<sup>126,127</sup> is imperative for practical Si MP anodes, which is capable of sufficiently capturing the pulverized particles despite their repeated extremely large volume change. In particular, the study associated with a new polymeric binder with



highly stretchable and elastic networks pointed to the effectiveness of highly elastic components that dissipates the stress during repeated volume change and keeps the pulverized Si particles coalesced.<sup>127</sup> This, in turn, led to the remarkable enhancement of battery characteristics such as cycle life and Coulombic efficiency (Figure 6.1).

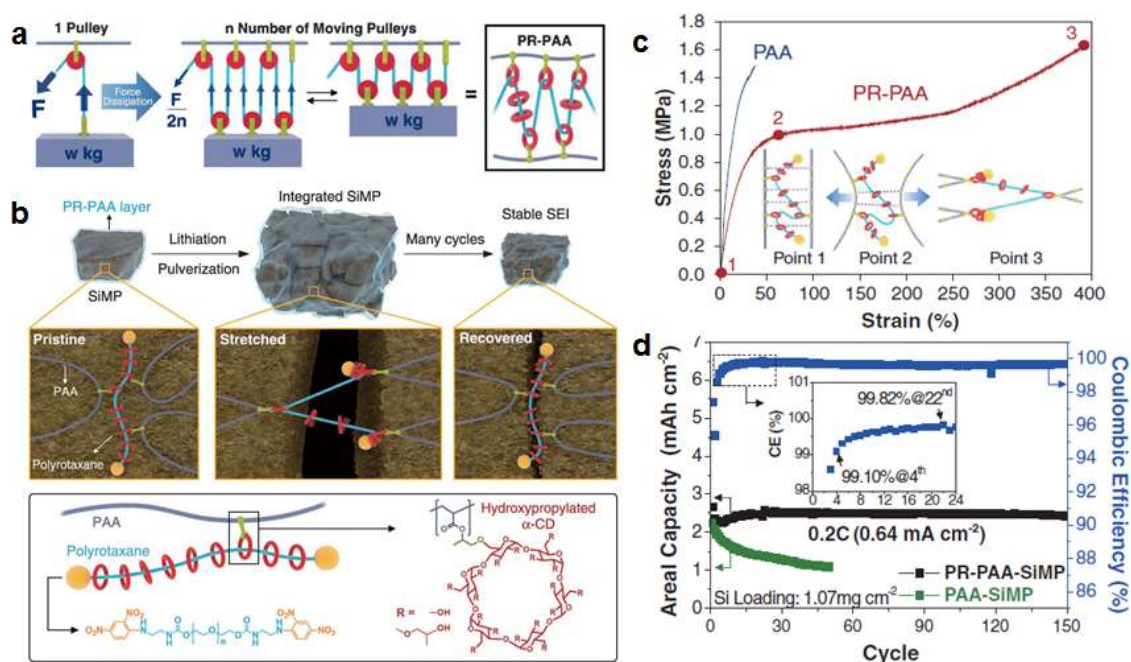


**Figure 6.1.** Polyrotaxane (PR)-polyacrylic acid (PAA) binder for Si MP anode.<sup>127</sup> (a, b) Proposed stress dissipation mechanism. (a) The pulley principle to lower the force in lifting an object. (b) Graphical representation of the operation of PR-PAA binder to dissipate the stress during volume changes of Si MPs, together with chemical structure of PR and PAA. (c) Comparison of stress-strain curves of PR-PAA and PAA films. (d) Cycling performance and corresponding Coulombic efficiency of coin half cell. From ref. 127. Reprinted with permission from AAAS.

Based on this concept, two approaches will be introduced for a Si MP anode to realize high battery performance. First, styrene-butadiene rubber (SBR) can be used as a spherical elastomeric component in a PPBT binder matrix, which is similar to CMC/SBR commercialized binder system. While PPBT retains relatively high electrical properties

and renders electrodes much stable through the formation of carboxylate bonds, PPBT is expected much susceptible to breakage during battery operation. SBR elastomer is likely to provide PPBT binder matrix with highly elastic characteristics, contributing to more effectively capturing the cracked/pulverized particles, which may result in stable Si anodes.

Second approach introduces an elastomeric component chemically integrated with SWNT-PPBT networks that are securely connected/anchored on the surface of Si MPs (Figure 6.2). The elastomeric unit also plays an important role in alleviating the collapse of SWNT electrical networks with PPBT links. For doing this, we can utilize a well-established method for the formation of chemical crosslinking through the reaction of PPBT carboxylic group with amino group ( $-NH_2$ ) of the elastomeric component.<sup>170</sup> This elastic networks, however, could completely wrap/cover around Si MP surface and rather prevent  $Li^+$  ion access to the active site, negatively impacting on their electrochemistry. Thus, acquiring ion transport channels within the elastic networks is a further challenge. Materials' surface chemistries that determine molecular interactions can be an important tool to start designing that structure. Specifically, based on similar physical affinities, SWNT networks wrapping on the Si MP surface mediated by a PPBT physical/chemical linker is of significance, but 'partial miscibility' (or 'controlled miscibility') of the elastomeric component with the active material surface is also important to prevent the elastomeric unit from completely covering the surface of active particles, and rather enable the formation of pores on their surface that helps ion accessibility. This rigorous consideration based on the materials' surface chemistries, coupled with electron and ion transport, will be our next works.

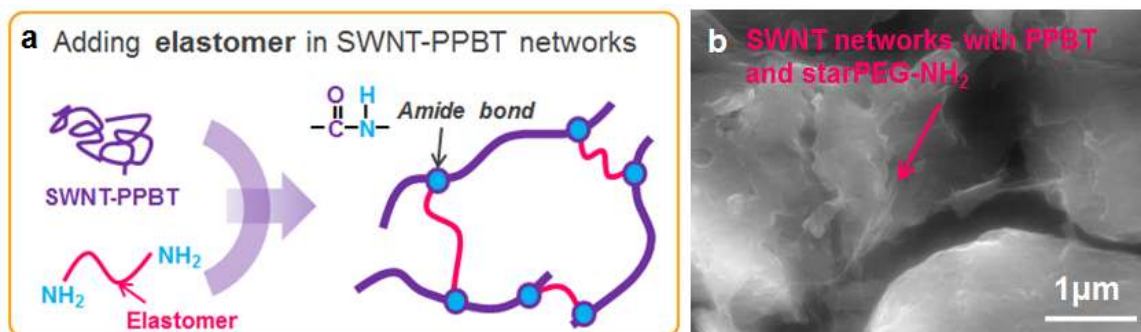


**Figure 6.2.** (a) Proposed SWNT-PPBT networks crosslinked with amino ( $\text{-NH}_2$ ) terminated elastomer. (b) SEM image of SWNT-PPBT networks crosslinked with star PEG terminated with  $\text{NH}_2$ .

## REFERENCES

- (1) K. Ozawa, *Lithium Ion Rechargeable Batteries*, WILEY-VCH Verlag GmbH, Weinheim, **2009**.
- (2) M. Wakihara, O. Yamamoto, *Lithium Ion Batteries: Fundamentals and Performance*, WILEY-VCH Verlag GmbH, Weinheim, **1998**.
- (3) Islam, M. S.; Fisher, C. A. J. Lithium and Sodium Battery Cathode Materials: Computational Insights into Voltage, Diffusion and Nanostructural Properties. *Chem. Soc. Rev.* **2014**, *43*, 185–204.
- (4) Huang, C.; Zhuang, S.; Tu, F. Electrode/Electrolyte Interfacial Behaviors of LiCoO<sub>2</sub>/Mixed Graphite Li-Ion Cells during Operation and Storage. *J. Electrochem. Soc.* **2013**, *160*, A376–A382.
- (5) Tarascon, J.-M.; Armand, M. Issues and Challenges Facing Rechargeable Lithium Batteries. *Nature* **2001**, *414*, 359–367.
- (6) Ogihara, N.; Kawauchi, S.; Okuda, C.; Itou, Y.; Takeuchi, Y.; Ukyo, Y. Theoretical and Experimental Analysis of Porous Electrodes for Lithium-Ion Batteries by Electrochemical Impedance Spectroscopy Using a Symmetric Cell. *J. Electrochem. Soc.* **2012**, *159*, A1034–A1039.
- (7) Birkl, C. R.; McTurk, E.; Roberts, M. R.; Bruce, P. G.; Howey, D. A. A Parametric Open Circuit Voltage Model for Lithium Ion Batteries. *J. Electrochem. Soc.* **2015**, *162*, A2271–A2280.
- (8) Chae, S.; Ko, M.; Kim, K.; Ahn, K.; Cho, J. Confronting Issues of the Practical Implementation of Si Anode in High-Energy Lithium-Ion Batteries. *Joule* **2017**, *1*, 47–60.
- (9) Chen, Z.; To, J. W. F.; Wang, C.; Lu, Z.; Liu, N.; Chortos, A.; Pan, L.; Wei, F.; Cui, Y.; Bao, Z. A Three-Dimensionally Interconnected Carbon Nanotube–Conducting Polymer Hydrogel Network for High Performance Flexible Battery Electrodes. *Adv. Energy Mater.* **2014**, *4*, 1400207.
- (10) Chan, C. K.; Peng, H.; Liu, G.; McIlwrath, K.; Zhang, X. F.; Huggins, R. A.; Cui, Y. High-Performance Lithium Battery Anodes Using Silicon Nanowires. *Nat. Nanotechnol.* **2008**, *3*, 31–35.
- (11) Liu, G.; Xun, S.; Vukmirovic, N.; Song, X.; Olalde-Velasco, P.; Zheng, H.; Battaglia, V. S.; Wang, L.; Yang, W. Polymers with Tailored Electronic Structure for High Capacity Lithium Battery Electrodes. *Adv. Mater.* **2011**, *23*, 4679–4683.

- (12) Kim, H.; Han, B.; Choo, J.; Cho, J. *Angew. Chem. Int. Ed.* Three-Dimensional Porous Silicon Particles for Use in High-Performance Lithium Secondary Batteries. **2008**, *47*, 10151–10154.
- (13) Derrien, G.; Hassoun, J.; Panero, S.; Scrosati, B. Nanostructured Sn–C Composite as an Advanced Anode Material in High-Performance Lithium-Ion Batteries. *Adv. Mater.* **2007**, *19*, 2336–2340.
- (14) Kim, I. T.; Magasinski, A.; Jacob, K.; Yushin, G.; Tannenbaum, R. Synthesis and Electrochemical Performance of Reduced Graphene Oxide/Maghemite Composite Anode for Lithium Ion Batteries. *Carbon* **2013**, *52*, 56–64.
- (15) He, C.; Wu, S.; Zhao, N.; Shi, C.; Liu, E.; Li, J. Carbon-Encapsulated Fe<sub>3</sub>O<sub>4</sub> Nanoparticles as a High-Rate Lithium Ion Battery Anode Material. *ACS Nano* **2013**, *7*, 4459–4469.
- (16) Luo, J.; Liu, J.; Zeng, Z. Ng, C. F.; Ma, L.; Zhang, H.; Lin, J.; Shen, Z.; Fan, H. J. Three-Dimensional Graphene Foam Supported Fe<sub>3</sub>O<sub>4</sub> Lithium Battery Anodes with Long Cycle Life and High Rate Capability. *Nano Lett.* **2013**, *13*, 6136–6143.
- (17) Yoon, T.; Kim, J.; Kim, J.; Lee, J. K. Electrostatic Self-Assembly of Fe<sub>3</sub>O<sub>4</sub> Nanoparticles on Graphene Oxides for High Capacity Lithium-Ion Battery Anodes. *Energies* **2013**, *6*, 4830–4840.
- (18) Bruck, A. M.; Cama, C. A.; Gannett, C. N.; Marschilok, A. C.; Takeuchi, E. S.; Takeuchi, K. J. Nanocrystalline Iron Oxide Based Electroactive Materials in Lithium Ion Batteries: The Critical Role of Crystallite Size, Morphology, and Electrode Heterostructure on Battery Relevant Electrochemistry. *Inorg. Chem. Front.* **2016**, *3*, 26–40.
- (19) Wu, M.; Xiao, X.; Vukmirovic, N.; Xun, S.; Das, P. K.; Song, X.; Olalde-Velasco, P.; Wang, D.; Weber, A. Z.; Wang, L.-W.; Battaglia, V. S.; Yang, W.; Liu, G. Toward an Ideal Polymer Binder Design for High-Capacity Battery Anodes. *J. Am. Chem. Soc.* **2013**, *135*, 12048–12056.
- (20) Wu, H.; Yu, G.; Pan, L.; Liu, N.; McDowell, M. T.; Bao, Z.; Cui, Y. Stable Li-Ion Battery Anodes by *In-Situ* Polymerization of Conducting Hydrogel to Conformally Coat Silicon Nanoparticles. *Nat. Commun.* **2013**, *4*, 1943.
- (21) Mazouzi, D.; Lestriez, B.; Roué, L.; Guyomard, D. Silicon Composite Electrode with High Capacity and Long Cycle Life. *Electrochem. Solid-State Lett.* **2009**, *12*, A215–A218.
- (22) Bridel, J.-S.; Azaïs, T.; Morcrette, M.; Tarascon, J.-M.; Larcher, D. Key Parameters Governing the Reversibility of Si/Carbon/CMC Electrodes for Li-Ion Batteries. *Chem*

- . *Mater.* **2010**, *22*, 1229–1241.
- (23) Magasinski, A.; Zdyrko, B.; Kovalenko, I.; Hertzberg, B.; Burtovyy, R.; Huebner, C. F.; Fuller, T. F.; Luzinov, I.; Yushin, G. Toward Efficient Binders for Li-Ion Battery Si-Based Anodes: Polyacrylic Acid. *ACS Appl. Mater. Interfaces* **2010**, *2*, 3004–3010.
- (24) Kovalenko, I.; Zdyrko, B.; Magasinski, A.; Hertzberg, B.; Milicev, Z.; Burtovyy, R.; Luzinov, I.; Yushin, G. A Major Constituent of Brown Algae for Use in High-Capacity Li-Ion Batteries. *Science* **2011**, *334*, 75–79.
- (25) Yang, Y.; Ruan, G.; Xiang, C.; Wang, G.; Tour, J. M. Flexible Three-Dimensional Nanoporous Metal-Based Energy Devices. *J. Am. Chem. Soc.* **2014**, *136*, 6187–6190.
- (26) Hiralal, P.; Imaizumi, S.; Unalan, H. E.; Matsumoto, H.; Minagawa, M.; Rouvala, M.; Tanioka, A.; Amaratunga, G. A. J. Nanomaterial-Enhanced All-Solid Flexible Zinc Carbon Batteries. *ACS Nano* **2010**, *4*, 2730–2734.
- (27) Wang, J.; Li, L.; Wong, C. L.; Madhavi, S. Flexible Single-Walled Carbon Nanotube/Polycellulose Papers for Lithium-Ion Batteries. *Nanotechnology* **2012**, *43*, 495401.
- (28) Choi, K.-H.; Cho, S.-J.; Chun, S.-J.; Yoo, J. T.; Lee, C. K.; Kim, W.; Wu, Q.; Park, S.-B.; Choi, D.-H.; Lee, S.-Y.; Lee, S.-Y. Heterolayered, One-Dimensional Nanobuilding Block Mat Batteries. *Nano Lett.* **2014**, *14*, 5677–5686.
- (29) Cho, S.-J.; Choi, K.-H.; Yoo, J.-T.; Kim, J.-H.; Lee, Y.-H.; Chun, S.-J.; Park, S.-B.; Choi, D.-H.; Wu, Q.; Lee, S.-Y.; Lee, S.-Y. Hetero-Nanonet Rechargeable Paper Batteries: Toward Ultrahigh Energy Density and Origami Foldability. *Adv. Funct. Mater.* **2015**, *25*, 6029–6040.
- (30) Chen, Z.; Ren, W.; Gao, L.; Liu, B.; Pei, S.; Cheng, H.-M. Three-Dimensional Flexible and Conductive Interconnected Graphene Networks Grown by Chemical Vapour Deposition. *Nat. Mater.* **2011**, *10*, 424–428.
- (31) Li, N.; Chen, Z.; Ren, W.; Li, F.; Cheng, H.-M. Flexible Graphene-Based Lithium Ion Batteries with Ultrafast Charge and Discharge Rates. *Proc. Natl. Acad. Sci.* **2012**, *109*, 17360–17365.
- (32) Kwon, Y. H.; Huie, M. M.; Choi, D.; Chang, M.; Marschilok, A. C.; Takeuchi, K. J.; Takeuchi, E. S.; Reichmanis, E. Toward Uniformly Dispersed Battery Electrode Composite Materials: Characteristics and Performance. *ACS Appl. Mater. Interfaces* **2016**, *8*, 3452–3463.
- (33) Armand, M.; Tarascon, J.-M. Building Better Batteries. *Nature* **2008**, *451*, 652–657.

- (34) Arico, A. S.; Bruce, P.; Scrosati, B.; Tarascon, J. M.; Schalkwijk, W. V. Nanostructured Materials for Advanced Energy Conversion and Storage Devices. *Nat. Mater.* **2005**, *4*, 366–377.
- (35) Chen, H.; Wang, C.; Dong, W.; Lu, W.; Du, Z.; Chen, L. Monodispersed Sulfur Nanoparticles for Lithium–Sulfur Batteries with Theoretical Performance. *Nano Lett.* **2015**, *15*, 798–802.
- (36) Bock, D. C.; Kirshenbaum, K. C.; Wang, J.; Zhang, W.; Wang, F.; Wang, J.; Marschillok, A. C.; Takeuchi, K. J.; Takeuchi, E. S. 2D Cross Sectional Analysis and Associated Electrochemistry of Composite Electrodes Containing Dispersed Agglomerates of Nanocrystalline Magnetite,  $\text{Fe}_3\text{O}_4$ . *ACS Appl. Mater. Interfaces* **2015**, *7*, 13457–13466.
- (37) Kang, B.; Ceder, G. Battery Materials for Ultrafast Charging and Discharging. *Nature* **2009**, *458*, 190–193.
- (38) Zhang, W. M.; Wu, X. L.; Hu, J. S.; Guo, Y. G.; Wan, L. J. Carbon Coated  $\text{Fe}_3\text{O}_4$  Nanospindles as a Superior Anode Material for Lithium-Ion Batteries. *Adv. Funct. Mater.* **2008**, *18*, 3941–3946.
- (39) de Guzman, R. C.; Yang, J.; Cheng, M. C. M.; Salley, S. O.; Ng, K. Y. S. A Silicon Nanoparticle/Reduced Graphene Oxide Composite Anode with Excellent Nanoparticle Dispersion to Improve Lithium Ion Battery Performance. *J. Mater. Sci.* **2013**, *48*, 4823–4833.
- (40) Tao, T.; Glushenkov, A. M.; Zhang, C.; Zhang, H.; Zhou, D.; Guo, Z.; Liu, H. K.; Chen, Q.; Hub, H.; Chena, Y.  $\text{MoO}_3$  Nanoparticles Dispersed Uniformly in Carbon Matrix: a High Capacity Composite Anode for Li-ion Batteries. *J. Mater. Chem.* **2011**, *21*, 9350–9355.
- (41) Lee, J. K.; Smith, K. B.; Hayner, C. M.; Kung, H. H. Silicon Nanoparticles–Graphene Paper Composites for Li Ion Battery Anodes. *Chem. Commun.* **2010**, *46*, 2025–2027.
- (42) Kim, J. S.; Nguyen, C. C.; Kim, H. J.; Song, S. W. Siloxane-Capped Amorphous  $\text{SiO}_x$ /Graphite with Improved Dispersion Ability and Battery Anode Performance. *RSC Adv.* **2014**, *4*, 12878–12881.
- (43) Knehr, K. W.; Brady, N. W.; Cama, C. A.; Bock, D. C.; Lin, Z.; Lininger, C. N.; Marschillok, A. C.; Takeuchi, K. J.; Takeuchi, E. S.; West, A. C. Modeling the Mesoscale Transport of Lithium-Magnetite Electrodes Using Insight from Discharge and Voltage Recovery Experiments. *J. Electrochem. Soc.* **2015**, *162*, A2817–A2826.

- (44)Bhattacharya, S.; Srivastava, A.; Pal, A. Modulation of Viscoelastic Properties of Physical Gels by Nanoparticle Doping: Influence of the Nanoparticle Capping Agent. *Angew. Chem.* **2006**, *118*, 3000–3003.
- (45)Corbierre, M. K.; Cameron, N. S.; Sutton, M.; Laaziri, K.; Lennox, R. B. Gold Nanoparticle/Polymer Nanocomposites: Dispersion of Nanoparticles as a Function of Capping Agent Molecular Weight and Grafting Density. *Langmuir* **2005**, *21*, 6063-6072.
- (46)Saunders, B. R.; Turner, M. L. Nanoparticle–Polymer Photovoltaic Cells. *Adv. Colloid Interfac.* **2008**, *138*, 1–23.
- (47)Tang, J.; Kemp, K. W.; Hoogland, S.; Jeong, K. S.; Liu, H.; Levina, L.; Furukawa, M.; Wang, X.; Debnath, R.; Cha, D.; Chou, K. W.; Fischer, A.; Amassian, A.; Asbury, J. B.; Sargent, E. H. Colloidal-Quantum-Dot Photovoltaics using Atomic-Ligand Passivation. *Nat. Mater.* **2011**, *10*, 765–771.
- (48)Singh, A. K.; Viswanath, V.; Janu, V. C. Synthesis, Effect of Capping Agents, Structural, Optical and Photoluminescence Properties of ZnO Nanoparticles. *J. Lumin.* **2009**, *129*, 874–878.
- (49)Green, M.; Harwood, H.; Barrowman, C.; Rahman, P.; Eggeman, A.; Festry, F.; Dobson, P.; Ng, T. A Facile Route to CdTe Nanoparticles and Their Use in Bio-Labeling. *J. Mater. Chem.* **2007**, *17*, 1989–1994.
- (50)Park, H. Y.; Schadt, M. J.; Wang, L.; Lim, I. S.; Njoki, P. P.; Kim, S. H.; Jang, M. Y.; Luo, J.; Zhong, C. J. Fabrication of Magnetic Core@Shell Fe Oxide@Au Nanoparticles for Interfacial Bioactivity and Bio-Separation. *Langmuir* **2007**, *23*, 9050-9056.
- (51)Cozzoli, P. D.; Kornowski, A.; Weller, H. Low-Temperature Synthesis of Soluble and Processable Organic-Capped Anatase TiO<sub>2</sub> Nanorods. *J. Am. Chem. Soc.* **2003**, *125*, 14539-14548.
- (52)Jadhava, N. V.; Prasad, A. I.; Kumara, A.; Mishra, R.; Dharad, S.; Babuc, K. R.; Prasad, C. L.; Misra, N. L.; Ningthoujam, R. S.; Pandeya, B. N.; Vatsa, R. K. Synthesis of Oleic Acid Functionalized Fe<sub>3</sub>O<sub>4</sub> Magnetic Nanoparticles and Studying Their Interaction with Tumor Cells for Potential Hyperthermia Applications. *Colloids Surface, B* **2013**, *108*, 158–168.
- (53)Ghosh, R.; Pradhan, L.; Devi, L. P.; Meena, S. S.; Tewari, R.; Kumar, A.; Sharma, S.; Gajbhiye, N. S.; Vatsa, R. K.; Pandey, B. N.; Ningthoujam, R. S. Induction Heating Studies of Fe<sub>3</sub>O<sub>4</sub> Magnetic Nanoparticles Capped with Oleic Acid and Polyethylene Glycol for Hyperthermia. *J. Mater. Chem.* **2011**, *21*, 13388–13398.
- (54)Parveen, S.; Rana, S.; Figueiro, R. A Review on Nanomaterial Dispersion, Microstr



- ucture, and Mechanical Properties of Carbon Nanotube and Nanofiber Reinforced Cementitious Composites. *J. Nanomater.* **2013**, 1–19.
- (55) Samanta, S. K.; Fritsch, M.; Scherf, U.; Gomulya, W.; Bisri, S. Z.; Loi, M. A. Conjugated Polymer-Assisted Dispersion of Single-Wall Carbon Nanotubes: The Power of Polymer Wrapping. *Acc. Chem. Res.* **2014**, *47*, 2446–2456.
- (56) Islam, M. F.; Rojas, E.; Bergey, D. M.; Johnson, A. T.; Yodh, A. G. High Weight Fraction Surfactant Solubilization of Single-Wall Carbon Nanotubes in Water. *Nano Lett.* **2003**, *3*, 269–273.
- (57) Liu, J.; Rinzler, A. G.; Dai, H. J.; Hafner, J. H.; Bradley, R. K.; Boul, P. J.; Lu, A.; Iverson, T.; Shelimov, K.; Huffman, C. B.; Rodriguez-Marcias, F. J.; Shon, Y. S.; Lee, T. R.; Colbert, D. T.; Smalley, R. E. Fullerene Pipes. *Science* **1998**, *280*, 1253–1256.
- (58) Abdelhamid, M. E.; O'Mullane, A. P.; Snook, G. A. Storing Energy in Plastics: A Review on Conducting Polymers and Their Role in Electrochemical Energy Storage. *RS C Adv.* **2015**, *5*, 11611–11626.
- (59) Song, C. K.; Eckstein, B. J.; Tam, T. L. D.; Trahey, L.; Marks, T. J. Conjugated Polymer Energy Level Shifts in Lithium-Ion Battery Electrolytes. *ACS Appl. Mater. Interfaces* **2014**, *6*, 19347–19354.
- (60) Patel, S. N.; Javier, A. E.; Stone, G. M.; Mullin, S. A.; Balsara, N. P. Simultaneous Conduction of Electronic Charge and Lithium Ions in Block Copolymers. *ACS Nano* **2012**, *6*, 1589–1600.
- (61) Patel, S. N.; Javier, A. E.; Balsara, N. P. Electrochemically Oxidized Electronic and Ionic Conducting Nanostructured Block Copolymers for Lithium Battery Electrodes. *ACS Nano* **2013**, *7*, 6056–6068.
- (62) Wu, S.-L.; Javier, A. E.; Devaux, D.; Balsara, N. P.; Srinivasan, V. Discharge Characteristics of Lithium Battery Electrodes with a Semiconducting Polymer Studied by Continuum Modeling and Experiment. *J. Electrochem. Soc.* **2014**, *161*, A1836–A184.
- (63) An, H.; Mike, J.; Smith, K. A.; Swank, L.; Lin, Y.-H.; Pesek, S. L.; Verduzco, R.; Lutkenhaus, J. L. Highly Flexible Self-Assembled V<sub>2</sub>O<sub>5</sub> Cathodes Enabled by Conducting Diblock Copolymers. *Sci. Rep.* **2015**, *5*, 14166–14176.
- (64) Javier, A. E.; Patel, S. N.; Hallinan, D. T.; Srinivasan, V.; Balsara, N. P. Simultaneous Electronic and Ionic Conduction in a Block Copolymer: Application in Lithium Battery Electrodes. *Angew. Chem., Int. Ed.* **2011**, *50*, 9848–9851.
- (65) Patel, S. N.; Javier, A. E.; Beers, K. M.; Pople, J. A.; Ho, V.; Segalman, R. A.; Balsara, N. P. Morphology and Thermodynamic Properties of a Copolymer with an Electro

- nically Conducting Block: Poly(3-ethylhexylthiophene)-block-poly(ethylene oxide). *Nano Lett.* **2012**, *12*, 4901–4906.
- (66)Oschmann, B.; Park, J.; Kim, C.; Char, K.; Sung, Y.-E.; Zentel, R. Copolymerization of Polythiophene and Sulfur To Improve the Electrochemical Performance in Lithium–Sulfur Batteries. *Chem. Mater.* **2015**, *27*, 7011–7017.
- (67)Ma, J.; Zhang, X.; Chen, K.; Han, X. Diamond-Shaped  $\text{Fe}_2\text{O}_3@\text{C}_{18}\text{H}_{34}\text{O}_2$  Core–Shell Nanostructures as Anodes for Lithium Ion Batteries with High Over Capacity. *RSC Adv.* **2014**, *4*, 9166–9171.
- (68)Guo, S.; Zhang, M.; Zhang, G.; Zheng, L.; Kang, L.; Liu, Z.-H. Synthesis of Novel  $\text{Mn}_3\text{O}_4$  Microsphere and Its Distinctive Capacitance Change during Electrochemical Cycling. *Powder Tech.* **2012**, *228*, 371–376.
- (69)Wu, Y.; Li, Y.; Ong, B. S. Printed Silver Ohmic Contacts for High-Mobility Organic Thin-Film Transistors. *J. Am. Chem. Soc.* **2006**, *128*, 4202–4203.
- (70)Zhu, S.; Marschilok, A. C.; Takeuchi, E. S.; Takeuchi, K. J. Crystallite Size Control and Resulting Electrochemistry of Magnetite,  $\text{Fe}_3\text{O}_4$ . *Electrochem. Solid-State Lett.* **2009**, *12*, A91–A94.
- (71)Zhu, S.; Marschilok, A. C.; Takeuchi, E. S.; Yee, G. T.; Wang, G.; Takeuchi, K. J. Nanocrystalline Magnetite: Synthetic Crystallite Size Control and Resulting Magnetic and Electrochemical Properties. *J. Electrochem. Soc.* **2010**, *157*, A1158–A1163.
- (72)Launay, H.; Hansen, C. M.; Almdal, K. Hansen Solubility Parameters for a Carbon Fiber/Epoxy Composite. *Carbon* **2007**, *45*, 2859–2865.
- (73)Bergin, S. D.; Sun, Z.; Rickard, D.; Streich, P. V.; Hamilton, J. P.; Coleman, J. N. Multicomponent Solubility Parameters for Single-Walled Carbon Nanotube–Solvent Mixtures. *ACS Nano* **2009**, *3*, 2340–2350.
- (74)Chang, M.; Choi, D.; Fu, B.; Reichmanis, E. Solvent Based Hydrogen Bonding: Impact on Poly(3-hexylthiophene) Nanoscale Morphology and Charge Transport Characteristics. *ACS Nano* **2013**, *7*, 5402–5413.
- (75)Chang, M.; Lee, J.; Kleinhenz, N.; Fu, B.; Reichmanis, E. Photoinduced Anisotropic Supramolecular Assembly and Enhanced Charge Transport of Poly(3-hexylthiophene) Thin Films. *Adv. Funct. Mater.* **2014**, *24*, 4457–4465.
- (76)Guerfi, A.; Kaneko, M.; Petitclerc, M.; Mori, M.; Zaghib, K.  $\text{LiFePO}_4$  Water-Soluble Binder Electrode for Li-Ion Batteries. *J. Power Sources* **2007**, *163*, 1047–1052.
- (77)Chou, K.-S.; Huang, K.-C.; Lee, H.-H. Fabrication and Sintering Effect on the Morph

- ologies and Conductivity of Nano-Ag Particle Films by the Spin Coating Method. *Nanotechnology* **2005**, *16*, 779–784.
- (78)Mihi, A.; Ocana, M.; Miguez, H. Oriented Colloidal-Crystal Thin Films by Spin-Coating Microspheres Dispersed in Volatile Media. *Adv. Mater.* **2006**, *18*, 2244–2249.
- (79)Hansen, C. M. *Hansen Solubility Parameters – a User’s Handbook*, CRC press: Boca Raton, FL, 2007.
- (80)Weisstein, E. *Sphere–Sphere Intersection*, Eric Weisstein’s World of Mathematics, 2009, <http://mathworld.wolfram.com/>.
- (81)Li, X. M.; Reinhoudt, D.; Crego-Calama, M. What Do We Need for a Superhydrophobic Surface? A Review on the Recent Progress in the Preparation of Superhydrophobic Surfaces. *Chem. Soc. Rev.* **2007**, *36*, 1350–1368.
- (82)Yamamoto, H. *Hansen Solubility Parameters (HSP) Double Sphere*, 2010, <https://pirika.com/>.
- (83)Zhu, M.; Park, J.; Sastry, A. M. Particle Interaction and Aggregation in Cathode Material of Li-Ion Batteries: A Numerical Study. *J. Electrochem. Soc.* **2011**, *158*, A1155–A1159.
- (84)Ligneel, E.; Lestriez, B.; Hudhomme, A.; Guyomard, D. Shaping of Advanced Ceramics: The Case of Composite Electrodes for Lithium Batteries. *J. Eur. Ceram. Soc.* **2009**, *29*, 925–929.
- (85)Guy, D.; Lestriez, B.; Bouchet, R.; Guyomarda, D. Critical Role of Polymeric Binders on the Electronic Transport Properties of Composites Electrode. *J. Electrochem. Soc.* **2006**, *153*, A679–A688.
- (86)Peterson, S. W.; Wheeler, D. R. Direct Measurements of Effective Electronic Transport in Porous Li-Ion Electrodes. *J. Electrochem. Soc.* **2014**, *161*, A2175–A2181.
- (87)Gomadam, P. M.; Weidner, J. W.; Zawodzinski, T. A.; Saabb, A. P. Theoretical Analysis for Obtaining Physical Properties of Composite Electrodes. *J. Electrochem. Soc.* **2003**, *150*, E371–E376.
- (88)Park, B.; Aiyar, A.; Park, M. S.; Srinivasarao, M.; Reichmanis, E. Conducting Channel Formation in Poly(3-hexylthiophene) Field Effect Transistors: Bulk to Interface. *J. Phys. Chem. C* **2011**, *115*, 11719–11726.
- (89)Knehr, K. W.; Brady, N. W.; Lininger, C. N.; Cama, C. A.; Bock, D. C.; Lin, Z.; Marschilok, A. C.; Takeuchi, K. J.; Takeuchi, E. S.; West, A.C. Mesoscale Transport in Magnetite Electrodes for Lithium-Ion Batteries. *ECS Trans.* **2015**, *69*, 7–19.

- (90) Murugappan, K.; Silvester, D. S.; Chaudhary, D.; Arrigan, D. W. M. Electrochemical Characterization of an Oleyl-coated Magnetite Nanoparticle-Modified Electrode. *ChemElectroChem* **2014**, *1*, 1211–1218.
- (91) Barton, A. F. M. *Handbook of Solubility Parameters and other cohesion parameters*, CRC press, 1983.
- (92) Goriparti, S.; Miele, E.; Angelis, F. D.; Fabrizio, E. D.; Zaccaria, R. P.; Capiglia, C. Review on Recent Progress of Nanostructured Anode Materials for Li-ion Batteries. *J. Power Sources* **2014**, *257*, 421–443.
- (93) Nitta, N.; Yushin, G. High-Capacity Anode Materials for Lithium-Ion Batteries: Choice of Elements and Structures for Active Particles. *Part. Part. Syst. Charact.* **2014**, *3*, 317–336.
- (94) Sun, Y.; Liu, N.; Cui, Y. Promises and Challenges of Nanomaterials for Lithium-Based Rechargeable Batteries. *Nature Energy* **2016**, *1*, 16071.
- (95) Xiong, Q. Q.; Tu, J. P.; Lu, Y.; Chen, J.; Yu, Y. X.; Qiao, Y. Q.; Wang, X. L.; Gu, C. D. Synthesis of Hierarchical Hollow-Structured Single-Crystalline Magnetite ( $\text{Fe}_3\text{O}_4$ ) Microspheres: The Highly Powerful Storage vs Lithium as an Anode for Lithium Ion Batteries. *J. Phys. Chem. C* **2012**, *116*, 6495–6502.
- (96) Liu, Y.; Zhan, Y.; Ying, Y.; Peng, X.  $\text{Fe}_3\text{O}_4$  Nanoparticle Anchored Layered Graphene Films for High Performance Lithium Storage. *New J. Chem.* **2016**, *40*, 2649–2654.
- (97) Zhang, W.; Bock, D. C.; Pelliccione, C. J.; Li, Y.; Wu, L.; Zhu, Y.; Marschilok, A. C.; Takeuchi, E. S.; Takeuchi, K. J.; Wang, F. Insights into Ionic Transport and Structural Changes in Magnetite during Multiple-Electron Transfer Reactions. *Adv. Energy Mater.* **2016**, 1502471.
- (98) Abraham, A.; Housel, L. M.; Lininger, C. N.; Bock, D. C.; Jou, J.; Wang, F.; West, A. C.; Marschilok, A. C.; Takeuchi, K. J.; Takeuchi, E. S. Investigating the Complex Chemistry of Functional Energy Storage Systems: The Need for an Integrative, Multiscale (Molecular to Mesoscale) Perspective, *ACS Cent. Sci.* **2016**, *2*, 380–387.
- (99) Mike, J. F.; Letkenhaus, J. L. Recent Advances in Conjugated Polymer Energy Storage. *J. Polym. Sci. B Polym. Phys.* **2013**, *51*, 468–480.
- (100) Bracco, G. *Surface Science Techniques*; Springer-Verlag: Berlin, Heidelberg, 2013.
- (101) Zhang, G.; Kim, G.; Choi, W. Visible Light Driven Photocatalysis Mediated via Ligand-to-Metal Charge Transfer (LMCT): An Alternative Approach to Solar Activation of Titania. *Energy Environ. Sci.* **2014**, *7*, 954–966.

- (102) Mukhopadhyay, A.; Joshi, N.; Chattopadhyay, K.; De, G. A Facile Synthesis of PEG-Coated Magnetite ( $\text{Fe}_3\text{O}_4$ ) Nanoparticles and Their Prevention of the Reduction of Cytochrome C *ACS Appl. Mater. Interfaces* **2012**, *4*, 142–149.
- (103) Reddy, M. J.; Kumar, J. S.; Rao, U.V. S.; Chu, P. P. Structural and ionic conductivity of PEO blend PEG solid polymer electrolyte. *Solid State Ion.* **2006**, *177*, 253–256.
- (104) Jow, T. R.; Shacklette, L. W. Electrochemical Characteristics of Alkali-Metal Doped Polyacetylene Electrodes. *J. Electrochem. Soc.* **1998**, *135*, 541–548.
- (105) Saikia, D.; Kumar, A. Ionic Conduction in P(VDF-HFP)/PVDF-(PC + DEC)- $\text{LiClO}_4$  Polymer Gel Electrolytes. *Electrochimica Acta* **2004**, *49*, 2581–2589.
- (106) Lan, Y.-K.; Huang, C.-I. A Theoretical Study of the Charge Transfer Behavior of the Highly Regioregular Poly-3 hexylthiophene in the Ordered State. *J. Phys. Chem. B* **2008**, *112*, 14857–14862.
- (107) Chu, P.-H.; Wang, G.; Fu, B.; Choi, D.; Park, J. O.; Srinivasarao, M.; Reichmanis, E. Synergistic Effect of Regioregular and Regiorandom Poly(3-hexylthiophene) Blends for High Performance Flexible Organic Field Effect Transistors. *Adv. Electron. Mater.* **2016**, *2*, 1500384.
- (108) Fan, X.; Shao, J.; Xiao, X.; Chen, L.; Wang, X.; Li, S.; Ge, H. Carbon Encapsulated 3D Hierarchical  $\text{Fe}_3\text{O}_4$  Spheres as Advanced Anode Materials with Long Cycle Lifetimes for Lithium-Ion Batteries. *J. Mater. Chem. A* **2014**, *2*, 14641–14648.
- (109) Meng, X.; Xu, Y.; Sun, X.; Wang, J.; Xiong, L.; Du, X.; Mao, S. Graphene Oxide Sheets-Induced Growth of Nanostructured  $\text{Fe}_3\text{O}_4$  for a High-Performance Anode Material of Lithium Ion Batteries. *J. Mater. Chem. A* **2015**, *3*, 12938–12946.
- (110) Brady, N. W.; Knehr, K. W.; Cama, C. A.; Lininger, C. N.; Lin, Z.; Marschilok, A. C.; Takeuchi, K. J.; Takeuchi, E. S.; West, A. C. Galvanostatic Interruption of Lithium Insertion into Magnetite: Evidence of Surface Layer Formation. *J. Power Sources* **2016**, *321*, 106–111.
- (111) Lee, S. H.; Yu, S.-H.; Lee, J. E.; Jin, A.; Lee, D. J.; Lee, N.; Jo, H.; Shin, K.; Ahn, T.-Y.; Kim, Y.-W.; Choe, H.; Sung, Y.-E.; Hyeon, T. Self-Assembled  $\text{Fe}_3\text{O}_4$  Nanoparticle Clusters as High-Performance Anodes for Lithium Ion Batteries via Geometric Confinement. *Nano Lett.* **2013**, *13*, 4249–4256.
- (112) Wu, J.; Yue, G.; Xiao, Y.; Lin, J.; Huang, M.; Lan, Z.; Tang, Q.; Huang, Y.; Fan, L.; Yin, S.; Sato, T. An Ultraviolet Responsive Hybrid Solar Cell Based on Titania/Poly(3-hexylthiophene). *Sci. Rep.* **2013**, *3*, 1283.

- (113) Nappini, S.; Bonini, M.; Bombelli, F. B.; Pineider, F.; Sangregorio, C.; Baglioni, P.; Nordèn, B. Controlled Drug Release under a Low Frequency Magnetic Field: Effect of the Citrate Coating on Magnetoliposomes Stability. *Soft Matter* **2011**, *7*, 1025–1037.
- (114) Nappini, S.; Magnano, E.; Bondino, F.; Piš, I.; Barla, A.; Fantechi, E.; Pineider, F.; Sangregorio, C.; Vaccari, L.; Venturelli, L.; Baglioni, P. Surface Charge and Coating of CoFe<sub>2</sub>O<sub>4</sub> Nanoparticles: Evidence of Preserved Magnetic and Electronic Properties. *J. Phys. Chem. C* **2015**, *119*, 25529–25541.
- (115) Yu, M. K.; Park, J.; Jon, S. Targeting Strategies for Multifunctional Nanoparticles in Cancer Imaging and Therapy. *Theranostics* **2012**, *2*, 3–44.
- (116) Wang, C.; Zhu, M.; Liu, H.; Cui, Y.; Chen, Y. A General Method for Mass and Template-free Production of Hierarchical Metal Oxide Spheres at Room-Temperature. *RSC Adv.* **2014**, *4*, 24176–24182.
- (117) Moreno-Castilla, C.; López-Ramón, M. V.; Carrasco-Marina, F. Changes in Surface Chemistry of Activated Carbons by Wet Oxidation. *Carbon* **2000**, *38*, 1995–2001.
- (118) Fujii, T.; de Groot, F. M. F.; Sawatzky, G. A.; Voogt, F. C.; Hibma, T.; Okada, K. In Situ XPS Analysis of Various Iron Oxide Films Grown by NO<sub>2</sub>-assisted Molecular-Beam Epitaxy. *Phys. Rev. B* **1999**, *59*, 3195–3202.
- (119) Thermo Scientific XPS, <http://xpssimplified.com/elements/carbon.php>.
- (120) Hollander, J. M.; Jolly, W. L. X-Ray Photoelectron Spectroscopy. *Acc. Chem. Res.* **1970**, *3*, 193–200.
- (121) Yang, J.; Zou, P.; Yang, L.; Cao, J.; Sun, Y.; Han, D.; Yang, S.; Wang, Z.; Chen, G.; Wang, B.; Kong, X. A Comprehensive Study on the Synthesis and Paramagnetic Properties of PEG-Coated Fe<sub>3</sub>O<sub>4</sub> Nanoparticles. *Appl. Surf. Sci.* **2014**, *303*, 425–432.
- (122) Bock, D. C.; Pelliccione, C. J.; Zhang, W.; Wang, J.; Knehr, K. W.; Wang, J.; Wang, F.; West, A. C.; Marschillok, A. C.; Takeuchi, K. J.; Takeuchi, E. S. Dispersion of Nanocrystalline Fe<sub>3</sub>O<sub>4</sub> within Composite Electrodes: Insights on Battery-Related Electrochemistry. *ACS Appl. Mater. Interfaces* **2016**, *8*, 11418–11430.
- (123) Taberna, P. L.; Mitra, S.; Poizot, P.; Simon, P.; Tarascon, J.-M. High Rate Capabilities Fe<sub>3</sub>O<sub>4</sub>-Based Cu Nano-Architected Electrodes for Lithium-Ion Battery Applications. *Nat. Mater.* **2006**, *5*, 567–573.
- (124) Li, Y.; Tan, B.; Wu, Y. Mesoporous Co<sub>3</sub>O<sub>4</sub> Nanowire Arrays for Lithium Ion Batteries with High Capacity and Rate Capability. *Nano Lett.* **2008**, *8*, 265–270.

- (125) Wang, Y.-Q.; Gu, L.; Guo, Y.-G.; Li, H.; He, X.-Q.; Tsukimoto, S.; Ikuhara, Y.; Wan, L.-J. Rutile-TiO<sub>2</sub> Nanocoating for a High-Rate Li<sub>4</sub>Ti<sub>5</sub>O<sub>12</sub> Anode of a Lithium-Ion Battery. *J. Am. Chem. Soc.* **2012**, *134*, 7874–7879.
- (126) Wang, C.; Wu, H.; Chen, Z.; McDowell, M. T.; Cui, Y.; Bao, Z. Self-Healing Chemistry Enables the Stable Operation of Silicon Microparticle Anodes for High-Energy Lithium-Ion Batteries. *Nat. Chem.* **2013**, *5*, 1042–1048.
- (127) Choi, S.; Kwon, T.-W.; Coskun, A.; Choi, J. W. Highly Elastic Binders Integrating Polyrotaxanes for Silicon Microparticle Anodes in Lithium Ion Batteries. *Science* **2017**, *357*, 279–283.
- (128) Shi, Y.; Peng, L.; Ding, Y.; Zhao, Y.; Yu, G. Nanostructured Conductive Polymers for Advanced Energy Storage. *Chem. Soc. Rev.* **2015**, *44*, 6684–6696.
- (129) Shi, Y.; Zhou, X.; Zhang, J.; Bruck, A. M.; Bond, A. C.; Marschilok, A. C.; Takeuchi, K. J.; Takeuchi, E. S.; Yu, G. Nanostructured Conductive Polymer Gels as a General Framework Material to Improve Electrochemical Performance of Cathode Materials in Li-Ion Batteries. *Nano Lett.* **2017**, *17*, 1906–1914.
- (130) Shi, Y.; Zhang, J.; Bruck, A. M.; Zhang, Y.; Li, J.; Stach, E. A.; Takeuchi, K. J.; Marschilok, A. C.; Takeuchi, E. S.; Yu, G. A Tunable 3D Nanostructured Conductive Gel Framework Electrode for High-Performance Lithium Ion Batteries. *Adv. Mater.* **2017**, *29*, 1603922.
- (131) Shi, Y.; Zhou, X.; Yu, G. Material and Structural Design of Novel Binder Systems for High-Energy, High-Power Lithium-Ion Batteries. *Acc. Chem. Res.* **2017**, *50*, 2642–2652.
- (132) Ban, C.; Wu, Z.; Gillaspie, D. T.; Chen, L.; Yan, Y.; Blackburn, J. L.; Dillon, A. C. Nanostructured Fe<sub>3</sub>O<sub>4</sub>/SWNT Electrode: Binder-Free and High-Rate Li-Ion Anode. *Adv. Mater.* **2010**, *22*, E145–E149.
- (133) Kim, J.-M.; Kim, J. A.; Kim, S.-H.; Uhm, I. S.; Kang, S. J.; Kim, G.; Lee, S.-Y.; Yoon, S.-H.; Lee, S.-Y. All-Nanomat Lithium-Ion Batteries: A New Cell Architecture Platform for Ultrahigh Energy Density and Mechanical Flexibility. *Adv. Energy Mater.* **2017**, 1701099.
- (134) Zhang, H.; Yu, X.; Braun, P. V. Three-Dimensional Bicontinuous Ultrafast-Charge and -Discharge Bulk Battery Electrodes. *Nat. Nanotechnol.* **2011**, *6*, 277–281.
- (135) Pikul, J. H.; Zhang, H. G.; Cho, J.; Braun, P. V.; King, W. P. High-Power Lithium Ion Microbatteries from Interdigitated Three-Dimensional Bicontinuous Nanoporous Electrodes. *Nat. Commun.* **2013**, *4*, 1732.

- (136) Chen, Z.; Kim, D. Y.; Hasegawa, K.; Osawa, T.; Noda, S. Over 99.6 wt%-Pure, Sub-Millimeter-Long Carbon Nanotubes Realized by Fluidized-Bed with Careful Control of the Catalyst and Carbon Feeds. *Carbon* **2014**, *80*, 339–350.
- (137) Kim, D. Y.; Sugime, H.; Hasegawa, K.; Osawa, T.; Noda, S. Sub-Millimeter-Long Carbon Nanotubes Repeatedly Grown on and Separated from Ceramic Beads in a Single Fluidized Bed Reactor. *Carbon* **2011**, *49*, 1972–1979.
- (138) Fan, T.; Pan, D.; Zhang, H. Study on Formation Mechanism by Monitoring the Morphology and Structure Evolution of Nearly Monodispersed Fe<sub>3</sub>O<sub>4</sub> Submicroparticles with Controlled Particle Sizes. *Ind. Eng. Chem. Res.* **2011**, *50*, 9009–9018.
- (139) Kwon, Y. H.; Minnici, K.; Huie, M. M.; Takeuchi, K. J.; Takeuchi, E. S.; Marschillok, A. C.; Reichmanis, E. Electron/Ion Transport Enhancer in High Capacity Li-Ion Battery Anodes. *Chem. Mater.* **2016**, *28*, 6689–6697.
- (140) Moroni, R.; Börner, M.; Zielke, L.; Schroeder, M.; Nowak, S.; Winter, M.; Manke, I.; Zengerle, R.; Thiele, S. Multi-Scale Correlative Tomography of a Li-Ion Battery Composite Cathode. *Sci. Rep.* **2016**, *6*, 30109.
- (141) Liu, J.; Moo-Young, J.; McInnis, M.; Pasquinelli, M. A.; Zhai, L. Conjugated Polymer Assemblies on Carbon Nanotubes. *Macromolecules* **2014**, *47*, 705–712.
- (142) Li, X.; Yang, J.; Hu, Y.; Wang, J.; Li, Y.; Cai, M.; Li, R.; Sun, X. Novel Approach Toward a Binder-Free and Current Collector-Free Anode Configuration: Highly Flexible Nanoporous Carbon Nanotube Electrodes with Strong Mechanical Strength Harvesting Improved Lithium Storage. *J. Mater. Chem.* **2012**, *22*, 18847–18853.
- (143) Jaumann, T.; Balach, J.; Klose, M.; Oswald, S.; Langklotz, U.; Michaelis, A.; Eckert, J.; Giebeler, L. SEI-Component Formation on Sub 5 nm Sized Silicon Nanoparticles in Li-Ion Batteries: The Role of Electrode Preparation, FEC Addition and Binders. *Phys. Chem. Chem. Phys.* **2015**, *17*, 24956–24967.
- (144) Kim, H.; Kim, H.; Kim, H.; Kim, J.; Yoon, G.; Lim, K.; Yoon, W.-S.; Kang, K. Understanding Origin of Voltage Hysteresis in Conversion Reaction for Na Rechargeable Batteries: The Case of Cobalt Oxides. *Adv. Funct. Mater.* **2016**, *26*, 5042–5050.
- (145) Shu, J.; Li, H.; Yang, R.; Shi, Y.; Huang, X. Cage-Like Carbon Nanotubes/Si Composite as Anode Material for Lithium Ion Batteries. *Electrochem. Commun.* **2006**, *8*, 51–54.
- (146) Chou, S.-L.; Zhao, Y.; Wang, J.-Z.; Chen, Z.-X.; Liu, H.-K.; Dou, S.-X. Silicon/Single-Walled Carbon Nanotube Composite Paper as a Flexible Anode Material for Lithium Ion Batteries. *J. Phys. Chem. C* **2010**, *114*, 15862–15867.



- (147) Xue, L.; Xu, G.; Li, Y.; Li, S.; Fu, K.; Shi, Q.; Zhang, X. Carbon-Coated Si Nano particles Dispersed in Carbon Nanotube Networks As Anode Material for Lithium-Ion Batteries. *ACS Appl. Mater. Interfaces* **2013**, *5*, 21–25.
- (148) Zhou, X.; Yin, Y.-X.; Wan, L.-J.; Guo, Y.-G. Facile Synthesis of Silicon Nanoparticles Inserted into Graphene Sheets as Improved Anode Materials for Lithium-Ion Batteries. *Chem. Commun.* **2012**, *48*, 2198–2200.
- (149) Zhou, X.; Yin, Y.-X.; Wan, L.-J.; Guo, Y.-G. Self-Assembled Nanocomposite of Silicon Nanoparticles Encapsulated in Graphene through Electrostatic Attraction for Lithium-Ion Batteries. *Adv. Energy Mater.* **2012**, *2*, 1086–1090.
- (150) Wang, B.; Li, X.; Zhang, X.; Luo, B.; Jin, M.; Liang, M.; Dayeh, S. A.; Picraux, S. T.; Zhi, L. Adaptable Silicon–Carbon Nanocables Sandwiched between Reduced Graphene Oxide Sheets as Lithium Ion Battery Anodes. *ACS Nano* **2013**, *7*, 1437–1445.
- (151) Minnici, K.; Kwon, Y. H.; Huie, M. M.; de Simon, M. V.; Zhang, B.; Bock, D. C.; Wang, J.; Wang, J.; Takeuchi, K. J.; Takeuchi, E. S.; Marschilok, A. C.; Reichmanis, E. High Capacity Li-Ion Battery Anodes: Impact of Crystallite Size, Surface Chemistry and PEG-Coating. *Electrochim. Acta* **2018**, *260*, 235–245.
- (152) Kwon, Y. H.; Park, J. J.; Housel, L. M.; Minnici, K.; Zhang, G.; Lee, S. R.; Lee, S. W.; Chen, Z.; Noda, S.; Takeuchi, E. S.; Takeuchi, K. J.; Marschilok, A. C.; Reichmanis, E. Carbon Nanotube Web with Carboxylated Polythiophene “Assist” for High-Performance Battery Electrodes. *ACS Nano* **Article ASAP** DOI: 10.1021/acsnano.7b08918.
- (153) Lee, J.-I.; Park, S. High-Performance Porous Silicon Monoxide Anodes Synthesized via Metal-Assisted Chemical Etching. *Nano Energy* **2013**, *2*, 146–152.
- (154) Ko, M.; Chae, S.; Ma, J.; Kim, N.; Lee, H.-W.; Cui, Y.; Cho, J. Scalable Synthesis of Silicon-Nanolayer-Embedded Graphite for High-Energy Lithium-Ion Batteries. *Nat. Energy* **2016**, *1*, 16113.
- (155) Lindström, H.; Södergren, S.; Solbrand, A.; Rensmo, H.; Hjelm, J.; Hagfeldt, A.; Lindquist, S.-E. Li<sup>+</sup> Ion Insertion in TiO<sub>2</sub> (Anatase). 2. Voltammetry on Nanoporous Films. *J. Phys. Chem. B* **1997**, *101*, 7717–7722.
- (156) Simon, P.; Gogotsi, Y.; Dunn, B. Where do batteries end and supercapacitors begin? *Science* **2014**, *343*, 1210–1211.
- (157) Dong, X.; Chen, L.; Liu, J.; Haller, S.; Wang, Y.; Xia, Y. Environmentally-Friendly Aqueous Li (or Na)-Ion Battery with Fast Electrode Kinetics and Super-Long Life. *Sci. Adv.* **2016**, *2*, e1501038.

- (158) Tao, Y.; Wei, Y.; Liu, Y.; Wang, J.; Qiao, W.; Ling, L.; Long, D. Kinetically-Enhanced Polysulfide Redox Reactions by Nb<sub>2</sub>O<sub>5</sub> Nanocrystals for High-Rate Lithium–Sulfur Battery. *Energy Environ. Sci.* **2016**, *9*, 3230–3239.
- (159) He, P.; Zhang, X.; Wang, Y.-G.; Cheng, L.; Xia, Y.-Y. Lithium-Ion Intercalation Behavior of LiFePO<sub>4</sub> in Aqueous and Nonaqueous Electrolyte Solutions. *J. Electrochem. Soc.* **2008**, *155*, A144-A150.
- (160) Wang, W. L.; Park, J.-Y.; Gu, H.-B. Enhanced Reaction Kinetic of Fe<sub>3</sub>O<sub>4</sub>-Graphite Nanofiber Composite Electrode for Lithium Ion Batteries. *Trans. Electr. Electron. Mater.* **2014**, *15*, 338–343.
- (161) Nguyen, V. H.; Wang, W. L.; Jin, E. M.; Gu, H.-B. Impacts of Different Polymer Binders on Electrochemical Properties of LiFePO<sub>4</sub> Cathode. *Appl. Surf. Sci.* **2013**, *282*, 444–449.
- (162) Mansour, N.; Momeni, A.; Karimzadeh, R.; Amini, M. Blue-Green Luminescent Silicon Nanocrystals Fabricated by Nanosecond Pulsed Laser Ablation in Dimethyl Sulfoxide. *Opt. Mater. Express* **2012**, *2*, 740–748.
- (163) Radvanyi, E.; De Vito, E.; Porcher, W.; Larbi, S. J. S. An XPS/AES Comparative Study of the Surface Behaviour of Nano-Silicon Anodes for Li-Ion Batteries. *J. Anal. At. Spectrom.* **2014**, *29*, 1120–1131.
- (164) Kim, H. J.; Choi, S.; Lee, S. J.; Seo, M. W.; Lee, J. G.; Deniz, E.; Lee, Y. J.; Kim, E. K.; Choi, J. W. Controlled Prelithiation of Silicon Monoxide for High Performance Lithium-Ion Rechargeable Full Cells. *Nano Lett.* **2016**, *16*, 282–288.
- (165) Lee, D. J.; Ryou, M.-H.; Lee, J.-N.; Kim, B. G.; Lee, Y. M.; Kim, H.-W.; Kong, B.-S.; Park, J.-K.; Choi, J. W. Nitrogen-Doped Carbon Coating for a High-Performance SiO Anode in Lithium-Ion Batteries. *Electrochem. Commun.* **2013**, *34*, 98–101.
- (166) Morita, T.; Takami, N. Nano Si Cluster-SiO<sub>x</sub>-C Composite Material as High-Capacity Anode Material for Rechargeable Lithium Batteries. *J. Electrochem. Soc.* **2006**, *153*, A425–A430.
- (167) Park, E.; Yoo, H.; Lee, J.; Park, M.-S.; Kim, Y.-J.; Kim, H. Dual-Size Silicon Nanocrystal-Embedded SiO<sub>x</sub> Nanocomposite as a High-Capacity Lithium Storage Material. *ACS Nano* **2015**, *9*, 7690–7696.
- (168) Choi, S.; Jung, D. S.; Choi, J. W. Scalable Fracture-Free SiOC Glass Coating for Robust Silicon Nanoparticle Anodes in Lithium Secondary Batteries. *Nano Lett.* **2014**, *14*, 7120–7125.
- (169) Burgess, R.; Buono, C.; Davies, P. R.; Davies, R. J.; Legge, T.; Lai, A.; Lewis, R.;

- Morgan, D. J.; Robinson, N.; Willock, D. J. The Functionalisation of Graphite Surfaces with Nitric Acid: Identification of Functional Groups and Their Effects on Gold Deposition. *J. Catal.* **2015**, *323*, 10–18.
- (170) Welzel, P. B.; Grimmer, M.; Renneberg, C.; Naujox, L.; Zschoche, S.; Freudenberger, U.; Werner, C. Macroporous StarPEG-Heparin Cryogels. *Biomacromolecules* **2012**, *13*, 2349–2358.

## VITA

Yo Han Kwon was born and raised in Seoul, South Korea. He received B.S. degree in Molecular System Engineering (Polymer Engineering) from Hanyang University in 2007 and M.S. degree in Chemical & Biomolecular Engineering from KAIST in 2009. His research topic at KAIST was controlling the phase separation of polymer blends and preparing semi-interpenetrating polymer networks (semi-IPNs) for DMFC membranes with a nanoscale water-channel structure. After graduation from KAIST, he had worked in Battery R&D at LG Chem (South Korea) for 5years, participating in the several projects for developing advanced battery materials and a new battery system having three-dimensional flexibility. He then joined the research group of Prof. Elsa Reichmanis in fall 2014 to pursue his PhD in the School of Chemical & Biomolecular Engineering at Georgia Tech.